Fracture of Brittle Materials and Bimaterial Interfaces in the Presence of Compressive Stresses

by

Anthony Taylor Owens

A dissertation submitted to the Graduate Faculty of
Auburn University
in partial fulfillment of the
requirements for the Degree of
Doctor of Philosophy

Auburn, Alabama
December 10, 2022

Keywords: Fracture, Adhesive, Bimaterial Interface, Compression

Copyright 2022 by Anthony Taylor Owens

Approved by

Dr. Hareesh V. Tippur, Chair, McWane Professor of Mechanical Engineering
Dr. Jeffrey C. Suhling, Quina Distinguished Professor of Mechanical Engineering
Dr. Robert L. Jackson, Professor of Mechanical Engineering
Dr. James Davidson, Gottlieb Endowed Chair Professor of Civil Engineering

Abstract

The present work is aimed at the experimental investigation of the effect of local compressive stress fields on a crack lying along an interface. This is relevant to problems such as interfaces found in adhesively bonded joints or interfaces found in composite materials. In both examples, the interface is between two materials with significantly different elastic properties, and the fracture behavior along the interface is a significant contributor to bulk material performance. Further, complex, multi-axis load cases arise that can result in either shear-tension or shear-compression load states along the interface.

An experimental procedure is developed that utilizes displacement fields measured using digital image correlation method to extract fracture parameters by coupling the full-field data with robust contour integration algorithms built into a commercial finite element code. A three-point bend semi-circular beam geometry is first utilized for the study of mixed-mode fracture in homogeneous materials experiencing quasi-static loads and then extended to dynamic conditions using a single-point impact configuration. The use of the geometry is subsequently extended to experiments where the crack is in the aforementioned state of shear-compression loading. A new test method is then introduced to allow a range of combined shear and compression load states on a crack lying along a bimaterial interface. Each experimental technique is critically evaluated. Detailed results for homogeneous and interface crack specimen geometries are presented to improve the understanding of the effect of compressive stress fields in the vicinity of the crack tip. Under the compressive load states, both the homogeneous and the interface behaviors undergo a marked increase in fracture toughness as the compression stress increases. An empirical relationship is derived to describe the response. The fracture toughness is shown to increase in a near-linear fashion as the compressive stress increases. The same observations

were made with respect to the dynamic fracture behavior as well. This contribution serves to quantify the relationship between in-plane stress states and fracture toughness under static and dynamic conditions, as well as along bimaterial interfaces.

Another significant contribution from the present study is the development of a numerical technique for improving the data reduction and post processing process. One of the challenges associated with the interface fracture experiments and the dynamic fracture experiments is the ability to reliably locate the crack tip location for post-test analyses. An image processing technique for edge detection is adapted for use in the crack tip identification problem. Analytical investigations are used to demonstrate the performance for a variety of experimental fracture problems.

Acknowledgments

Support from an entire community of individuals around me has made this endeavor possible. The guidance received from the faculty in the Department of Mechanical Engineering and Department of Civil Engineering at Auburn, especially my advisor, Dr. Hareesh Tippur, is gratefully acknowledged. His insight into this topic has been invaluable and it goes without saying that I would not have learned what I have learned without his guidance. I would also like to thank Dr. Thomas Denney from the Department of Electrical Engineering for serving as the external reader for this work. This work would not have been possible without the countless discussions with those colleagues that I work side by side with day in and day out as well as those associates and mentors that are spread across the materials and mechanics community. Their advice has facilitated this effort and I am appreciative of their continual encouragement, insight, and general camaraderie. Lastly, without the support of my wife, Amanda, children, Will and Caroline, and my other immediate family in this pursuit, none of this would be possible, as they are all my foundation and inspiration. Without them, I would have not made it a fraction of the way down this path.

Table of Contents

List of Tables

List of Figures

List of Abbreviations

ASTM	American Society for Testing and Materials
C	Celsius
DIC	Digital Image Correlation
DMA	Dynamic Mechanical Analysis
DSR	Decompose, shift, reconstruct method
deg	Degrees
FE	Finite element
G_C	Critical strain energy release rate
GPa	Gigapascals
kN	kilo-Newton
$K_{I,CR}$	Critical mode I stress intensity factor
$K_{II,CR}$	Critical mode II stress intensity factor
m	Meters
mm	Millimeters
MATLAB	Matrix Laboratory
MERR	Maximum Energy Release Rate
MTS	Maximum Tangential Stress
MPa	Megapascals
MPa-√m	Megapascal square root meter

N	Newton
NMS	Non-Maximal Suppression
PMMA	Polymethyl methacrylate
s	seconds
SCB	Semi-circular beam
SEM	Scanning Electron Microscope
SIF	Stress intensity factor
TETA	Triethylenetetramine
WWFE	Worldwide failure exercise
°	Degrees

Chapter 1

Introduction

Composite materials offer many advantages in terms of structural performance. More precisely, they have high specific strength and stiffness, which makes them favorable for many applications. Their elastic modulus and tensile strength properties are generally very high along the direction of the fibers, and their density is low relative to more traditional materials like steel or aluminum. In recent years, composite materials have been sought for a wide range of applications. In commercial aviation, rising operating costs have motivated aircraft manufacturers to pursue structural weight reduction techniques using composite materials. In the automotive and sporting goods industries, composite materials have been widely used to improve performance for a pervasive range of products to include drive shafts, frame components, body panels, baseball bats, golf clubs, and a multitude of other things. As composite manufacturing technologies evolve, production capacities across the industry for fiber reinforced composites and their constituent materials increases, and thus they become more feasible to use from a cost standpoint and are being exploited for use in numerous industries.

Despite their many advantages from a structural standpoint, as with any material, fracture considerations are an important factor in structural applications of composites. The importance of fracture in overall structural performance of composites is seen as the key motivator for the present work. More specifically, the key areas relevant to fracture that motivate the current work are adhesively bonded structural joints and fiber-matrix interface behavior.

First and foremost, fracture behavior plays an important role in adhesively bonded interfaces that are often used in composite structures. The need for such joining arrangements arises from a challenge that persists with many composite structural applications which is the ability to attach secondary components and structures to primary composite structures. Composite materials tend to have relatively low bearing strength, thus fastening through traditional methods such as bolts, screws, or rivets often requires localized buildups to successfully transfer mechanical loads across a joint in a structural assembly. The cost and fabrication complexity associated with these localized buildups make attachment through adhesive bonding an attractive process, leading to more optimized and weight-efficient designs. Adhesively bonded joints that can transfer load via lap shear type arrangements offer many advantages. Depending on the application, excessively thick material buildups can be avoided, thus reducing the complexity of the overall laminate. The disadvantage of such an arrangement, however, is the difficulty to assess the structural performance of the adhesive joint. Due to the complexity associated with the stress distribution in the adhesive layer and the interfacial properties, analysis is not a trivial process, and it is imperative to understand the fracture behavior of such joint arrangements.

Secondly, fracture becomes an important consideration in the overall performance of the material system due to the interface between the matrix material and the reinforcing material. The interface between the fiber and matrix is a critical feature in the overall system. In tension-dominated load cases, a fiber-matrix interface may be desired that maximizes uniformity of load across the many filaments in the lamina. Whereas, in a compression-dominated load case, the desire might be to obtain an interface that maximizes fiber stability to prevent micro-buckling in the individual reinforcing filaments and maximize compressive strength. In material formulation and composite material design, a significant amount of attention is often given to the characteristics of the fiber-matrix interface to include chemical and mechanical surface treatment of the structural reinforcing filaments and formulation of the matrix chemistry to achieve a specific interface behavior, tailored to a specific application.

1.1 General concepts in fracture mechanics

To state it concisely, the field of fracture mechanics is generally concerned with the initiation and propagation of crack and crack-like defects in materials. Well before the many recent advancements in fracture mechanics, mankind has generally demonstrated an adept understanding of fracture. For instance, the concept of using a simple wedge to split one piece of material (e.g., firewood) into smaller pieces of material demonstrates an intuitive understanding of fracture and is itself an interesting anisotropic fracture problem.

Events in the last century, however, have served to spur further progress in the field. One famous example that is commonly cited in fracture texts is that of the DeHavilland Comet [1, 2]. One of the first jetliners, which went into service in the 1950's, suffered two catastrophic failures with significant loss of life. After extensive investigation and testing, it was determined that the fuselage fractured in flight due to failures initiating at the corners of cutouts in the fuselage for viewing windows. These locations featured sharp corners which caused local areas of stress concentration that provided the conditions for crack initiation and propagation under fatigue loading.

Investigation of the mechanics of fracture processes dates back several hundred years; however, pioneering work by Inglis [3] began to develop an understanding of states of stress in the vicinity of elliptical holes. Later advancements by Griffith [4] made significant contributions to the field when he began to understand fracture processes in terms of the strain energy in the locality of a crack. Irwin [5] and Orowan [6] further advanced Griffith's work. The general principle of this early work considered a flaw in a material undergoing external work. The key mechanisms of consumption of this energy are elastic strain energy, plastic deformation near the flaw, and eventually creation of new surfaces through the process of fracture. For a given state of stress, once a critical flaw size is achieved, there is sufficient energy in the system to create new surfaces. The generic form of the Griffith equation that relates critical flaw size and stress at failure using the critical strain energy release rate, G_C, is

$$\sigma_f = \sqrt{\frac{EG_C}{\pi a}} \qquad [1\text{-}1]$$

An alternative to the energy balance approach is the stress intensity factor approach which examines the state of stress near the crack tip. Typically, three different pure modes of fracture are considered: Mode I, which considers tensile opening of a crack, Mode II, which considers in-plane shear deformation of a crack, and Mode III, which considers out-of-plane shear deformation of a crack as illustrated in Figure 1-1.

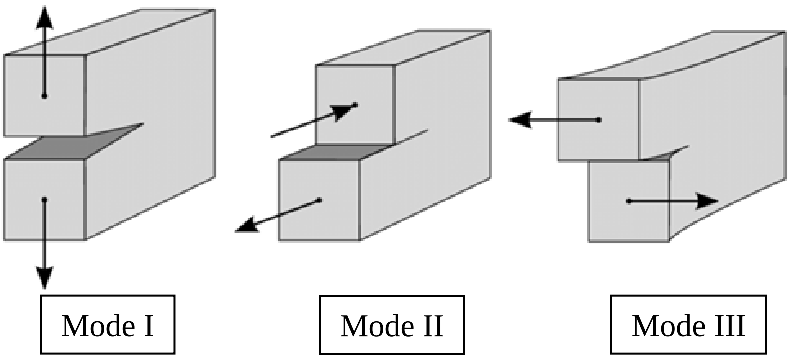

Figure 1-1: Illustration of modes of fracture

For the general Mode I case, the solution developed by Westergaard [7] relates the stress to the radial distance from the crack tip (in polar coordinates), r, and the angular position along the crack surface, θ. The solution introduces the stress intensity factor, K_I. In its most simple form, the relationship follows the general form shown in [1-2].

$$\sigma_X = \frac{K_I}{\sqrt{2\pi r}} \cos\frac{\theta}{2} \tag{1-2}$$

The relationship is dependent on geometry and has been developed for a wide range geometries.

1.2 Mechanics of lap shear joints

As previously stated, one of the motivations of the present work is to improve the understanding of fracture mechanics as it relates to the design of adhesively bonded structural joints. The stress field in an adhesively bonded joint is quite complex and is complicated by the stress concentrations at each end of the adhesive layer as well as the fact that it involves an interface between two elastically dissimilar materials. Volkerson [8] developed a closed form solution for analysis of stress fields in a lap joint based on an extension of the mechanics of shear lag in fastened joints. The closed form solution assumes that shear stresses are constant through the thickness of the adhesive layer and that the adhesive is in a state of pure shear. The solution was derived using the assumption that the adherends themselves were being loaded in a uniaxial state of tension. The tensile stress is maximum at one end of the overlap and diminishes gradually to zero as you move along the length of the adhesive layer. The second adherend follows the opposite pattern. The solution was developed for single and double lap shear joints. The basic expression derived by Volkerson is available in [1-3]:

$$\tau(x) = \frac{\lambda P}{4}\left[\frac{\cosh(\lambda x)}{\sinh(\lambda c)} - \frac{E_i t_i - 2E_o t_o}{E_i t_i + 2E_o t_o} * \frac{\sinh(\lambda x)}{\cosh(\lambda c)}\right] \quad [1\text{-}3]$$

$$\lambda^2 = \frac{G_a}{t_a}\left(\frac{1}{E_o t_o} + \frac{2}{E_i t_i}\right) \quad [1\text{-}4]$$

The subscripts *o*, *i*, and *a* denote the respective components relative to the outer adherend, inner adherend, and adhesive. The parameter *P* denotes the loading applied at the end of the inner adherend, and the parameter *c* is half the length of the adhesive. The origin of the *x*-coordinate is in the middle of the adhesive. It is important to understand this general stress distribution, as it has implications to the performance of the structural joint. To give an example, parameters such as the adhesive thickness and the elastic properties of the adherend can influence the distribution and maximum amplitude of this shear stress distribution. Goland and Reissner [9] extended the solution to address shortcomings in Volkerson's approach. Specifically, they extended the analysis to account for the flexural loads in a traditional lap shear test specimen due to the eccentricity of the adherends. Since the axes of the two adherends are offset from one another, a bending moment is developed in the region of the overlap. This extension introduces the concept of peel stress in the joint and includes the effects of peel stress on the mechanics of the load transfer in the joint.

From an experimental standpoint, several techniques have been used to understand the general mechanics of lap shear geometries. Specifically, early efforts used photoelasticity and moiré methods to develop the fundamental understanding of adhesive joints. Even though it wasn't technically an adhesively bonded joint, in 1912, Coker [10] characterized the shear stress distribution in an overlapping arrangement. His work utilized a plate of photoelastic material with three rows of holes.

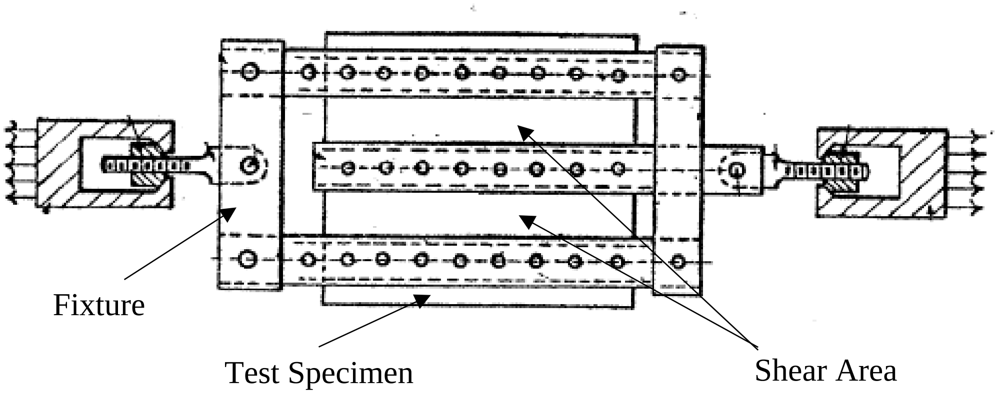

Figure 1-2: Shear test geometry from [10]

The two outer rows of holes were used to pull the test specimen and the center row of holes was used to restrain the specimen. Due to this arrangement, the regions between the rows of holes become analogous to two long, narrow plates loaded in pure shear. This load case would be similar to a double lap shear test coupon where the adherends were very stiff relative to a more compliant thin layer of adhesive. Obviously, this is not an ideal representation, but it results in a shear stress distribution that shares many of the same characteristics as that of a lap shear geometry. The work showed that in general the directions of principal stresses were inclined at an angle of 45° relative to the axis of the load frame. At the edges of the plate, however, the principal directions changed rapidly. Wider plates produced a more gradual change in the orientations of principal directions, demonstrating the general distribution of shear strain proposed by Volkerson [8].

McLaren and McInnes [11] studied the effect of adherend eccentricity using photoelasticity. They conducted two sets of experiments. One set utilized 12.7 mm thick adherends with a simulated layer of adhesive included in the geometry. Simulated adhesive thicknesses ranged between 0 and 12.7 mm. The entire model was a single casting of epoxy. The second set of experiments used aluminum adherends that were bonded together using an adhesive having an elastic modulus that was about 5% of that of the aluminum adherends. For each test, the load was applied through attachments that allowed the load direction to freely follow the rotation of the test sample as the adherends deformed in bending. They experimentally observed that at the center of the adhesive layer (in the length direction), shear stress was essentially zero. It was instead, in a state of axial tensile stress and normal stress (or peel stress). Generally, they made similar observations to those predicted analytically in [9].

Kutscha [12] studied stress distributions in adhesively bonded joints using 2024-T3 aluminum alloy adherends. The adherends and the adhesive layer were relatively thin as compared to the previously reviewed studies. Specifically, the aluminum adherends had a thickness of 1.63 mm and the adhesive had a thickness ranging from 0.737 mm to 0.787 mm. The intent of Kutscha's study was to understand the effect of the length of the overlap in the joint. Care was taken to size the test specimen such that a condition of plane strain existed in the adhesive layer. The aluminum adherends were bonded together using a photoelastic plastic. To acquire the stress field data, a standard polariscope was utilized. Some key observations were that the peak stress value, which occurs at the stress concentration where the adhesive terminates, increased as a function of overlap length. Generally, their experimental measurements agreed well with those predicted analytically using the techniques presented in [9].

Cooper and Sawyer [13] performed photoelastic experiments that studied the relationship between adhesive and adherend stiffness effects. The authors created models with three different configurations. The first model utilized adherends and an adhesive layer that were the same. The second model utilized adherends bonded together with an adhesive, however, the adhesive had the same elastic modulus as the adherends. The last model utilized a soft epoxy material for the adhesive layer. The modulus of this adhesive layer was much lower than that of the adherend. Their work further validated the proposed analytical techniques presented in [9].

Sen and Jones [14] studied the distributions of stress and strain in double lap bonded joints that were bonded together with a viscoelastic adhesive. Their work compared finite element simulations with experimental results from photoelastic and photoviscoelastic examinations of four different geometries of double lap joints. Burger and Voloshin [15, 16] and Mallik, et al. [17] studied adhesive joints in composite structures using half fringe photoelasticity. The half fringe photoelasticity technique was used to automate the data collection, analysis, and display process for the full-field normal stresses for single lap joint experimental models. Specifically, they studied isotropic to isotropic joints and isotropic to orthotropic joints. More recently, Lei, et al. [18] studied shear stresses in an aluminum to epoxy joint loaded in a double lap shear configuration. The work was interesting in that it employed a phase-shifting method to evaluate the fringe contour experimental measurements. The four-step color phase shifting method utilized four images acquired at varying angles of the polarizer axes relative to the optical axis ($\beta = 0, \pi/8, \pi/4$, and $3\pi/8$). The isoclinic parameter was obtained directly for 0 to $\pi/4$ and extended to $\pi/2$. The isoclinic data was then unwrapped from the $\pi/2$ intervals. The isotropic regions were initially unwrapped and then the stress concentrations were unwrapped after that. Lei’s work extended this four-step procedure to include additional images using a circular polariscope setup. The authors studied the shear load transfer across the interface in the double lap shear configuration and were able to plot full-field contours of the shear stress in the epoxy. Additionally, the authors were able to observe residual shear stresses that had accumulated due to coefficient of thermal expansion mismatch during the curing process. By collecting experimental data in the unloaded state, this shear stress could be de-coupled from the shear stress induced by mechanical loading.

Post, et al. [19, 20] studied displacement fields in adhesively bonded joints using high sensitivity moiré interferometry. The technique was used to generate contour maps of in-plane displacement components, *u* and *v*, in thick adherend lap joints. Pristine lap joints and cracked lap joints were both studied. In terms of the optical configuration, the setup is documented in detail in [20]. In summary, a mold was used to transfer a high resolution crossed line metallic film grating pattern onto the sample. The mold resulted in a thin layer of epoxy (approximately 0.0254 mm) on the specimen surface with the phase grating imprinted into it. Two incident beams of light at two different angles were used to create a virtual reference grating. When the lines of the reference grating lines were perpendicular to the x-axis, the interference pattern resulted in a map of the x-direction displacements, *u*. When the lines of the reference grating were parallel to the *x*-axis, the interference pattern resulted in a map of the *y*-direction displacements, *v*. The optical arrangement was such that both reference gratings were present during the experiment, but the reference grating light from one of the directions could be selectively blocked out. The specimen diffraction grating had a frequency of 1,200 lines per mm and the reference grating had a frequency of 2,400 lines per mm. The basic test specimen was a single lap shear specimen. The study also included test specimens with a cracked adhesive configuration. The geometry for those tests was slightly different. Fig. 6 shows the same data at the midpoint of the overlap region and at the edge of the overlap region.

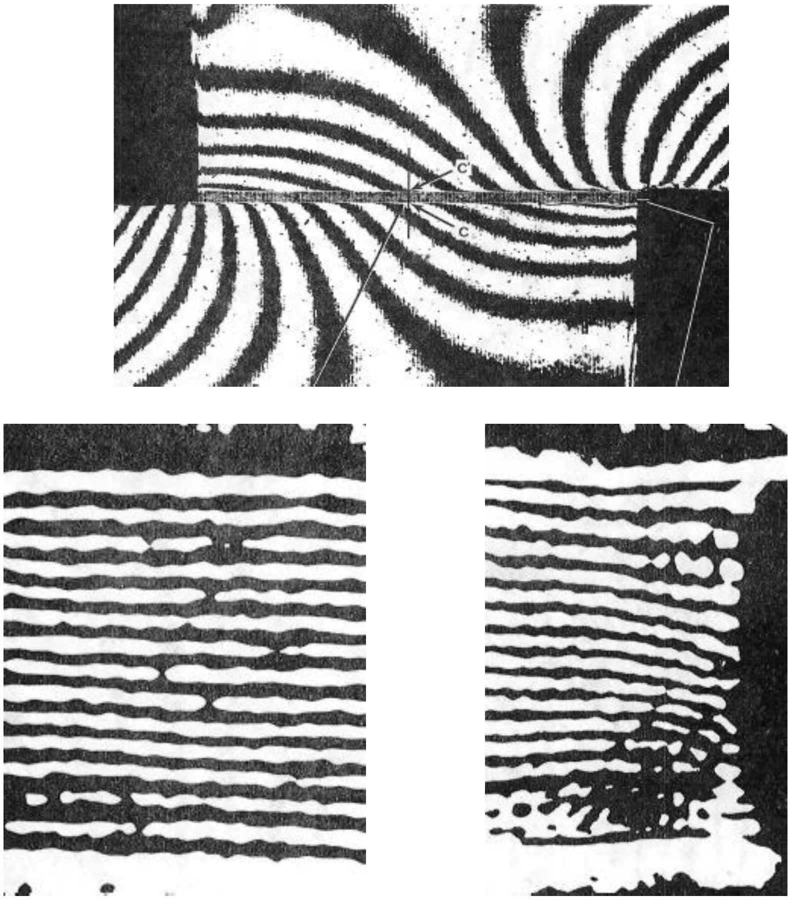

Figure 1-3: High resolution displacement results for overall (top) and enlarged fringe map from [20] in the center of the joint (lower, left) and edge of joint (lower, right)

As noted by the authors, the fringes were parallel with each other and generally parallel with the adherend surfaces in the adhesive layer. In both test specimen configurations, the adherends were 2024 aluminum and the adhesive was FM-73 rubber toughened epoxy film adhesive. The high frequency fringes were able to capture very high-resolution displacement data in the adherends as well as in the adhesive layer itself.

Another research work was published by Asundi [21] that focused on similar measurements. A similar thick lap shear specimen configuration was studied with an adhesive layer thickness of approximately 0.305 mm. The adherends were made of aluminum and the adhesive was Araldite resin AWl06 and hardener HV9530. The moiré interferometry setup consisted of a grating with a frequency of 600 lines per mm and a Helium-Neon laser was utilized to illuminate the test sample surface. Coherent light was incident on the specimen surface from two equal and opposite angles such that a virtual grating was created with a frequency that was twice that of the frequency created on the specimen surface. The authors were able to extract the relative displacement data at various positions along the length of the adhesive layer.

In 1996, Tsai, et al. [22] published experimental investigations into thick-adherend lap shear specimens. The adherends were 9.53 mm thick aluminum and the adhesive was Cytec FM300.08. The overlap region had a 9.53 mm length. The specimens were approximately 25.4 mm wide. With respect to the optical setup, a moiré grating with a frequency of 1,200 lines per mm was attached to the edge of the specimen in the region of interest. The system was configured to provide x-direction and y-direction displacement data during the tests using a portable achromatic interferometer. KGR-1 extensometers were used to generate shear strain data during the test as well. The test specimen also utilized a strain gage rosette to determine shear strain. One of the objectives of the study was to evaluate the effect of load eccentricity on the shear strain distribution in the adhesive. This is likely due to the out-of-plane moment that is created in the specimen.

In 2002, Mollenhauer, et al. [23] published work from the study of adhesively bonded joints in the context of composite repairs. Their main interest area was with respect to lifetime service prediction and had a goal of developing an accurate description of loading and environment history as well as their effects on adherends and adhesive. The work sought to apply a beam-spline variational analysis method (BSAM) to model the elastic and failure behavior of the joint. The comparisons were made with experimental data obtained using moiré interferometry. The test specimen was prepared by applying a diffraction grating to the edge of the specimen. A phase-shifting technique was used to extract the displacement data. For the experiments, the geometry was that of a double lap joint. IM7/3501-6 panels were used with a 24-ply quasi-isotropic layup. FM300-2M film adhesive was used as the adhesive. A milling operation was used to clean up any resin flow and ensure a well-formed edge in the vicinity of the stress concentration. The authors commented that to properly capture the elastic behavior in the adherends themselves, a ply-level analysis was necessary as opposed to using an assumption that the adherends were homogeneous, orthotropic bodies. This level of detail would become critical for prediction of failure initiation and its progression. The authors showed reasonable agreement between the displacement and strain predictions obtained from the moiré experiments with those obtained from the BSAM model with ply-level details included in the adherends.

More recently, in 2010, Tsai, et al. [24] studied stress distributions in double lap shear joint configurations containing laminated composite adherends. Two configurations of composite adherends were studied, one being a unidirectional laminate and the other being a quasi-isotropic laminate. An epoxy film adhesive, EA9628NW, was used for the adhesive layer. The adherend had a thickness of 1.98 mm and the straps had a thickness of 1 mm each. The adhesive layer measured approximately 0.15 mm. The adherend as well as the strap were both fabricated from AS4/3502 carbon-epoxy prepreg. Moiré interferometry was utilized with a grid containing gratings in both directions affixed to the test specimen. The grating had a frequency of 1,200 lines per mm in each direction. A virtual grating of 2,400 lines per mm was created with the interferometer.   Two different laminates were used for the adherend, and each exhibited similar shapes in the distribution of shear strains along the length of the adhesive layer in that the shear strain is maximum near the edge and minimum near the center. Quasi-isotropic test samples had a relatively lower ratio between maximum and minimum values within the distribution. This is likely due to the difference in axial modulus values for the two adherend scenarios. The FEM comparisons were generated using linear-elastic finite element models, and the predictions agreed reasonably well.

In 2011, Ruiz, et al. [25] utilized high sensitivity moiré to investigate stress distribution in double lap shear joints comprised of aluminum adherends bonded to other aluminum adherends as well as aluminum adherends bonded to composite adherends. The 7075 Aluminum alloy and IM7/8552 carbon fiber reinforced epoxy were utilized with FM73M film adhesive. The cured adhesive layer was approximately 0.15 mm with an overlap of 24.9 mm in the all-aluminum configuration and 0.19 mm with an overlap of 12.45 mm in the hybrid configuration. The sample width was 24.9 mm for both. With respect to the optical measurements, a 532 nm laser was used to illuminate the sample. A crossed-line grating with a frequency of 600 lines per mm was used on the test sample with the reference grating having a frequency of approximately 1,200 lines per mm. The test sample gratings were produced by coating a mold with aluminum in a vacuum deposition chamber. The aluminum coating was transferred to the edge of the double lap joint using a clear epoxy resin. The displacement and strain data were obtained using a 2-dimensional phase unwrapping process. Spatial distributions of longitudinal, peel, and shear strain through the thickness of the adhesive layer were obtained with the setup in [25]. Strain distributions were consistent with those obtained in other research works. The results were ultimately compared, with good agreement, to those distributions obtained with finite element techniques using elastic and elastic-plastic material models.

1.3 Fracture in bimaterial interfaces

To further develop the importance of fracture in adhesively bonded interfaces, there are three key modes of failure warrant attention: Failure in the bulk adhesive material, failure in the adherend, and failure along the interface between the adherend and adhesive. This failure along the interface is of particular interest to the present work. Williams [26] initially examined the state of stress in the region of an interface crack between two materials and determined the characteristic oscillating stress singularity. Rice and Sih [27, 28] examined the problem of an infinite plate with an interfacial crack and showed that the stress intensity factor approach can be extended to interfacial cracks. Additional noteworthy contributions to the understanding of interfacial cracks came from Cherepanov [29], England [30], and Erdogan [31]. Hutchinson, et al. [32] studied a crack parallel to an interface between two dissimilar materials and developed techniques for understanding conditions that would promote crack propagation near the interface. Yao and Wang [33] developed an approach for analyzing interface cracks using a conservation integral approach. Shih and Asaro [34] developed full-field numerical solutions for a crack which lies along the interface of an elastic-plastic medium and a rigid substrate. Their technique enabled extraction of complex stress intensity factors for interface cracks.

With regards to experimental work, Gent and Kinloch [35] studied tensile rupture of viscoelastic materials adhered to rigid steel substrates and suggested that an energy criterion may be appropriate for predicting fracture. Their observations suggested that the fracture process may be comprised of both reversible and irreversible influences. Liechti and Knauss [36, 37] introduced a bimaterial beam with a biaxial load frame capable of controlling very small displacements. They investigated the interface between Pyrex glass and polyurethane using a Michelson interferometry technique. The optical clarity of the two adherends was required due to the selection of the optical technique. Their work investigated the applicability of various crack propagation criteria and found that crack growth is possibly governed by a combination of local normal and shear displacements that is equal to the magnitude of the displacement vector, and that in the limit of infinitesimal strains, this reduces to an energy release rate criterion. Charalambides, et. al [38] developed a test specimen based on a beam comprised of two dissimilar materials. They developed analytical solutions for the strain energy release rates and stress intensity factors and performed experimental studies on an aluminum bonded to polymethyl methacrylate. Cao and Evans [39] published results from experimental investigations that considered fracture along interfaces of four different geometries including symmetric and asymmetric cantilever beam specimens, a four-point flexure sample, and a cylindrical tension sample. Their work explored mode mixity and concluded that the interface fracture resistance increased as the phase angle increased. Evans, et al. [40] developed techniques for measuring interface fracture energy over a wide range of phase angles as well. The work mainly reported results on debonding in brittle matrix ceramic and intermetallic composites. Several test geometries were investigated in their work. Two geometries from their work that are particularly relevant to adhesive interfacial fracture are illustrated in Figure 1-4 and Figure 1-5.

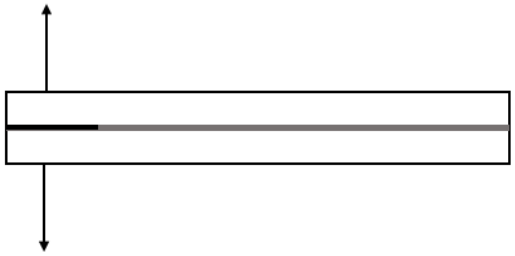

Figure 1-4: Double cantilever beam geometry

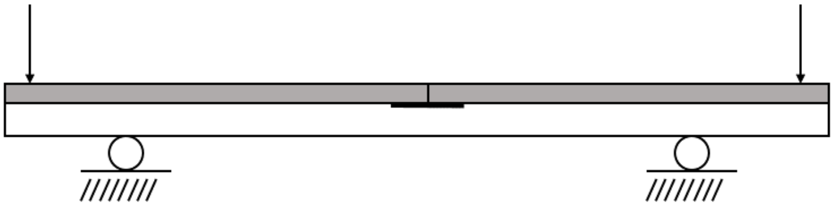

Figure 1-5: Interfacial decohesion geometry with an interface crack lying along the interface between a thin coating material and a substrate

To restate the purpose for the current work, the major focus is to understand interfacial fracture involving stiff adherends adhesively bonded together. Liechti and Chai [41] developed an edge cracked bimaterial strip with glass and epoxy as illustrated in Figure 1-6. A biaxial loading device was used to control the loading ratio between normal and tangential directions and thus control mode mixity of a crack propagating under steady conditions. They were able to use the specimen geometry to study influences of crack face friction under in-plane conditions. Optical interferometry was used to extract crack opening displacements.

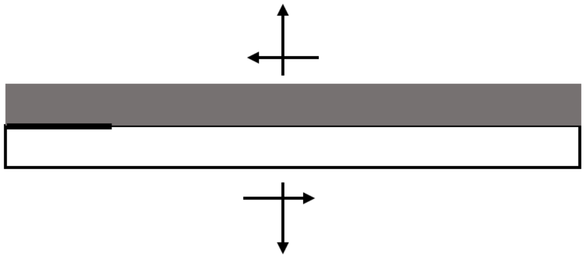

Figure 1-6: Edge-cracked, interfacial test specimen with biaxial shear and tension loading

Reedy and Guess [42] studied the effects of epoxy adhesive thickness on the stress concentration in the presence of a corner stress using a butt tensile bonded steel to epoxy joint geometry as illustrated in Figure 1-7. They observed decreasing strength with increasing bond thickness, the joint tensile strength decreased. They observed that by measuring the fracture toughness at a single adhesive thickness, they were able to predict the overall joint strength at other thicknesses.

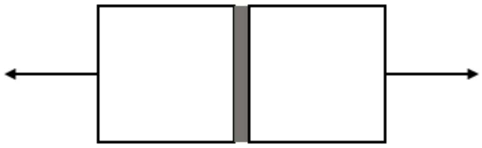

Figure 1-7: Butt tensile geometry

Experimental studies were performed by Loh, et al. [43] to understand the role of moisture in the interfacial failure of mild steel plates bonded together using Araldite AV119 epoxy. Their work utilized a mixed-mode flexure test geometry as illustrated in Figure 1-8. The geometry was configured such that the upper adherend overhangs the lower adherend and one of the support points only loads the upper adherend. This produces an opening mode stress along the interface in addition to the shear stress produced from the bending.

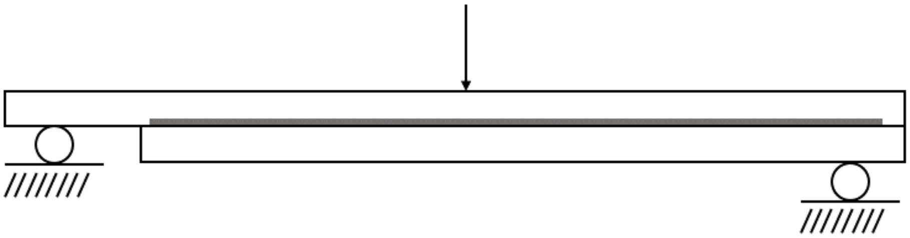

Figure 1-8: Mixed-mode flexure geometry

1.4 Role of compression in fracture behavior

The lap shear behavior of interest often plays an important role in structural failure, and as stated, it is further complicated by the complexity of material failure in the region of an interface between dissimilar materials. However, this particular influence is not only limited to the adhesively bonded joint problem and is not only limited to pure shear situations or mixed-mode tensile-shear situations. The evolution of shear behavior is often governed by formation, coalescence, and propagation of microcracks in the laminate. The local normal stress state can influence this behavior and is presumed to result in effects. Limited work has been performed to quantify the effects of crack surface friction and far-field transverse compression on the fracture behavior along an interface. Several authors have worked to address the problem analytically. Melville [44] discussed the role of crack face friction on the mode II stress intensity factor and derived expressions to describe the role of friction. Early work by Comninou and Schmueser [45] considered the problem of a crack in a medium under a combined remote compressive and shear loading, resulting in a partially closed crack. Additional compressive loading caused the crack opening to decrease in size under increasing compression loads. Comninou and Dundurs [46] developed a numerical solution for the case of pure shear loading using an elastic dislocation approach. More recently, Qian and Sun [47] proposed that the classical definition of strain-energy release rate becomes zero or unbounded depending on the strength of the singularity. Their team analytically investigated the fiber pull-out problem in a combined shear-compression stress state. Their work suggested that an alternate fracture criterion is necessary in this class of problems. An interfacial softening model was proposed in [48] for treatment of cracks in concrete based on observations of shear crack behavior at varying compressive loads. An alternate softening behavior was implemented in a model to handle such cases. Isaacson, et al. [49] conducted a progression of studies to investigate crack propagation in both brittle and ductile homogeneous materials. His work was extended to investigate crack kinking in those materials. While a number of studies and experimental efforts have given attention to the relationship between shear and compression in bulk material behavior, overall, only limited attention has been given in the experimental mechanics community to quantifying the effects of compression on apparent shear behavior at an interface crack. Thus, the present effort serves to extend the fundamental understanding of the fracture mechanics component of shear failure in the presence of an in-plane compressive load.

1.5 Fracture under dynamic loading conditions

While a great deal of attention has been given to the study of the mode I fracture problem under dynamic initiation and propagation conditions (for instance, the noteworthy work by Ravichandar and Knauss [50]), a more limited amount of work has been devoted to mixed-mode problems. One work [51] utilized an eccentrically loaded three-point bending specimen coupled with coherent gradient sensing to characterize mixed-mode fracture of PMMA. The method of digital image correlation was used with a similar impact-bending setup to investigate particle-filled epoxy under mixed-mode fracture conditions in [52]. The Brazilian disc geometry was used for investigation of mixed-mode fracture by prior authors including that presented in [53]. This approach has its challenges in that the two crack tips that are present in the specimen introduce experimental challenges in terms of which of the two would initiate first. Having two separate crack propagation events creates a subsequent asymmetry during crack growth. More recently, Gao, et al. [54] introduced a method to utilize the notched semi-circular bend geometry coupled with a split-Hopkinson bar setup for mode I fracture parameter extraction. He proposed that the transmitter bar strains be used to compute the force balance in the test specimen (and thus the specimen load history) for stress intensity factor calculation.

With respect to rubber-toughened epoxies, Kinloch, et al. [55] investigated the quasi-static mode I fracture response with a focus on microstructural evaluation and identification of various potential toughening mechanisms. The work was followed by a separate study [56] to include characterization of rate-dependent effects at different, but low, strain rates. A study was later performed by Pearson and Yee [57] to investigate the effects of particle size on the toughening of rubber-modified epoxies. Their work contributed to the understanding of microstructural effects of rubber particles in mode I fracture. A comprehensive review was published by Bagheri, et al. [58] documenting the history of the usage of rubber to toughen epoxies and a quite extensive survey of the literature with respect to characterization of the effects on toughness.

1.6 Objectives

Prior work suggest that material and adhesive performance is affected by constraint effects, more specifically, apparent lap shear strength increases with compressive load. Therefore, there is a need for evaluating quasi-static and dynamic fracture parameters for crack initiation and crack propagation in homogeneous epoxy-based adhesive materials and along bimaterial interfaces under mixed-mode conditions to understand these phenomena. This work is primarily motivated by improving the understanding of failure in the vicinity of an interface between two dissimilar materials that have severe dissimilarities in elastic properties, namely the interface between an adherend material such as steel and a compliant epoxy-based adhesive material. It is hypothesized that macroscale material and interface performance is governed by local fracture mechanics. Hybrid methods utilizing optically measured fracture parameters, coupled with microstructural evaluation can reveal the role of material constraint on macroscale behavior.

Hence, the following are the primary objectives of this research:

- Investigate mixed-mode quasi-static fracture in homogeneous materials
- Quantify dynamic fracture behavior under mixed-mode conditions in homogeneous materials
- Evaluate material fracture response under compressive states of stress
- Examine fracture in bimaterial interfaces
- Characterize the apparent interface fracture toughness under compressive stress states

1.7 Organization of the dissertation

In addition to this introductory chapter, this dissertation is organized into the following sections:

- In the second chapter, several measurement methods are described in detail and an experimental procedure is developed that utilizes displacement fields measured using digital image correlation to extract fracture parameters by coupling the measured data with robust contour integration algorithms built into a commercial finite element code. A script is developed to post-process output data from digital image correlation and use the data to build the requisite finite element model for further processing.
- In the third chapter, a semi-circular beam geometry is examined for the study of mixed-mode fracture in homogeneous materials undergoing quasi-static loading. Initial results are presented to validate the method for application to the present

problems of interest. Results from a series of experiments are presented concerning the mixed-mode fracture behavior, to include crack-normal compression stress states.

- In the fourth chapter, a new test methodology is introduced for interfacial fracture and an in-depth verification is performed on the interfacial fracture experimental setup. Several baseline experiments are analyzed in detail to assess the fitness of the method. Experimental measurements are compared directly with predicted results from finite element models. Various effects of the specimen and fixture geometry are analyzed and discussed in detail. Specific test considerations are noted with respect to practical implementation of the method. Detailed results are presented from experiments using the fixture under compression-shear loading. A complementary set of results are collected for interface crack geometries containing mixed-mode tension-shear loading. An empirical relationship is derived to describe the observed relationships.
- In the fifth chapter, the homogeneous specimen geometry is adapted for studying the dynamic behavior using a long bar loading apparatus. Finite element simulations are used to identify specific details and specific desired test configurations. The setup is studied in detail using validation experiments and the epoxy-based adhesive material is studied under dynamic, mixed-mode conditions. The experimentation includes test geometries to collect both tension-shear and compression-shear fracture parameters.
- In the sixth chapter, a numerical technique is introduced for automating and improving the data reduction and post processing approach by more reliably

locating the instantaneous crack tip in the full-field displacement data. While this is relevant to all the experiments conducted in the present work, this is particularly significant for the dynamic fracture investigations. The method seeks to demonstrate improvement over manual methods for locating the crack tip position. Coupling the improved crack tip identification technique with the domain integral based post-processing methods, is shown to improve fracture parameter extraction consistency. The ability of the crack tip identification methodology to properly locate a crack tip position is tested numerically against benchmark cases generated using finite element models of the dynamic experiments. Detailed results from dynamic experiments are presented.

- In the last chapter, conclusions are drawn from the overall effort and recommendations are made for future research activities.
- Finally, three separate appendices are included. First, potential alternate interface crack specimen geometries were investigated numerically. Second, select excerpts of MATLAB® scripting code are included for key parts of the script used for locating the dynamically propagating crack. Lastly, select excerpts of MATLAB® scripting code are included for the general hybrid DIC-FE methodology.

Chapter 2

Measurement Methods and Post Processing Techniques

At the core of the experimental effort undertaken in the present work is the use of measured full-field displacement data in two orthogonal planar directions and the subsequent extraction of fracture quantities of interest derived from the measured displacements. This chapter details the measurement of the displacement data via optical techniques based on the method of digital image correlation, and the subsequent reduction of the displacement data into the fracture quantities of interest.

2.1 Basics of digital image correlation

Two-dimensional digital image correlation (DIC) is a technique for measuring full-field planar displacements/deformations of an object experiencing load. The method was introduced in the early 1980's [59, 60, 61, 62] and has attained a great deal of popularity in recent years. The general principle involves applying a random pattern to the surface of an object of interest. As mechanical loads are imposed on the object, the random pattern/speckles follow the deformation of the surface of the object being tested. A digital camera is used to capture a series of speckle images as the object undergoes deformation during a loading event. Once the images are recorded, displacement fields can be computed by comparing subsequent deformed images in the series with the undeformed reference image.

To describe the technique briefly, consider a set of two random speckle images, the first being an image in the reference state, and the second in the deformed state. Each image is segmented into an array of sub-images (or, subsets, facets), as illustrated in Figure 2-1. The image correlation process seeks to track the position of each sub-image in the reference state as it follows surface deformations. This is accomplished by matching gray scale features of the subsets of the reference image with those in the deformed state.

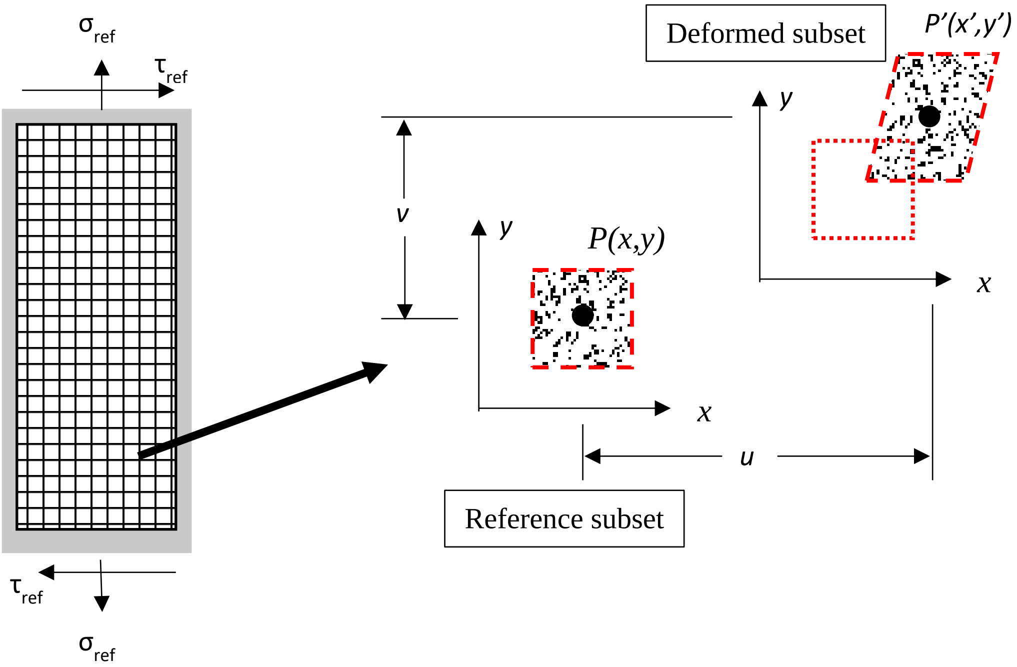

Figure 2-1: Digital image correlation grid pattern (left) and sub-image illustration (right) in the reference and deformed states

A technique that is commonly used for tracking sub-image features is based on the normalized cross-correlation coefficient, C_{CC}, evaluated as:

$$C_{CC} = \frac{\sum_{(i,j)\in S}\left(f\left(\tilde{x}_{ref,i}, \tilde{y}_{ref,j}\right) - f_m\right)\left(g\left(\tilde{x}_{cur,i}, \tilde{y}_{cur,j}\right) - g_m\right)}{\sqrt{\sum_{(i,j)\in S}\left[f\left(\tilde{x}_{ref,i}, \tilde{y}_{ref,j}\right) - f_m\right]^2 \sum_{(i,j)\in S}\left[g\left(\tilde{x}_{cur,i}, \tilde{y}_{cur,j}\right) - g_m\right]^2}} \qquad [2\text{-}1]$$

where *f* and *g* represent the intensity distributions within the subsets of the reference and deformed images respectively and are defined as:

$$f_m = \frac{\sum_{(i,j)\in S} f\left(\tilde{x}_{ref,i}, \tilde{y}_{ref,j}\right)}{n(S)} \qquad [2\text{-}2]$$

$$g_m = \frac{\sum_{(i,j)\in S} g\left(\tilde{x}_{cur,i}, \tilde{y}_{cur,j}\right)}{n(S)} \qquad [2\text{-}3]$$

where *n* is the number of points within the subset *S* and:

$$\tilde{x}_{cur,i} = x_{ref,i} + u_{rc} + \frac{\partial u}{\partial x_{rc}}\left(x_{ref,i} - x_{ref,c}\right) + \frac{\partial u}{\partial y_{rc}}\left(y_{ref,j} - y_{ref,c}\right) \qquad [2\text{-}4]$$

$$\tilde{y}_{cur,j} = y_{ref,j} + v_{rc} + \frac{\partial v}{\partial x_{rc}}\left(x_{ref,i} - x_{ref,c}\right) + \frac{\partial v}{\partial y_{rc}}\left(y_{ref,j} - y_{ref,c}\right) \qquad [2\text{-}5]$$

$$\tilde{x}_{ref,i} = x_{ref,i} + u_{rr} + \frac{\partial u}{\partial x_{rr}}\left(x_{ref,i} - x_{ref,c}\right) + \frac{\partial u}{\partial y_{rr}}\left(y_{ref,j} - y_{ref,c}\right) \qquad [2\text{-}6]$$

$$\tilde{y}_{ref,j} = y_{ref,j} + v_{rr} + \frac{\partial v}{\partial x_{rr}}\left(x_{ref,i} - x_{ref,c}\right) + \frac{\partial v}{\partial y_{rr}}\left(y_{ref,j} - y_{ref,c}\right) \qquad [2\text{-}7]$$

The variables *u* and *v* represent displacements in the global *x*- and *y*-directions respectively. Quantities associated with the reference image are denoted by *ref*, and *i* and *j* subscripts are pixel locations relative to the center of the corresponding subset. Subscripts *rr* denote transformations within the reference image and *rc* denote transformations between reference and current images. The typical correlation process seeks to maximize the cross-correlation coefficient. By doing so, a given subset from the reference image can be identified and tracked in the deformed image, and thus, the displacement of that subset will be known. This process is repeated for all subsets and all deformed images to create a full-field measure of displacements and the associated history.

2.1.1 DIC in the study of fracture

Several researchers have utilized full-field measurement approaches to understand material fracture. Over-deterministic least squares error minimization technique based on full-field optical measurements and analytical stress field solutions for evaluating opening-mode stress intensity factors in cracked specimens, introduced by Sanford [63, 64], has been a popular approach. Subsequently, others have reported utilizing measured displacements from digital image correlation [65, 66, 67] in conjunction with least squares regression analysis to identify fracture parameters. Kirugulige [68, 69] extended one of these approaches to the investigation of mixed-mode behavior under dynamic loading conditions to measure stress intensity factor histories for propagating cracks for various materials including functionally graded materials. Yoneyama [70] demonstrated the extraction of the *J*-integral from cracked specimen using displacement data from digital image correlation. His work employed a local approach to estimate strains from which stresses and strain energy densities could be computed in a domain around the crack tip. Yates, et al. [71] investigated the effects of fatigue on cracked specimens using the least squares approach with displacements from digital image correlation method. Their research included extraction of the so-called *T*-stress values, used in two-parameter fracture mechanics, as well.

2.2 Hybrid DIC-FE Approach

The current work seeks to utilize full-field displacement data from digital image correlation measurements coupled with a finite element model to reliably extract fracture parameters for an edge-cracked specimen. This approach is beneficial as it couples a convenient-to-implement displacement measurement technique adaptable to a wide range of problems with a data extraction methodology that is based on proven algorithms in mature software tools. The basic workflow is as follows: full-field displacements are measured in two orthogonal in-plane directions using DIC, the coordinates of the DIC output points are utilized to build a finite element mesh with connectivity that follows traditional finite element node ordering conventions, and then, robust algorithms within a commercial finite element package are used to extract domain integral quantities and decompose them into mixed-mode stress intensity factors. The general concept is similar to the coupled experimental-numerical approach used by Tippur and Chiang [72] where displacements measurements from moiré experiments were mapped onto a finite element model to extract fracture parameters. Dubois, et al. [73] has recently utilized a coupled approach that includes digital image correlation and finite element analyses to extract fracture parameters from experiments on timber materials. The measured displacement data was used to compute the kinematic state of the crack faces, while the finite element solution was used to evaluate the stress intensity factors. Isaac, et al. [74] utilized a similar hybrid approach to investigate effects of build orientation on fracture in additively manufactured materials.

2.2.1 Digital image correlation details

In the present work, the Ncorr [75] software was utilized for performing DIC. Ncorr is an open-source code developed in the MATLAB® software environment for performing subset-based two-dimensional DIC. It utilizes well-documented and accepted solution practices and provides flexibility for developers. The normalized cross-correlation (as defined in [2-1]) is used for providing the initial guess for subset matching at the seed points. Sub-pixel accuracy is then achieved by using the Inverse Compositional Gauss-Newton (ICGN) method to perform a nonlinear optimization using the normalized least squares criterion, C_{LS}:

$$C_{LS} = \sum_{(i,j)\in S}\left[\frac{f(\tilde{x}_{ref,i},\tilde{y}_{ref,j}) - f_m}{\sqrt{\sum_{(i,j)\in S}\left[f(\tilde{x}_{ref,i},\tilde{y}_{ref,j}) - f_m\right]^2}} - \frac{g(\tilde{x}_{cur,i},\tilde{y}_{cur,j}) - g_m}{\sqrt{\sum_{(i,j)\in S}\left[g(\tilde{x}_{cur,i},\tilde{y}_{cur,j}) - g_m\right]^2}}\right]^2 \qquad [2\text{-}8]$$

This prevents the normalized cross-correlation computation from having to be made for all subset points. The process serially works its way out from the initial seed point. Even though this process cannot be directly parallelized, Ncorr, breaks the region of interest up into smaller regions. This reliability-guided digital image correlation (RG-DIC) computation procedure can then be executed across a number of computer processors in parallel.

2.2.2 Speckle patterning

The ability to maximize the cross-correlation coefficient detailed above is dependent on the uniqueness of each of the sub-images. Thus, the technique is founded on the general characteristics of the pattern/speckles on the object surface. The pattern must be random and generally isotropic. High contrast between the speckles and the background as well as consistency in the size of the speckles is also desirable with the black speckles covering approximately 50% of the white background. The desirable speckle size is related to the resolution of the camera, and the typical speckle size spanning 3-5 pixels of the sensor is recommended. Patterns consisting of large variations in the size and spacing of speckles can result in correlation difficulties. Since the speckle size and imaging optics are directly related to the measurement resolution, patterning techniques have been developed to address image correlation problems across a myriad of length scales from nanoscale all the way to problems involving deformations in massive geographic features on the earth's surface. Thus, the patterning technique is only limited by the user's imagination and creativity.

2.2.3 Extraction of fracture parameters

Many commercial finite element (FE) packages offer options for the extraction of fracture parameters. Specifically, the ABAQUS® finite element software package offers a multitude of options for extracting fracture parameters using path independent contour integration-based approaches. For the present effort, a script was developed to manage this process. The Ncorr code first creates a MATLAB® data file with the *u*- and *v*-displacement data from the DIC analysis. The data is stored in two arrays where each entry contains a displacement value associated with the spatial location of a given subset centroid. Once the displacements are known, the workflow as shown in Figure 2-2 is followed.

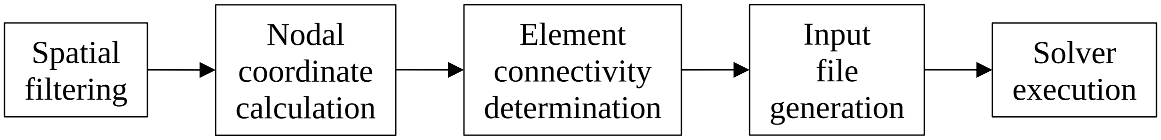

Figure 2-2: Digital image correlation data post processing

2.2.4 Treatment of noise

One important consideration of utilizing the DIC technique is the treatment of noise in the measured displacements. Due to the discontinuous nature of the displacement data due to the crack, generic smoothing techniques (e.g., moving average filters, etc.) are not appropriate in this application. Also, measurement noise is common to many experimental techniques, and it becomes more important with DIC in situations where displacement measurement is not the end objective. The objective of the current work is to extract contour integral quantities out of the measured displacement data. Thus, derived quantities such as strain and/or stress are of importance and factor into the quality of the resulting measurement. It is, therefore, necessary to properly treat noise such that in the stress and displacement gradient-based contour integral quantities can be accurately extracted. To that end, an image processing technique was adapted to post-process the displacement data prior to mapping it into the finite element model. A guided filter was chosen to improve the smoothness of the DIC data but minimize the smoothing effect in regions where the large gradients are attributed to the stress field and not experimental noise. The basic concept of guided filtering involves choosing a square window of data surrounding a data point of interest (i.e., $N \times N$ data points illustrated in Figure 2-3) and considering the local statistics of the window to calculate the output values of the filtered data at the point of interest. The output at a given data point q can be calculated based on a weighted average of the data points p from the sub-array of data points.

$$q_i = \sum_j W_{ij}(I)\, p_j \qquad [2\text{-}9]$$

where i and j are spatial coordinates within the window, and the filtering kernel, W, is a function of the guidance image or guidance data set. The guidance data set can be formed beforehand based on knowledge of features within the image such as edges. As proposed by He, et al., [76], the output q at a given data point is a linear transform of the guidance data set, I, calculated from the coefficients, a_k and b_k, in a window or sub-array of data points, w_k, as:

$$q_i = a_k I + b_k \qquad [2\text{-}10]$$

where the coefficients, a_k and b_k, are defined as:

$$a_k = \frac{\frac{1}{\omega}\sum_{i\in w_k} I_i p_i - \mu_k \bar{p}_k}{\sigma_k^2 + \epsilon} \tag*{[2-11]}$$

$$b_k = \bar{p}_k - a_k \mu_k \tag*{[2-12]}$$

The filtering input data is given as p, with $\bar{p}_k$ being the average of the data within the sub-array of data. The mean intensity value within the sub-array of the guidance data set is μ, σ_k^2 is the variance, ω is the number of data points in the sub-array of the guidance data set, and ϵ is a regularization parameter that penalizes the contributions of large values of a_k. Thus, the value of ϵ results in an increased or decreased degree of smoothing. The filtered output at each data point is calculated multiple times because each data point is involved in multiple overlapping sub-arrays of data. Thus, the final output of a given data point can be computed as the average of all the individual computations of the output for that data point.

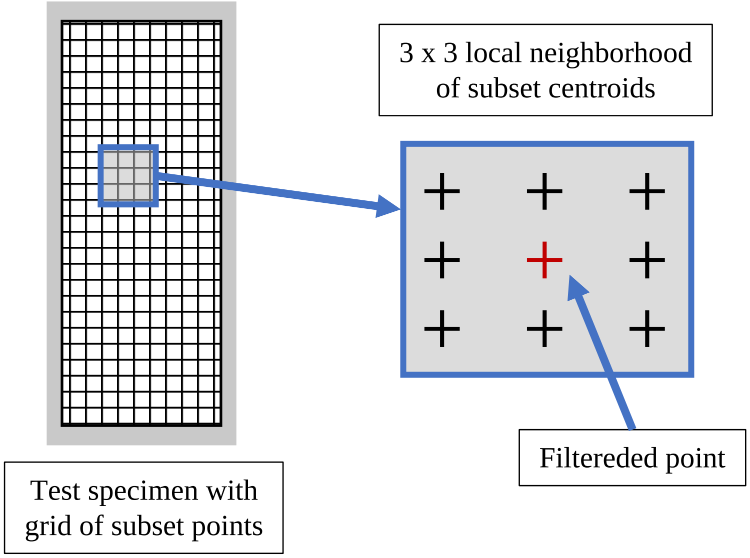

Figure 2-3: Illustration of filter neighborhood for n = 3

This filtering technique has a few interesting characteristics that are especially applicable to the current work. First and foremost is that this smoothing technique has an intrinsic edge-preserving property. Considering an area where the gradients are steep, the variance can be very high. An example of this would be at an edge of the specimen or, more importantly, adjacent to one of the crack faces. A window of data points that is centered over an edge would contain very high local variance. Because the edges of the specimen can be identified in the image, the image and the subsequent output displacement data can be used as a guide for the filter and thus mitigate this effect from the local variance. Filtering techniques such as moving average filters, on the other hand, result in significant unwanted smoothing near edges. Using the guided approach, the edge is largely preserved. Alternate edge preserving filters can cause gradient reversal issues. The technique proposed in [76] alleviates this issue. In general, more smoothing occurs in areas with low variance and less smoothing occurs in areas with high variance while generally preserving edges and gradients.

2.2.5 Assembly of the finite element mesh

Once the smoothing calculation has been performed, the script calculates the coordinates of each of the subset points based on the known pixel size, subset size, and subset spacing. The grid of DIC output points is structured with uniform spacing in the *x*- and *y*-directions. The data is read into the MATLAB® script in the form of a data structure with two separate arrays for the horizontal and vertical displacement data. In each data array, the column position of each point corresponds to the *x*-location of the output point and the row position of each point corresponds to the *y*-location of the output point. The nodal coordinates are simply the row or column position multiplied by the subset spacing. Once the nodal coordinates are known, the script utilizes the array indices of the nodal position data to establish the element connectivity using the ABAQUS® element connectivity convention where the first node is in the lower left quadrant. Other nodes of the element are ordered in a counterclockwise direction as shown in Figure 2-4.

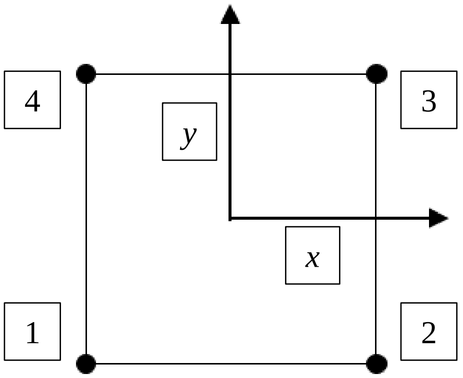

Figure 2-4: ABAQUS® typical element connectivity for 4-noded elements

Once the nodal positions and element connectivity have been determined, the script then writes the node and element data into a text file in the proper ABAQUS® input file order and syntax. The script also prompts the user to identify the approximate crack position within the output data and additional points along the crack face. This information is used for identifying the node numbers for each contour domain and establishing the crack tip location and crack orientation for the ABAQUS® domain integral output request. Lastly, the script writes the material property definitions for the model into an include file that is referenced in the ABAQUS® input file, as well as the appropriate output requests are written to extract the fracture parameters of interest. The ABAQUS® structural solver is then executed to compute the fracture parameters.

2.2.6 Extraction of stress intensity factors

To extract the stress intensity factors for a given specimen and load-step, a contour integral technique is utilized. The energy release rate can be computed using a domain (area) integral instead of the traditional line integral. The *J*-integral, as presented in Shih, et. al [77], is defined as:

$$J = \int_{A}^{\cdot} \left(-W\delta_{ij} + \sigma_{ij} \frac{\partial u_j}{\partial x_1} \right) \frac{\partial q_1}{\partial x_1} dA, \quad (i,j = 1,2) \qquad [2\text{-}13]$$

where *A* is the area of the domain or the area that includes the crack tip being evaluated, q_1 is a weighting function that equals 1 on the outer boundary of the domain and 0 on the inner boundary of the domain. The strain energy density is denoted as *W*, *u* is the displacement vector, and σ_{ij} is the Cauchy's stress tensor. This domain integral can be decomposed into the two stress intensity factors K_I and K_{II} for modes I and II, respectively, using the relationship:

$$J = \frac{1}{E}(K_I^2 + K_{II}^2) \qquad [2\text{-}14]$$

The ABAQUS® finite element software employs an interaction integral technique to partition *J* and extract the two stress intensity factors based on the technique described in [34].

2.3 Least squares regression analysis of crack tip displacement fields

2.3.1 Analysis of stationary crack tips

As previously stated, one of the objectives of the present work is to assess the validity of the proposed hybrid DIC-FE displacement mapping approach to the study of fracture behavior. It is recognized that several techniques are available for extracting fracture parameters, and more specifically, contour/domain integral quantities and stress intensity factors from full-field displacement data measured using digital image correlation. However, the proposed hybrid DIC-FE approach offers several advantages. First, it offers the ability to leverage previously developed robust algorithms for domain integration and mode decomposition that are available in commercial finite element solvers. Second, it is suitable for a broad range of problems that include dissimilar material interface crack problems. Further, this type of approach extends well to fractures involving more complex material behaviors as it can be utilized with a range of nonlinear and anisotropic material models.

To demonstrate the validity of this technique, experimental results using the hybrid method were compared not only to a linear, elastic finite element model of an analogous test specimen, but also compared to stress intensity factors extracted using the more common approach of over-deterministic least squares analysis of displacement data near the crack tip was utilized to calculate the stress intensity factors.

The over-deterministic least squares results are computed using the equations reported in [78] for the crack sliding (u_x) and crack opening displacements (u_y):

$$\begin{aligned} u_x = & \sum_{n=1}^{N} \frac{(K_I)_n}{2\mu} \frac{r^{\frac{n}{2}}}{\sqrt{2\pi}} \left\{ \kappa \cos\frac{n}{2}\theta - \frac{n}{2}\cos\left(\frac{n}{2}-2\right)\theta + \left\{\frac{n}{2} - (-1)^n\right\} \cos\frac{n}{2}\theta \right\} \\ & + \sum_{n=1}^{N} \frac{(K_{II})_n}{2\mu} \frac{r^{\frac{n}{2}}}{\sqrt{2\pi}} \left\{ \kappa \sin\frac{n}{2}\theta - \frac{n}{2}\sin\left(\frac{n}{2}-2\right)\theta \right. \\ & \left. + \left\{\frac{n}{2} - (-1)^n\right\} \sin\frac{n}{2}\theta \right\} + T_x \end{aligned} \tag{2-15}$$

$$\begin{aligned} u_y = & \sum_{n=1}^{N} \frac{(K_I)_n}{2\mu} \frac{r^{\frac{n}{2}}}{\sqrt{2\pi}} \left\{ \kappa \sin\frac{n}{2}\theta + \frac{n}{2}\sin\left(\frac{n}{2}-2\right)\theta - \left\{\frac{n}{2} + (-1)^n\right\} \sin\frac{n}{2}\theta \right\} \\ & + \sum_{n=1}^{N} \frac{(K_{II})_n}{2\mu} \frac{r^{\frac{n}{2}}}{\sqrt{2\pi}} \left\{ -\kappa \cos\frac{n}{2}\theta - \frac{n}{2}\cos\left(\frac{n}{2}-2\right)\theta \right. \\ & \left. + \left\{\frac{n}{2} - (-1)^n\right\} \cos\frac{n}{2}\theta \right\} + T_y \end{aligned} \tag{2-16}$$

In the above equations, μ is the material shear modulus, and r and θ are the polar coordinates with crack tip as the origin and $\kappa = \frac{3-\upsilon}{1+\upsilon}$ for plane stress and υ is the Poisson's ratio. The coefficients K_I and K_{II}, when n = 1, are the mode I and mode II stress intensity factors. For digital image correlation experiments, the u_x and u_y fields are known for a set of points surrounding the crack tip. In terms of terminology, the displacement fields are also referred to as $u_x = u$ and $u_y = v$ for consistency with typical digital image correlation nomenclature. By selecting a group of points in the vicinity of the crack, a set of linear equations can be formed to determine the $(K_I)_n$ and $(K_{II})_n$. Using an over-deterministic approach, the experimental crack opening displacement can be used for extracting mode I fracture components whereas the crack sliding displacements can be used for mode II fracture components. However, it has been shown that by transforming experimental in-plane Cartesian displacements into radial (u_r) and angular (u_θ) displacements, more accurate SIFs can be found in mixed-mode problems [67]. That is, the Cartesian displacement components can be transformed into polar coordinate displacement components as shown in [2-17] - [2-19].

$$\begin{Bmatrix} u_r \\ u_\theta \end{Bmatrix} = \begin{bmatrix} \cos\theta & \sin\theta \\ -\sin\theta & \cos\theta \end{bmatrix} \begin{Bmatrix} u_x \\ u_y \end{Bmatrix} \qquad [2\text{-}17]$$

$$\begin{aligned} u_{rk} = {} & \left\{ \sum_{n=1}^{N} (K_I)_n f_{In}(r_k, \theta_k) + \sum_{n=1}^{N} (K_{II})_n f_{IIn}(r_k, \theta_k) \right\} \cos\theta_k \\ & + \left\{ \sum_{n=1}^{N} (K_I)_n g_{In}(r_k, \theta_k) + \sum_{n=1}^{N} (K_{II})_n g_{IIn}(r_k, \theta_k) \right\} \sin\theta_k \qquad [2\text{-}18] \\ & + T_x \cos\theta_k + T_y \sin\theta_k \end{aligned}$$

$$u_{\theta k} = \left\{ \sum_{n=1}^{N} (K_I)_n f_{In}(r_k, \theta_k) - \sum_{n=1}^{N} (K_{II})_n f_{IIn}(r_k, \theta_k) \right\} \sin\theta_k$$

$$+ \left\{ \sum_{n=1}^{N} (K_I)_n g_{In}(r_k, \theta_k) + \sum_{n=1}^{N} (K_{II})_n g_{IIn}(r_k, \theta_k) \right\} \cos\theta_k \qquad [2\text{-}19]$$

$$- T_x \cos\theta_k + T_y \sin\theta_k$$

where *f* and *g* are the functions from Equations [2-15] and [2-16] and T_x and T_y are terms representing rigid body motion. Using this technique, these equations can be expanded out to any number of higher order terms. The over-determined equation set can be formed and solved for minimizing the least squares error to compute values of K_I, K_{II}, T_x, and T_y.

2.3.2 Analysis of propagating crack tips

For a propagating crack, other considerations must be factored in. The opening and sliding displacements can be written as:

$$u_x = \sum_{n=1}^{N} \frac{(K_I)_n B_I(C)}{2\mu} \sqrt{\frac{2}{\pi}} (n+1) \left\{ r_1^{n/2} \cos\frac{n}{2}\theta_1 - h(n) r_2^{n/2} \cos\frac{n}{2}\theta_2 \right\}$$

$$+ \sum_{n=1}^{N} \frac{(K_{II})_n B_{II}(C)}{2\mu} \sqrt{\frac{2}{\pi}} (+1) \left\{ r_1^{n/2} \cos\frac{n}{2}\theta_1 \right. \qquad [2\text{-}20]$$

$$\left. - h(\bar{n}) r_2^{n/2} \cos\frac{n}{2}\theta_2 \right\}$$

$$u_y = \sum_{n=1}^{N} \frac{(K_I)_n B_I(C)}{2\mu} \sqrt{\frac{2}{\pi}} (n+1) \left\{ -\beta_1 r_1^{n/2} \sin\frac{n}{2}\theta_1 - \frac{h(n)}{\beta_2} r_2^{n/2} \sin\frac{n}{2}\theta_2 \right\}$$

$$+ \sum_{n=1}^{N} \frac{(K_{II})_n B_{II}(C)}{2\mu} \sqrt{\frac{2}{\pi}} (+1) \left\{ \beta_1 r_1^{n/2} \cos\frac{n}{2}\theta_1 \right. \qquad [2\text{-}21]$$

$$\left. + \frac{h(\bar{n})}{\beta_2} r_2^{n/2} \cos\frac{n}{2}\theta_2 \right\}$$

In the above equations, μ is the material shear modulus, and r and θ are the polar coordinates with crack tip as the origin and $\kappa = \frac{3-\upsilon}{1+\upsilon}$ for plane stress. The longitudinal and shear wave speeds are defined as $C_L = \sqrt{\frac{(\kappa+1)\mu}{(\kappa-1)\rho}}$ and $C_S = \sqrt{\frac{\mu}{\rho}}$ respectively. The non-dimension quantities, $\beta_1 = \sqrt{1-\left(\frac{c}{C_L}\right)^2}$ and $\beta_2 = \sqrt{1-\left(\frac{c}{C_S}\right)^2}$ are used to compute the spatial variations of $r_m = \sqrt{X^2 + \beta_m^2 Y^2}$ and $\theta_m = \tan^{-1}\left(\frac{\beta_m Y}{X}\right)$ based on the crack speed, c. Also, B_I, B_{II}, D, and h are defined in [2-22].

$$B_I(c) = \frac{(1+\beta_2^2)}{D}, \qquad B_{II}(c) = \frac{2\beta_2}{D}$$

$$D = 4\beta_1\beta_2 - (1+\beta_2^2)^2$$

$$h(n) = \begin{cases} \dfrac{2\beta_1\beta_2}{1+\beta_2^2} & \text{for even } n \\ \dfrac{1+\beta_2^2}{2} & \text{for odd } n \end{cases} \qquad [2\text{-}22]$$

$$h(\bar{n}) = h(n+1)$$

Chapter 3

Quasi-static Fracture of Homogeneous Adhesive Material

The current chapter builds on the general methods documented in Chapter 2 towards the study of quasi-static behavior of a homogeneous epoxy-based adhesive material. A specimen geometry is explored analytically, and the experimental methodology is examined in detail. Resulting fracture parameter measurements are presented to included fracture under mixed-mode, shear-tension and shear-compression stress states.

3.1 Quasi-static fracture experiments

In order to explore the implementation of the proposed workflow, an edge-cracked semi-circular beam (SCB) geometry was utilized. This geometry offers many attractive features in that it can produce pure mode I and II and a wide range of mixed-mode fractures.

3.1.1 Test specimen geometry

The SCB test specimen geometry was first introduced to study mechanics problems involving cored concrete and rock [79, 80, 81] cylinders. In the investigation of geological materials such as rocks, many tools exist for extracting specimens in the form of circular cylinders out of the ground. Those cylinders can readily be sliced into disks and then cut in half to produce the semi-circular geometry. The same is true for engineered materials such as concrete and asphalt. Test samples for many different physical measurements are based on cylindrical geometry due to the widespread use of the coring process. For these reasons, this specimen geometry is finding widespread use which warrants critical evaluation from the fracture mechanics community.

The general specimen geometry and loading configuration are illustrated in Figure 3-1 where *R* is the radius of the specimen, *a* is the crack length, *β* is the crack angle with respect to the horizontal axis of the specimen, and *S* is the half span. The Cartesian crack tip coordinates are denoted by the *x*- and *y*-axes parallel and perpendicular to the crack, respectively. The corresponding crack tip polar coordinates *r* and *θ* are as shown.

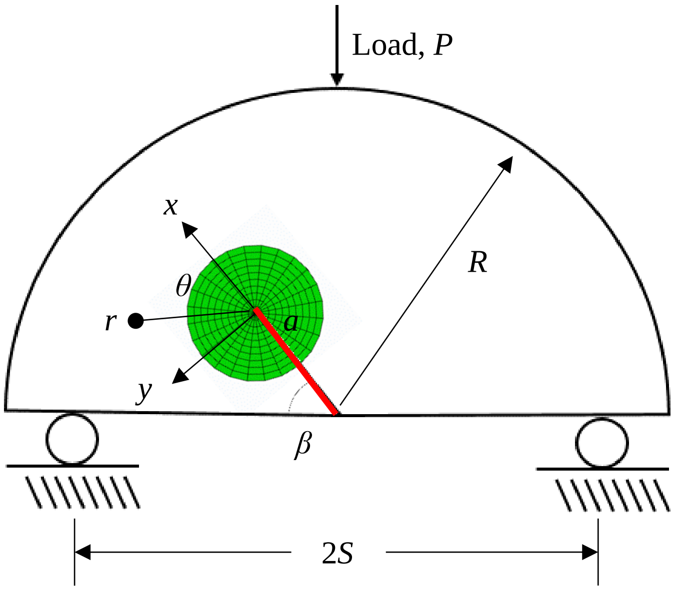

Figure 3-1: Semi-circular beam bending test configuration with typical crack tip mesh

As investigated in [81], the stress intensity factors at the crack tip, and therefore the mode mixity, are controlled by the geometric parameters of the test setup namely, *R*, *a*, *β*, and *S*. Normalized stress intensity factors, Y_I and Y_{II}, relative to the Griffith crack problem are defined as:

$$Y_{I;II} = \frac{K_{I;II}}{\sigma_0\sqrt{\pi a}} \qquad [3\text{-}1]$$

where K_I and K_{II} are the mode I and mode II stress intensity factors, $\sigma_0 = \frac{P}{2Rt}$, t being the specimen thickness.

3.1.2 Finite element model

Lim [81] explored the geometric effects and developed analytical expressions for mode I stress intensity factors for the SCB geometry. To characterize the relevant conditions for the present work and determine the desirable specimen dimensions, a similar process was followed. A finite element model was developed in ABAQUS® to mimic the geometry illustrated in Figure 3-1 and explore the effects of different geometric parameters, namely the support span, crack inclination angle, and crack length. A base geometry of approximately 100 mm in diameter was chosen as a convenient and practical size from an experimental standpoint. For investigation of cast and/or injected polymeric materials, this was considered a reasonable specimen size for fabrication purposes. Several analysis runs were performed to determine an acceptable element size for the model. Three different mesh sizes were analyzed, global element edge lengths of 1.3 mm, 0.6 mm, and 0.3 mm, to determine the sensitivity to the desired output quantity, stress intensity factor. Given that the stress intensity factors are being extracted using a contour domain integral, the method itself is relatively mesh independent. The three mesh sizes produced stress intensity factors within 1% of each other. Therefore, the parametric study utilized the 0.6 mm global mesh seed size. The model was meshed using 4-noded plane stress, fully integrated elements (ABAQUS® element type, CP4S). The full model assembly contained approximately 17,000 elements and 17,000 nodes. On the lower edge of the test specimen, steel rollers were modeled. A steel platen was modeled at the top edge of the specimen with a load applied to the top of the platen. Frictionless contacts were assumed at the interface between the specimen and the adjacent components. A seam was created in the model to represent the initial edge crack. The mesh contained concentric rings of elements radiating out from the crack tip as illustrated in Figure 3-1. At the physical crack tip in the model, the 4-noded elements were collapsed down to triangular elements by having two of the nodes reside at the same location.

3.1.3 Parametric study: Specimen design

The role of various span to radius (S/R) and crack length to radius (a/R) ratios on crack tip SIF were evaluated. Because overly long cracks can interact with the boundaries of the specimen, consideration was given to crack length. Also, the crack inclination angle was considered because low crack angles can be difficult to fabricate and can result in fragile specimens. The normalized stress intensity factors and mode mixities are shown for one of the span ratios in Figure 3-2 where the mode mixity is defined as $\varphi = \tan^{-1}\left(\frac{K_{II}}{K_I}\right)$.

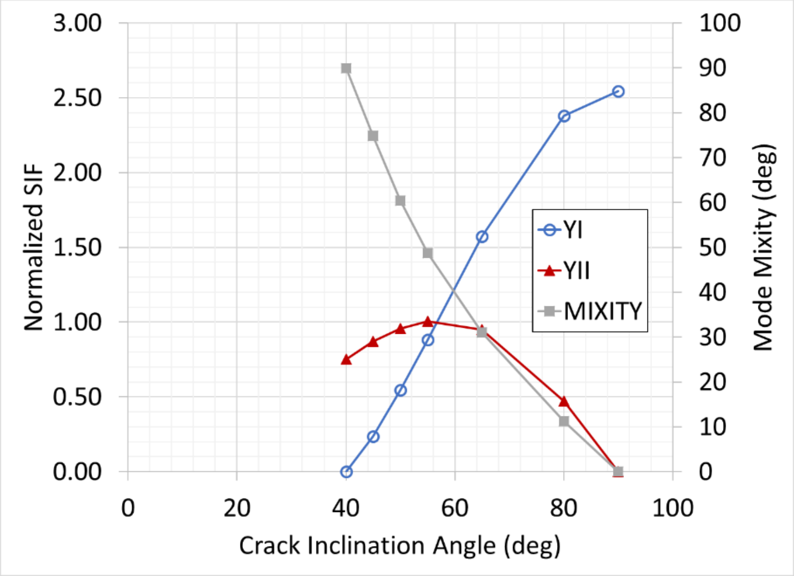

Figure 3-2: Normalized mode I and mode II SIF with resulting mode mixity ranging from pure mode I and pure mode II for a/R = 0.375 and S/R = 0.5

Evidently, the pure mode I and II cases occur at crack inclination angles of 90° and approximately 40°, respectively. The effect of span and crack angle on mode I and mode II stress intensity factors for three different *a*/*R* ratios is shown in Figure 3-3.

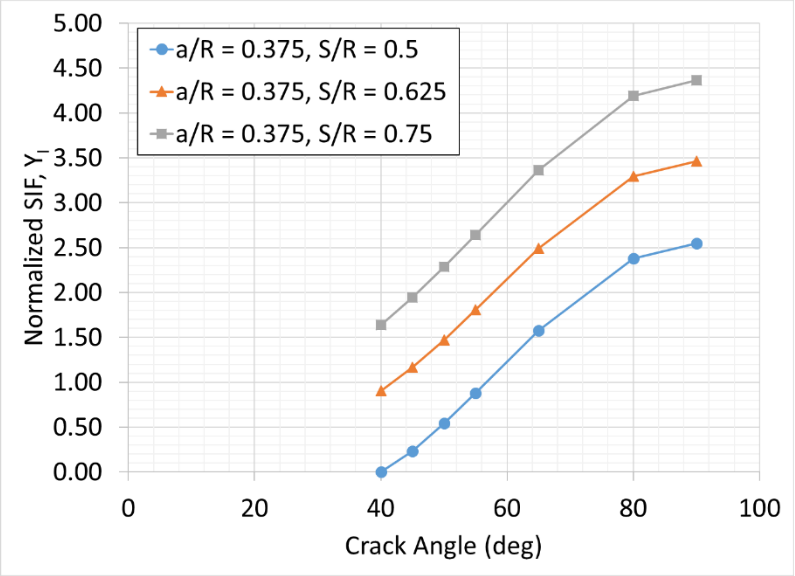

(a)

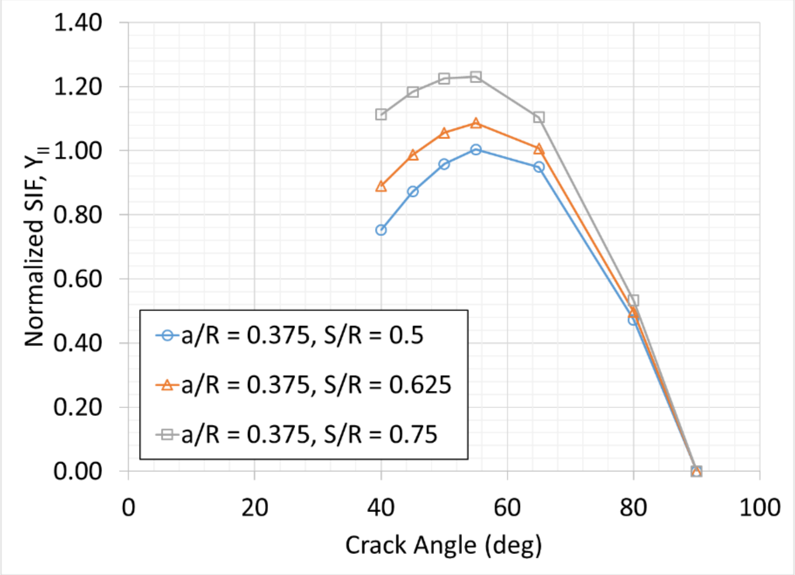

(b)

Figure 3-3: Effect of varying span ratios and crack angles on SIF (a) Mode I and (b) Mode II

3.2 Test specimen fabrication

With the specimen geometry well defined, the following section details the process of specimen fabrication.

3.2.1 Homogeneous material samples

Rubber-toughened epoxy test specimens were fabricated for development and demonstration of each phase of the proposed experimental procedure. For the quasi-static homogeneous material specimens, an aluminum mold was fabricated with multiple semi-circular cavities of the desired in-plane dimensions (100 mm diameter). Due to a large selection of epoxy-based adhesives that are commercially available, an epoxy formulation representative of a broad range of epoxy-based adhesive materials from the standpoint of elastic and failure properties was chosen. An epoxy-amine formulation was chosen to act as a surrogate for several specific materials of interest to the present work. The epoxy formulation of interest is a basic mix of difunctional bisphenol A/epichlorohydrin derived liquid epoxy resin (EPON^{TM} 828) with triethylenetetramine (TETA, EPIKURE^{TM} 3234) curing agent. Bisphenol A is synthesized by a process where phenol is combined with acetone in the presence of an acid catalyst to produce the chemical and is used in a very wide range of material formulations. The amine hardener formulation allows a great latitude in creating formulations to fit a wide variety of application needs. TETA is a cycloaliphatic amine that generates sufficient reactivity in the formulation to achieve a moderate glass transition temperature with a room temperature cure, recognizing that it is impossible to maximize simultaneously several of the thermal and mechanical properties, however, the present formulation achieves a desirable balance of toughness, strength, glass transition temperature, and modulus to mimic the target material system.

Based on manufacturer recommendations, the two components were mixed at a ratio of 100:13 by weight. Prior to mixing, the EPON^{TM} 828 was heated to 66°C and allowed to sit at that temperature for approximately 1 hour to allow any entrapped air to migrate to the surface. The core-shell rubber particles (Paraloid 2691) were then mixed in at a ratio of 10% by weight. A Flacktek Speed Mixer, shown in Figure 3-4, was used to mix the core-shell rubber particles into the epoxy. This mixer uses a Dual Asymmetric Centrifuge (DAC) to rotate an angled cup clockwise, around a main central axis, while counter-rotating the cup upon its own axis. This motion forces materials to flow against itself inside the cup while also removing entrapped air. The mixture was mixed for 5 minutes, reheated to 66°C, and then mixed for 5 more minutes. After mixing, the epoxy with the dispersed rubber particles was allowed to fully cool to room temperature prior to adding in the curing agent using the same mixer.

Figure 3-4: Flacktek speed mixer used in preparing epoxy-based adhesive specimens

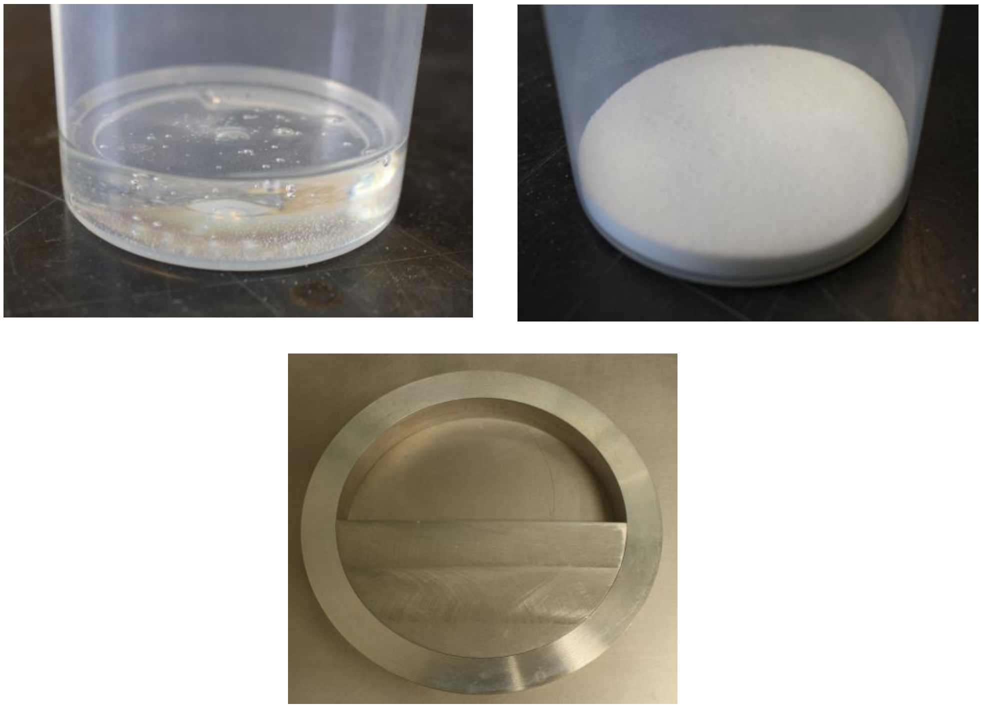

Figure 3-5: Components used for preparing the epoxy-based adhesive: Epoxy (upper left), core shell rubber particles (upper right), and specimen mold (lower center)

The epoxy and core shell rubber particles are shown in Figure 3-5. The amine hardener was mixed in for approximately 7 minutes to avoid the risk of an exothermic reaction to initiate in the mixing cup prior to pouring into the mold. The epoxy mixture was then poured into the mold cavity (Figure 3-5). A sharp razor was inserted into the mold with the help of a template to align the razor blade in the desired orientation. A clip was attached to the razor blade to hold it in place while the epoxy cured. The samples were cured for approximately 24 hours at room temperature followed by a post cure for 2 hours at 93°C. The face of each test sample was then milled flat to the desired thickness of 6.4 mm.

This fabrication method was selected for two primary reasons. First, the cast-in-place razor blade forms a very repeatable crack with consistent lengths and consistent crack tip geometry from sample to sample. Second, it minimizes the amount of post-cure machining and thus any local damage in the vicinity of the crack tip. The only machining operation required after curing is to machine the top face of the sample down until the desired thickness is achieved. Photos of the finish machined test sample and the crack are shown in Figure 3-6.

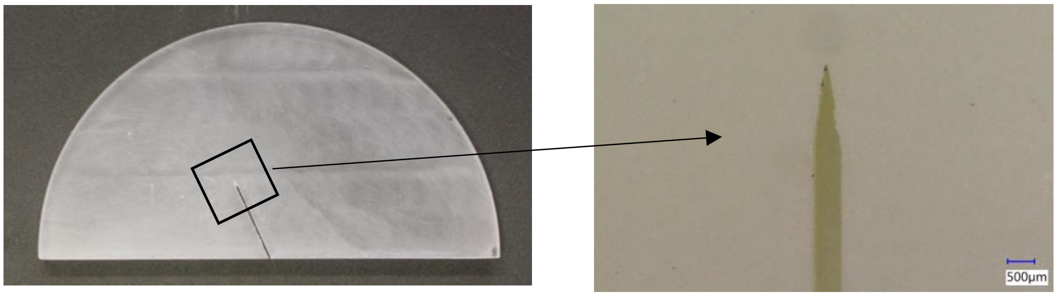

Figure 3-6: Cast SCB fracture sample with an inclined crack (left) and close-up of the crack tip produced by the razor blade insert during casting (right)

3.2.2 Pattern application

Poor speckle patterns can result in unwanted measurement noise, while proper patterning techniques can achieve high quality results in DIC. For the present work, each of the test samples were painted with high quality flat white oil-based enamel paint. The painted surface was then sanded with fine grit sandpaper to create a clean, smooth surface. Finally, a textured rubber stamp was utilized to transfer archival quality ink onto the test sample surface. The ink stamp and resulting pattern are shown in Figure 3-7.

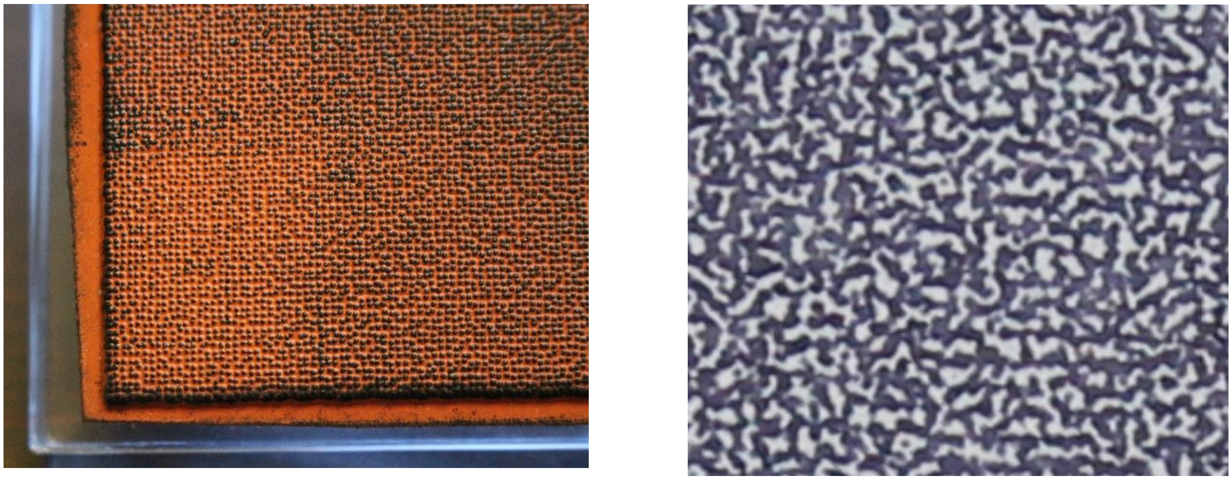

Figure 3-7: Textured rubber ink stamp (right) and resulting stamped pattern on specimen after 5-6 applications of ink stamp (right)

The textured stamp had a nominal feature size of 180 microns. The stamp was applied to the specimen surface 5-6 times to achieve an acceptable quantity of speckles on the white background. With each subsequent application of the ink stamp, the stamp was slightly rotated relative to the specimen to ensure a generally isotropic and stochastic pattern.

The speckle patterning technique for displacement measurement using DIC is often unique to a specific application. It is thus advantageous to assess the overall quality of the speckle pattern prior to proceeding with fracture characterization step. Several techniques have been proposed for speckle pattern quality determination. For the present work, the mean intensity gradient metric [82] was adopted. This metric has been demonstrated [82] as a reasonable global parameter for overall pattern assessment. Mean bias error and standard deviation of measured displacements are both strongly related to this metric. The mean intensity gradient is defined as:

$$\delta_f = \sum_{i=1}^{W} \sum_{j=1}^{H} \frac{|\nabla f(i,j)|}{(W \times H)} \qquad [3\text{-}2]$$

where W and H are image width and height, $|\nabla f(i,j)| = \sqrt{f_x(i,j)^2 + f_y(i,j)^2}$ is the modulus of local intensity gradient and f_x and f_y are the local derivatives at a given pixel. The derivatives are computed using the central difference method. In [82], a mean intensity gradient in excess of 20 resulted in the lowest amounts of mean bias error and displacement standard deviation of all the speckle patterns analyzed. Sub-image samples were extracted from 5 images of 5 different test specimens. The average mean intensity gradient from those specimens was calculated to be 22.3.

3.3 General material behavior

To acquire the elastic properties of the baseline material, tension and compression tests were performed. The tension testing was conducted using ASTM D 638 [83] as a guideline using the Type I specimen geometry shown in Figure 3-8.

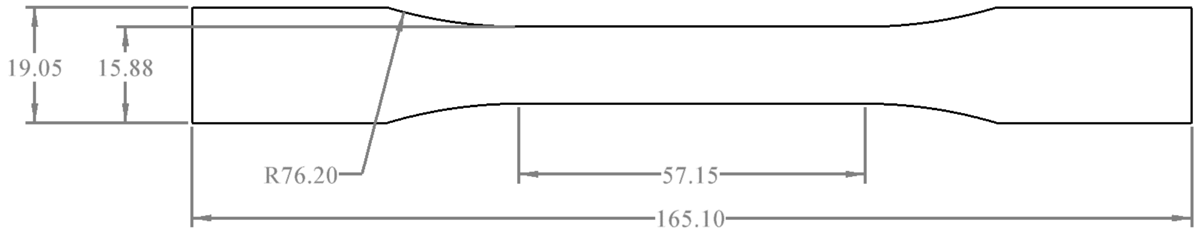

Figure 3-8: Tensile sample geometry (dimensions shown in millimeters)

The compression testing was conducted using ASTM D 695 [84] as a guideline using a right circular cylinder specimen with a nominal diameter of 15.9 mm. Test specimens were cast and cured using the previously described mixing process combined with the molds shown in Figure 3-9. For the tension specimens, all features were cast into the specimen except for the thickness dimension. After the post-cure process, the top face of each tension specimen was machined down to achieve the desired thickness and ensure a flat specimen with parallel surfaces. For the compression specimens, the end face of each compression cylinder was machined down to achieve the desired height and achieve parallel end faces. The diameter was left in the as-cast geometry.

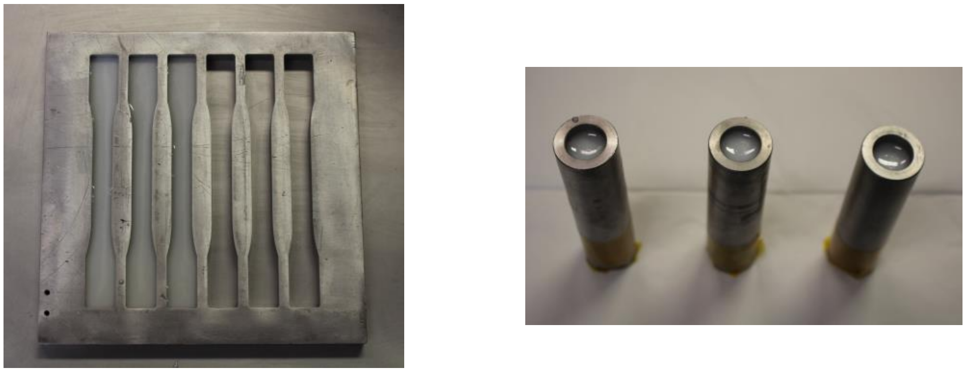

Figure 3-9: Specimens as-cast in mold for dogbone tension geometry (left) and right circular cylinder specimens for compression (right)

The uniaxial tension tests were also used as a benchmarking case for the performance of the digital image correlation procedure. Stress-strain response measured using strain gages was compared to the stress-strain response measured using the proposed digital image correlation methodology to include the same speckle patterning methodology. For the digital image correlation process, the pixel size was approximately 0.05 mm. A subset size of radius 45 pixels and a subset spacing of 5 pixels was chosen for the data analysis. These benchmarking comparisons showed excellent agreement between the strain gage data and the data derived from digital image correlation measurements across several specimens and the digital image correlation results produced elastic modulus measurements consistent with those obtained from the strain gage results. The comparison between the two data sources is shown in Figure 3-10.

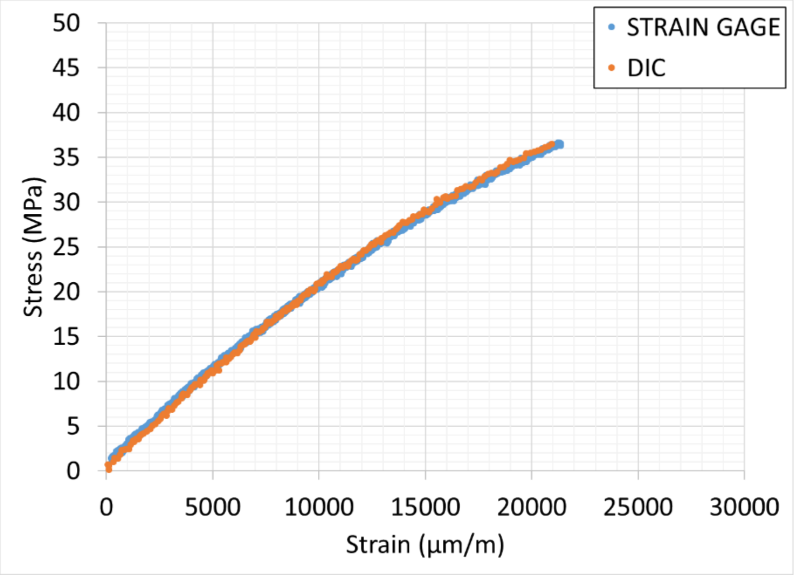

Figure 3-10: Tensile stress-strain response of the adhesive material studied

In tension, the material behaves in a generally elastic-brittle fashion. The material is mildly non-linear. For the compression test geometry, the gage section is fairly small, and the behavior is much more nonlinear, resulting in a significant amount of deflection. Therefore, the testing was executed with only DIC results during the test, with strain calculations being extracted along the axis of the cylinder. The typical compression stress-strain response is shown in Figure 3-11. The results are truncated at 100,000 microstrain for clarity. The specimens did not exhibit definitive failure in compression but continued to increase in strain until the onset of densification (e.g., the stress level began to increase again) or the specimen began to buckle due to material instabilities. A failed tensile sample and a compression sample under load is shown in Figure 3-12.

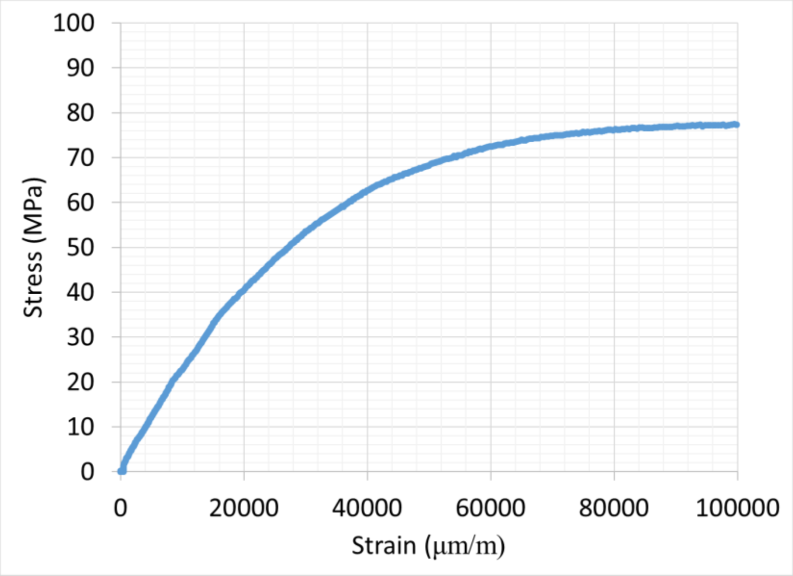

Figure 3-11: Compressive stress-strain response of the adhesive studied

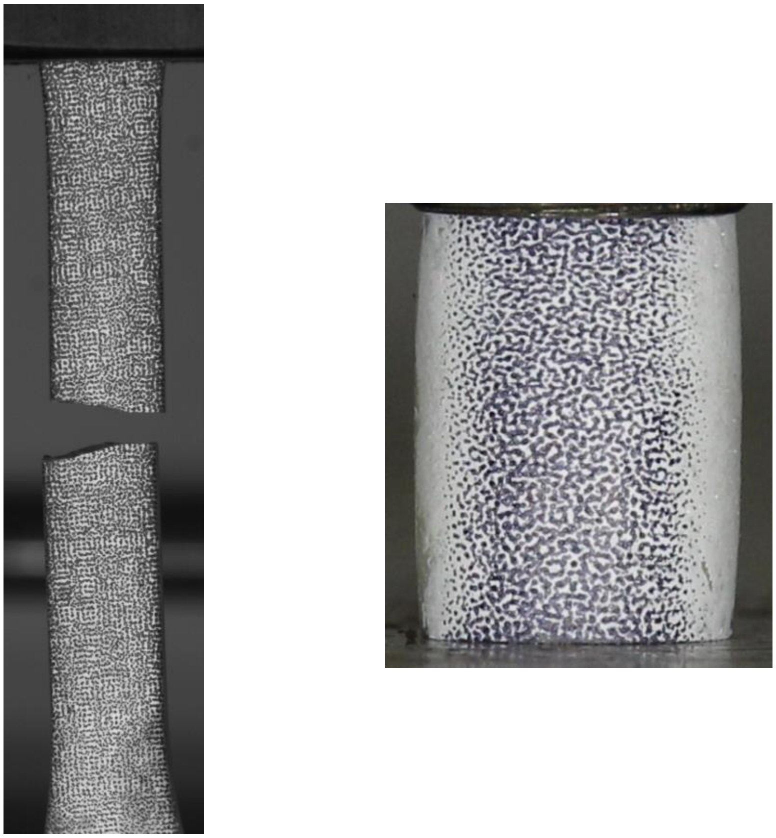

Figure 3-12: Failed tensile specimen showing brittle gage-section tensile failure (left) and compression specimen deformation shown under load at high strains showing slight “barreling” due to load (right)

The material properties of the epoxy formulation are summarized in Table 3-1. The standard deviation for the elastic modulus is shown as well for reference. The elastic properties were consistent across a range of test specimens and within the range of expected values based on the available vendor data for the epoxy matrix and associated core shell rubber particle filler.

Table 3-1: Test specimen material properties

Elastic modulus	2.2 GPa (±0.12 MPa)
Poisson's ratio	0.33
Density	1107 kg/m^3

3.4 Static semi-circular beam experiments

3.4.1 Optical configuration

For this series of quasi-static tests on the homogeneous material, a Canon EOS T5i single lens reflex digital camera was used for acquiring 14-bit images with a sensor resolution of 5196 × 3464. The camera was placed such that the focal plane of the camera was approximately 1.1 meters from the face of the sample. With the approximate specimen width of 100 mm, the edges of the specimen are located at a maximum of approximately 2.5° from the optical axis. The area of interest is smaller than this total specimen width, and thus paraxial approximation holds well. A 105 mm lens was utilized for imaging the specimen. With this lens, the calibration factor was approximately 0.051 mm for each test. The digital image correlation parameters are summarized in Table 3-2.

Table 3-2: Digital image correlation parameters for static experiments

Hardware Parameters			**Analysis Parameters**	
Camera Manufacturer	Canon		Software	Ncorr
Camera Model	T5i		Manufacturer	Open source
Image Resolution	5184 × 3456		Image Filtering	Guided filter
Lens Manufacturer	Canon		Sub-image Radius	45 pixels
Focal Length	105 mm		Step Size	5 pixels
Field of View	50 mm × 50 mm			
Image Scale	19.6 pixels/mm			
Stereo Angle	N/A			
Image Acquisition Rate	1 fps			
Patterning Technique	Ink stamp			
Approximate Feature Size	5-7 pixels			

3.4.2 Investigation of DIC and filtering parameters

A parametric study was conducted to investigate the appropriate subset size and subset spacing for this experimental work. The Ncorr software utilizes circular subsets. Subset radii ranging from 5 to 60 pixels, and subset spacing (step size) values ranging from 5 to 20 pixels were explored. A subset radius of 45 pixels and subset spacing of 5 pixels was selected for subsequent experiments. Resulting displacement contours are plotted in Figure 3-13. As evidenced in the figure, the larger subsets radii appear to decrease the noise in the displacement field. While the larger subset spacing qualitatively appears to result in lower noise, the smaller subset spacing was chosen based on the desire to balance noise with spatial resolution.

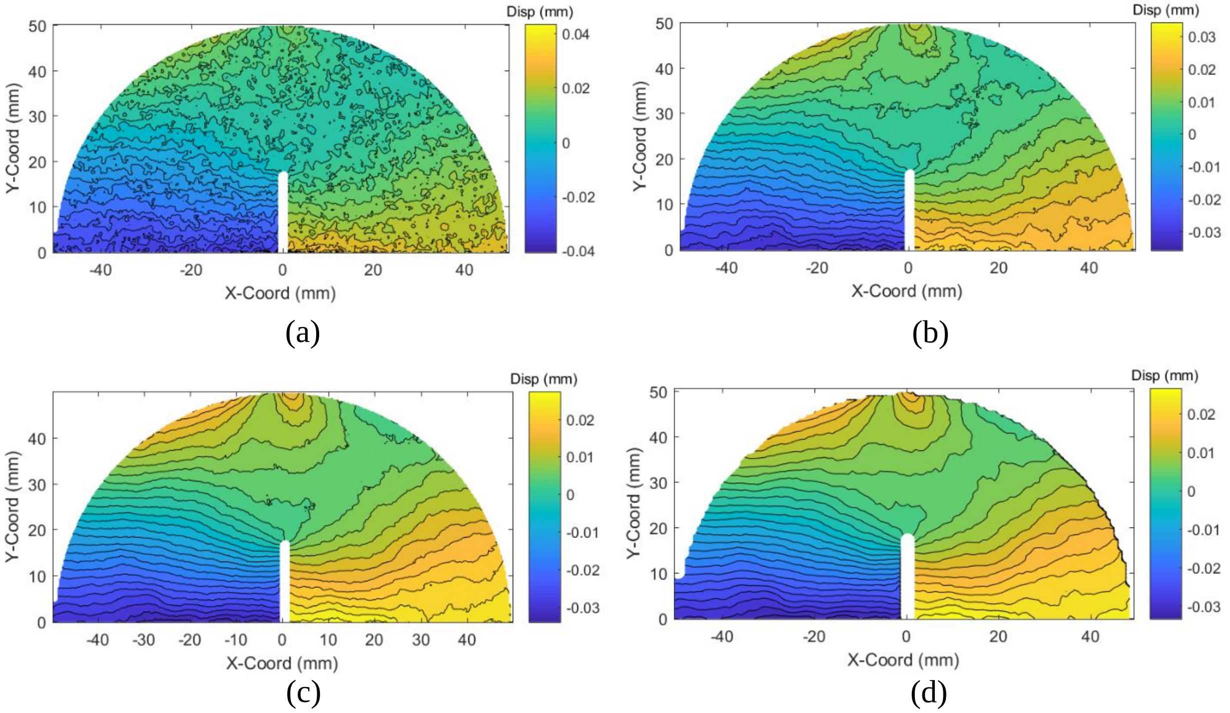

(a) (b)

(c) (d)

Figure 3-13: Opening displacement contours from 90° crack orientation experiment (pure mode I) at 400 N for different subset radii and spacing: (a) 15 pixel radius, 5 pixel spacing, (b) 30 pixel radius, 5 pixel spacing, (c) 45 pixel radius, 5 pixel spacing, (d) 45 pixel radius, 15 pixel spacing

As previously discussed, it is often advantageous to address noise when using digital image correlation. A numerical study was performed to qualitatively evaluate the effects of each of the filtering variables (details provided in earlier section 2.2.4) on the displacement results, specifically, the neighborhood size and filtering parameter. As the size of the neighborhood increases and/or higher values of the filtering parameter are chosen, it is possible to over smooth the image. There are also diminishing returns in terms of the effectiveness of the filter since points closer to the edge of the neighborhood for a given point have less effect on the filtered results. The performance of the filter is best illustrated using displacement contour plots (Figure 3-14) at lower loads where more experimental noise is present. A comparison is shown of contour plots of an unfiltered data set compared to the filtered counterparts from three different neighborhood sizes (3, 5, and 7 subset points). For a given neighborhood size, *n*, each subset center point is filtered based on the n x n grid of points surrounding it (see Figure 2-3). As can be seen, there is a noticeable difference in the noise in the unfiltered (a) vs filtered (b, c, d) contour plots. However, as the neighborhood size increases, the observed difference becomes less apparent. For the present work, a neighborhood size of 5 and a filtering parameter of 0.01 was chosen.

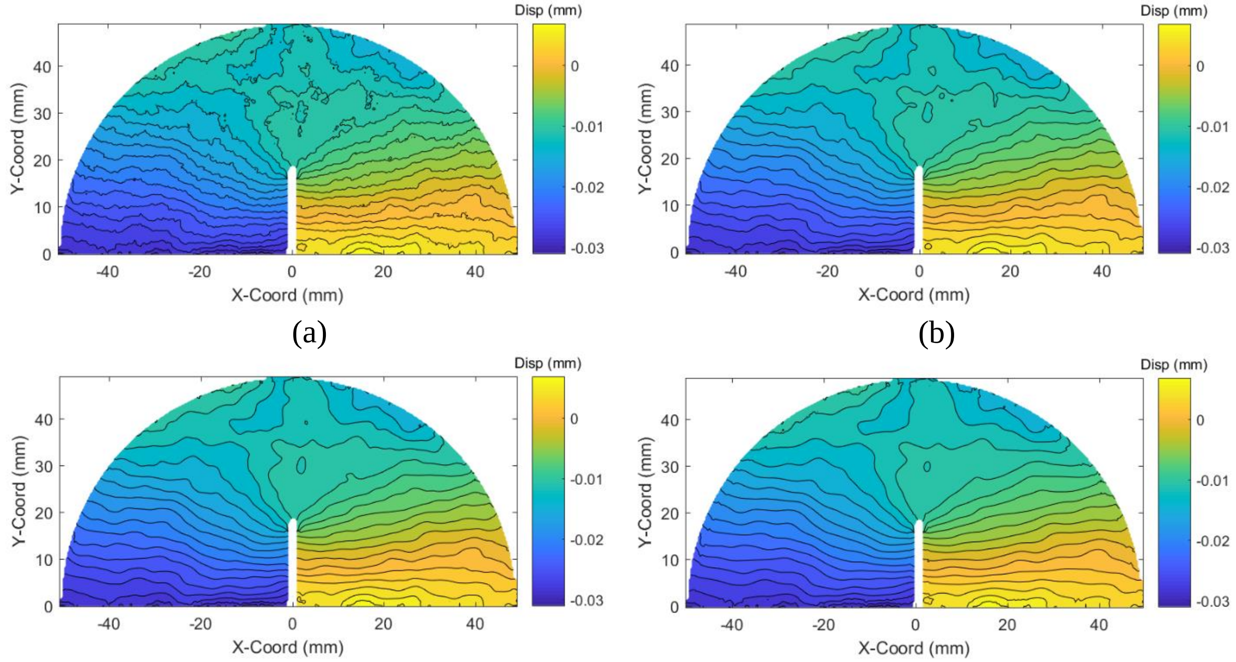

(a) (b)

(c) (d)

Figure 3-14: Effect of filtering on displacement contour noise: (a) Unfiltered, (b) Neighborhood size, n = 3, (c) n = 5, (d) n = 7

3.5 Comparison of results

3.5.1 Mode I and Mode II comparisons

Initial tests were conducted with a three-point bend fixture that utilized a roller at each of the support points and a flat platen to apply the load at the top of the specimen. It should be noted that the sensitivity of this specimen geometry to frictional effects at the supports and symmetry was first noticed and analyzed numerically. It was found to be an important consideration for practical implementation. Critical evaluation and further discussion of these results is detailed in later sections. The tests were conducted on a Tinius Olsen uniaxial load test frame. The specimens were loaded under displacement control at a rate of 0.25 mm/min. The camera was controlled remotely to acquire images at uniform intervals of 1 second. A 44.5 kN capacity load cell (accuracy = 0.04% of full scale) was used to measure the applied load. The Ncorr software was used to perform the speckle image correlations to quantify displacements. The measured displacement data and associated DIC output coordinate locations were used to directly build a finite element mesh as previously described in section 2.2.5. Based on the subset spacing (5 pixels), and the pixel scale factor (~0.051 mm), the resulting distance between neighboring output points was 0.30 mm in the DIC grid.

It is important to first verify that the contour integral quantified using the proposed methodology is indeed path independent. ABAQUS® by default performs the contour integral computation for individual sets of elements that enclose the crack tip. To verify the path independence of the *J*-integral, successive contours must be extracted at increasing radial extents from the crack tip. The specifics of this computation can be configured by the user. Depending on how the output request is configured, the elements considered in each contour integral computation can be automatically determined by the ABAQUS® pre-processor, or it can be specified by the user. Due to the orientation of the crack (at some arbitrary angle) and the structure of the gridded displacement output data, it was necessary to customize the definition of the contour integral domains. The standard process was not adequately reliable in selecting nodes and elements for the contour domain and often resulted in abnormally shaped contour domains at distances farther away from the crack tip. Therefore, an automated process for defining groups of nodes and elements at increasing radii away from the crack tip was created and implemented in the MATLAB® post-processing script. An example of the selected nodes is illustrated in Figure 3-15.

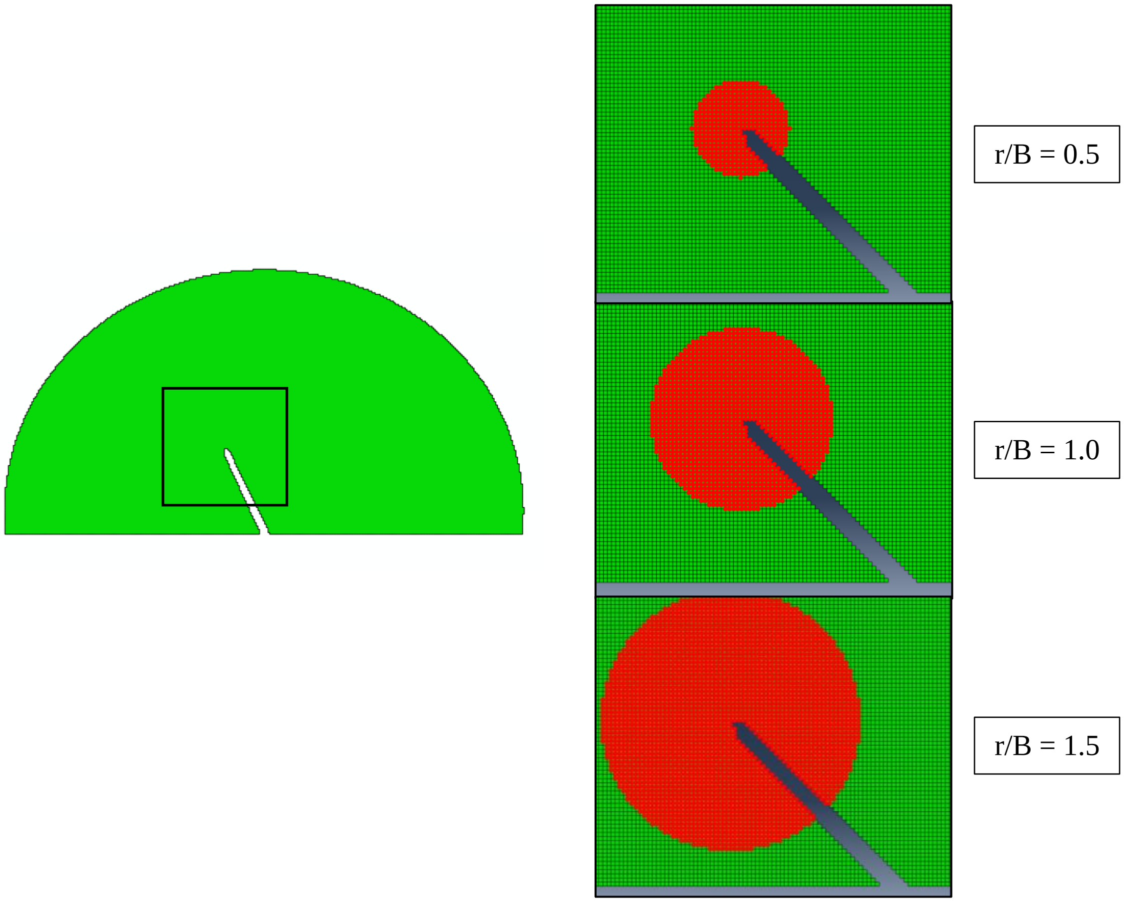

Figure 3-15: Example of node locations from circular contour around crack tip utilized in domain integral calculation (green squares are FE model elements, red-highlighted points are nodes included in contour integral evaluation)

The *J*-integral output is plotted as a function of the ratio of radius to specimen thickness (r/B) in Figure 3-16 (a) for the pure mode I case and in Figure 3-16 (b) for the near mode II case, where r is the radial distance from the crack tip and B is the specimen thickness. For reference, a value of $r/B = 3$ corresponds to a contour radius of 19.1 mm.

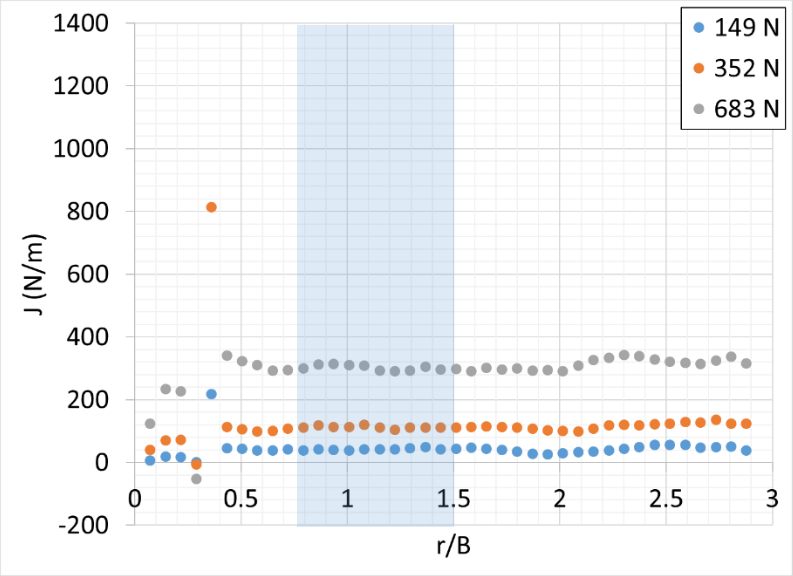

(a)

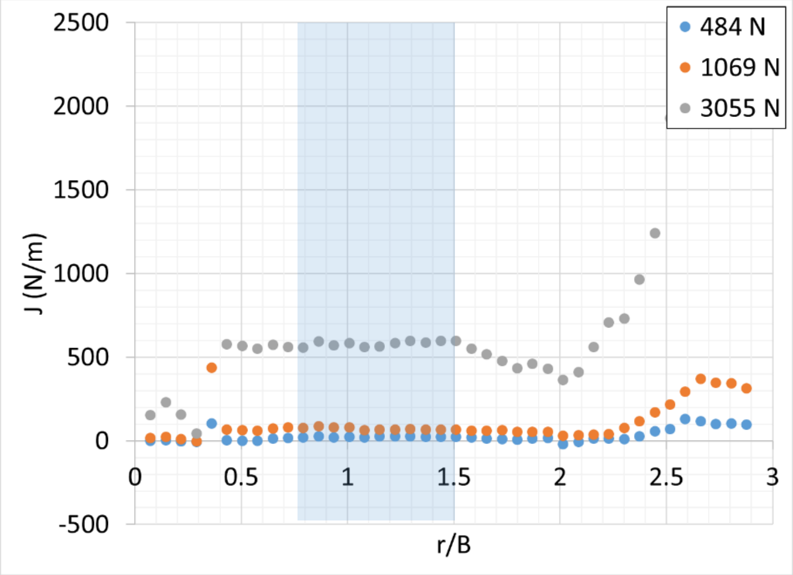

(b)

Figure 3-16: Path independence of the *J*-integral from hybrid DIC-FE approach at different load steps for (a) pure Mode I test, (b) pure Mode II test

Generally, as the radius of the contour increases, the *J*-integral values remain relatively constant. This does not hold true for points within the zone approximately *r/B* = 0.5 (or ~3 mm) from the crack tip. This can be attributed to a combination of factors including crack tip stress triaxiality, inelastic deformations, errors in identifying the crack tip position, and potential mesh size dependencies. Otherwise, the value remains relatively constant, even at very low loads for the mode I case. For the mode II case, the value remains relatively constant for $0.5 \leq {}^{r}/_{B} \leq 2$. The same effects persist at very small radii as with the mode I case. Outside of this range, the individual contours reach the edge of the test specimen, and some path dependence on the *J*-integral output values is seen.

One particularly interesting advantage of this technique is that the selection of crack tip position is much less critical when compared to the least squares approach. To ascertain this, the mode I experimental data were analyzed by intentionally selecting erroneous locations for the crack tip. Those erroneous locations were chosen across a range of positions within approximately 1.5 mm of the nominal location of the crack tip (as identified in the speckle image). This was considered to be a large range relative to an experimentalist's ability in most cases to correctly identify the crack tip at this specimen scale. The computed *J*-integral values for the mode I case are plotted in Figure 3-17 (a) for a select load level. Evidently, they are invariant relative to the crack tip position selection. A similar exercise was performed for one of the mixed-mode cases (65° crack inclination angle), and comparisons were made with respect to SIF computations. These comparisons, shown in Figure 3-17 (b), indicate that the method is rather robust in this regard.

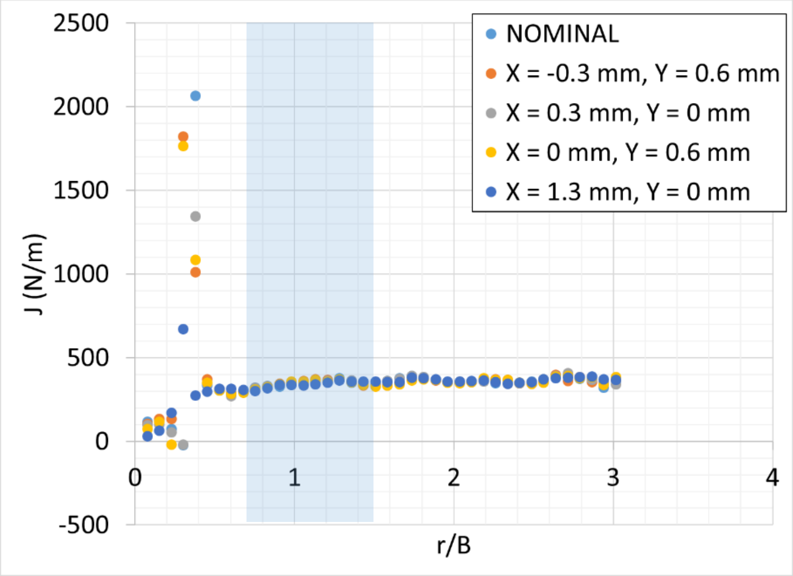

(a)

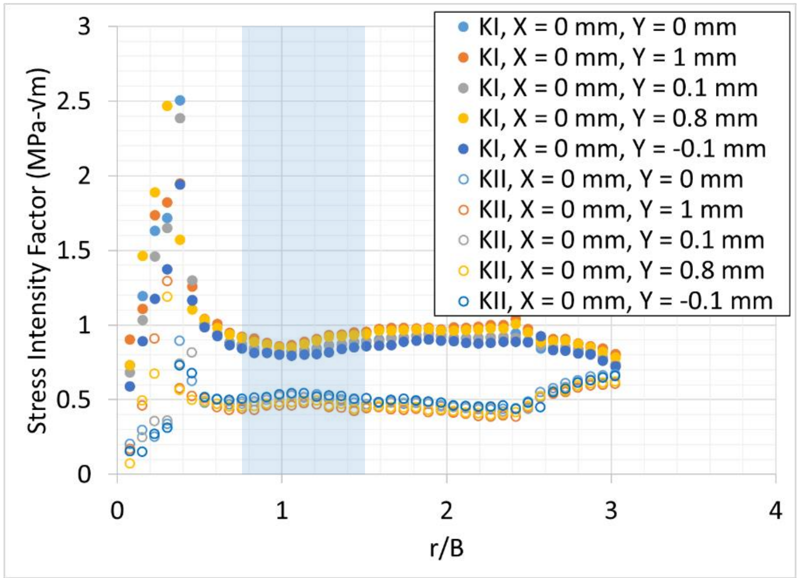

(b)

Figure 3-17: Sensitivity of fracture parameters due to crack tip position selection for (a) the *J*-integral for mode I case (load = 840 N) and (b) K_I and K_{II} for a mixed-mode case (crack angle = 65º, load = 1200 N)

3.5.2 Mixed-mode experiments

One sample from each crack orientation angle was loaded to a predefined load before failure to generate displacement data for extracting the fracture parameters namely K_I and K_{II} for comparing them with the ones from the baseline methods. The comparisons are plotted in Figure 3-18 for the linear elastic finite element model (FEM), over-deterministic least squares (LS) analysis, and the hybrid DIC-FE approach. The differences between each method and the predicted results are summarized in Table 3-3. The results generally agree well with each other for both mode I and mode II stress intensity factors. Note that the initial tests for the 90°, 80°, and 65° samples were performed to lower loads as they are expected to fail at lower loads due to the higher mode I contribution. Further discussion with respect to potential differences between the experiments and the linear finite element model are detailed in later sections.

Table 3-3: Estimates of difference between predicted and experimental results for quasi-static case

	DIC-FE vs FEM		**LS vs FEM**	
Angle	**K_I**	**K_{II}**	**K_I**	**K_{II}**
(deg)	(Mpa-√m)	(Mpa-√m)	(Mpa-√m)	(Mpa-√m)
45	0.160	0.028	0.091	0.021
50	0.032	0.024	0.032	0.025
55	0.184	0.027	0.164	0.033
65	0.075	0.063	0.068	0.055
80	0.054	0.011	0.043	0.008
90	0.108	0.053	0.115	0.014

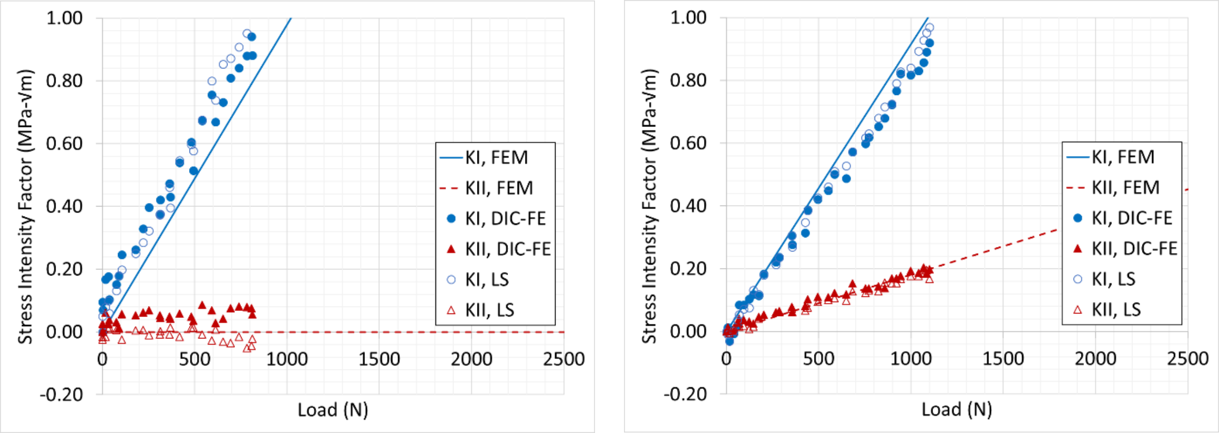

90° (Mode I)

80°

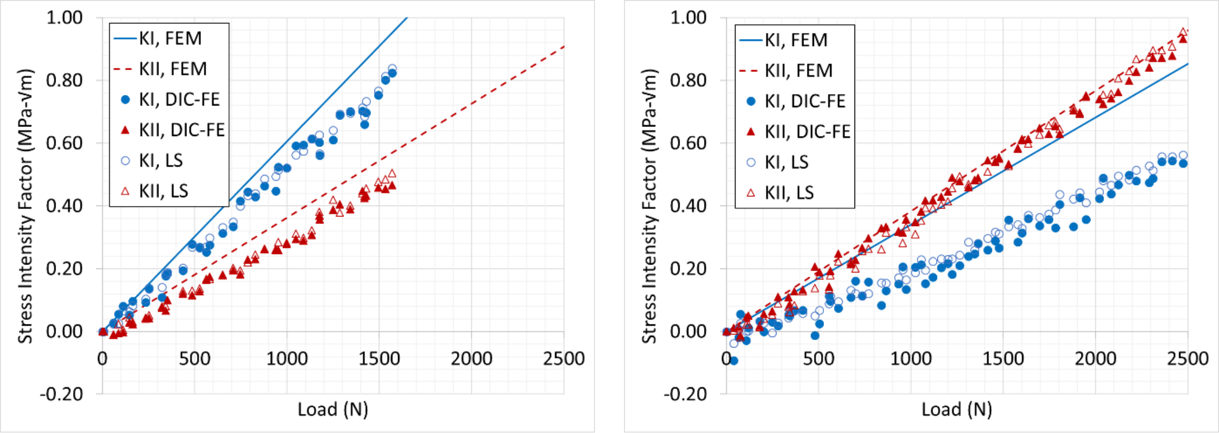

65°

55°

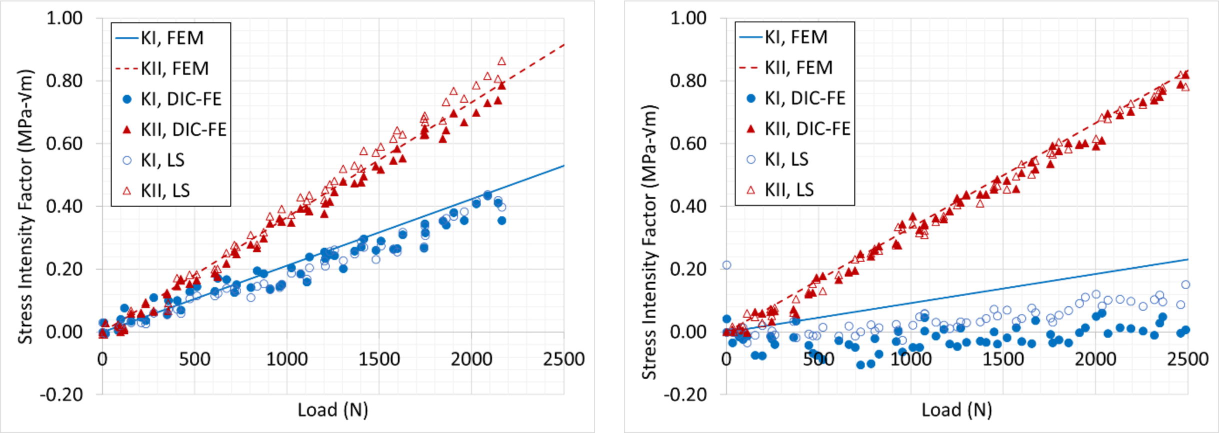

50°

45°

Figure 3-18: Stress intensity factors extracted for different mode mixities from homogeneous experiments under quasi-static conditions

3.5.3 Additional SCB specimen considerations

As described previously (in section 3.1.1), the SCB specimen geometry offers many features that are beneficial to study mixed-mode fracture. Specifically, it is convenient from a fabrication standpoint, and it can achieve a full range of mode mixities, from pure mode I to pure mode II. However, there are several implementation challenges that must be addressed. First, this specimen geometry has a relatively short support span, *S*, relative to the radius, *R*. Furthermore, the ratio of the support span to the crack length, *a,* is also relatively small. Therefore, there is room for errors due to asymmetry in the support locations relative to the crack. Second, small amounts of lateral load at the supports from friction (in the case of a fixed support pin) and rolling resistance (in the case of a free roller support) have potential negative influence on the results. The typical method for extracting fracture parameters using this geometry usually involves measuring the applied force at crack initiation and inputting that to a finite element model to infer the critical crack tip parameters such as SIF. While doing so, the lateral components of load at the supports are typically not considered since frictionless contacts are assumed by default.

During the course of conducting experiments using this specimen design, two different support configurations noted above were considered. Note that unless stated otherwise, the reported results utilized the roller support. Each of the two support points consisted of a steel roller that was free to rotate on a hardened and polished steel pin. Additionally, lubricant was also applied to each pin to further minimize friction. For the mode I case, a separate experiment was conducted that utilized more common fixed support pins that were not free to rotate. The extracted stress intensity factors are plotted versus load for each of the two experiments in Figure 3-19.

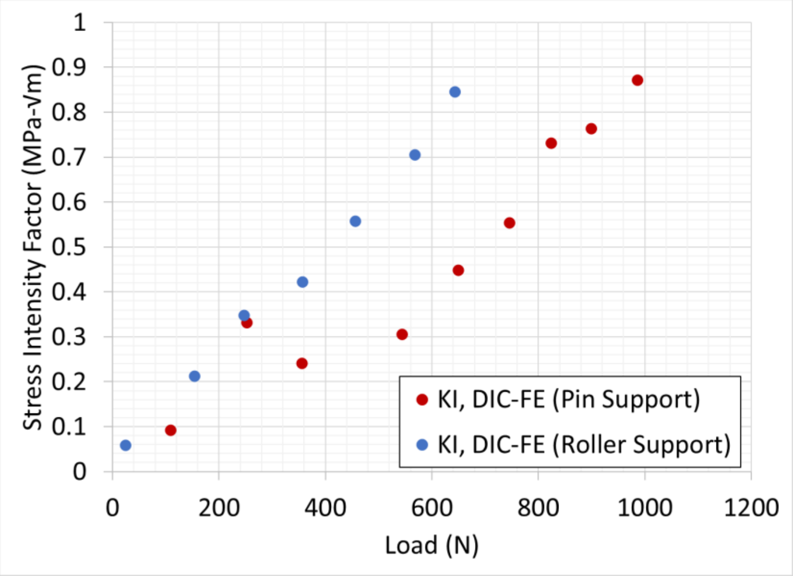

Figure 3-19: Comparison of experimentally measured SIFs obtained from fixed support and roller support fixtures showing suspected stick-slip behavior

The slope of the stress intensity factor vs. load history is noticeably different between the two experiments. For instance, the load at which the specimen reached a stress intensity factor of 0.5 MPa-√m for the fixed pin support was over 50% higher than the load required to achieve the same value for the roller pin support. Additionally, the SIF values for the pin support seem to suggest a stick-slip behavior between the specimen and the pin. That is, an abrupt drop in SIF value at ~250 N is evident in Figure 3-19 followed by an increase with increasing loads. It is suspected that this is largely due to the frictional effects at the support pin creating a closing moment that reduces the crack tip stresses. As the load increases, the frictional force would be proportional to the normal load at the pin and can contribute to the closing moment significantly.

A finite element model with friction at the two supports was used to test this hypothesis. In the mode I case, the observed/apparent mode I value can be potentially higher than the actual mode I value if friction is not accounted for. The effect of friction on observed mode I behavior is shown in Figure 3-20. The coefficient of friction between the bottom edge of the specimen and the support pin was increased and each model was loaded to the same load. These results suggest that at a coefficient of friction value of 0.2, which would be representative of an epoxy material sliding on a fixed steel pin, the actual mode I SIF could be roughly 60% of the mode I SIF as observed based on applied load.

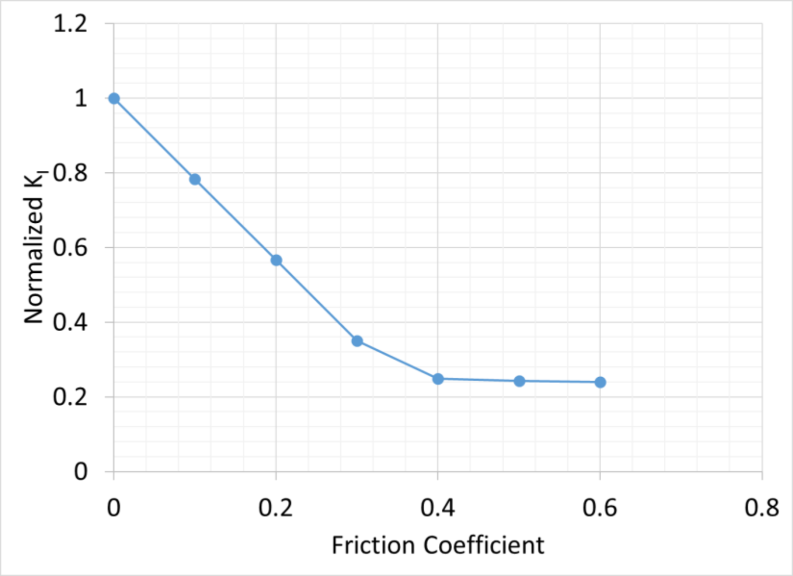

Figure 3-20: Effect of support pin friction on mode I stress intensity factor for 90° sample

A similar effect can be seen in the mixed-mode case where overall specimen load is much higher in magnitude. In the mixed-mode cases where the vertical load can be significantly higher, this effect could get exacerbated as illustrated in Figure 3-21 for the response of mode mixity. For the frictionless assumption, the mode mixity is pure mode II whereas for the case where the friction coefficient is equal to 0.2, the mode mixity is 40° which is substantially different from the intended 90°.

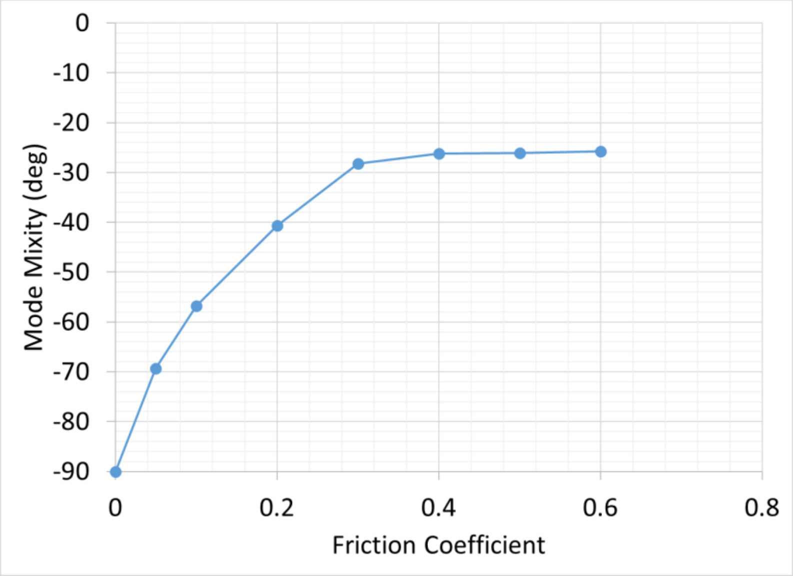

Figure 3-21: Effect of support pin friction on mode mixity for 40° crack orientation

For the mode I case, increase in the friction coefficient can lead to drastic reductions in inferred mode I stress intensity factor. It should also be noted that even in the scenario of a perfectly frictionless rolling support, the rolling resistance between the hardened steel roller and the softer specimen material can have a similar effect, however, it is expected that it would be less severe.

In addition to the effects of lateral frictional forces at the support points, other considerations seem important for this geometry as well. Due to the short support span in the SCB specimen geometry, small amounts of asymmetry in the support location, can introduce relatively significant changes to the mode mixity. In Figure 3-22, mode mixity is plotted for various states of misalignment for the 90° crack orientation. A modest asymmetry expressed in terms of the ratio of the left half-span to the right half-span of 1.1 could result in approx. 3° mode mixity.

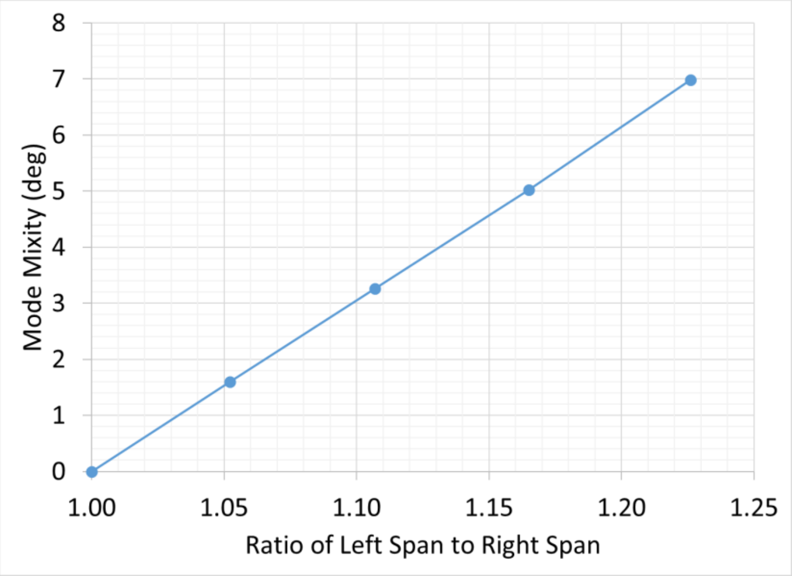

Figure 3-22: Effect of support asymmetry on mode mixity for 90° crack orientation

Similar observations have been made by other authors [85] where discrepancies between critical stress intensity factors extracted using analytical expressions with failure load approached twice the value of critical stress intensity factors extracted using full-field displacements from DIC. These observations and the ones in the present work underscore the importance of specimen alignment and support configuration when using SCB specimen geometry.

The results presented thus far confirm that the geometry itself can produce the desired experimental results. The specimen geometry behaves as expected and the hybrid method for acquiring the results demonstrates a marked improvement in the reliability of the data due to removing uncertainties with respect to load and support point effects.

3.6 Experimental Results

3.6.1 Mixed-mode fracture tests

A series of fracture tests were first performed to utilize this approach to extract the critical stress intensity factors across a range of mode mixities. Each of the test specimens exhibited brittle failure with the load increasing monotonically up to failure when the load instantaneously decreased. Representative load-displacement histories are plotted in Figure 3-23. The minor nonlinearities observed during the tests are attributed to fixture settling, nonlinear material response at the load point or support points, and possible rolling or sliding friction at the support points.

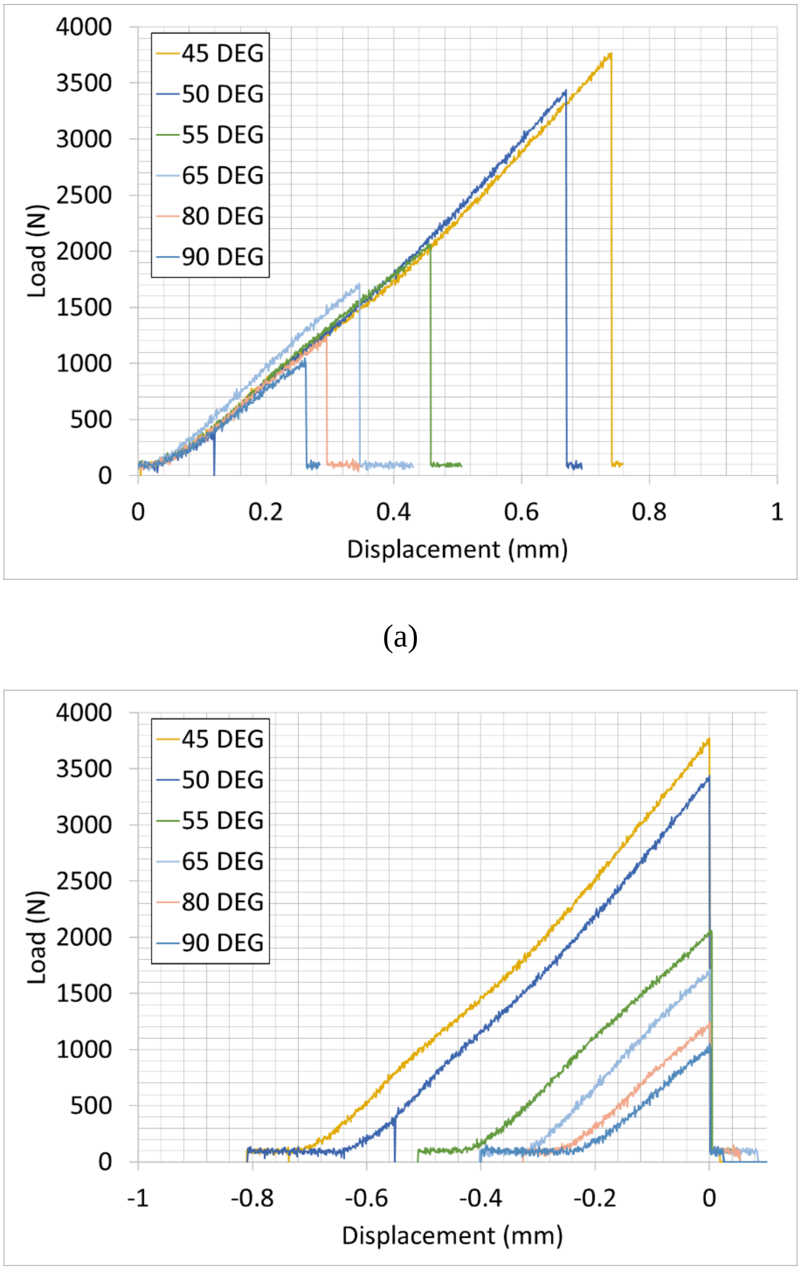

(a)

(b)

Figure 3-23: Load histories for each crack inclination angle. (a) Plot with displacement of zero corresponding to start of experiment and (b) Plot with displacement of zero corresponding to failure point

Multiple test samples were cast and tested for each crack inclination angle. The stress intensity factors for each mode were extracted at failure using the hybrid DIC-FE post-processing technique. The mode mixity at failure was computed and plotted for different crack inclination angles. The measured values of mode mixity from the hybrid DIC-FE approach agree well with the expected response from the finite element model as shown in Figure 3-24. The deviation is slightly more pronounced as the mode II case is approached, but the general agreement is still good.

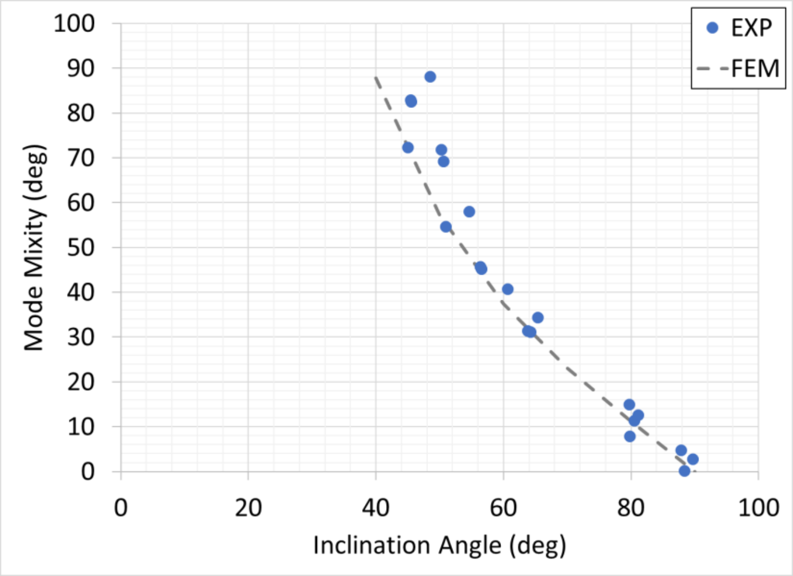

Figure 3-24: Comparison of mode mixity for different crack angles in the SCB specimen with the corresponding FEM computations for quasi-static experiments

The two critical stress intensity factors, K_{Icr} and K_{IIcr}, from each of the experiments are plotted as a crack initiation envelope in Figure 3-25.

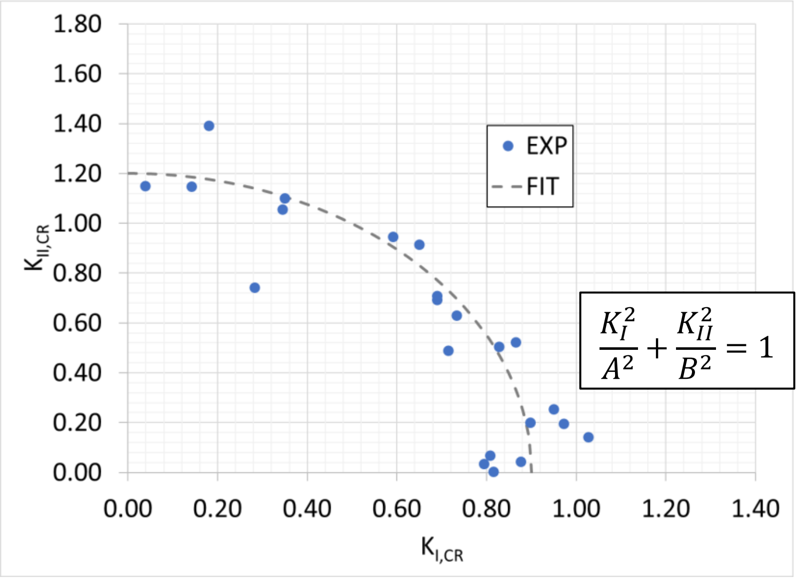

Figure 3-25: Envelope of critical stress intensity factors from quasi-static experiments with homogeneous material samples

The curve fit is of the form $\frac{K_I^2}{A^2} + \frac{K_{II}^2}{B^2} = 1$ where the variable *A* and *B* represent the approximate mode I and mode II critical stress intensity factors. The values of *A* and *B* for the fit are 0.9 and 1.2. While there appear to be some outliers in this data set, this testing includes all data collected in the earliest experimental phase of the work. The scatter in the data is likely most attributable to minor inconsistencies that are inherent to quasi-static experiments. For instance, due to the slow load rate, several factors such as load frame vibration and other external noise can become meaningful at these time scales. Some of the scatter is also attributable to the variability in the material considering these data represent several batches of cast specimens.

3.6.2 Crack propagation direction behavior

For each crack inclination angle, the expected crack propagation angles were calculated using the maximum tangential stress criterion for brittle materials using the load results and the finite element models. This criterion states that the crack is assumed to crack grow when the maximum average tangential stress in the region ahead of the crack tip reaches its critical value and the crack growth direction corresponds with the direction of the maximum average tangential stress along a constant radius around the crack tip. The near-crack-tip tangential stress for a mixed-mode crack in a homogeneous, isotropic linear elastic material as described in [86] is,

$$(\sigma_{\theta\theta})_{cr} = \frac{1}{\sqrt{2\pi r}} \cos\frac{\theta}{2}\left[K_{Icr}\cos^2\frac{\theta}{2} - \frac{3}{2}K_{IIcr}\sin\theta\right] + O\left(r^{\frac{1}{2}}\right) \qquad [3\text{-}3]$$

where K_{Icr} and K_{IIcr} are the critical mode I and mode II stress intensity factors, respectively. By taking the derivative with respect to the angular coordinate, θ, the angle of crack propagation can be found using:

$$[K_{Icr}\sin\theta_0 + K_{IIcr}(3\cos\theta_0 - 1)] = 0 \qquad [3\text{-}4]$$

where θ_0 is the crack propagation direction. Here, it should be noted that the higher order terms (e.g. $O\left(r^{\frac{1}{2}}\right)$) in Williams' asymptotic stress fields are considered to be negligible. For each test specimen, analysis of failed specimen images was used to measure the crack initiation direction. More recently, it has been suggested [87] that the so-called *T*-stress, the second higher order term in the asymptotic stress field, may play an important role in the crack growth behavior. It is suggested that considering the *T*-stress in the maximum tangential stress computation provides better agreement with predicted crack propagation conditions. In this form, the modified maximum tangential stress criteria is computed (MMTS) using:

$$\sigma_{\theta\theta} = \frac{1}{\sqrt{2\pi r}} \cos\frac{\theta}{2}\left[K_I\cos^2\frac{\theta}{2} - \frac{3}{2}K_{II}\sin\theta\right] + T\sin^2\theta + O\left(r^{\frac{1}{2}}\right) \qquad [3\text{-}5]$$

and thus, the resulting derivative becomes:

$$[K_I\sin\theta_0 + K_{II}(3\cos\theta_0 - 1)] - \frac{16T}{3}\sqrt{2\pi r_c}\cos\theta_0\sin\frac{\theta_0}{2} = 0 \qquad [3\text{-}6]$$

where T is the T-stress, and r_c is a critical value of radial distance away from the crack tip and is considered to be a material parameter. The T-stress is related to the in-plane constraint effect and can affect the local crack growth mechanics. The T-stress is extracted from the linear, elastic finite element model using an auxiliary solution of a line load applied in the plane of crack propagation and along the crack line as described in [88].

Separately, the maximum energy release rate (MERR) is often used as a criterion by which to evaluate crack propagation direction. The stress intensity factors at the tip of the kinked crack can be defined as linear combinations of the stress intensity factors of the parent crack as:

$$K_I^k = c_{11}K_I + c_{12}K_{II} \quad [3\text{-}7]$$

$$K_{II}^k = c_{21}K_I + c_{22}K_{II} \quad [3\text{-}8]$$

where the coefficients, c_{ij}, are defined in references [89] and [90] and the energy release rate is defined as:

$$G^k = \frac{1}{E}\left({K_I^k}^2 + {K_{II}^k}^2\right) \quad [3\text{-}9]$$

and the crack propagation direction is found by identifying the stress intensity factors that maximize the energy release rate, G.

To assess these two sets of crack propagation direction, the values for a given crack inclination angle as measured from fractured specimens were averaged for comparison with the finite element counterparts. The crack propagation directions, as calculated from Equation [3-5] and [3-6], are compared to the experimental average crack propagation directions in Figure 3-26. In general, the average propagation directions were fairly consistent with low standard deviations. The measured values of kink angle are particularly difficult to ascertain. However, for this test series, multiple measurements were averaged together, the resulting values were plotted along with error bars indicating one standard deviation above and below the average measured value. The predicted values were generally lower than the observed ones, however, when the *T*-stress is considered, the agreement between the predicted propagation directions and the experimentally measured directions is much closer.

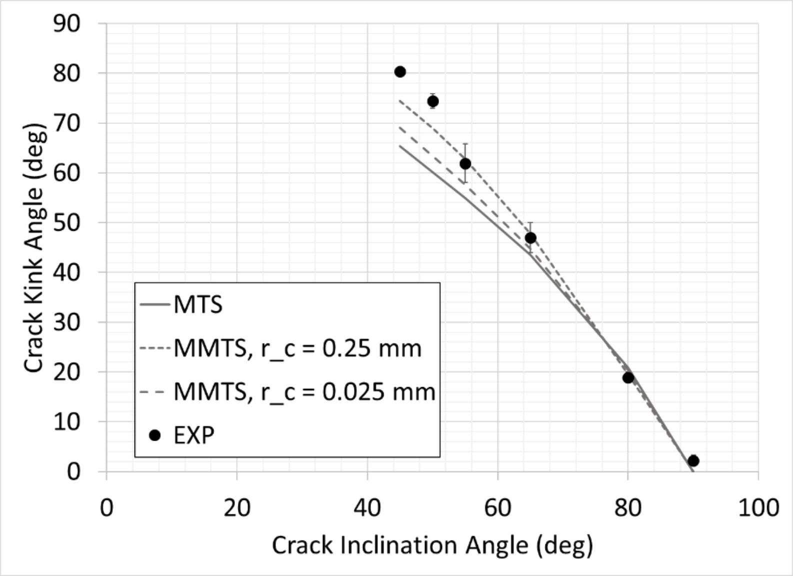

Figure 3-26: Comparison of crack propagation direction with FE predictions based on different implementations of the MTS criterion and modified-MTS criterion

The photographs of failed specimens representative of each inclination angle are shown in Figure 3-27 to visually demonstrate the direction in which the crack initiates. The kink angle values were fairly consistent across multiple test specimens tested at a given angle.

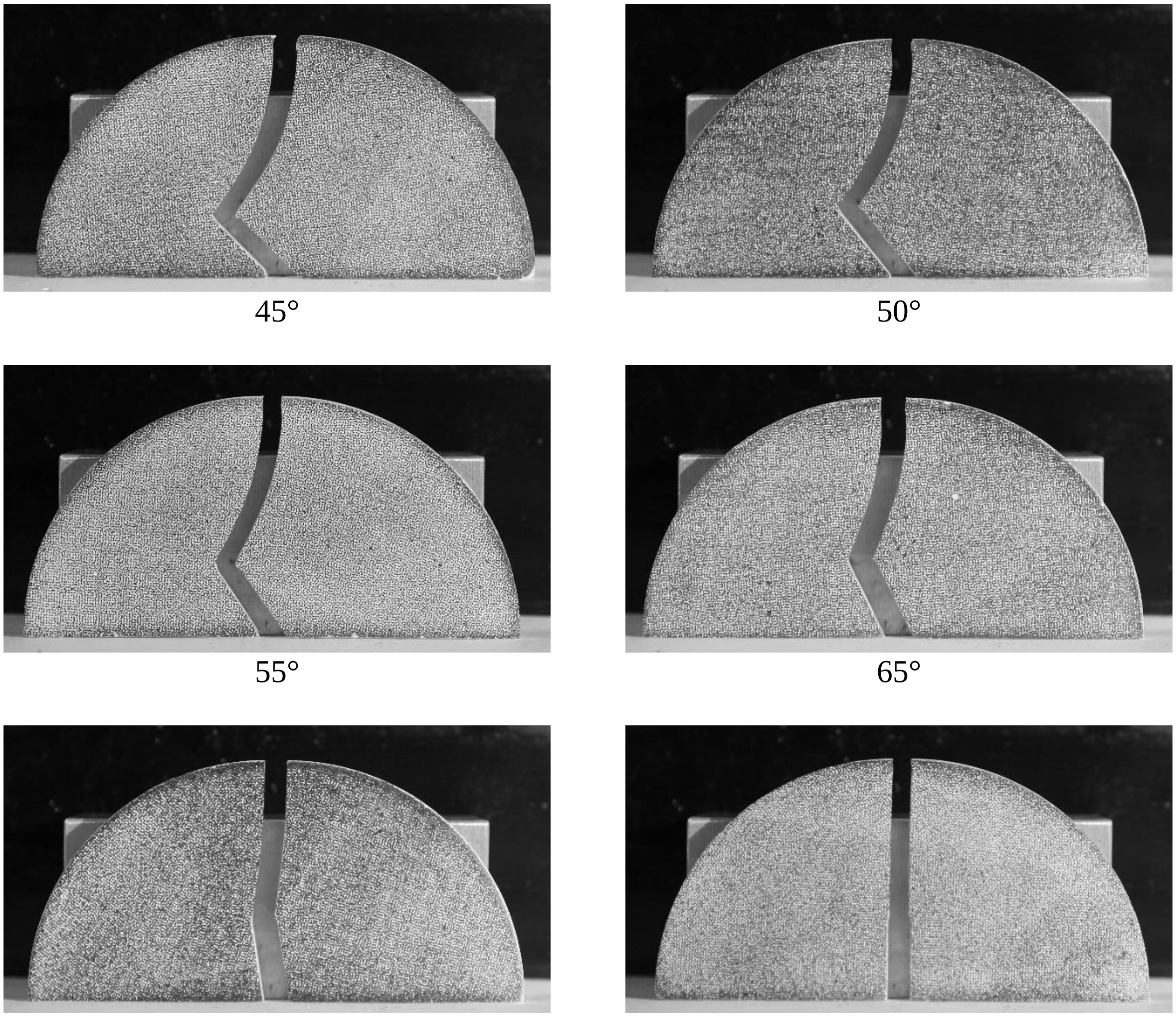

45° 50°

55° 65°

80° 90°

Figure 3-27: Images of failed SCB test specimens

3.6.3 Effect of in-plane compression stress

The static test setup for the homogenous material specimens was further adapted to investigate fracture at lower crack inclination angles. As the angle drops below approximately 45°, the mode I stress intensity factor becomes negative. A series of tests was performed at 40°, 35°, and 30° to further quantify what happens at these negative mode I conditions. The results of the negative mode I experiments are plotted with the results from the full range of mode mixities in Figure 3-28. The mode II stress intensity factor at failure continues to increase as the apparent mode I stress intensity factor becomes increasingly negative. Angles lower than 30° were not tested, because at sufficiently low angles, the crack tip is too close to the specimen edge and path dependent artifacts become apparent in the stress intensity factor outputs. The critical pure mode II stress intensity factor was approximately 1.2 MPa-√m (based on the location of the *y*-axis intercept of the curve fit). The apparent increase was observed to be as high as 60% at the tested levels of negative mode I stress intensity factor.

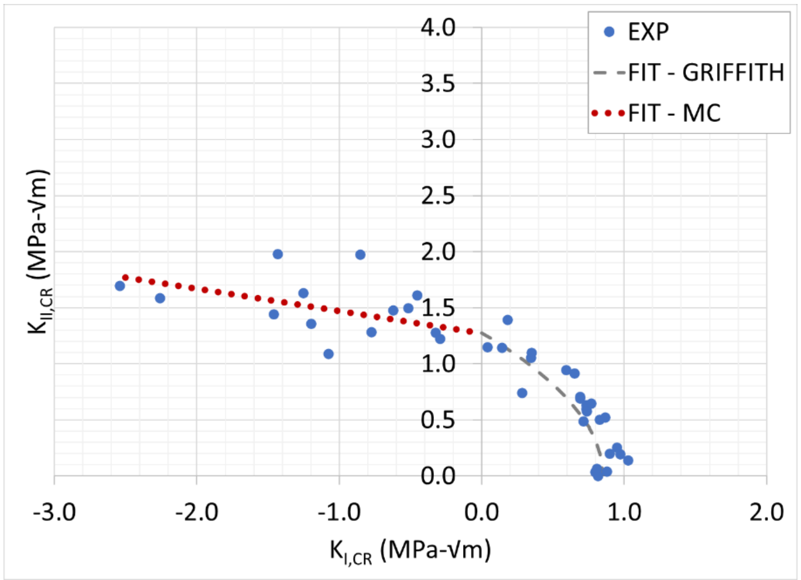

Figure 3-28: Critical stress intensity factors including in-plane compression state from quasi-static tests

The relationship, $\frac{K_I^2}{A^2} + \frac{K_{II}^2}{B^2} = 1$, has been found to fit the shear-tension fracture behavior well and is commonly used for reporting purposes in the fracture mechanics community. However, the Griffith failure envelope is also commonly used as an approximation to relate the strength behavior in the shear and normal directions. Whitaker [91] presents this criterion as a parabolic relationship between shear loading, τ, and normal loading, σ. The equation is:

$$\tau^2 = 4T_0(T_0 + \sigma) \qquad [3\text{-}10]$$

Taking a similar approach, this parabolic relationship was chosen to relate the shear and normal stress intensity factors at crack initiation in the present work. With respect to the relationship when compressive loading is present, the Mohr-Coulomb failure criterion has been widely used in material model applications to describe behavior in materials that exhibit increasing shear strength with compressive stress and is particularly interesting in the context of the present work. It has found widespread use in geotechnical community. The failure criterion is typically presented as a set of linear equations in principal stress space describing the conditions for which an isotropic material will fail. It is commonly presented in terms of normal and shear stress and is illustrated graphically in Figure 3-29. It can be further described as a line that fits tangent to a series of Mohr's circles that increase in diameter as the in-plane normal stress becomes increasingly negative. The slope of the line, φ, is referred to as the friction angle.

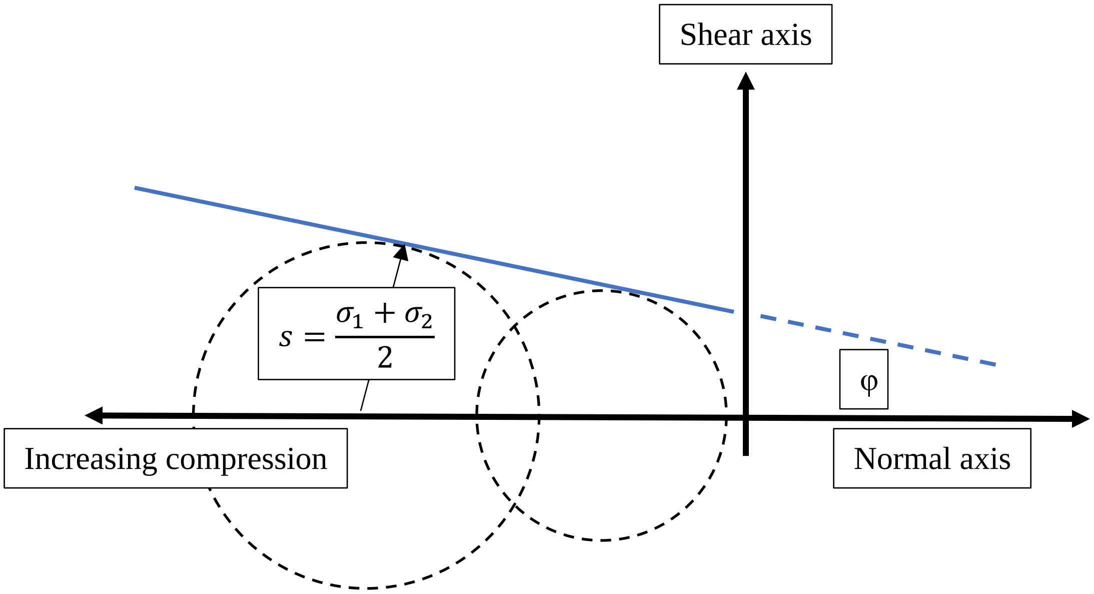

Figure 3-29: Illustration of Mohr-Coulomb failure envelope

While the present work is focused on stress intensity factors and not on in-plane stresses at failure, the analogy is still reasonable in the sense that the observed critical mode II stress intensity factor at failure has an apparent increase as mode I stress intensity factor at failure becomes increasingly negative. The linear relationship is plotted with the data from the quasi-static experiments in Figure 3-28. A friction angle of 0.2 rad (11.5°) was found to fit the experimental data well. The curve fit parameters for the Griffith and Mohr-Coulomb fits are summarized in Table 3-4.

Table 3-4: Summary of curve fit parameters for Griffith and Mohr-Coulomb fit (quasi-static)

	Parameter			
	Griffith		**Mohr-Coulomb**	
Test Series	$\mathbf{T_0}$	**A**	**c**	**φ**
Quasi-static, homogeneous	0.85	0.75	1.30	0.20

Chapter 4

Interface Fracture

One of the objectives of the current work is to experimentally investigate the effect of local compressive stress fields on a crack lying along an interface. The current chapter builds on the measurement and data processing methodologies presented in Chapters 2 and 3 and introduces a test fixture for meeting this objective. The characteristics of the fixture and specimen geometry are examined on several validation experiments. Finally, results are presented that quantify the relationship between interface fracture behavior and compression along the interface.

4.1 Development of a test apparatus for crack closure conditions

In the interest of applying the current methods to investigate the conditions surrounding a defect or crack that lies on one of the interfaces where a softer material is sandwiched between two stiffer materials, several test fixture approaches were considered. Ultimately, a lap shear arrangement was chosen for further development.

4.1.1 General fixture description

The proposed fixture is shown schematically in Figure 4-1. The shear test sample is comprised of a polymer layer sandwiched between two stiffer adherends. The test sample is mounted between two semi-circular plates that can be rotated to adjust the ratio of compression to shear loading that occurs in the test specimen, thus generating the desired combined load state in the specimen. This is conceptually similar to a Brazilian disc specimen geometry. The load is applied to the top of the fixture using a pin attached to the crosshead of the uniaxial load frame. The bottom of the fixture is supported by two pins slightly off the centerline of the fixture to stabilize the fixture. The load mixity is controlled by the fixture rotation angle, β, which can be adjusted to any angle. Pins are used to keep the fixture halves assembled at very low angles of fixture rotation. Each fixture half has a small step that engages the end of the specimen.

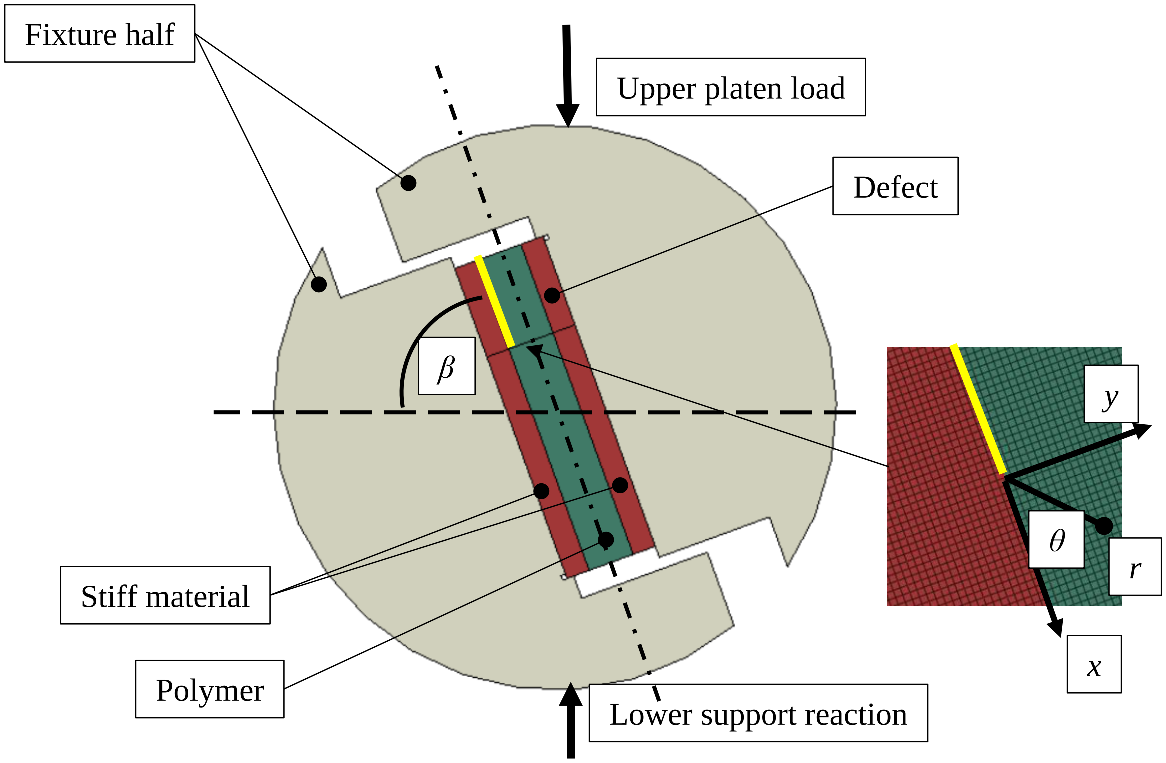

Figure 4-1: Illustration of steel-epoxy-steel sandwiched lap shear geometry loaded in biaxial load fixture, shown with typical crack tip mesh

4.1.2 Extraction of stress intensity factors using contour integral method

To extract the stress intensity factors, a similar contour integral approach was utilized as was described in previous chapters. The energy release rate can be computed using a domain (area) integral. The *J*-integral, as presented by Shih, et. al [77], is defined as in Equation [2-13]. This domain integral can be decomposed into the two stress intensity factors K_I and K_{II} for modes I and II, respectively. The ABAQUS® finite element software employs an interaction integral technique to partition *J* and extract the two stress intensity factors based on the technique described in [34]. For a crack along an interface between two dissimilar materials, the stress intensity factors are the real and imaginary parts of a complex stress intensity factor. This can be described using the interface traction values in [4-1].

$$(\sigma_{22} + i\sigma_{12})_{\theta=0} = \frac{(K_I + K_{II})r^{i\varepsilon}}{\sqrt{2\pi r}} \qquad [4\text{-}1]$$

where $\varepsilon = \frac{1}{2\pi}\ln\frac{1-\beta}{1+\beta}$ and $\beta = \frac{G_1(\kappa_2-1)-G_2(\kappa_1-1)}{G_1(\kappa_2+1)+G_2(\kappa_1+1)}$ where *G* is the shear modulus of each material and $\kappa = \frac{3-\nu}{1+\nu}$, with υ being the Poisson's ratio.

4.1.3 Displacement-based stress intensity factor extraction

In addition to the contour integral approach, mode II stress intensity factors can be estimated using sliding displacements along the crack surfaces based on the relationship in Equation [4-2]. Given that much of the crack face is in contact, the mode I stress intensity factors cannot be estimated using this approach.

$$|\delta| = \frac{c_1 + c_2}{4\pi\sqrt{1 + 4\epsilon^2}\cosh(\pi\epsilon)}|K|\sqrt{2\pi r} \qquad [4\text{-}2]$$

where ε is defined above, $c_i = \frac{\kappa_i+1}{\mu_i}$ for *i* = 1,2 and the complex displacement field is defined as $\delta = \Delta v + i\Delta u$ with *v* and *u* being the sliding displacements and opening displacements along the crack faces in the coordinate system illustrated in Figure 4-2. Using this relationship, a regression analysis of the displacements along the points on the crack surfaces, the magnitude of the stress intensity factor can be estimated.

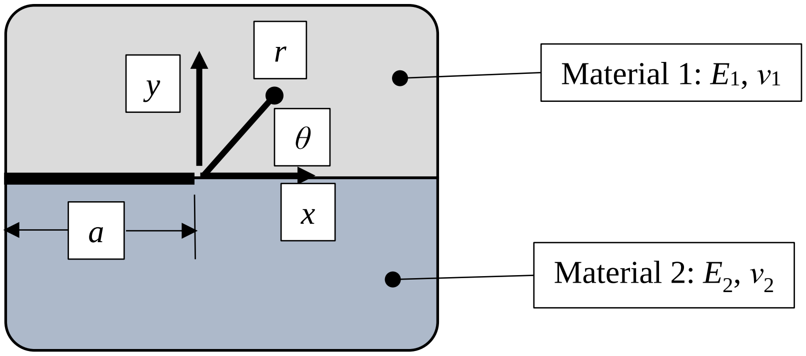

Figure 4-2: Interface crack coordinate system

4.1.4 Finite element model of test fixture

In order to design the specific details of this fixture and properly size the geometry, a finite element model was created in ABAQUS®. The following parameters were studied: adhesive thickness, adherend thickness, crack length, overall specimen length, and crack position (left/lower interface vs. right/upper interface). One desire of the test fixture design was to create a mixed-mode load state in the specimen with a near-uniform shear and compressive stress along the length of the specimen. A second goal was to create a geometry that lends itself to controlled fabrication of the specimen as well as stability and repeatability during the experiment to allow for practical implementation. A mesh refinement study was performed on the specimen with several element edge lengths evaluated. The domain integral extraction approach is relatively mesh size independent. An element edge length of 0.25 mm was determined to be appropriate for the test specimen mesh. The specimen was meshed with approximately 35,000 plane stress elements and 35,500 nodes.

4.1.5 Initial analytical results

Based on the outcome of a series of modeling studies considering different ratios of specimen length to height and different ratios of adhesive thickness to adherend thickness, a specimen geometry with an overall length of 76.2 mm and overall total thickness of 25.4 mm was identified as having the desired stress distribution characteristics and was chosen for this experimental study. The adherends have a thickness of 6.4 mm thickness leaving a nominal adhesive layer thickness of 12.7 mm and overall sample thickness of 25.4 mm. Analyses were run with the crack at the lower interface of the test specimen as well as at the upper interface of the test specimen. The general trends are similar between the two configurations. The most noteworthy results are shown in Figure 4-3 as shown from the analysis runs with the crack at the lower interface. The presence of the negative normal stress near the crack tip contributes to overall suppression of the shear stress and thus a decrease in the strength of the singularity.

As shown in the figure, at a fixture angle of approximately 75 degrees from horizontal, the far field stress normal to the interface ahead of the crack tip is approximately zero across the majority of the interface. As expected, the normal stress increases with increasing fixture angle. Secondly, and more importantly, the stress normal to the interface changes the strength of the shear stress singularity. This was also noted in the derivation of the analytical solution in [47]. One other finding from the analytical investigation was that the uniformity of the stress normal to the interface could be improved by introducing a slight offset of the load application point. The load is shown in Figure 4-1 as being aligned to the geometric center of the specimen.

However, more uniform stress distribution was found to occur when the load application point was aligned to the geometric center of the top face of the specimen.

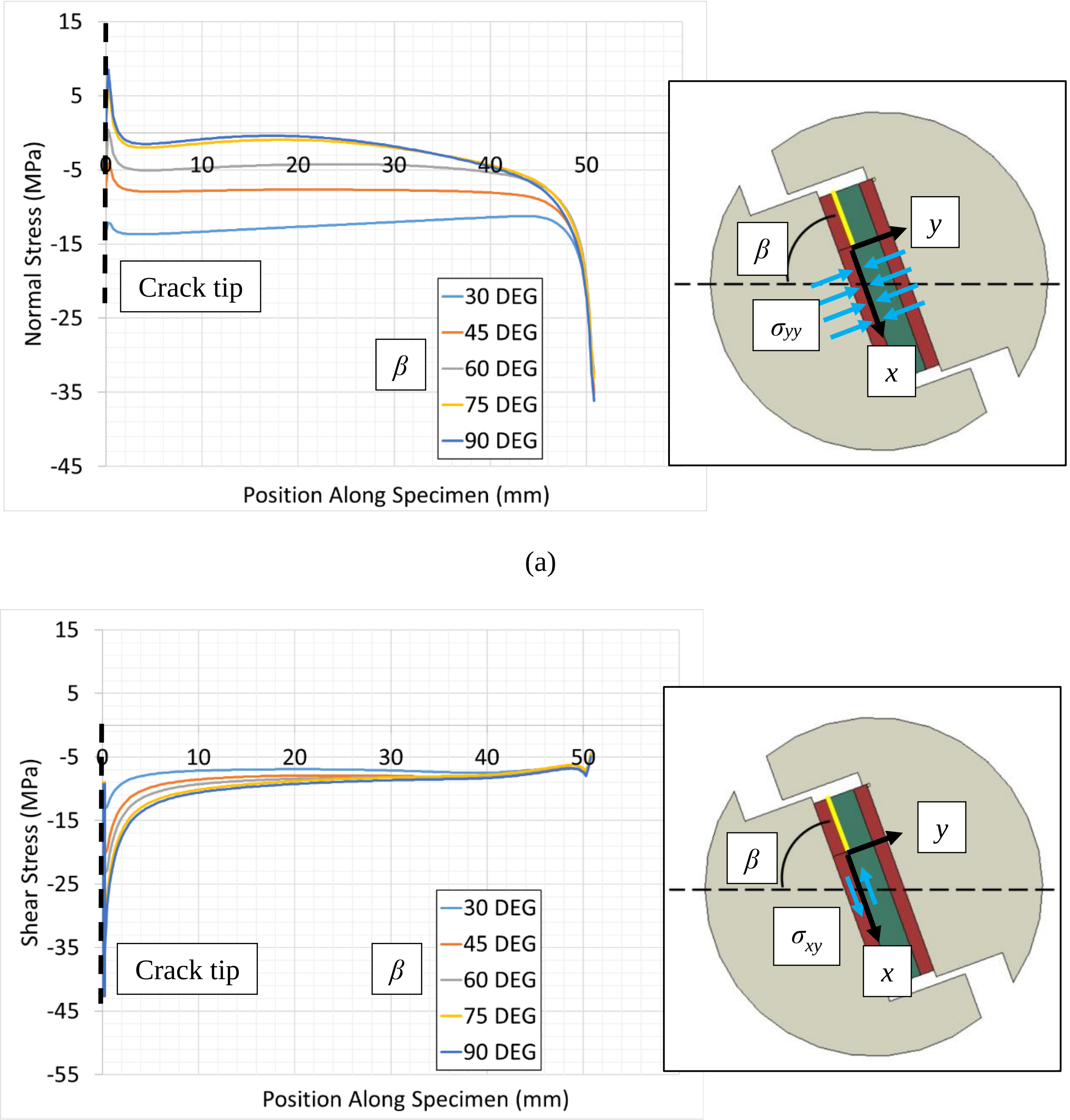

(a)

(b)

Figure 4-3: Stress distribution along interface of bimaterial lap shear geometry for (a) in-plane compression stress (acting normal to the interface) and (b) shear stress

4.1.6 Expected effects of friction at crack faces

One benefit of using the proposed data extraction technique is that it removes many of the uncertainties with respect to the fixture and test specimen. In many experimental methods for fracture mechanics, a closed form solution is not available for the specimen geometry, especially in more complex fracture arrangements. Therefore, the typical approach is to measure a load history and thus a failure load for the test specimen and then that measured failure load is applied to an analogous finite element model of the test geometry to compute the stress intensity factor at failure. While this is a convenient approach, and can provide reasonably accurate measurements, there are many uncertainties that can contribute to errors and should be accounted for accordingly. Two particular examples include load point alignment and support point alignment. In the current problem, crack face sliding friction is also an uncertainty. Thus, using the proposed method of extracting quantities directly from the measured deformations on the specimen surface, removes these uncertainties and provides a more robust approach. However, it is still beneficial to the experimentalist to understand these affects for interpretation of the results. The crack face sliding friction is largely unknown without specific testing to measure the relationship between shear traction and normal tractions along the interface. Further, these phenomena are often difficult to reliably model due to rate-dependence and nonlinear effects. A study was completed using an FE model to estimate this effect assuming a constant friction coefficient along the crack faces. A contact interaction was included in the FE model along the crack faces between the adhesive and the adjacent adherend. For each fixture orientation angle (mode mixity), a range of friction coefficients were assumed from 0 to 0.5. The results are plotted in Figure 4-4. As expected, increases in the friction reduce the observed stress intensity factor, meaning that for a given load, the actual stress intensity factor is lower than what the stress intensity factor would be if friction weren’t present. The affect is much more pronounced at specimen orientations that are further away from the pure mode II case (e.g. higher compressive stress) since increases in compressive loads increase the frictional effects and, therefore, increase the load that is resisting crack sliding. The proposed steel to epoxy sample is expected to have a coefficient of friction, μ ~ 0.2-0.3 [92].

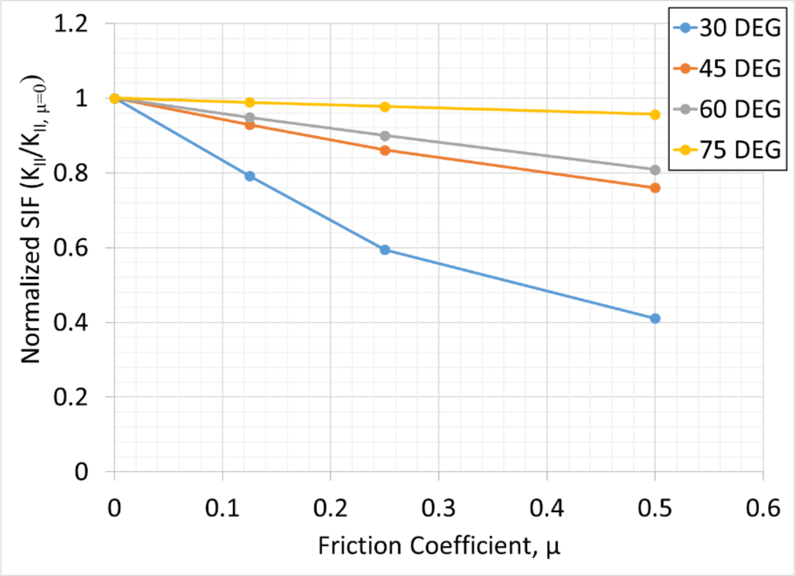

Figure 4-4: Expected reduction in observed K_{II} due to friction along crack faces in interface crack specimen geometry based on FE investigations

Possibly the more important observation regarding crack face friction is that the sliding friction is expected to have some slight influence on the invariance of the stress intensity factor (contour dependence). This effect is illustrated in Figure 4-5. However, as will be discussed in later sections, the affect is relatively benign across the fixture inclination angles of interest (45° to 75° from the horizontal). Also, the variation is relatively benign in the range of expected friction coefficients. The crack face itself is comprised of a machined steel surface sliding against epoxy-based material. An assumption of $0.2 \leq \mu \leq 0.4$ is expected to be reasonable.

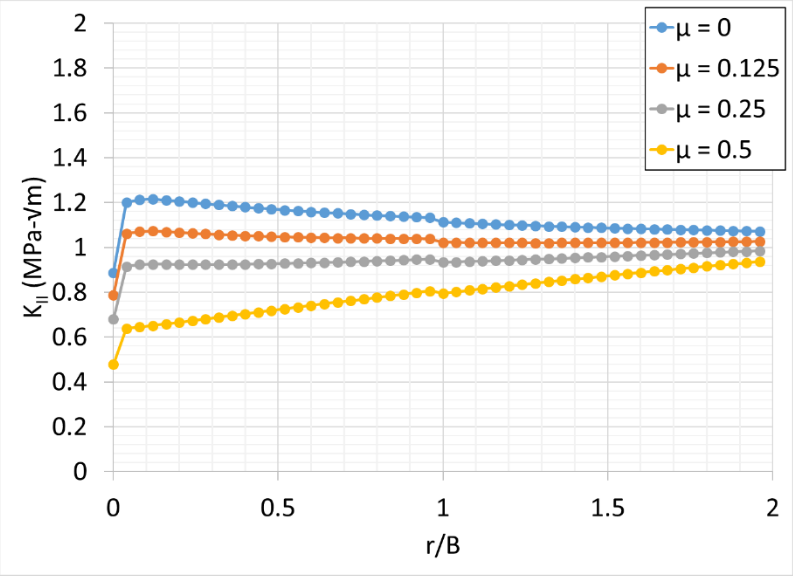

Figure 4-5: Expected effects of crack sliding friction on K_{II} invariance based on FE investigations

Across the anticipated range of *r/B*, with *B* being the specimen thickness, values for stress intensity factor extraction, the affect would be expected to be less than 10%. More importantly, for the analysis assuming μ = 0.25, the mode II stress intensity factor values are almost path independent. This is noteworthy and supports the claim that even with sliding friction along the crack faces, stress intensity factors extracted from experimental data should be reliable.

4.2 Test apparatus for crack opening conditions

The primary advantage of the fixture introduced in the present chapter is to investigate the conditions in the test specimen while under a mixed-mode state of combined shear and compression where the crack is generally in a state of closure conditions. It is also of interest to investigate a similar bimaterial interface under opening conditions to complement the shear-compression results. To that end, an asymmetric four-point bending specimen was chosen to explore this complementary behavior where the mode I component of the stress intensity factor is generally positive in the test specimen. This geometry has been previously studied, and, more specifically, the works reported in [93] and [94] are of particular relevance because of the similarity in the material mismatch parameter, ε. The test geometry is shown in Figure 4-6.

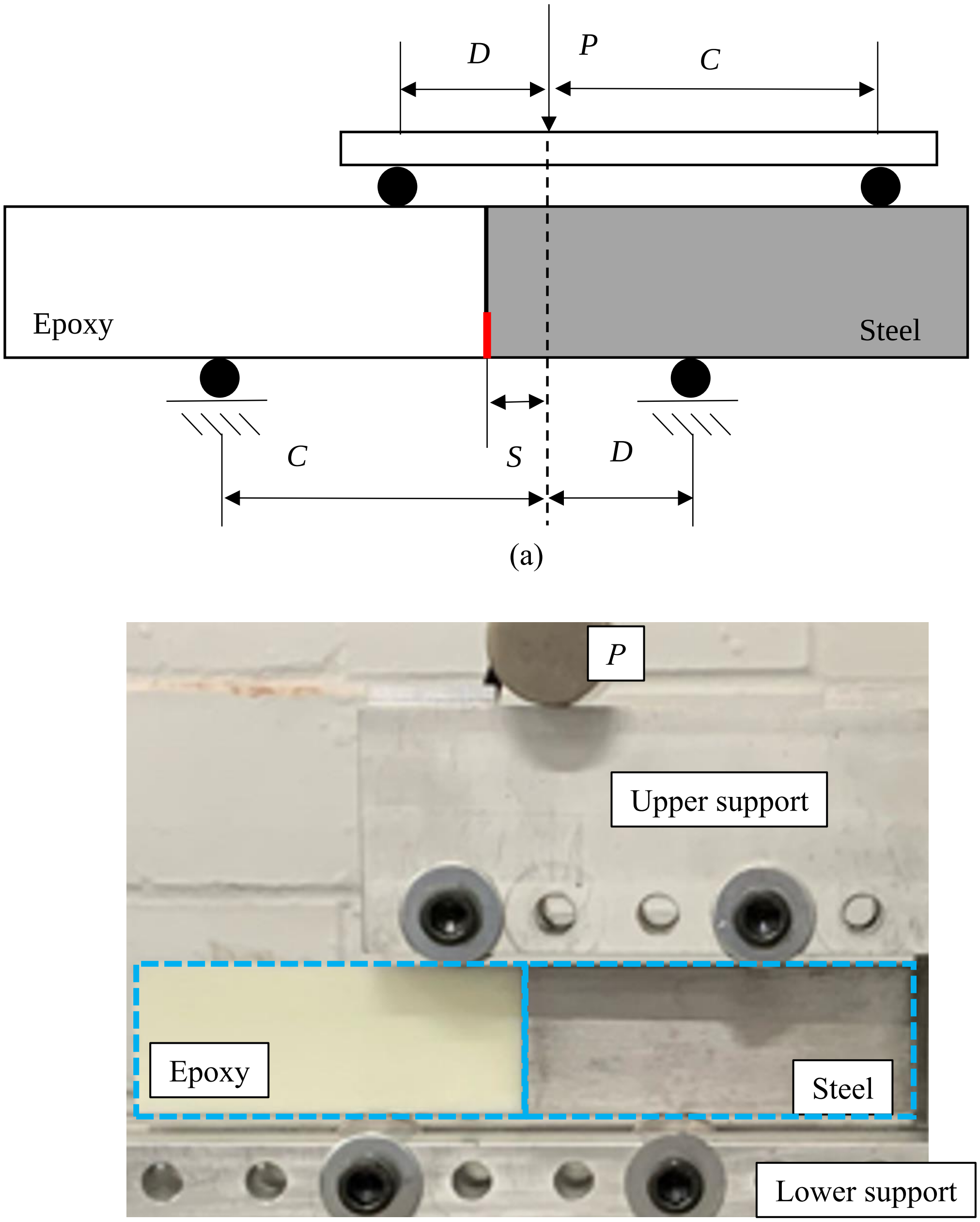

(a)

(b)

Figure 4-6: Schematic (a) and photograph (b) of asymmetric four-point bend setup (negative shear configuration)

The setup is configured such that the load is aligned to a location offset from the interface and the distance between the load point and each support point, dimensions *C* and *D*, are held constant. By varying the distance, *S*, from the interface to the load application point, the ratio of shear and transverse load on the interface can be controlled. The present work utilized a sample with a height of 38 mm, a total length of 203 mm, and a thickness of 6.4 mm. The ratio *C/W* was held constant at 1.27 and the ratio *D/W* was held constant at 0.63. The geometry was studied parametrically in a finite element model to understand the suitable support configurations for the present work. Two configurations were explored, one setup as illustrated in Figure 4-6 where the shear is acting along the interface's "-*x*" direction, and a second configuration where the shear is acting along the interface's "+*x*" direction. The two configurations are referred to as "negative" and "positive," respectively. The normalized stress intensity factors and mode mixity for each configuration are plotted as a function of offset ratio, *S/W*, in Figure 4-7 and Figure 4-8 respectively.

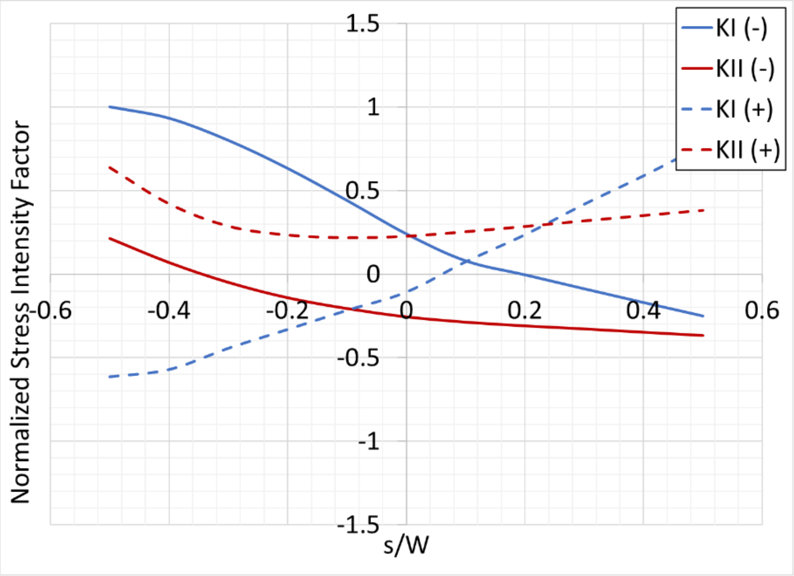

Figure 4-7: Stress intensity factors from asymmetric four-point bend test setup

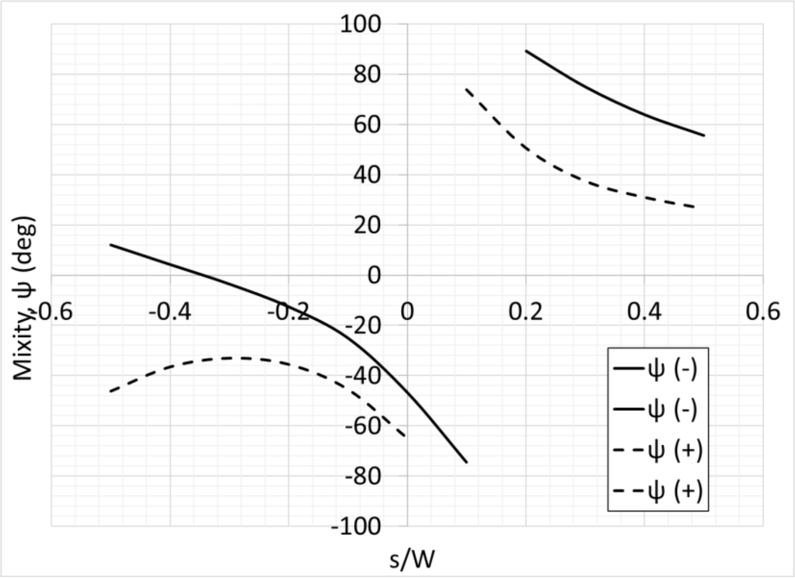

Figure 4-8: Mode mixity from asymmetric four-point bend test setup

It is evident that a wide range of mode mixities can be achieved using this test configuration. To complement the results from the constrained interface fixture introduced in the present work, the intent is to use the asymmetric fixture for the locus of points in the fracture envelope where both K_I and K_{II} are positive. Therefore, the "positive" configuration was chosen with positive values of *S/W* to achieve those conditions specifically (represented by the dashed line in the first quadrant of the graph in Figure 4-8). It should be noted that a single specimen configuration will not achieve a full range of mode mixities without other changes to the geometry, however, this will adequately span the range of mixity values to capture the shear-tensile fracture behavior. It should be noted that a significant parametric study was performed on the test specimen geometric dimensions and fixture setup to plan this experimental series.

Table 4-1: Summary of parametric study configurations

Configuration	**Upper pins**	**Lower pins**	**Load pin to specimen**	**Load pin to load frame**
1	Frictionless	Frictionless	Frictionless	Frictionless
2	Friction	Friction	Friction	Friction
3	Frictionless	Frictionless	Frictionless	Friction

The most noteworthy findings were the importance of the support points and are summarized in Figure 4-9.

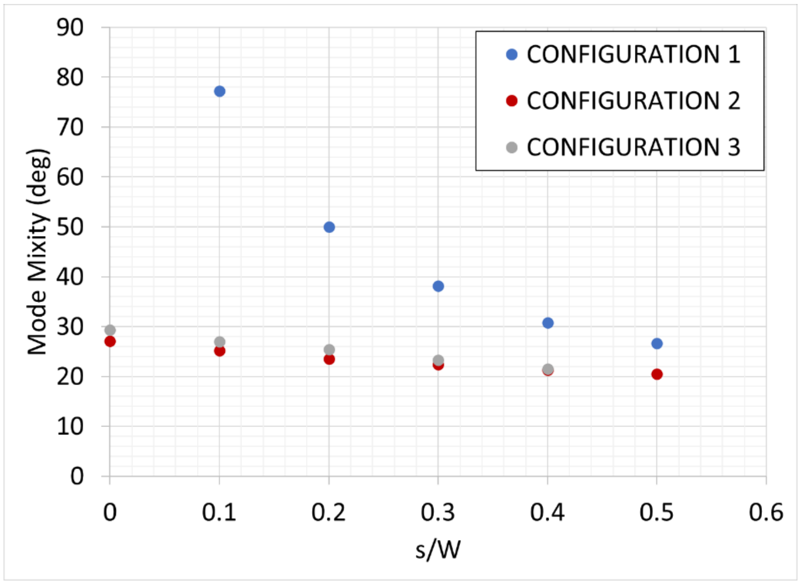

Figure 4-9: Mode mixity results for different support point configurations

This study confirms that having free rollers at the support points instead of fixed pins was important to avoid or minimize the support point friction. The friction affects the mode mixity in the test specimen due to the presence of lateral loads at the support points. Also, having free rotation at the point of load application is important for similar reasons. This study underscores the importance of fixture assumptions that are made in extracting fracture quantities using methods that are not full-field measurements.

4.3 Test specimen fabrication

For the interfacial experiments, specimens were created using steel adherends with a layer of rubber-toughened epoxy between them. The steel adherends were machined to the desired width, thickness, and length. The surface of the adherends were grit blasted with #80 size aluminum oxide grit and then cleaned with acetone. Three different procedures were investigated to form the starting crack/disbond. The first trial was to grit blast the entire adherend surface and then apply a release coating to the desired location of the initial crack section on the interface. This method worked, however, due to the surface roughness from the grit blasting process, it was difficult to get the initial crack to consistently release in the precrack section after the initial cure. The second trial was to apply a piece of Teflon tape to the desired location of the initial crack on the interface. The Teflon tape provided a consistent precrack along the interface, however, due to the thickness of the Teflon tape, the interface crack did not have the desired geometry at the crack tip. The geometry was similar to that of a blunt notch with the width of the tape thickness rather than a sharp crack. The third trial was to mask off the area on the adherend for the desired precrack area such that the masked region was not grit blasted. After the surrounding area of the adherend was grit blasted, the mask was removed and a layer of release coating (Frekote 700-NC) was applied to the area that was masked during grit blasting. The release coating is a solvent-based moisture curing sealant for the surface that is typically used for mold release applications in composite processing. It produces a thin surface coating on the adherend in the desired precrack region (Figure 4-10). This method worked well, and with a minimal amount of load applied to the specimen after the cure, the crack faces could be consistently released prior to the test. The aluminum mold (Figure 4-11) was used to hold the adherends parallel and at the appropriate spacing while the epoxy layer was cast.

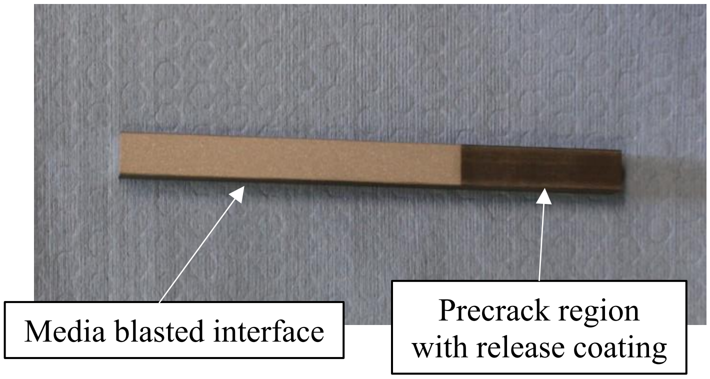

Figure 4-10: Adherend with surface preparation complete

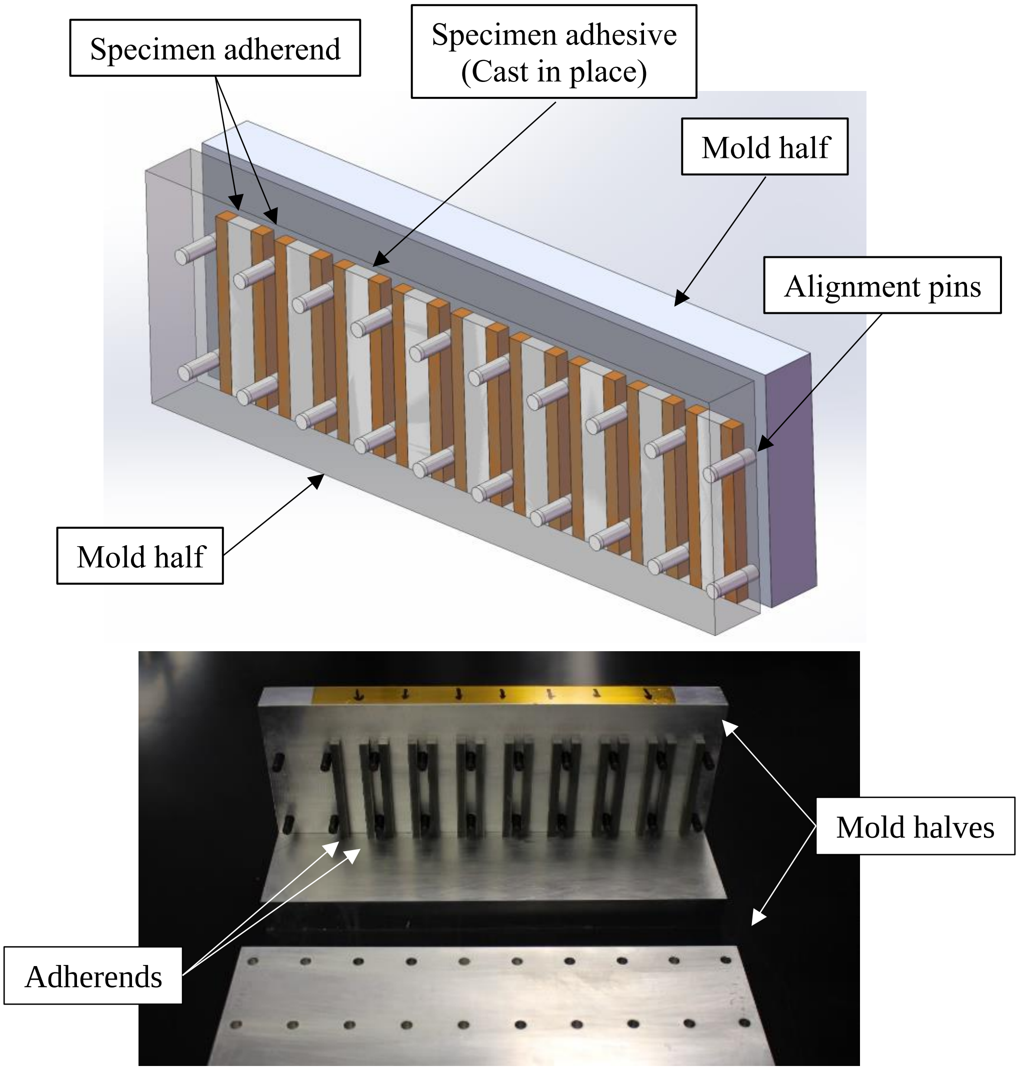

Figure 4-11: Interface crack specimen mold, CAD rendering (top) and photograph (bottom)

4.4 Displacement field mapping considerations for hybrid DIC-FE approach

In case of homogeneous materials, the digital image correlation output data could be conveniently used to construct an FE model mesh with the nodal positions corresponding directly to the DIC output points. However, the interfacial fracture problem is slightly more complex in terms of mapping the data between the two models. In the homogeneous sample, the post-processing model can have a jagged mesh in the region of the crack. Since the area integral approach considers a large domain of elements, missing data along the crack faces where elements would have spanned across the crack faces is acceptable and contributes negligibly to the output data since the stress in those elements is relatively low and the number of elements in question is only a small percentage of the overall element count in the domain used for the *J*-integral computations. However, for the interface crack problem, the mesh along the interface must be much more structured, primarily because the material on each side of the interface has different elastic properties. There are digital image correlation subsets that span the interface and therefore contain material on both sides of the interface. Secondly, for the mesh in the model used to extract the data, the elements along the interface cannot span across the interface because of the differing elastic properties. Because of the dissimilarities that exist between the desired finite element mesh and the structured DIC output grid, a more nuanced mapping technique was required. The dissimilarities between the two grids are shown in Figure 4-12.

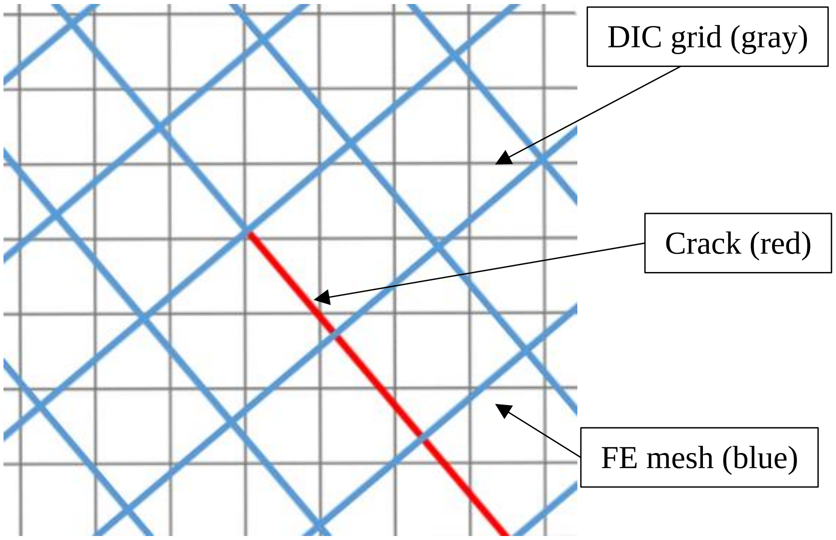

Figure 4-12: Misaligned DIC and FE grids with the FE grid intentionally shown to be coarser than the DIC grid for clarity

As illustrated, the desired structured FE mesh is aligned with the test specimen and, more specifically, aligned with the interface and crack. The element edges are generally aligned to be parallel and perpendicular to the interface. Whereas, for experimental convenience, the camera is oriented in a typical upright fashion and the resulting DIC output points are aligned to this original image coordinate system, with the *y*-direction oriented vertically and the *x*-direction oriented horizontally. One possible way to resolve this would be for the camera to be rotated such that the resulting DIC output points would align closely with the FE mesh. This would not be practical, however, because the critical feature of interest, the interface and crack, is an almost perfectly straight feature. Due to things like optical distortion from the lens and camera misalignment, it would be difficult for these meshes to align perfectly, thus would still require some transformation of displacement data. Also, the desired FE mesh may not be the same density as the DIC output grid and, further, there may be a need for non-uniform density (e.g., finer mesh in the region of the interface crack) in the FE mesh. For these reasons, several different techniques were considered for mapping the displacement data onto the FE discretization. Special attention must be given to this process due to the inherent noise in the DIC data and the desirable mesh features for proper contour integration in the FE model. Since the DIC data is on a uniformly spaced grid, this is especially important for the cases that contain cracks that are not oriented at 90° (see Figure 4-12).

4.4.1 Rotation of image using interpolation

The first approach assessed for handling data mapping from the DIC grid to FE grid was to simply rotate the images prior to performing the image correlation. To rotate the image, the coordinate locations of each pixel in the original image are transformed to new coordinate positions using a simple rotation. Interpolation was then used to map the rotated intensity values onto a uniform grid. For the present work, area weighting approach was utilized. The area weighting approach works by first rotating the pixel coordinates (or indices) using a simple affine rotation. The rotated coordinates are now located at positions that are not uniformly spaced in the global *x*- and *y*-coordinate frame. The intensity values of these points are then mapped onto destination pixel locations that are on a uniform spacing using area weighting. For a given position in the rotated version of the image, the four surrounding pixels are located as illustrated in Figure 4-13.

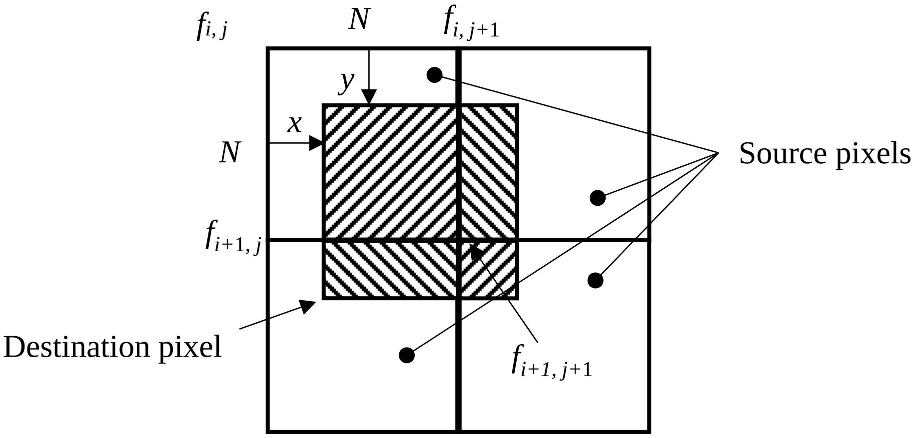

Figure 4-13: Illustration of area weighting for intensity mapping

The resulting intensity value *F* at the destination pixel can then be computed using:

$$F = \frac{1}{N^2}\begin{bmatrix} (N-x)(N-y)f_{i,j} + x(N-y)f_{i,j+1} \\ +y(N-x)f_{i+1,j} + xyf_{i+1,j+1} \end{bmatrix} \qquad [4\text{-}3]$$

where *f* is the intensity of the source pixels, *x* and *y* are the horizontal and vertical shift distances and *N* is the edge length of each of the source pixels. The key advantage of this method is that the image can be rotated to align it with the local crack coordinates such that the resulting DIC output points would also align to the local crack coordinates. Such an aligned mesh enables formulation of uniformly sized, symmetric contours for evaluating the domain integral. The key disadvantage, however, is that it requires a rotation of the raw image. This rotation can be problematic because the pixel intensity data in the unrotated image coordinate system must be interpolated to form the rotated image. Even though several standard image processing techniques are available for accomplishing this, it produces unwanted degradation to the original image data as shown in the comparison in Figure 4-14. The noise that is introduced (see comparison of rotated image and source image) is undesirable for the image correlation process.

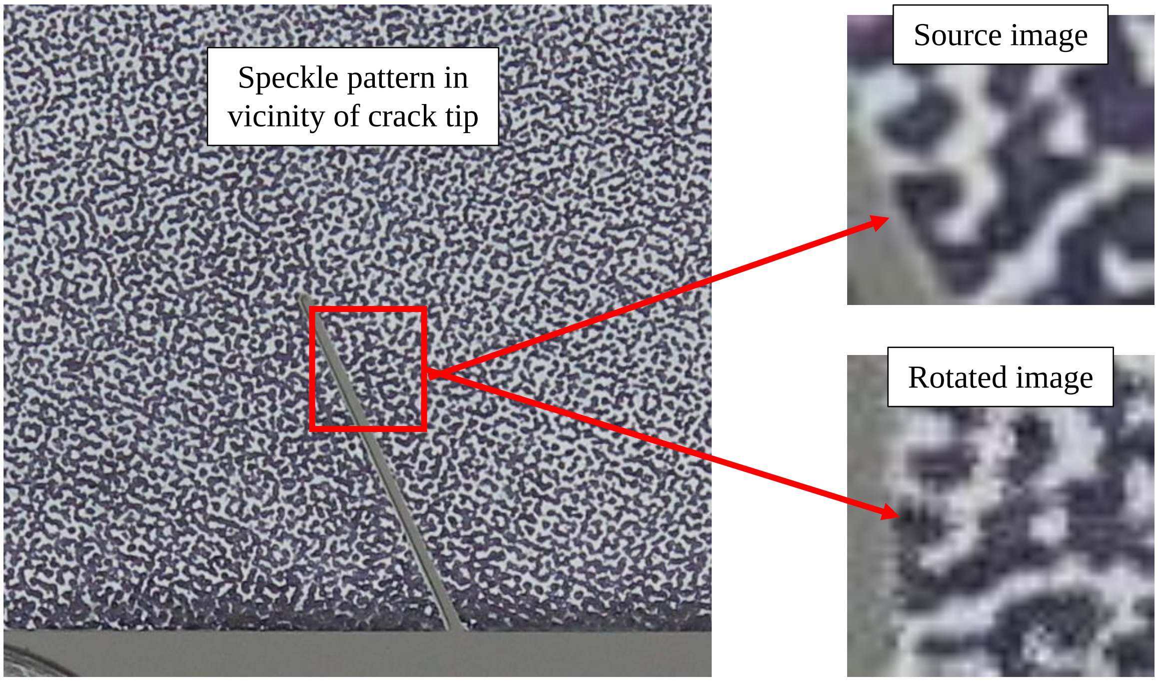

Figure 4-14: Noise introduced into image by pixel rotation process

4.4.2 Rotation of DIC output data using bilinear interpolation

The second approach assessed for handling mapping between the DIC output data and the FE model was to perform the image correlation on the original images, and then perform a mapping operation to rotate the DIC output data relative to an FE mesh that is aligned with the crack. In this approach, the rotated DIC output data points do not align with the FE mesh as illustrated in Figure 4-12. The general concept is that for a given node in the FE mesh, it is necessary to locate the neighboring DIC output points, and then use the displacements at those DIC output points as source data to determine the displacement at the destination node in the FE mesh. This method is attractive because the use of mapped field quantities in the FE analysis community is commonplace, and therefore, numerous methods can be used for determining the mapped nodal displacements. Many techniques can readily be implemented to perform mapping between significantly dissimilar meshes. For the present work, due to the structured nature of the DIC data, a simple bilinear interpolation method was implemented as,

$$f(x,y) = a_0 + a_1 x + a_2 y + a_3 xy \tag{4-4}$$

where the coefficients can be found by solving the following system of linear equations:

$$\begin{bmatrix} 1 & x_1 & y_1 & x_1 y_1 \\ 1 & x_1 & y_2 & x_1 y_2 \\ 1 & x_2 & y_2 & x_2 y_1 \\ 1 & x_2 & y_2 & x_2 y_2 \end{bmatrix} \begin{bmatrix} a_0 \\ a_1 \\ a_2 \\ a_3 \end{bmatrix} = \begin{bmatrix} f(Q_{11}) \\ f(Q_{12}) \\ f(Q_{21}) \\ f(Q_{22}) \end{bmatrix} \tag{4-5}$$

where $Q_{11} = (x_1, y_1)$, $Q_{12} = (x_1, y_2)$, $Q_{21} = (x_2, y_1)$, and $Q_{22} = (x_2, y_2)$. This method has the advantage that any grid of DIC displacement data can be mapped onto any FE mesh; therefore, the mesh surrounding the crack tip can be structured to whatever is desired depending on the problem of interest. The disadvantage with this method, however, is that again this process introduces undesirable uncertainty and degradation of the data due to numerical interpolation.

4.4.3 Rotation of DIC output data using cubic convolution

The third approach tested, cubic convolution interpolation, is a widely used technique in image processing for obtaining interpolated data from a uniform grid of data points. The method implemented by Keys [95] has found widespread use in many such applications. This method essentially considers a neighborhood of nearest points and fits a smooth curve through the points to find the value. The method has been shown to produce good results across a range of interpolation problems and is well-suited for the current work due to the uniformly spaced output data points association with the digital image correlation process.

When *(x,y)* is a point in the subgrid of $[x_i, x_{j+1}] \times [y_k, y_{k+1}]$, the interpolation function is defined as:

$$g(x,y) = \sum_{l=-1}^{2}\sum_{m=-1}^{2} c_{j+l,k+m}\, u\left(\frac{x - x_{j+1}}{h_x}\right) u\left(\frac{y - y_{k+m}}{h_y}\right) \qquad [4\text{-}6]$$

where x and y are the sampling coordinates, h_x and h_y are the x and y coordinate sampling increments, and $c_{jk} = f(x_i, y_k)$. The interpolation kernel, u is simplified to:

$$u(s) = \begin{cases} \frac{3}{2}|s|^3 - \frac{5}{2}|s|^2 + 1 & 0 < |s| < 1 \\ -\frac{1}{2}|s|^3 + \frac{5}{2}|s|^2 - 4|s| + 2 & 0 < |s| < 1 \\ 0 & 0 < |s| \end{cases} \qquad [4\text{-}7]$$

In the work by Keys [95], this mapping technique was shown to exhibit reasonably accurate interpolation results while exhibiting good convergence characteristics and maintaining computational efficiency.

4.4.4 Assessment of displacement mapping techniques

An initial comparison was performed to determine the general feasibility of mapping using one of the homogeneous material experiments since the homogeneous experiments can be post-processed with no mapping for a baseline comparison. Stress intensity factors were extracted for the contours falling in the range of $0.75 \leq {}^{r}/_{B} \leq 1.5$ for a given load and the average and standard deviation of stress intensity factor was computed across that range. The results of this comparison are summarized in Table 4-2.

Table 4-2: Path independence evaluation for K_{II} for 40° case for three different mapping approaches

Method	**Average (MPa-√m)**	**Standard Deviation (MPa-√m)**	**Coefficient of Variation (%)**
No mapping	0.645	0.026	4.0%
Rotate data	0.629	0.050	8.0%
Rotate image	0.624	0.040	6.4%

The average values were very close to each other across the three post-processing methods, as all were within about 3% of each other. As expected, the approach involving no rotations and circular contours around the crack tip yields the most consistent value of stress intensity factor in the region of interest (i.e., the standard deviation is the lowest relative to its average value). However, the other two mapping approaches do not introduce an overwhelming amount of noise for the desired output quantity, K_{II}.

4.5 Verification experiments

For the purposes of obtaining the desired optical setup for this specimen geometry and understanding some of the nuances of the behavior of the test fixture, one of the interface cracked test specimens was loaded in the proposed fixture at a 45° angle to provide a mixed-mode case with both opening and sliding displacements. The purpose of this experiment was threefold. The first goal was to ensure that expected displacement data as predicted from prior finite element solutions matched the experimentally measured data within acceptable errors. The second goal was to compare output quantities of interest (for instance specimen shear and normal stress distributions and stress intensity factors) agreed well between the experiment and the predicted behavior. These two goals enable the third goal of the experiment which was to verify the optical setup (camera, camera position, lens, and lighting), the speckle pattern, and the overall hybrid mapping technique used to extract the desired experimental quantities from the measured displacement data. The test specimen and fixture are shown in Figure 4-15.

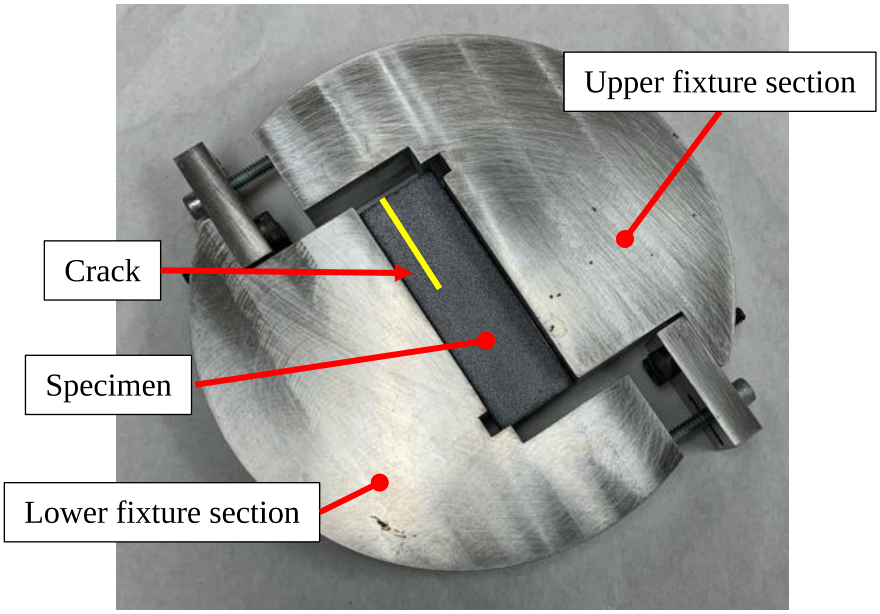

Figure 4-15: Photograph of test fixture with specimen assembled into fixture

An optical setup was arranged for this set of experiments similar to the arrangement utilized for the experiments on the quasi-static, homogeneous material specimens. The DIC parameters are summarized in Table 4-3.

Table 4-3: Digital image correlation parameters for interface experiments

Hardware Parameters			**Analysis Parameters**	
Camera Manufacturer	Allied Vision		Software	Ncorr
Camera Model	G507B		Manufacturer	Open source
Image Resolution	2464 × 2056		Image Filtering	Guided filter
Lens Manufacturer	Sigma		Sub-image Radius	45 pixel
Focal Length	75 mm		Step Size	5 pixels
Field of View	25 mm × 50 mm			
Image Scale	18.7 pixels/mm			
Stereo Angle	N/A			
Image Acquisition Rate	1 fps			
Patterning Technique	Ink stamp			
Approximate Feature Size	5-7 pixels			

The normal and shear stresses along the interface are plotted in Figure 4-16. These values were derived from the experimental data mapped using each of the two mapping methods. It should be noted that due to noise and potential mesh misalignment at the actual interface, these values are taken along a line that is parallel to the interface at a distance of $r/B = 0.05$ from the interface. The values from the bilinear and cubic mapping processes were each compared with results generated using a linear elastic FE model. The overall shape of each stress distribution ahead of the crack tip agrees quite well between the experimental results and the finite element simulation.

A few slight differences are notable in these comparisons. First, some averaging or smoothing is apparent in the region very close to the crack tip. This can be attributed to the smoothing introduced from the finite subset size in the correlation process as well as from the smoothing introduced from the filtering process. This is not viewed as an issue for the present work because the fracture quantities of interest are derived from contour integrals which consider stress distributions further away from the crack tip. Secondly, there is some slight discrepancy in magnitude of the stresses which is likely due to uncertainty in the magnitude of the load at the specific image selected for post-processing. In terms of comparing the two mapping techniques, the two methods resulted in very similar output, however, the cubic convolution approach was observed to be slightly smoother under certain circumstances and was therefore chosen as the preferred method for this work.

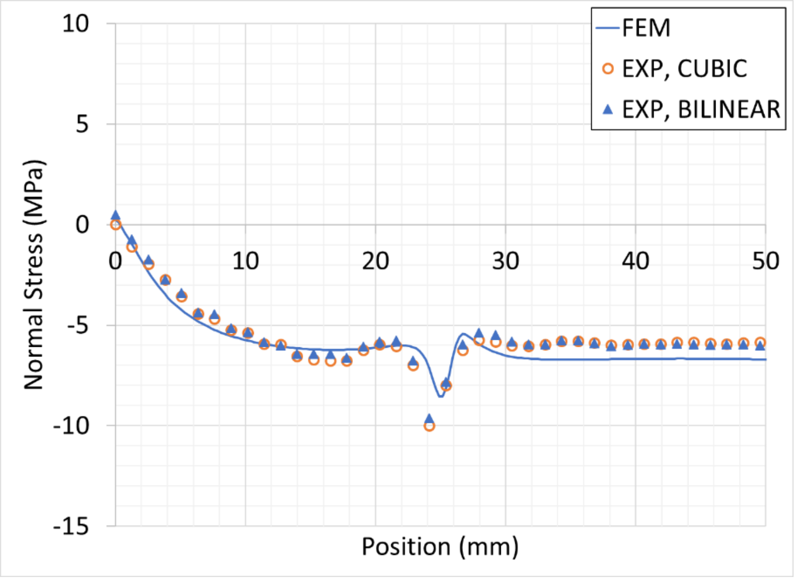

(a)

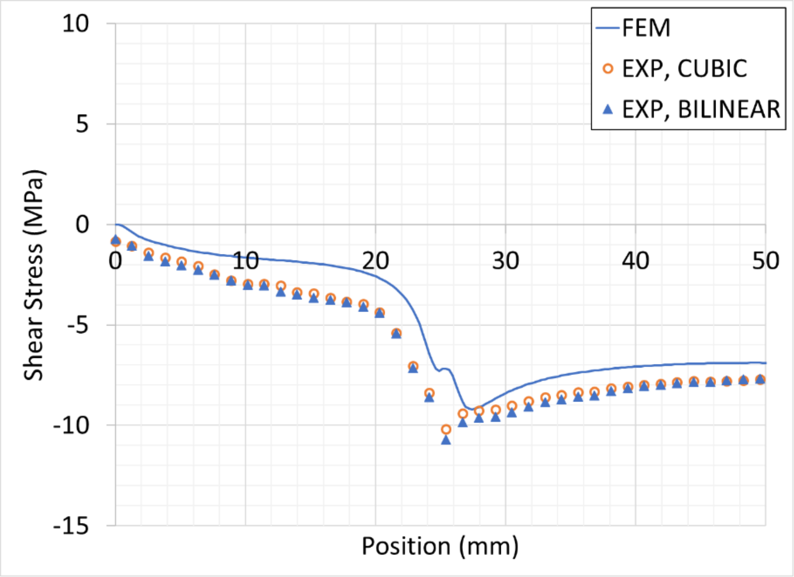

(b)

Figure 4-16: Comparison of experimental results and finite element solutions for (a) shear stress along the interface and (b) normal stress along the interface at 4 kN

Next, similar comparisons were generated for the 75° experiment, which is the loading angle resulting in a pure mode II condition. These comparisons are plotted in Figure 4-17. As expected, the stress normal to the interface is very low. The experimental results agree quite well with the expected results from the FE models with a few exceptions similar to those noted for the 45° experiment (differences are summarized in Table 4-4).

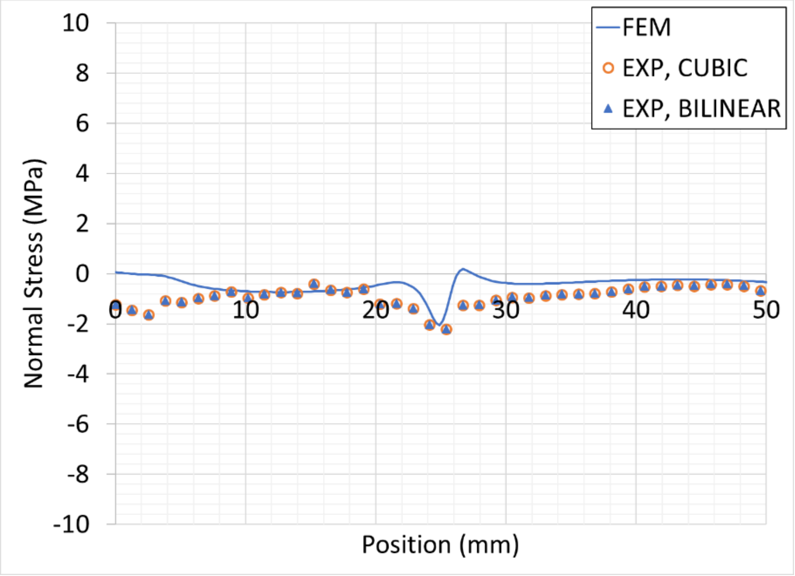

(a)

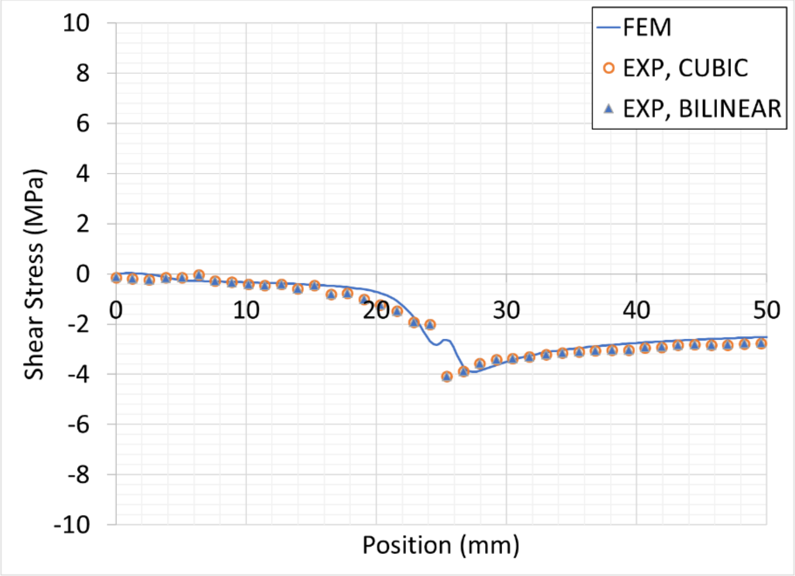

(b)

Figure 4-17: Comparison of experimental results and finite element solutions for 75° test for (a) shear stress along the interface and (b) normal stress along the interface at 4 kN

Table 4-4: Estimates of difference between predicted and experimental results for interface stresses

	DIC-FE vs FEM	
Angle (deg)	**Normal Stress (MPa)**	**Shear Stress (MPa)**
45	0.708	1.017
75	0.405	0.225

Next, stress intensity factors were extracted at various load steps from the experimental data. The mode II stress intensity factor, which is of primary interest to the present work, is plotted as a function of distance from the crack tip in Figure 4-18. As shown in the figure, the stress intensity factor is relatively invariant of contour position. More specifically, the range of $0.75 \le {}^{r}/_{B} \le 1.75$ is shown to have limited variation. Outside of this range, other effects such as contact between the adherend and the fixture and interaction at the second specimen interface contribute to the creation of path dependencies in the output.

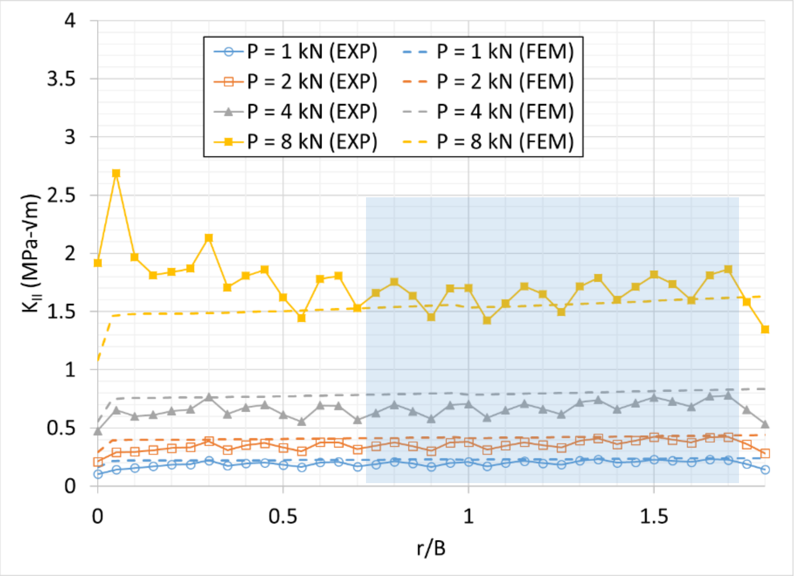

Figure 4-18: Comparison of FE model predictions with experimental results for mode II stress intensity factors at different experimental loads for interface crack geometry

It is noteworthy that considering less predictable factors such as friction along the crack faces and experimental noise, the output is relatively consistent across that range. This suggests that the hybrid method, as implemented, is relatively robust to several of the uncertainties associated with the experiment. For instance, some averaging occurs along the uncracked section of the interface where a limited number of image correlation subsets contain pixels on both sides of the interface. This contributes to smoothing across the interface. One other challenge is alignment of the two grids (nodal coordinates of FE mesh and subset centroid locations of DIC grid) during the mapping process. It is possible during the alignment process that an image correlation output point on one side of the interface may contribute to the displacement values at nodes on the other side of the interface in the mapped model. Even still, with these complexities considered, for a given load, the standard deviation is no more than approximately 7% of the average value across the range of interest. For instance, at P = 4 kN, the average stress intensity factor across the range of interest from the experimental data is 1.71 MPa-√m and the standard deviation of stress intensity factor is only 0.1 MPa-√m. It is also noteworthy that across that same range, the same level of noise is observed to very low loads, well below expected failure loads. The agreement between the experimental values and those from FEM are in reasonably good agreement given some of the previously mentioned experimental factors.

While these stress-based comparisons provide good insight into the mechanics of the test specimen, it should be pointed out that these are derived quantities, and it is therefore essential to also understand any inconsistencies between the expected displacement fields and the observed displacement fields near the crack. This enables a more complete interpretation of the mechanical behavior. The opening (or closing) and sliding displacement contours are plotted for the finite element analysis as well as the experimental results in Figure 4-19 for a region extending to a distance of *r/B* = 2 ahead of the crack tip and behind the crack tip. For clarity, the displacements from the steel adherend are not shown in these comparisons, as they are very small relative to the displacements in the epoxy.

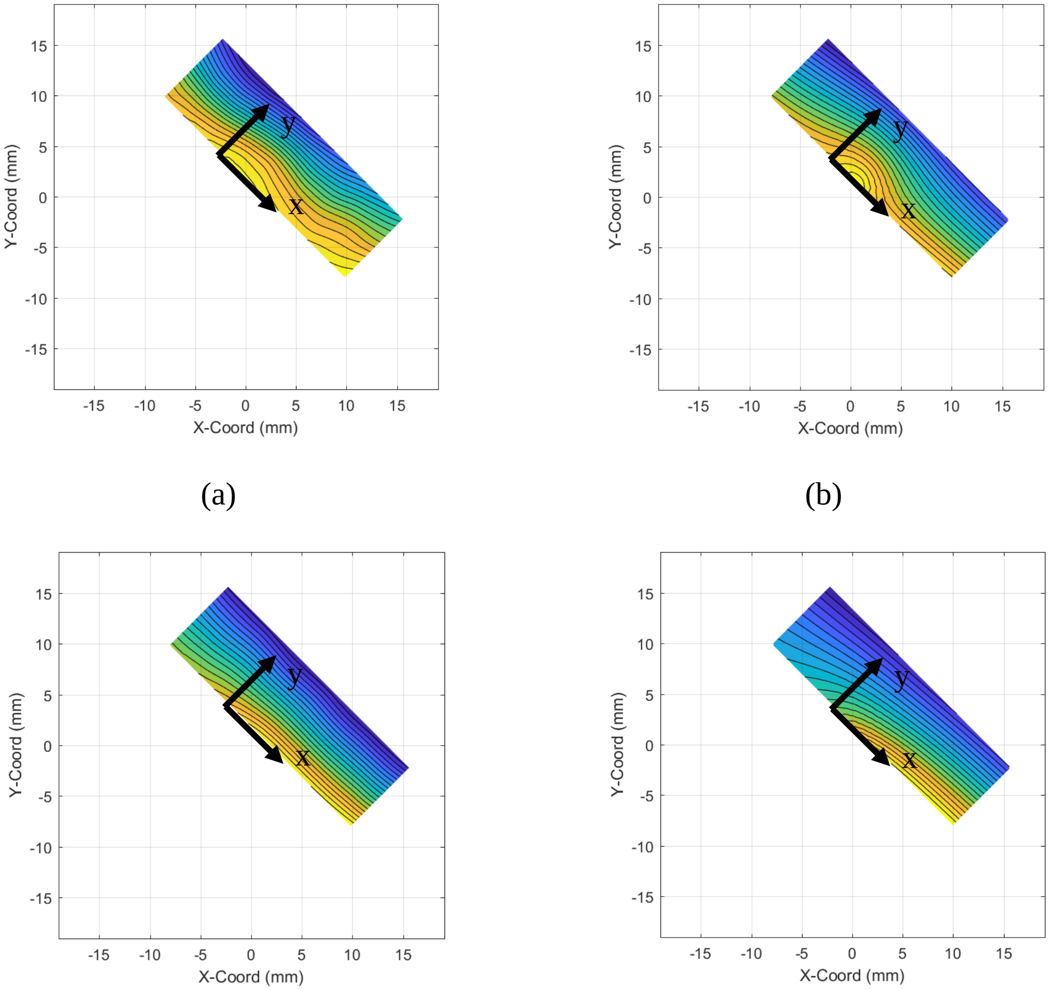

(a) (b)

(c) (d)

Figure 4-19: Opening displacement contours (a) experimental and (b) FEM, sliding displacement contours (c) experimental and (d) FEM in epoxy near crack tip at 4 kN load

A few things are evident from these plots, the first being the consistency between the measured displacements and the predicted displacements both in terms of magnitude and pattern.

The opening (closing) displacement contours lines are generally parallel to one another with the exception of the expected disturbance near the crack tip, implying that the two steel adherends are generally moving closer together, compressing the layer of epoxy. Ahead of the crack tip, the sliding displacements are uniformly parallel as the two steel adherends are sliding relative to one another.

To make further assessments of the results extracted using the proposed fixture and proposed mapping approach, the mode II stress intensity factors were calculated as a function of load for three different methods. First, Equation [4-2] was used to calculate the SIF using the crack sliding displacements from the pure FE model. Second, the domain integral method was used with the linear, elastic finite element model. And lastly, the domain integral method coupling the experimentally measured displacements with the hybrid DIC-FE mapped model was used. As shown in Figure 4-20, the three methods are generally in good agreement across the load range. It is expected that the differences observed here are likely due to assumptions about the model (for instance friction acting on the crack faces), as well as experimental noise.

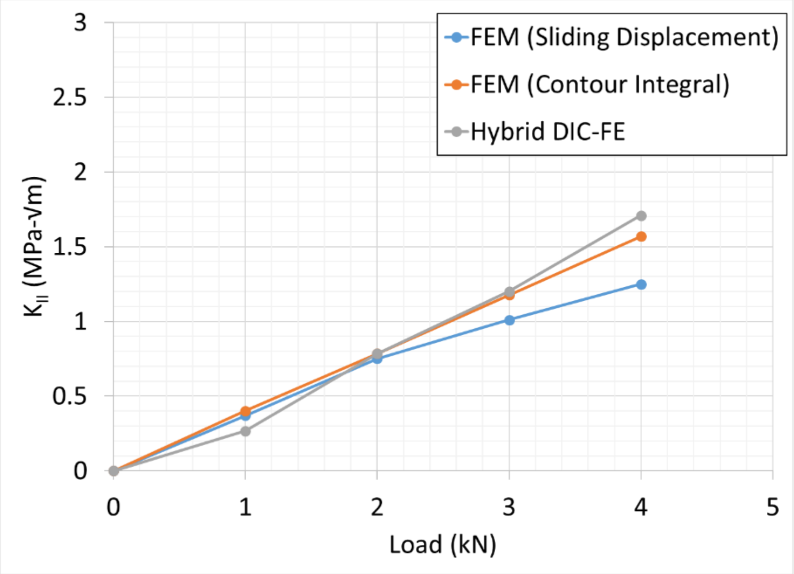

Figure 4-20: Mode II SIF as a function of load for different methods of data extraction

4.6 Results and discussion

With the general behavior of the homogeneous adhesive material characterized for the mixed-mode shear-compression state, an experimental study was performed using the interface crack specimen developed in the present work to achieve another of the primary objectives of the work. A series of failure tests were performed at varying angles with the previously described steel to epoxy to steel sandwich specimen. Multiple angles were tested in this test series ranging from 30˚ to 75˚ (as measured from the horizontal axis). Due to the intrinsic mode mixity associated with the interface between the dissimilar materials, the upper end of this range (75˚) represented the test configuration that is approximately pure mode II based on the analytical studies and verified with the experimental measurements. The results are plotted in Figure 4-21. As expected, the critical stress intensity factor increases as the severity of the crack closure conditions increase. At lower fixture inclination angles (e.g. closer to pure mode II), the response is somewhat linear with a slight increase in critical stress intensity factor with increasing closing force. However, at higher angles relative to the vertical orientation, the response behaves in a more exponential fashion.

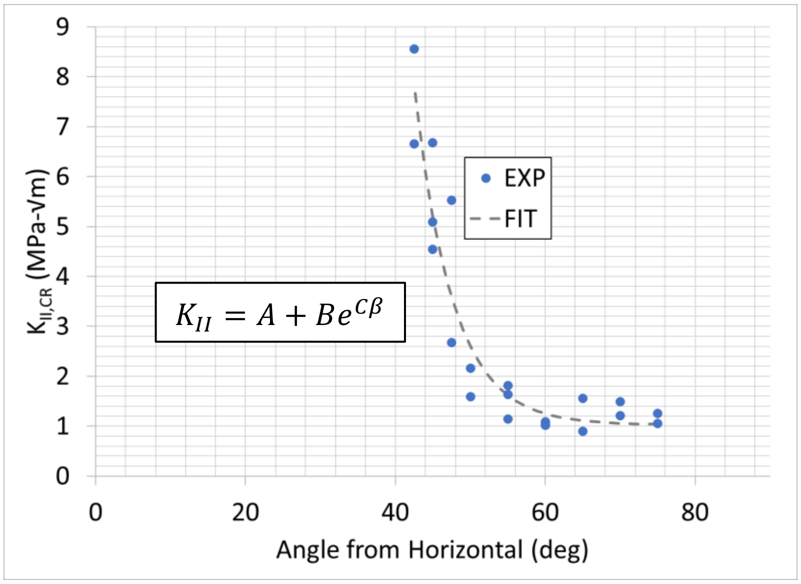

Figure 4-21: Critical stress intensity factors for in-plane compression state from interface experiments (parameters *A* = 1.03, *B* = 0.00065, *C* = 0.19)

There are several observations that are worth noting from the testing of specimens with compression. At angles closer to pure mode II, the general failure was sudden and catastrophic. The test frame load increased up to the point of failure and then abruptly dropped, indicating immediate and full crack propagation along the interface. However, with the test fixture oriented at the 45° angle, this was not the case. Specifically, at a certain load, the specimen began to undergo an uncertain number of abrupt small jumps, akin to stick-slip behavior. The load history became highly nonlinear and actually decreases as the crack continued to propagate slowly along the interface. The critical stress intensity factors reported here are based on the first propagation (or suspected initiation) of the crack.

In addition to the dependencies with respect to the inclination angle, it is also worth investigating the state of the mode I component at failure. In a physical sense, a mode I stress intensity factor implies an opening displacement of the crack. However, in the current situation, the crack faces are in contact and thus, a negative stress intensity factor would imply crack face interpenetration, which is clearly not present in the current experiment. For the interface crack, the stress intensity factors are simply the real and imaginary components of the complex stress intensity factor, and since the values are extracted based on contour integration of the near crack tip stress fields, the mode I stress intensity factors should be interpreted as describing the general state of stress within the contour domain. The mode I and mode II values were extracted for each experiment for the load at which the crack propagates. For most of the tests, this point was obvious, as the test samples failed in a catastrophic fashion upon crack initiation. For a few of the tests (at angles of less than 45˚ from the horizontal orientation), the evolution of the crack growth was much slower. As noted above, for these cases, the values were extracted at the first increase in crack length. The relationship between mode I and mode II stress intensity factors at failure is plotted in Figure 4-22. It is noteworthy that as the mode I component becomes increasingly negative, the critical mode II stress intensity factor increases almost linearly, similar to the observation from the homogeneous sample. However, for this case, the slope of the line is much steeper. In the homogeneous tests (both static and dynamic), the apparent friction angle was approximately 11.5˚ whereas for this data, the Mohr-Coulomb friction angle is much higher, approximately 50˚. For reference, experimental data as-tested using the asymmetric bending fixture documented in section 4.2 are include in the plot and seem to fit well with the trend from the shear-compression tests.

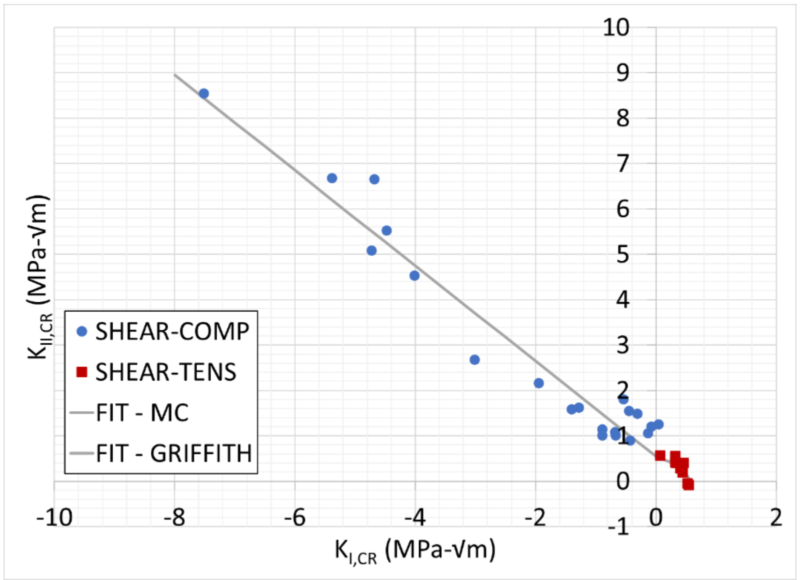

Figure 4-22: Critical stress intensity factors for interface crack geometry

As previously outlined in 3.6.3, for the Mohr-Coulomb criteria, a linear relationship is used to describe the shear vs. compression behavior, with *φ* being the slope of the line or friction angle. For the homogeneous results, a friction angle of 0.2 was found to fit the data well for both the quasi-static and dynamic test results. However, for the interface specimens, the line is much steeper, and a value of *φ* = 1.05 was found to fit well. The various parameters of the curve fits are summarized in Table 4-5.

Table 4-5: Summary of curve fit parameters for Griffith and Mohr-Coulomb fit for interface crack

	Parameter			
	Griffith		**Mohr-Coulomb**	
Test Series	**T_0**	**A**	**c**	**φ**
Interface crack	0.55	0.50	0.55	1.05

Optical micrographs of the failed interface crack specimens are shown in Figure 4-23 for a location just ahead of the original crack tip taken at a magnification of 30X on a Keyence optical microscope. One image was taken from a sample that was tested at a high fixture angle (thus creating a near mode II failure) while the other was taken from a sample that was tested at a relatively low fixture angle (thus creating a much more significant compressive load). The key distinction that is observed at the lower magnification is the presence of large bands of white surface features that suggest a significant amount of plastic deformation at crack initiation.

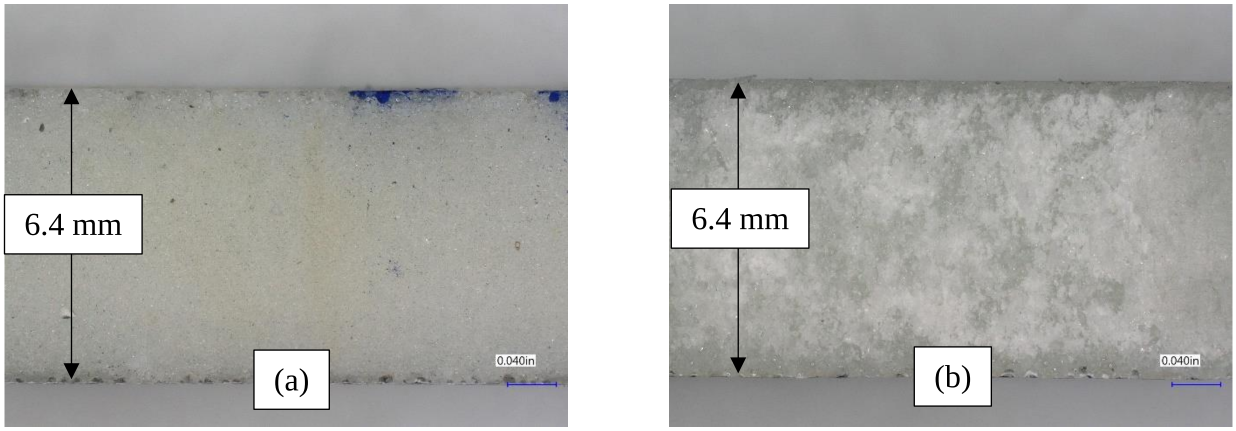

Figure 4-23: Optical micrographs of interface crack failure surface at 30X for (a) low compression stress and (b) high compression stress

Chapter 5

Dynamic Fracture of Homogeneous Adhesive Material

The current chapter extends the study of homogeneous material behavior to address dynamic response. The methods used for characterizing fracture behavior under stress wave loading are developed and evaluated in detail. A series of experiments are carried out to quantify the mixed-mode behavior and compare it to the earlier quasi-static counterparts.

5.1 Dynamic fracture experiments

As previously stated, there is a pervasive need to understand fracture in polymers and polymer-matrix composites. However, in many of the circumstances thus far identified, it is not only of interest to understand the general fracture behavior, but of equivalent importance is an understanding of this behavior under dynamic loading conditions. In practice mechanical, structural, and thermal loads for many applications can occur at a variety of timescales. Additionally, the polymeric constituent materials that make up composite laminates and adhesively bonded composite structures exhibit time-dependent responses. In this context, another objective of the current work is to investigate the merits of a semi-circular beam geometry for use in the study of mixed-mode dynamic fracture.

A long bar apparatus was utilized for subjecting the test specimen to the dynamic loading conditions. The method was adapted from work initially reported in [96]. The test setup is shown schematically in Figure 5-1 . In this setup, a gas gun is used to accelerate a 305 mm long, 25.4 mm diameter 7075-T6 aluminum striker bar up to the desired velocity. The striker bar is propelled into a 1.83 m long, 25.4 mm diameter 7075-T6 aluminum long bar. The striker bar creates an elastic longitudinal stress wave that propagates the length of the long bar into the test specimen. A strain gage located on the long bar enables measurement of the load history that is being transmitted to the test specimen. A trigger and a delay generator were used to control the image acquisition through the ultra high speed camera.

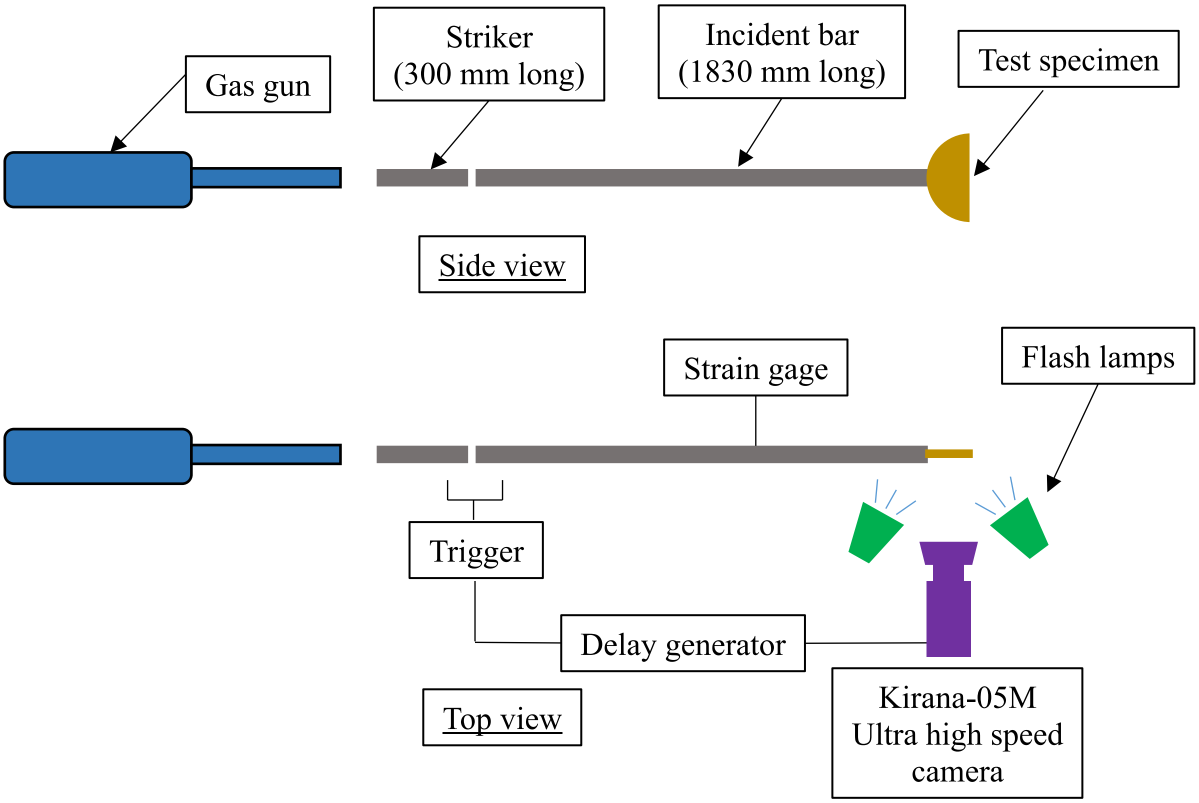

Figure 5-1: Experimental setup (side view and top view) of stress wave loading apparatus for dynamic mixed-mode fracture

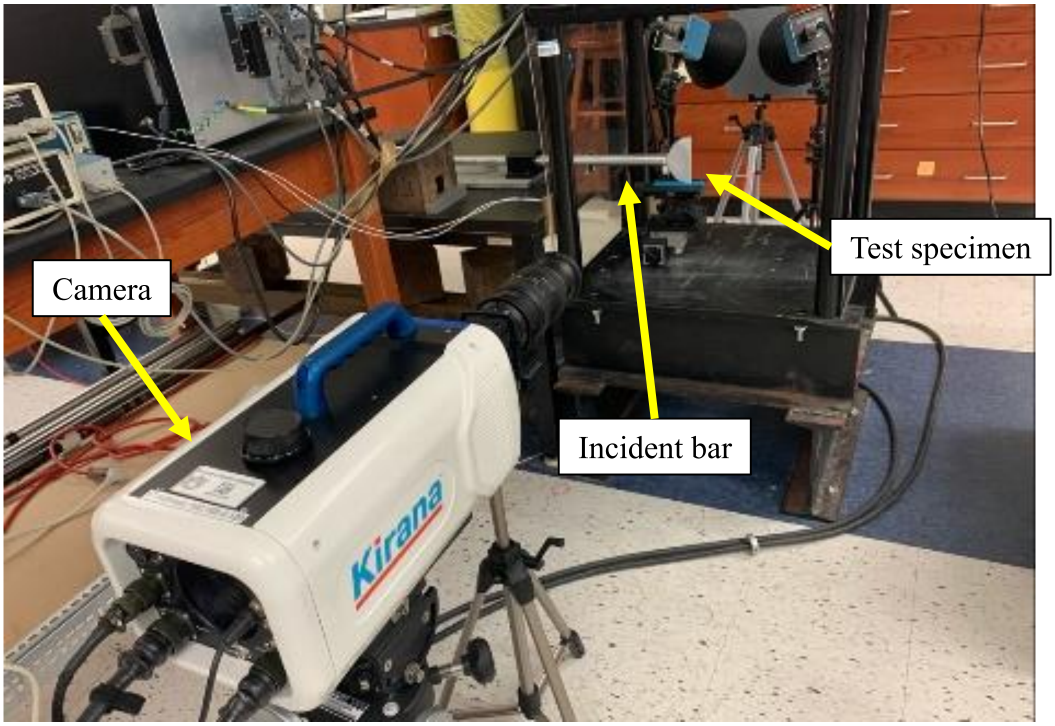

Figure 5-2: Photograph of experimental setup with ultrahigh speed camera in the foreground and long bar apparatus in the background

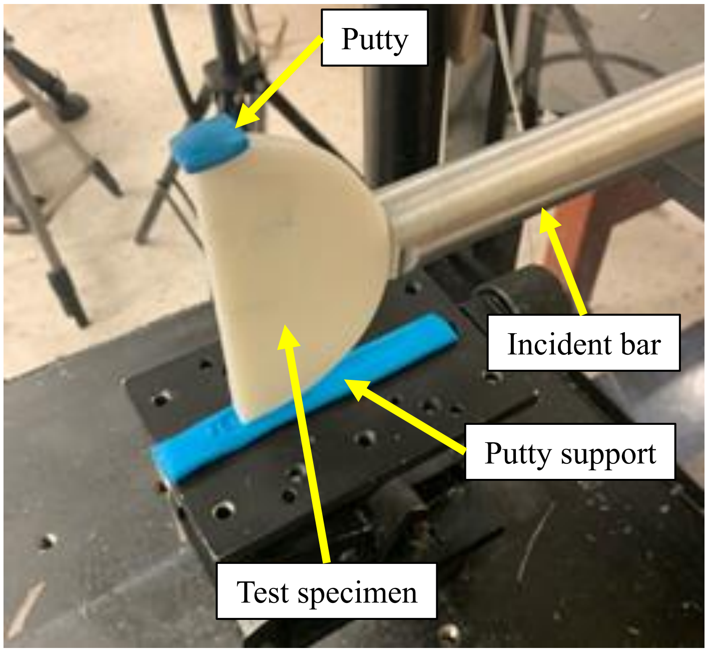

Figure 5-3: Photograph of test specimen mounted on support stage at free end of long bar apparatus

One characteristic of this setup is that the incident wave can be tuned according to experimental needs. First, the initial ramp can be modified by introducing a pulse shaper between the striker and the incident bar. By altering the impedance of the pulse shaper, the initial ramp can be extended. Secondly, the overall duration of the loading wave can be adjusted by increasing or decreasing the length of the striker bar. Lastly, the overall magnitude of the loading wave can be adjusted by increasing or decreasing the velocity at impact.

The loading configuration is advantageous for several other reasons as well. First, the single point, inertially driven load case eliminates several issues associated with more complex three-point or four-point loading arrangements that include a separate transmitter bar. In those test configurations, boundary conditions, support point friction, and other factors become a bigger consideration. Some of these were examined with respect to the static configuration in 3.5.3. Separately, in two bar setups, the incident, reflected, and transmitted strain signals are required to estimate the specimen force history. A set amount of time is required to achieve specimen force equilibrium such that the force balance equations are reliable. Also, wave dispersion must be factored into the force history estimate. Extracting stress intensity factors from surface displacement measurements using the proposed domain integral approach eliminates the need for an accurate estimate of the specimen force history.

5.1.1 Long bar apparatus characterization

For development of post-processing methodologies and detailed investigation of the test geometry and setup, specimens were tested with 19 mm cracks inclined at two different angles (90° and 50° from the horizontal). These were chosen specifically because they represented the extreme cases of pure mode I and pure mode II respectively from the accompanying quasi-static experiments. It is necessary to acquire images during three key experimental regimes. First, images prior to stress wave arrival are necessary to be used as reference images in the image correlation process. Next, adequate image acquisition is necessary prior to crack initiation in order to estimate critical stress intensity factors at crack initiation. Lastly, adequate image acquisition is necessary as the crack propagates across the test specimen. For these experiments, the camera frame rate was set to 500,000 frames per second with acquisition beginning 250 micro-seconds after the striker bar contacts the incident bar. This time delay was determined experimentally. It is based on the time required for the wave to propagate the length of the incident bar and into the specimen. For the 1.9 m aluminum incident bar, the elastic wave requires approximately 370 microseconds to propagate the bar's length. The time delay (250 micro-seconds), followed by the 360 micro-second time period of image acquisition (180 frames) allows adequate time to capture a series of images prior to loading, crack initiation, and crack propagation in the specimen. The test specimen was positioned at a distance of approximately 0.9 m from the focal plane of the camera resulting in the edges of the region of interest being located within 2° of the optical axis to minimize paraxial effects. The test specimen was mounted to an adjustable micromechanical support stage using a strip of ~5mm thick putty. It is assumed that the impedance mismatch between the putty and the test specimen material is sufficient to limit any transmission of elastic waves into the putty and further into the support. Another strip of putty is also placed on the upper edge of the specimen to ensure symmetry in the event any energy is lost through the boundary with the putty. The gun was pressurized to 45 kPa for an approximate striker impact velocity of 8 m/s. A strain gage was used to measure the axial strain in the incident bar due to bar wave propagation. The strain gage was wired in a Wheatstone bridge circuit as illustrated in Figure 5-4. For the present experiment, an active strain gage was only present in one leg of the Wheatstone bridge circuit. The remaining three legs contained resistors of equivalent resistance.

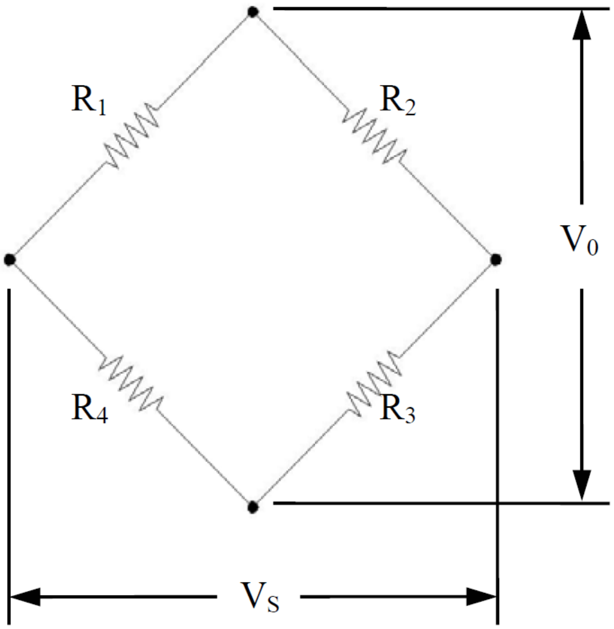

Figure 5-4: Wheatstone bridge

With a known excitation voltage, V_S, and known gage resistance values, the strain is related to the change in resistance of the active strain gage and can be related to the output voltage V_O.

$$\varepsilon = \frac{4V_O}{V_S G_C (GF)} \qquad [5\text{-}1]$$

Where G_C is the signal conditioner gain and GF is the gage factor that relates resistance changes to strain in the strain gage. A strain gage with a nominal resistance of 350Ω and a gage length of 3.2 mm was mounted on the transmitter bar at the midpoint of the bar. An Ectron 563H signal conditioner was used to amplify the output voltage and a Lecroy Waverunner 104Xi was used for measuring the output voltage. A nominal excitation voltage of 10V was used for the strain measurements. The typical shape of the incident bar loading wave recorded is shown in Figure 5-7 with predicted strain history from a finite element model that will be discussed later.

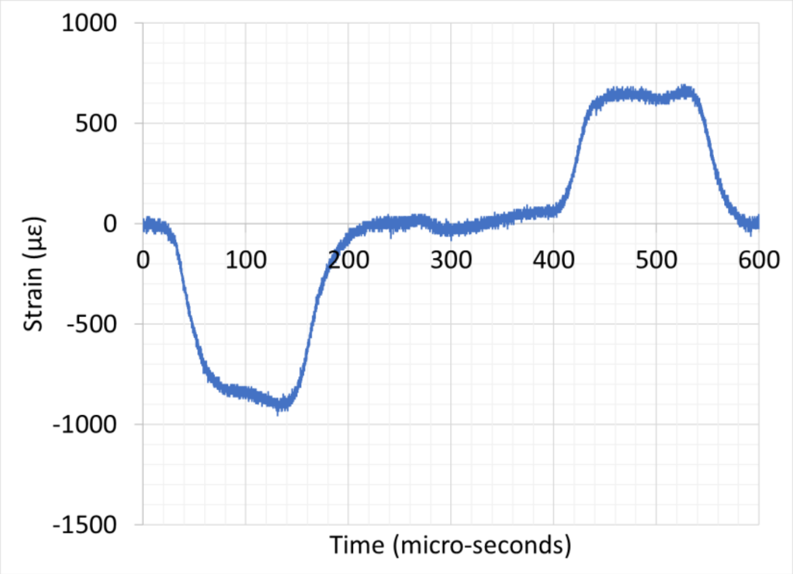

Figure 5-5: Typical incident bar strain history showing incident and reflected pulses

Due to the striker to incident bar impact dynamics, the length of the pulse is expected to be equivalent to the length of time it takes an elastic wave to propagate twice the length of the striker bar, or 120 micro-seconds for the 300 mm aluminum striker bar in this experiment. This is in good agreement with the measured pulse. As plotted, the strain begins to ramp up at approximately 40 micro-seconds, and it begins to ramp down at approximately 155 micro-seconds. Some dispersion is expected between the impact end of the bar and the strain gage location.

A photogate timer was used to measure the relationship between gas gun pressure and striker bar velocity. A series of tests with increasing pressures ranging from 27.6 to 137.9 kPa were run. The relationship is plotted in Figure 5-6 as measured.

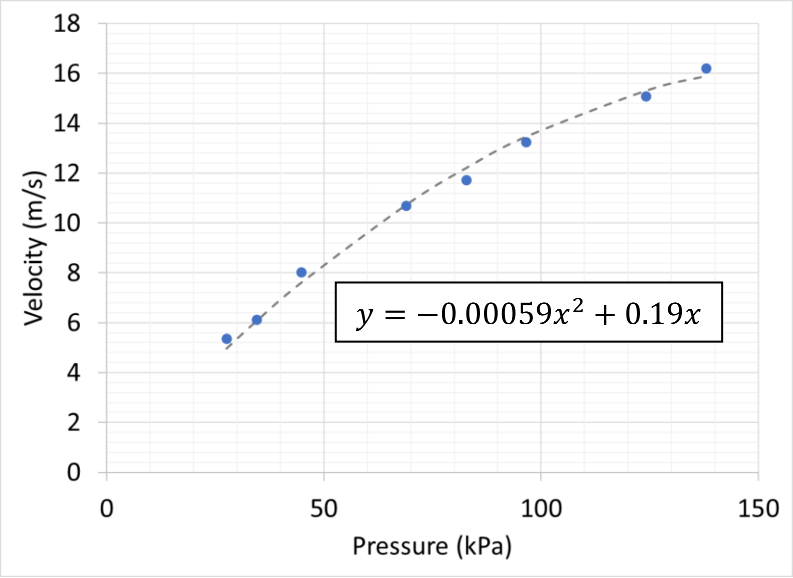

Figure 5-6: Relationship between striker bar velocity and gas gun pressure

A second order polynomial fit, $y = Ax^2 + Bx$, is shown in Figure 3-2. A fit was found using coefficients A = -0.00059 and B = 0.19.

5.1.2 Numerical investigations

A dynamic model of the experimental setup was created in the ABAQUS® finite element modeling software. The explicit model included the aluminum striker, the aluminum long bar, and the epoxy test specimen. The test specimen was modeled using approximately 87,000 solid 8-noded reduced integration elements (C3D8R) with approximately 98,000 nodes. An elastic modulus of 2.2 GPa and a density of 1.11 g/cc was used for the epoxy specimen. An elastic modulus of 69 GPa and a density of 2.8 g/cc was used for the aluminum striker and long bar. The bar was modeled with a flat end contacting the semicircular periphery of the test specimen. An initial velocity was prescribed for the striker bar and contact was modeled at the interface between the striker bar and the long bar as well as between the long bar and the test specimen. The automatic time stepping scheme was utilized in the explicit model.

Two options were considered for introducing the experimentally derived force history into the test specimen. The first option is to estimate the force history using the incident and reflected strain signals in the incident bar and apply the force history directly to the specimen. The second option is to model the aluminum striker bar and incident bar with contact at the incident to striker interface and striker to specimen interface. Each of the two approaches have advantages and disadvantages.

The incident and reflected signals (Figure 5-5) must be aligned which is a nontrivial step and can result in uncertainty depending on the method chosen for signal alignment. In addition, considering the signal is measured at some distance away from the specimen, uncertainty due to wave dispersion could be a factor as well. These uncertainties are typically addressed in traditional two bar setups by using the one-dimensional equations of motion at the specimen faces to assess the estimated input force using the incident, reflected, and transmitted signals. The limitation with the second approach is uncertainty associated with the contact descriptions at the two interfaces. The second approach is also more computationally intensive but reliable. A comparison between the experimental incident strain signal and the simulated strain signal is plotted in Figure 5-7.

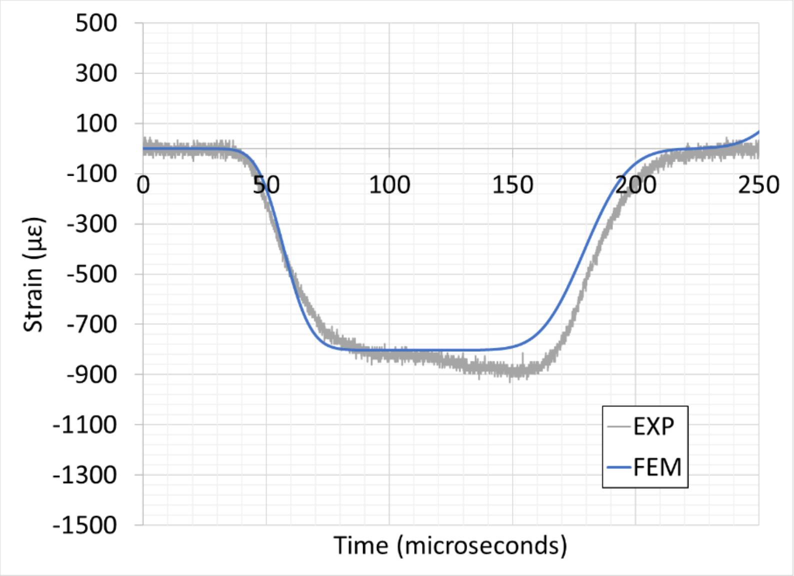

Figure 5-7: Typical incident bar strain history comparing measurements from experimental tests with expected strains from finite element model

For each of the initial model runs, the nodal coordinates along each crack face and the nodal displacements along each crack face were extracted and used to estimate the stress intensity factors by using a regression analysis as the radial distance, r, approaches 0 of the relationship:

$$\left(K_{I;II}\right)_{app} = \frac{E\sqrt{2\pi}}{8\sqrt{r}}(v;u);\ (r, \theta = \pi) \qquad [5\text{-}2]$$

Due to the typical run time of the full explicit finite element model, a second, but implicit, finite element model was created. The implicit model was developed first to improve the computational efficiency. The faster run time enables a significantly higher number of runs to be performed to explore the experimental parameter space and adjust those parameters (crack angle, impact velocity, etc.) to achieve the desired experimental results. The implicit model also allows the use of contour integration for extraction of the crack tip quantities of interest. The stress intensity factor histories extracted from the implicit, dynamic model using the domain integral method were in excellent agreement with the stress intensity factor histories extracted from the explicit model using crack face opening and sliding displacements. Additionally, strains extracted from the incident bar in the implicit, dynamic model had excellent agreement with the strain values measured experimentally during the characterization of the apparatus. The test specimen in the implicit model utilized approximately 2,500 4-noded reduced integration plane stress elements (CPS4R) and approximately 2,500 nodes. The same elastic property assumptions were made for implicit model as were assumed for the explicit model. The implicit model is illustrated in Figure 5-8.

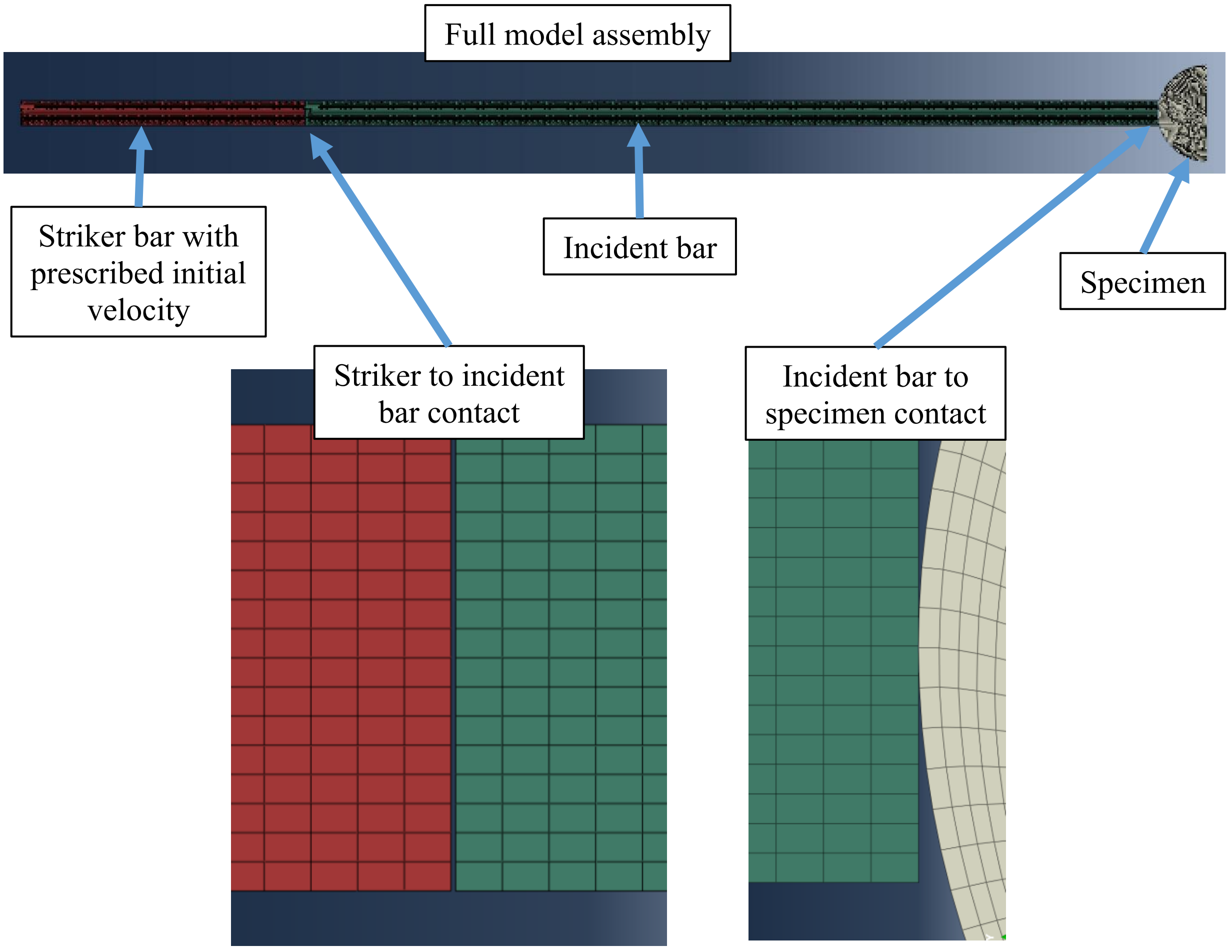

Figure 5-8: FE model for parametric studies for dynamic fracture testing

An example of the stress intensity factor output for a specimen with an angled crack is plotted in Figure 5-9. The mode mixity within the test specimen is largely influenced by the timing of the arrival of the elastic wave at the crack tip. Early in the loading event the elastic deformation in the region of the crack tip is dominated by sliding motion in the crack tip coordinate system. After some period of time, the elastic deformation begins to be influenced by crack opening displacements. Thus, as the inclination angle of the crack is increased or decreased, this timing is altered, thus influencing the mode mixity history at the crack tip.

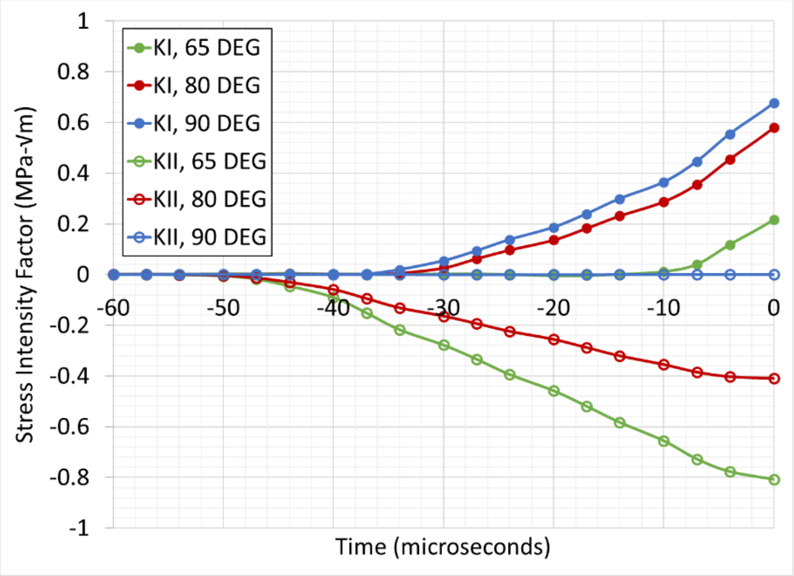

Figure 5-9: Time history of extracted stress intensity factors extracted from finite element model using domain integral approach (t = 0 corresponds to the time at which K_{eff} = 0.7 MPa-√m)

For crack inclination angles that are less than 90° relative to the horizontal, the state of mode mixity at the crack tip is initially one of pure model II but as the crack begins to be influenced by the opening displacement, the mode mixity continues to evolve. The mixity at failure is dependent upon the critical effective stress intensity factor for a given sample geometry (crack length and crack inclination angle). For the finite element-based parametric studies, an effective critical stress intensity factor, K_{eff}, of 0.7 MPa-√m was assumed for computing mode mixity at failure where $K_{eff} = \sqrt{K_I^2 + K_{II}^2}$. This number was based on initial mode I dominated dynamic experiments to be discussed later. Using this model, an extensive parametric study was executed to understand key relationships between the experimental parameters, namely how impact velocity, crack length, and crack inclination angle relate to mode mixity at failure. This was completed to enable planning for an optimal experimental configuration and ensure a wide range of mode mixities could be achieved from pure mode I to pure mode II.

The first comparisons were performed to determine the relationship between crack length and mode mixity at failure. Three crack lengths, 16 mm, 19 mm, and 22 mm, were analyzed with an impact velocity of 8 m/s. As shown in Figure 5-10, the mode mixity at failure for the specimen with the shorter crack length is less sensitive to changes in crack inclination angle and thus, even at very shallow cracks (below 65° from the horizontal), pure mode II does not appear to be possible at the analyzed velocity. The longer cracks (19 mm and 22 mm), however, approach pure mode II at angles of 65° and 70° from the horizontal respectively. Based on these results, for a given material system with a given fracture toughness, it appears that crack length can be a useful experimental variable for sizing the specimen geometry to achieve a desired range of mode mixities.

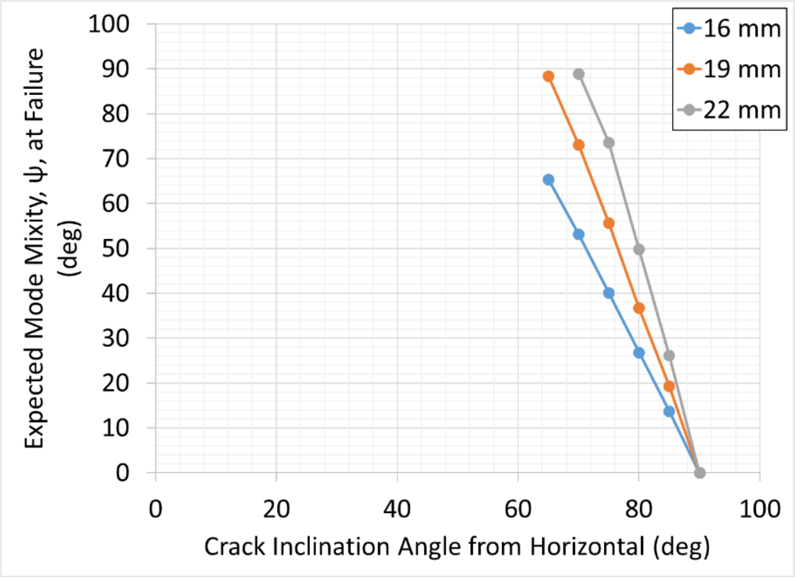

Figure 5-10: Finite element predictions of mode mixity at failure for different crack angles for three different crack lengths (simulated impact velocity of 8 m/s)

It is also interesting that at longer crack lengths, the crack inclination angle has a more significant influence on mode mixity at failure (e.g. small changes in crack inclination angle lead to large changes in mode mixity). This may be undesirable from an implementation standpoint if, for instance, results are targeted for a specific mode mixity. Therefore, the crack length can be used to control that sensitivity. As stated, these results are based on a critical effective stress intensity factor of 0.7 MPa-√m. For a material with a higher or lower fracture toughness, it would be necessary to lengthen or shorten the crack length to achieve the desired balance of sensitivity between changes in crack inclination angle and mode mixity at failure. For the current proposed experiments, a crack length of 19 mm was selected as having a satisfactory balance of mode mixity sensitivity. With the 19 mm crack length, a series of analyses were executed to understand the influence of striker initial velocity on the apparent mode mixity at failure. The results of those analyses are plotted in Figure 5-11.

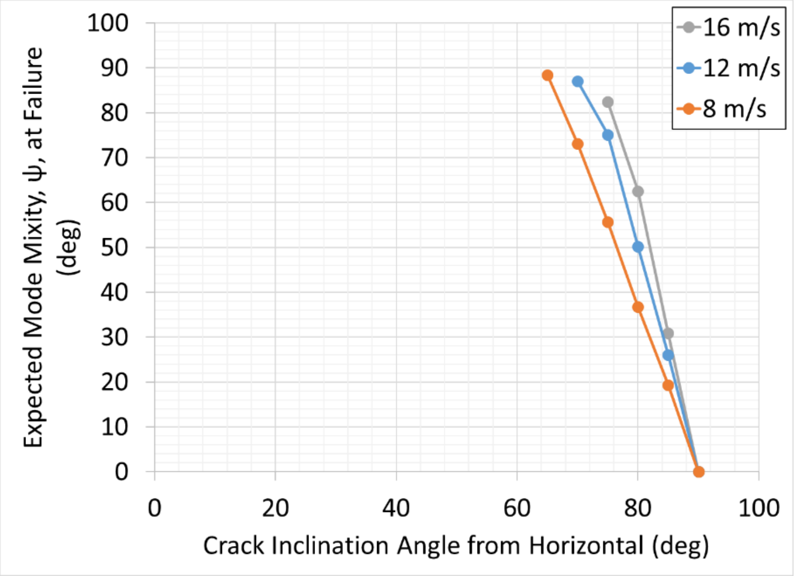

Figure 5-11: Finite element predictions of mode mixity at failure for different crack angles for a 19mm crack length with simulated impact velocities of 8, 12, and 16 m/s

As the striker velocity increases, the apparent mode mixity at crack initiation becomes more sensitive to changes in crack inclination angle. Thus, for really high striker velocities, very small changes in crack inclination angle are expected to result in very large changes in mode mixity at failure for a given material. Again, this may also be undesirable from an implementation standpoint. Likewise, for slower striker velocities, the experimental setup may not be able to achieve pure mode II conditions. Thus, the central finding from these results is that by using crack inclination angle, crack length, and impact velocity, a range of mode mixities can be achieved at a range of possible strain rates. A velocity of 8 m/s was chosen for experiments. For this combination of geometric parameters, a velocity of 8 m/s allows a sufficiently wide range of crack inclination angles to be tested to achieve the desired range of mode mixities. At lower velocities, the full range of mode mixities is less likely to be achievable, and for higher impact velocities, small changes in inclination angle result in large changes in mode mixity.

With respect to strain rate, it is important to understand the dynamic conditions during the loading event and the range of apparent strain rates within the test specimen during the loading event. The techniques that are being used to extract fracture parameters in this work have an underlying assumption that the material behaves in a rate-independent manner. While this limitation could be overcome with implementation of the relevant material phenomena via a user subroutine, the intent is to first develop the methodology with the most practical material model. Viscoelasticity is generally ignored, and it is assumed that a linear, elastic material model is valid during the loading event. The dynamic finite element model was used to explore the nature of the dynamic loading within the test specimen during the loading event. Given the geometry of the test specimen, and the fact that the stress state is not generally uniaxial, the in-plane principal strain was chosen as a variable for understanding the specimen strain rates. In-plane principal strains were extracted for all the elements located near the crack tip, and specifically in the specific domain from which fracture quantities are being extracted. The results are summarized in Table 5-1.

Table 5-1: Summary of expected strain rates in domain of interest near crack tip at expected time of initiation

Angle (deg)	**Maximum (s^{-1})**
65	365.7
80	237.9
90	358.0

As noted in the table, the rate is generally bound by the range of 10^1 to 10^2 s^{-1}. The strain rate history is plotted for reference in Figure 5-12 with t = 0 corresponding to the expected time of initiation.

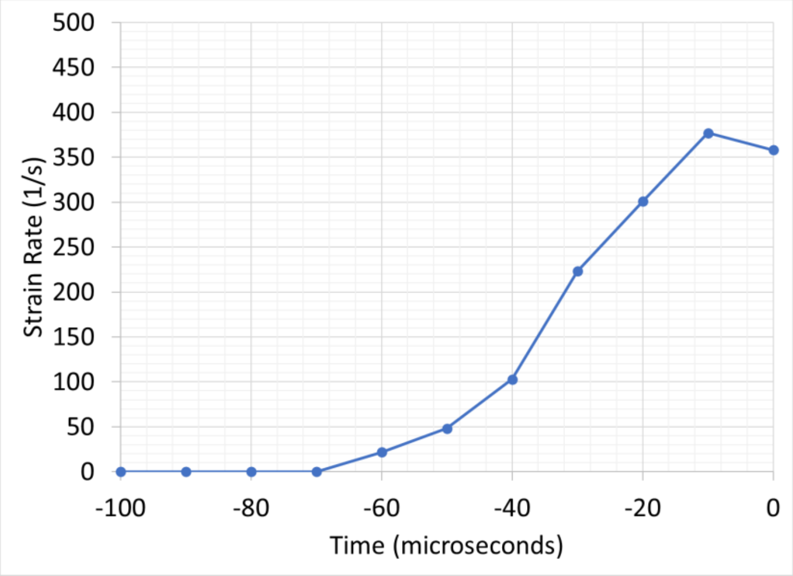

Figure 5-12: Predicted strain rate history in region $r/B \leq 2$ for pure mode I geometry (90°)

For certain polymers, a single order of magnitude increase in loading rate can create significant variations in mechanical properties. This is an important point in validating the inherent assumptions within the linear, elastic material model. The viscoelastic behavior of the polymer material of interest will be discussed in later sections to validate the assumptions regarding the material model.

5.1.3 Specimen edge boundary condition considerations

For the dynamic experiments, putty was used to lightly hold the specimen in the correct position on the adjustable stage such that it was initially in contact with the incident bar. A second piece of putty was utilized on the opposite specimen edge to minimize any unanticipated effects of asymmetric acoustic impedance at the specimen boundary. The effects of various boundary condition assumptions were evaluated using the elasto-dynamic FE model. Four different specimen edge boundary conditions were investigated: free-free, putty on one edge only, putty on both edges, and putty on both edges but with one piece of putty fixed. The four boundary condition assumptions are illustrated in Figure 5-14.

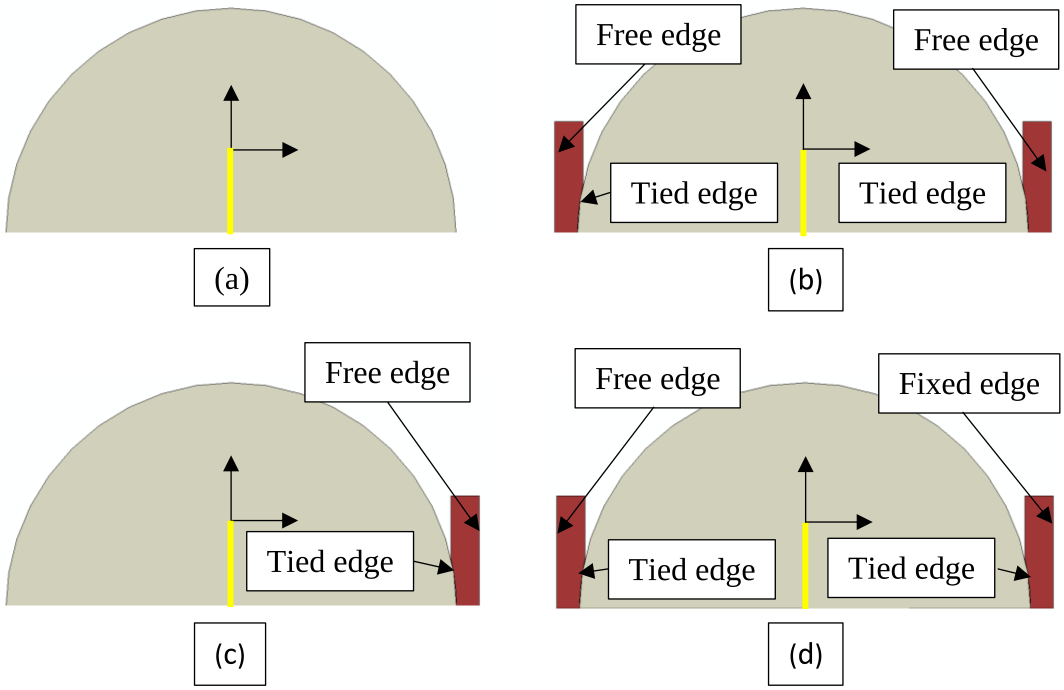

Figure 5-13: Analysis configurations for boundary condition study

In the absence of mechanical property data for the putty material, the analysis runs were executed using three different values for the elastic modulus of the putty to cover the range of the expected elastic modulus based on similar materials. Further, the analysis was focused on the mode I case (β = 90°) where asymmetric effects would be most pronounced. The results are summaryized in Table 5-2.

Table 5-2: Expected effects of putty based on mode I numerical study

Putty elastic modulus		**Boundary Condition**		**Mixity**
(kPa)	**Configuration**	**Edge 1**	**Edge 2**	**(deg)**
1000	a	None	None	0.018
	b	Putty, free	Putty, free	0.901
	c	Putty, free	None	0.907
	d	Putty, free	Putty, fixed	0.901
10000	a	None	None	0.018
	b	Putty, free	Putty, free	0.904
	c	Putty, free	None	0.916
	d	Putty, free	Putty, fixed	0.904
100000	a	None	None	0.018
	b	Putty, free	Putty, free	0.918
	c	Putty, free	None	0.965
	d	Putty, free	Putty, fixed	0.918

The results of the model show that for the 90° case (pure mode I), introduction of the putty on only one edge results in a slight asymmetry in the loading behavior, which results in a slight mode mixity (<1°). As long as the modulus of the supporting material is low (<1000 kPa), the effect is negligible for the epoxy being tested here. However, the model revealed that this symmetry effect would need to be better understood should the modulus of the support material be close to the modulus of the test specimen. While this effect would be undesirable for the pure mode I case, it would be less of a factor for the mixed-mode cases where other asymmetries are already present. The analytical investigation suggests, though, that for experimental consistency, it is desirable to ensure that the positioning of the putty on the lower specimen edge be consistent from experiment to experiment but may not be necessary on the upper edge.

5.1.4 Considerations for use of hybrid DIC-FE method for dynamic conditions

The proposed methodology utilizes a hybrid approach where measured displacements are mapped onto a finite element model. In ABAQUS®, the potential limitation with this technique is that the domain integral approach is only available for quasi-static simulations. It is necessary, therefore, to verify that kinetic energy effects are properly accounted for in the results.

In order to investigate this concern, a mode I fracture specimen was analyzed numerically using two different approaches. First, a full dynamic simulation of the long bar experiment was executed using the previously described explicit model. The displacements on the surface of the test specimen were extracted and post-processed using the over-deterministic, least squares method outlined in 2.3 the mode I stress intensity factor history. This simulation included the striker to incident bar impact, the resulting stress wave propagation in the incident bar, and the subsequent stress wave propagation into the test sample to load it inertially. This numerical technique should appropriately capture all kinetic energy effects. Second, an implicit, dynamic simulation of the long bar experiment was executed. Again, this simulation included the striker to incident bar impact, the resulting stress wave propagation in the incident bar, and subsequent stress wave propagation into the test sample. The previously outlined domain integral methodology (section 2.2.6) was utilized to extract the mode I stress intensity factors from this analysis. Each of the simulations made the same assumptions with respect to material properties as the earlier simulations. The striker impact velocity was assumed to be 8 m/s. The specimen geometry assumed a 19 mm crack length oriented 90° from the horizontal.

The mode I stress intensity factor histories from each approach is plotted in Figure 5-14. The two methods show good agreement. Some differences would be expected in the explicit results simply from the least squares error minimization approach itself; however, the two approaches show good agreement.

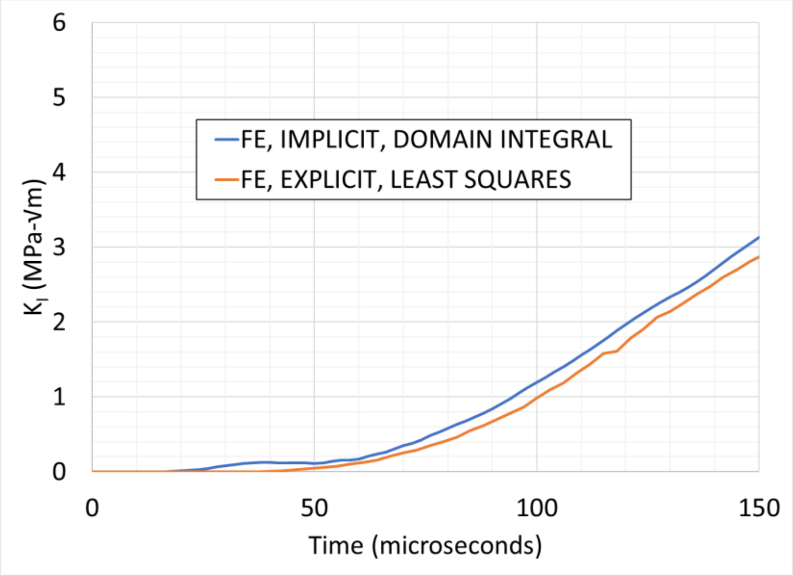

Figure 5-14: SIF history for different analytical model assumptions

5.2 Dynamic semi-circular beam experiments

The next phase of work focused on utilization of this test geometry for dynamic measurements. Characterization of the dynamic loading apparatus was documented in earlier sections and the following section reports the findings with respect to specimen behavior during dynamic loading.

5.2.1 Rate dependent material considerations

As discussed in section 5.1.2, one key consideration for the proper treatment of the experimental results is the understanding of the rate dependent nature of the polymer as it is necessary for proper extraction of fracture quantities of interest using the previously defined methods. Up to the point of crack initiation, it is expected and assumed that the material is behaving in an elastic manner with a highly localized plastic zone (small-scale yielding) in the vicinity of the crack. Using the contour integral approach, to extract the mode I and mode II stress intensity factors requires knowledge of the elastic modulus of the material. For dynamic conditions, it is necessary to know the relationship between elastic modulus and strain rate to properly interpret the results. To assess the rate dependent elastic behavior of the epoxy material, dynamic mechanical analysis was performed, and a technique known as the *decompose, shift, reconstruct* (DSR) method as proposed by Mulliken and Boyce [97] was used to estimate the rate-dependence of the elastic modulus. This method does not provide a direct measure of the elastic modulus; however, the rate-dependence can be assessed by measuring the storage and loss moduli. The storage and loss moduli of the epoxy were measured as a function of temperature using a single cantilever beam cyclic load test in a TA instruments Dynamic Mechanical Analysis (DMA) machine at three different frequencies (strain rates). The first step in the process is to use the loss modulus as a function of temperature to identify the transition temperatures for the polymer. The lower transition point, known as the beta transition, is the temperature associated with polymer chain mobility. The higher transition point, known as the alpha transition, is associated with the temperature at which the polymer changes from a glassier state to a rubbery state. These transition points are illustrated in the loss modulus curve plotted in Figure 5-15. It should be noted here that the plots are normalized separately to view the response on the same scale. For this material, the magnitude of the loss modulus is typically <5% of the storage modulus.

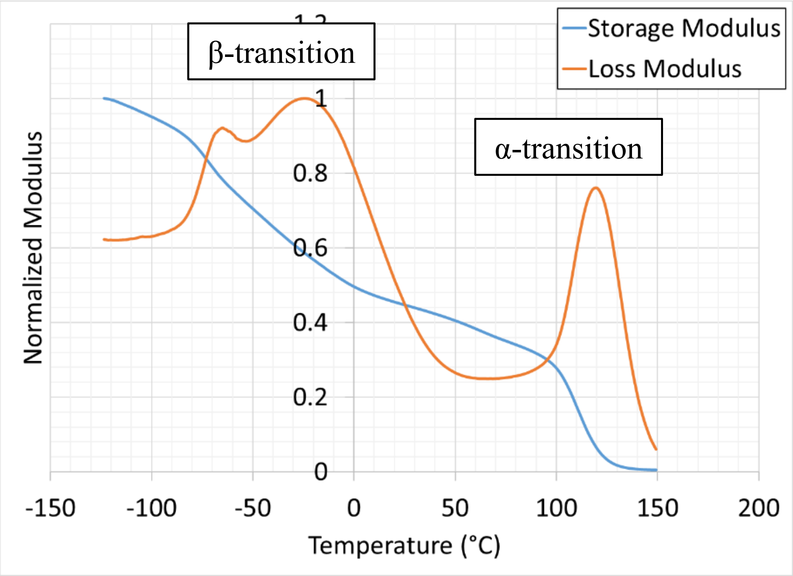

Figure 5-15: Measured storage and loss modulus showing α- and β-transitions

The temperature at which these two transition points occur is related to strain rate. By measuring the loss moduli at multiple frequencies, these shift temperatures can be estimated at different strain rates. As shown in Figure 5-15, for the epoxy, used in the current investigation, it was determined that the α-transition point (which is most relevant to the current work) shifts at a rate of approximately 5°C per decade of increase in frequency or strain rate, meaning that for a factor of 10 increase in frequency (strain rate), the transition temperature changes by 5°C. Once these transition points are known, the storage modulus curve can be decomposed into different components associated with each of these transition points as illustrated in Figure 5-16. The original storage modulus is shown in the blue line, the beta section is shown in gray, and the alpha section is shown in orange.

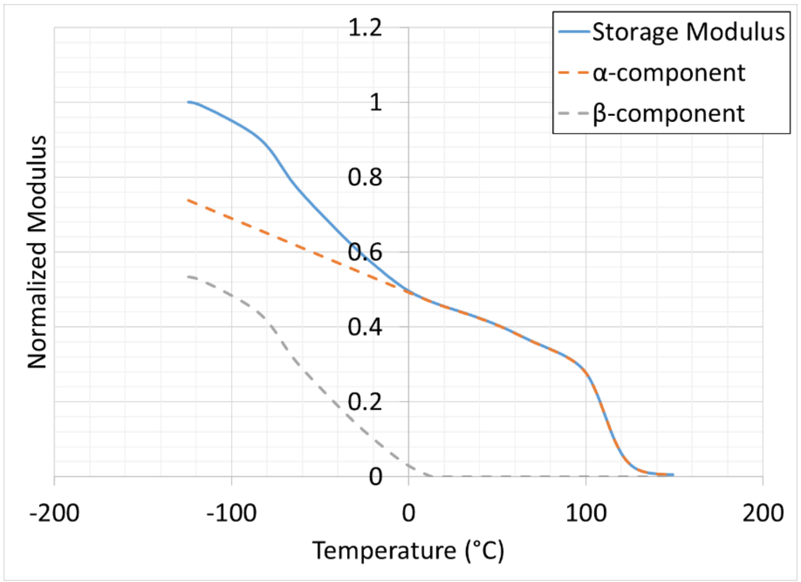

Figure 5-16: Measured storage modulus decomposed into α- and β-components

The two segments of the storage modulus curve can then be shifted along the temperature axis by their respective shift values (5°C for the alpha component). Once the two curve segments are shifted according to their respective shift values, they are then reconstructed into a single storage modulus curve. This technique was demonstrated to work well across a range of strain rates for PMMA and polycarbonate in [97] as well as EPON 826 in [98] by comparing predicted response to measured responses at different rates using split Hopkinson bar testing. This prior work also demonstrated the ability to predict not only strain rate effects on elastic properties but also strain rate effects on yield behavior was demonstrated using an extension of this technique as well. The shifted storage modulus curves for the EPON 828 from the present work are shown in Figure 5-17 for a range of strain rates from 10^{-3} s^{-1} to 10^{3} s^{-1}. While this is not a direct measurement of the rate-dependence of elastic modulus, it is a good indicator of the expected rate-dependence.

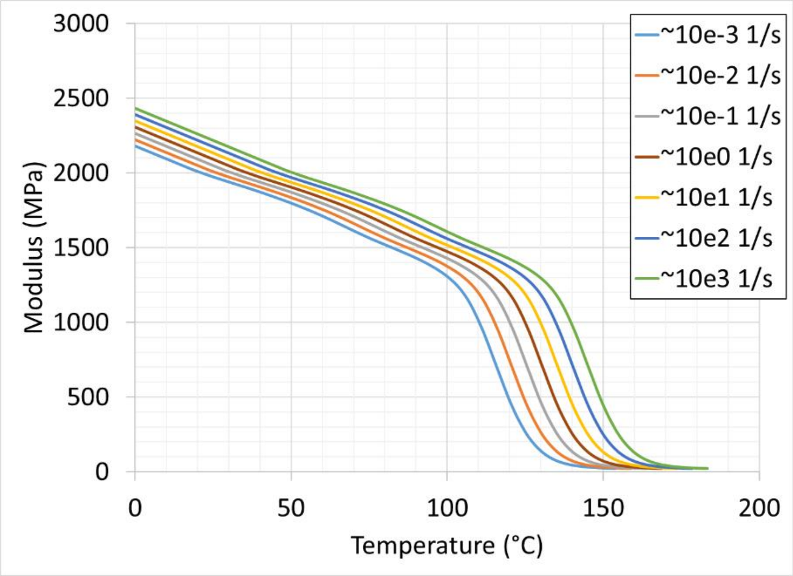

Figure 5-17: Shifted storage modulus curves at a range of strain rates

Based on these results, the elastic modulus of the adhesive is expected to have some rate dependence, particularly at higher and lower temperatures where the material may be operating near one of its transition points. For the present work, however, the primary interest is in the room temperature behavior. Considering dynamic fracture testing at room temperature, the rate dependent elastic effects are expected to be minimal with the modulus being expected to shift less than 4% across the expected strain rate regime (100 to 102 s-1) for the current geometry and under the current impact conditions. Predicted elastic modulus values are tabulated in Table 5-3.

Table 5-3: Estimated rate dependence of elastic modulus based on DSR method (values in italics are extrapolated

Strain Rate (s^{-1})	**Predicted Modulus (GPa)**
~10^{-3}	2.00
~10^{-2}	2.04
~10^{-1}	2.08
~10^{0}	*2.13*
~10^{1}	*2.17*
~10^{2}	*2.21*
~10^{3}	*2.25*
~10^{4}	*2.29*

5.3 Initial dynamic experiments

Based on the findings from initial finite element analyses, an initial set of fracture tests was conducted with the proposed geometry with a striker velocity of 8 m/s. For each test, the striker velocity, incident bar strain, and specimen images were all recorded. The camera was operating at a frame rate of 500,000 frames per second. The Ncorr software was used to perform the speckle image correlations to quantify displacements in the two orthogonal in-plane directions. Based on the subset spacing (5 pixels), and the pixel scale factor (~0.06 mm), the resulting distance between neighboring output points was 0.36 mm. The digital image correlation parameters are summarized in Table 5-4.

The displacement data is post-processed using the same approach as presented in earlier sections. The data is minimally filtered, the grid of DIC output data is used to create a finite element model, the ABAQUS® structural solver is executed, and the domain integral approach is used to extract the desired fracture output quantities.

Table 5-4: Digital image correlation parameters for dynamic experiments

Hardware Parameters			**Analysis Parameters**	
Camera Manufacturer	Kirana		Software	Ncorr
Camera Model	05M		Manufacturer	Open source
Image Resolution	924 × 768		Image Filtering	Guided filter
Lens Manufacturer	Nikkor		Sub-image Radius	45 pixels
Focal Length	80-400 mm		Step Size	5 pixels
Field of View	50 mm × 50 mm			
Image Scale	16.7 pixels/mm			
Stereo Angle	N/A			
Image Acquisition Rate	500,000 fps			
Patterning Technique	Ink stamp			
Approximate Feature Size	5-7 pixels			

The primary objective of the first set of experiments was to quantify any variations with respect to contour path dependence and further evaluate the validity of the model. By validating the finite element model (documented in earlier sections), the model can be utilized for detailed experimental planning (determination of specific crack inclination angles for testing). It also enables future exploration to evaluate the fitness of the experimental setup for study of material behavior at higher or lower strain rates as well as the capability of the experimental setup for investigating other materials.

Using the hybrid DIC-FE approach documented in earlier sections, the domain integral quantities were extracted from the model. For reference, the mesh in the post-processing model is inherited directly from the DIC output data. Therefore, each node in the post-processing model utilizes the same displacement values from its associated DIC output data point. ABAQUS® by default performs the contour integral computation for individual sets of elements that enclose the crack tip. To evaluate path dependence, successive contours must be extracted at increasing radial extents from the crack tip.

It is noteworthy that the *J*-integral is invalid for transient problems until a steady state is reached. This is typically assumed to be 2-3 reverberations of the elastic wave based on the longitudinal wave speed. This time period is not achieved given the duration of the ramp up in stress intensity factor is on the order of 60-80 micro-seconds. However, the full displacement fields are being extracted which include all specimen inertial effects. As was evidenced in Figure 5-14, the simulated results show good agreement between SIF values extracted using the domain integral approach and those extracted using the least-squares approach.

The stress intensity factor output is plotted as a function of the ratio of *r*/*B* in Figure 5-18 for the pure mode I case (90° crack inclination angle) and in Figure 5-19 for the near mode II case (65° crack inclination angle), where *r* is the radial distance from the crack tip and *B* is the specimen thickness.

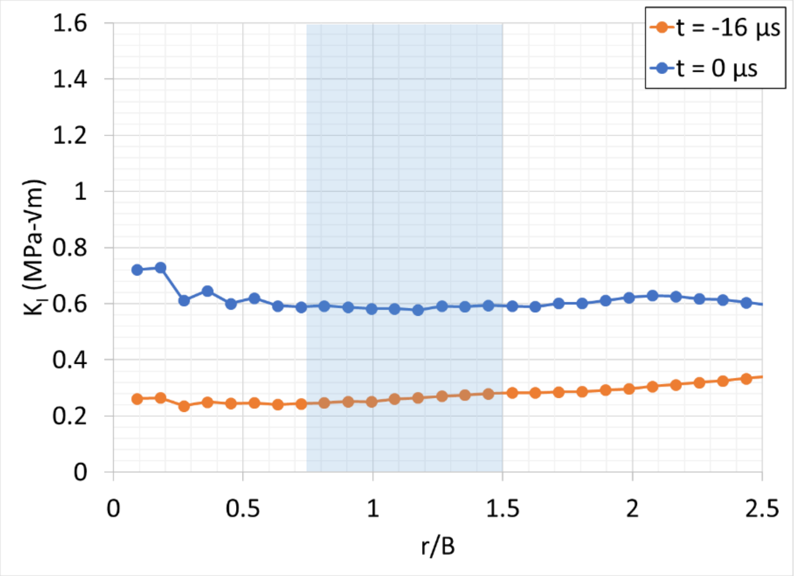

Figure 5-18: Stress intensity factor contour dependence at various time points for pure mode I test

For reference, a value of *r*/*B* = 3 corresponds to a contour radius of 19.1 mm. For each of these scenarios, one set of contour outputs is plotted for a time point near crack initiation ($t \approx 0$

μs) and another set of contour integral outputs is plotted for a time point earlier in the loading event, approximately halfway to crack initiation. As shown in the figure, the stress intensity factors are relatively invariant of contour location even at early time points well before crack initiations.

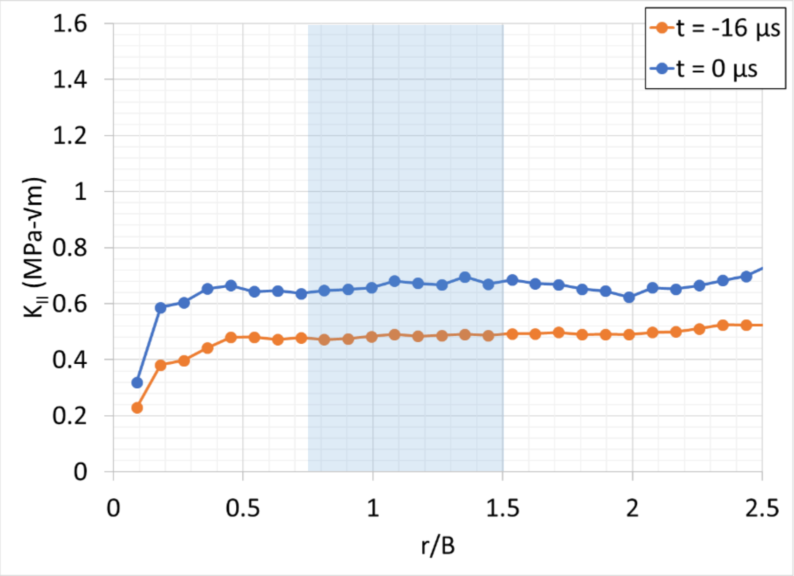

Figure 5-19: Stress intensity factor contour dependence at various time points for pure mode II test

The full set of images were then processed for each of three separate tests: mode I, mode II, and a select mixed-mode case. Up to the point of crack initiation, the results were compared with predictions from the finite element models used for designing the experiment. The entire stress intensity factor histories were also compared with results computed using the least squares regression of the crack tip displacement fields method outlined in Equations [2-15] - [2-22]. Those results are plotted in Figure 5-20 with error estimates summarized in Table 5-5.

Several noteworthy observations can be made from these comparisons. First, the expected stress intensity factor history from the finite element solutions agrees very well with the experimental responses extracted using the over-deterministic least squares method as well as the hybrid DIC-FE results. Post-initiation, the linear, dynamic finite element model data is not available, however, the least squares calculations match well with the hybrid DIC-FE results.

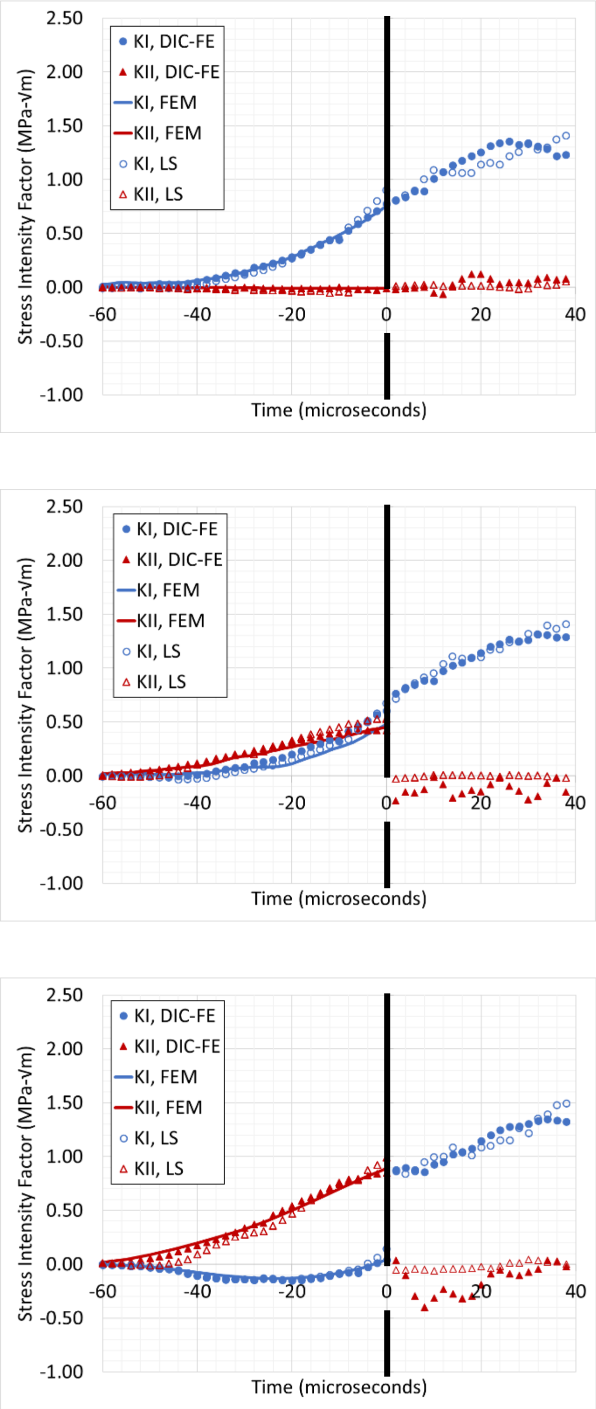

Figure 5-20: Stress intensity factor histories for 90° (top), 80° (center), and 65° (bottom) dynamic experiments with homogeneous test sample

Table 5-5: Estimates of difference between predicted and experimental results for dynamic case

	DIC-FE vs FEM		**LS vs FEM**	
Angle	**K_I**	**K_{II}**	**K_I**	**K_{II}**
(deg)	(Mpa-√m)	(Mpa-√m)	(Mpa-√m)	(Mpa-√m)
65	0.015	0.025	0.014	0.064
80	0.050	0.027	0.042	0.051
90	0.013	0.004	0.037	0.019

In general, for each case, the mode II stress intensity factor rapidly decreases to near zero slightly after initiation and approaches zero as the crack approaches a pure mode I propagation state. The slope of the stress intensity factor history undergoes very little change between the pre- and post-initiation states. This implies that the initial crack is likely very sharp geometrically. For each of the curves, the mode I stress intensity factor plateaus at approximately 1.4 MPa-√m.

Displacement contours were also plotted to visualize and further understand the evolution of the elastic deformation in the vicinity of the crack tip. As evidenced in Figure 5-21, the opening displacement is very symmetric *in magnitude*, implying a mode I dominant deformation field at the point of initiation that persists well into the crack propagation event. This is consistent with the stress intensity factor history plots in Figure 5-20 (a). In the following contour plots presented in Figure 5-22, the displacement fields are asymmetric and dominated by sliding displacement at the point of initiation, however, early in the propagation event, the deformation pattern quickly approaches a symmetric in magnitude of opening displacement field as would be expected for a pure mode I crack. This is confirmed in the stress intensity factor histories previously shown in Figure 5-20 (c).

The initial dynamic experiments demonstrate the capability of the semi-circular beam geometry coupled with the long bar apparatus as a functional method for measuring mixed-mode fracture behavior. The results show very good agreement with predictions from the finite element model, supporting the versatility of the test geometry for further investigation of fracture behavior. Frictional effects and effects due to span asymmetries (discussed regarding the quasi-static work) become irrelevant under dynamic conditions due to single point impact and a very short time response of interest.

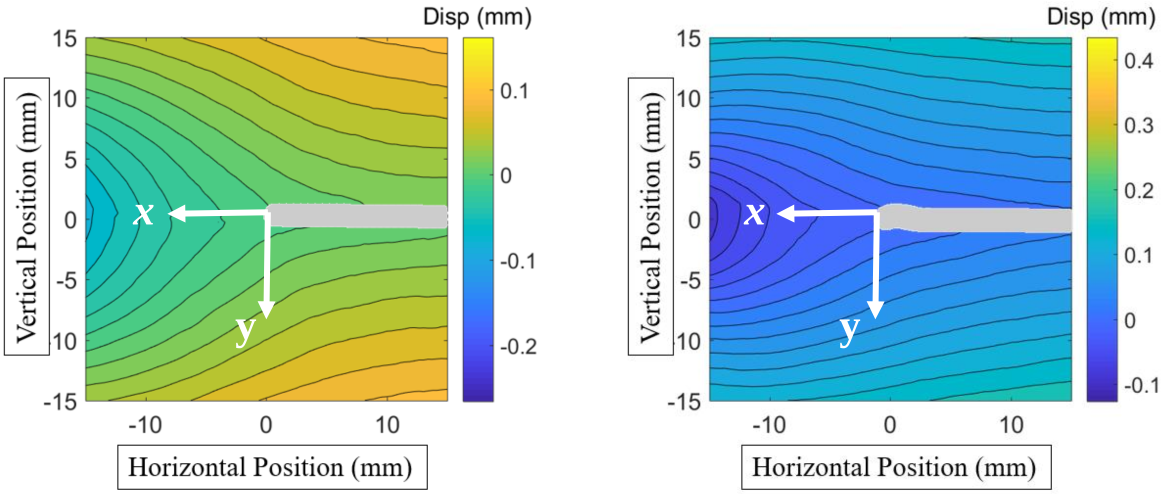

(a) Pre-initiation sliding

(b) Post-initiation sliding

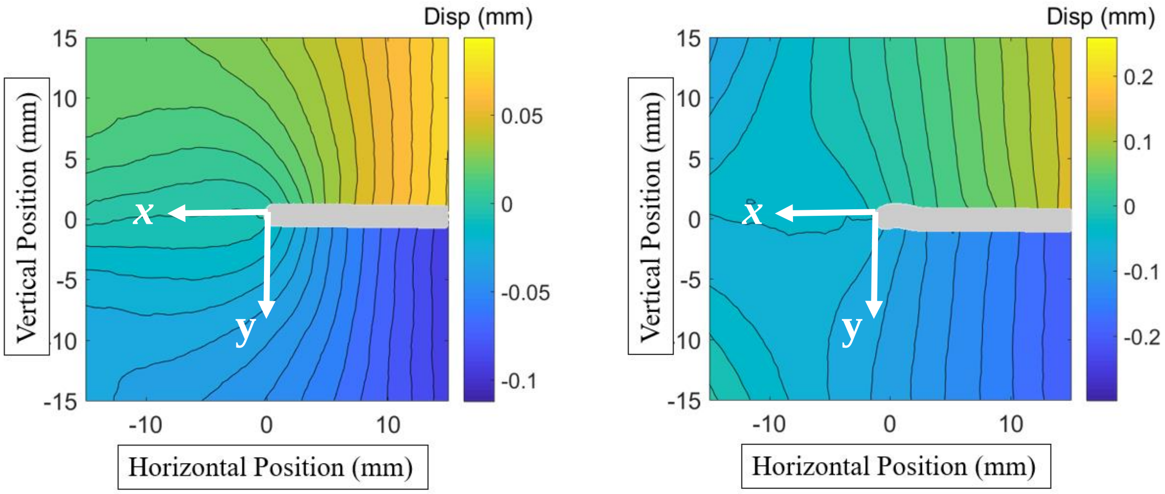

(a) Pre-initiation opening

(b) Post-initiation opening

Figure 5-21: Displacement contour plots for 90° experiment for time points prior to (a) and after crack initiation (b)

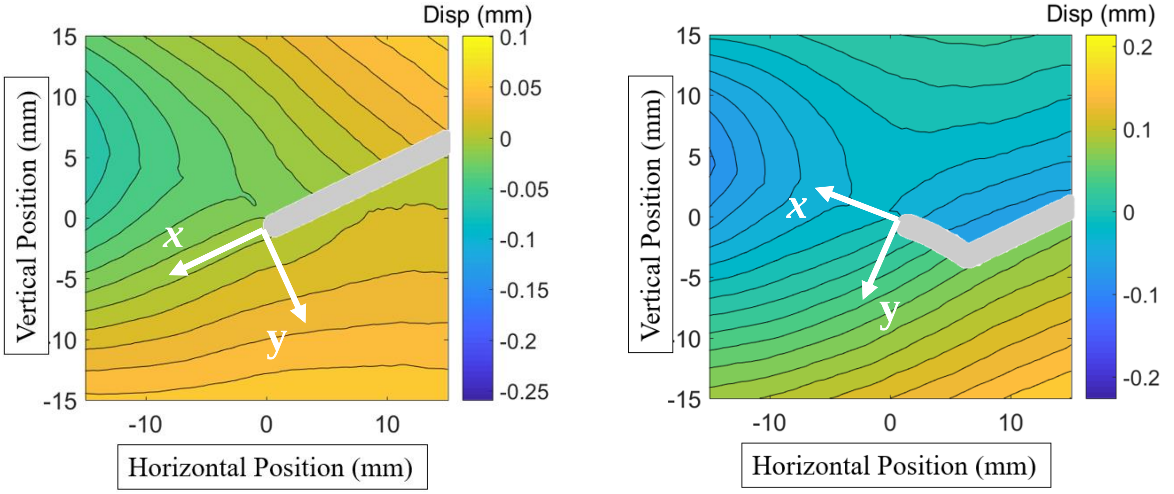

(a) Pre-initiation sliding

(b) Post-initiation sliding

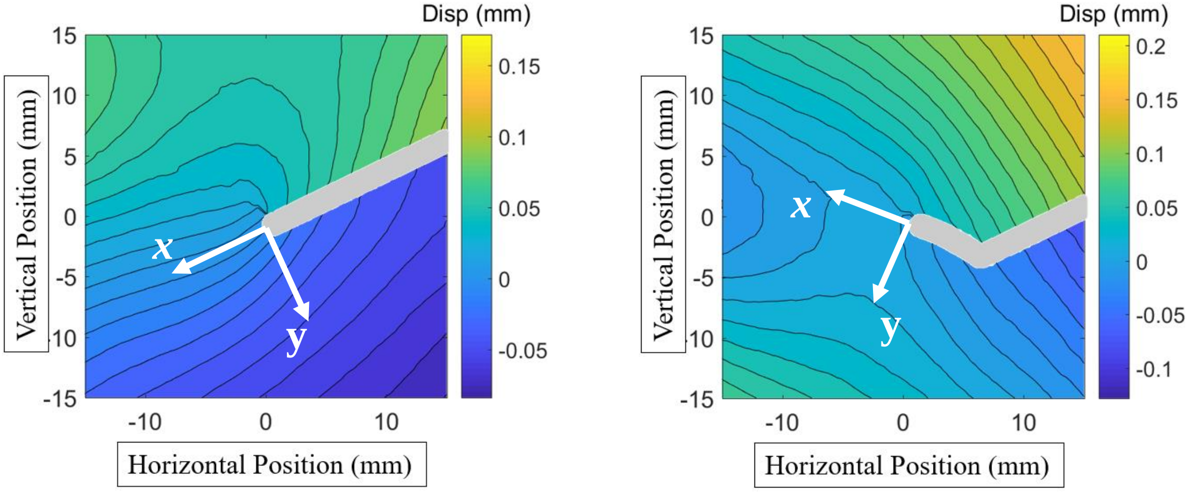

(a) Pre-initiation opening

(b) Post-initiation opening

Figure 5-22: Displacement contour plots for 65° dynamic experiment for time points prior to (a) and after crack initiation (b)

5.4 Results and discussion

The prior quasi-static experimental data was used as a point of reference to the experimental study documented in the current chapter to determine the effect of strain rate on the fracture response. Elevated strain rate loading can have a variety of effects depending on the material and the property of interest. Prior testing demonstrated that the elastic properties of the material within the strain rate regime of interest are fairly insensitive to strain rate, however, that relationship does not necessarily extend to other behaviors (yield behavior and fracture response).

5.4.1 Mixed-mode fracture envelope

The first series of elevated strain rate tests was focused on crack inclination angles in excess of 65° where the mode I component of the stress intensity factor is expected to be positive at failure (based on companion finite element simulations). The mode mixity at failure from this set of tests is plotted as compared to the finite element predictions in Figure 5-23. It should be noted that the FE model predictions reported here are based on the mode mixity corresponding to the instant in the analysis where the effective stress intensity factor reaches a certain value. The relationship between crack inclination angle and mode mixity is relatively linear and generally agrees well with the results predicted by the FE simulations.

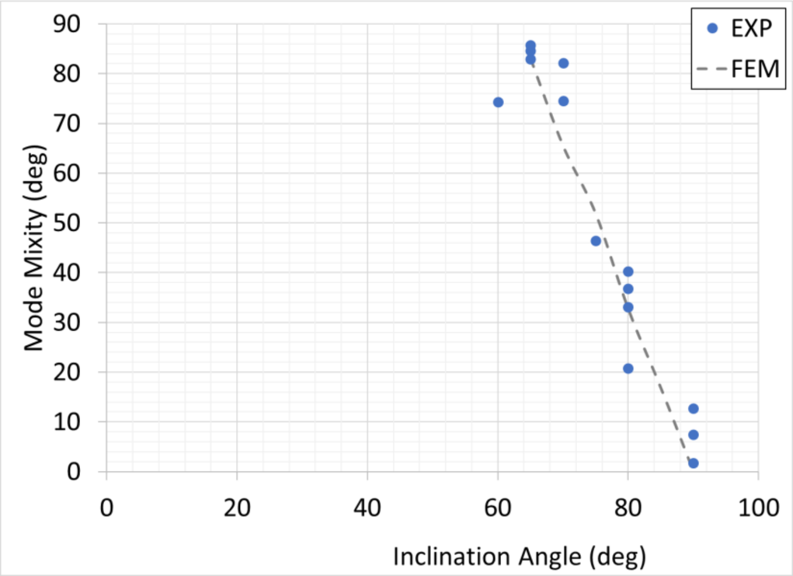

Figure 5-23: Comparison of mode mixity for different crack angles in the SCB specimen with the corresponding FEM computations for dynamic experiments

Critical stress intensity factors across the full range of mode mixities were also extracted from this set of tests. For each test case, the results were extracted using the DIC-FE method and are plotted in Figure 5-24.

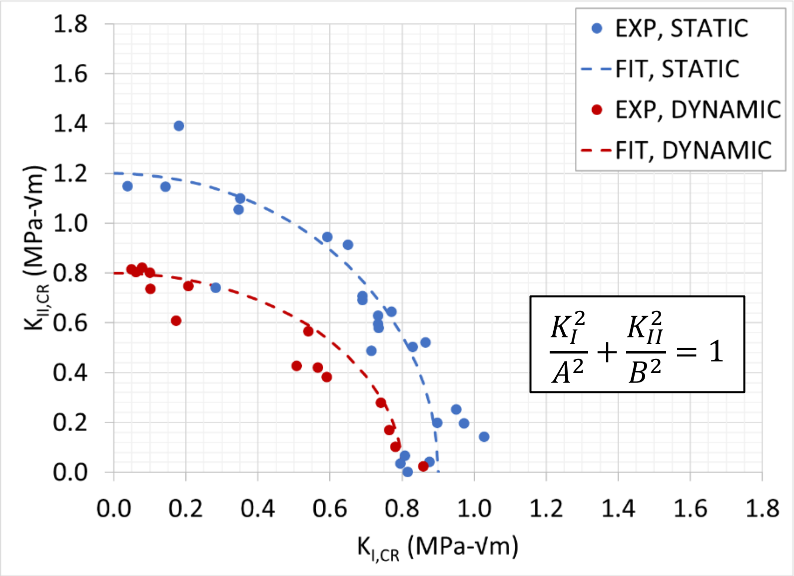

Figure 5-24: Critical stress intensity factors for static and dynamic experiments

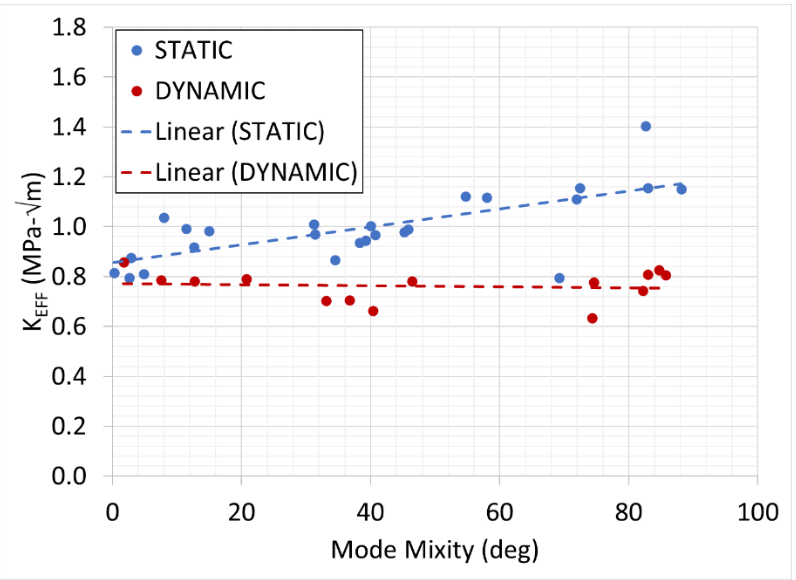

Figure 5-25: Relationship between effective critical stress intensity factor and mode mixity

An alternative representation of the mixed-mode fracture behavior of this adhesive is shown in Figure 5-25. The curve fit parameters are summarized in Table 5-6.

Table 5-6: Summary of curve fit parameters for homogeneous samples using elliptical fit

Test Series	**A**	**B**
Quasi-static, homogeneous	0.9	1.2
Dynamic, homogeneous	0.8	0.8

Here, the effective stress intensity factors at crack initiation, $K_{eff} = \sqrt{K_I^2 + K_{II}^2}$, under static and dynamic loading conditions are plotted as a function of mode mixity by the red solid symbols. Again, for comparison, the quasi-static counterparts are shown for the same material by the blue solid symbols. A linear fit is also shown on the plot for both sets of data. Under dynamic conditions, within the experimental scatter, the critical effective stress intensity factors are relatively constant with respect to mode mixity. On the contrary, for the quasi-static experiments, this is not true; a perceivable increasing trend in the critical effective stress intensity factors with mode mixity (or, increasing critical mode II values) is evident. Approximately 38% higher value of critical K_{eff} under mode II conditions relative to the pure mode I value can be estimated from the plot. The relationship between effective stress intensity factor and mode mixity varies by material. For instance, Lim, et. al. [99] observed a general decrease in effective stress intensity factor with increasing mode mixity for soft rock. Miller [100] observed a similar decreasing trend for a rubbery particulate composite. In a study of mixed-mode fracture in epoxy, however, Jamali, et. al. [101] observed an increase in strain energy release rate of approximately 2.47X across the range of mode mixities from pure mode I to pure mode II and noted similar trends in other epoxies.

The dynamic results were measurably lower than the complementary static values, with a larger change in the two sets of data occurring in the shear-dominated regime near the pure mode II case. It is believed that this might be due to strain rate effects in shear, where the shear response is more sensitive to strain rate effects than under tension dominant conditions. The material exhibits an elastic-brittle response in tension, whereas, in compression and shear, the material exhibits greater ability to deform nonlinearly (assumed to be from plasticity). For certain materials (to include polymers), inelastic behavior can be significantly affected by loading rate, and that is likely the case here. The rate effect typically manifests itself in decreased plasticity and increased strength. Several prior works have observed a similar effect with respect to the differences between static and dynamic fracture toughness. Work by Kalthoff, et al. [102] reported results from dynamic experiments where the initial dynamic stress intensity factor (at crack initiation) was lower than its static counterpart. However, dynamic values from later in the propagation were higher than their static counterparts. Marur, et al. [103] performed tests on particulate composites comprised of epoxy and alumina nanoparticles.

Their results also demonstrated lower fracture toughness in dynamic conditions relative to their static counterparts for studies involving two different particle sizes and multiple volume fractions. Joudon, et al. [104] reported dynamic stress intensity factor values that were 88-91% of their static equivalent for a neat epoxy material. Pittman and colleagues [105] studied mode I stress intensity factors for 2 separate epoxy systems. One system, PR-520, exhibited static critical SIF values that were higher than the dynamic SIF values, whereas the other system, 3502, exhibited dynamic critical SIF values that were lower than the dynamic SIF values. These seem to support the observed rate dependent behavior of fracture envelopes.

5.4.2 Crack propagation direction

For each test specimen, image analysis was used to measure the crack initiation direction and the results are compared in Figure 5-26. Given the difficulties in precise measurement of crack kink angles from the initial crack tip, reasonable agreement between the experimental results and those predicted by the two crack propagation direction criteria, the maximum tangential stress criteria and the maximum energy release rate criteria is evident.

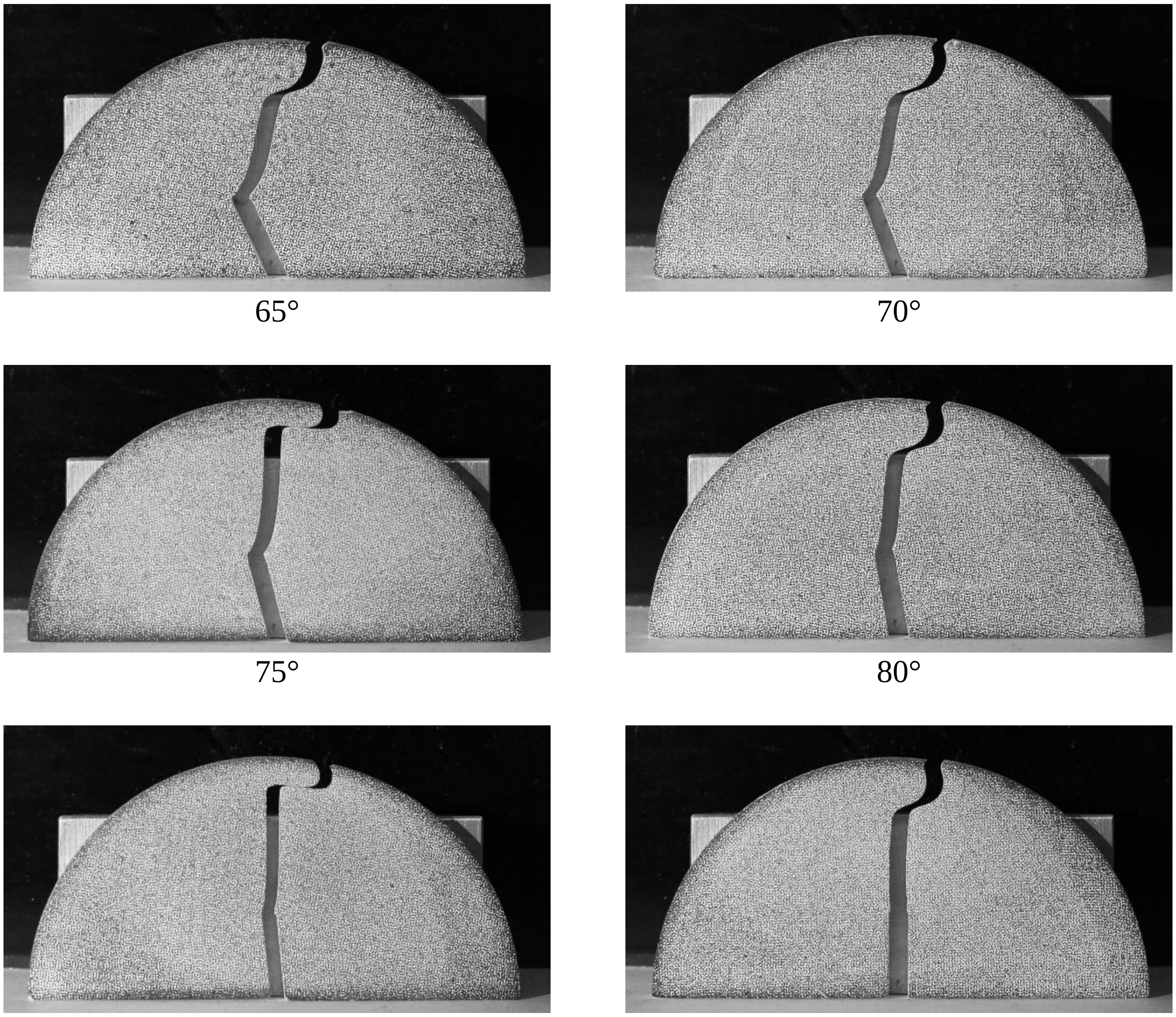

65° 70°

75° 80°

85° 90°

Figure 5-26: Images of failed dynamic SCB test specimens

The measured crack kink angles agree well with the kink angles predicted from the two criteria used in the FE model, considering the difficulty of estimating the kink angle from the failed specimen crack surfaces. Two points on the edge are used to estimate the angle and the further those two points are apart, the more the estimate will tend to underestimate the kink angle.

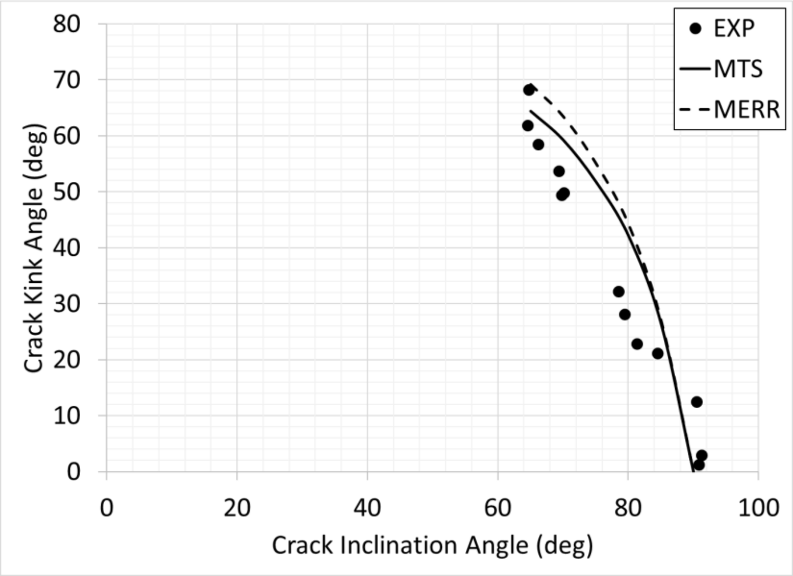

Figure 5-27: Comparison of crack propagation direction with FE predictions

5.4.3 Effect of in-plane compression

Additionally, complimentary dynamic experiments were also performed to quantify the effect of compression on the fracture initiation behavior. Namely, for the 8 m/s impact condition, crack inclination angles or 60°, 55°, and 50° were performed to achieve the in-plane compressive state at crack initiation. The results are plotted with the accompanying Mohr-Coulomb fit in Figure 5-28. The same friction angle was found to fit well for the dynamic experiments as well.

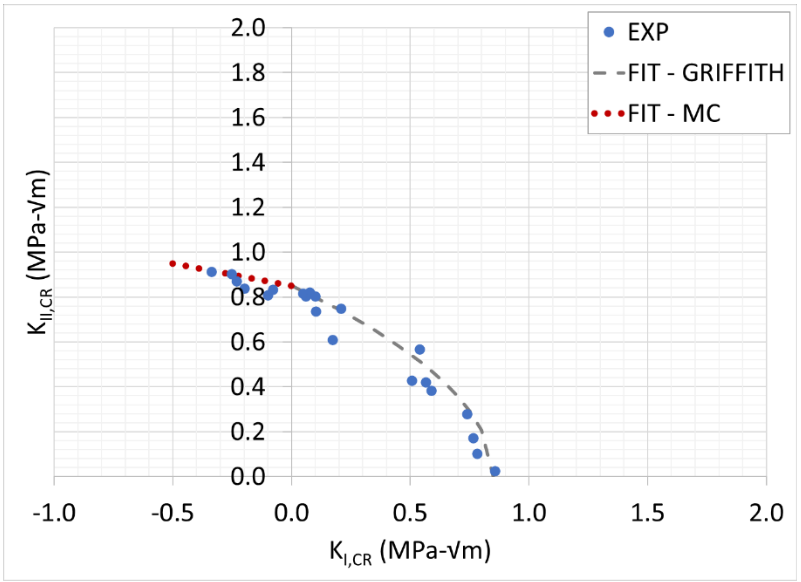

Figure 5-28: Critical stress intensity factors including in-plane compression state from dynamic tests

Table 5-7: Summary of curve fit parameters for Griffith and Mohr-Coulomb fit for homogeneous tests

	Parameter			
	Griffith		**Mohr-Coulomb**	
Test Series	**T_0**	**A**	**c**	**φ**
Quasi-static, homogeneous	0.85	0.75	1.30	0.20
Dynamic, homogeneous	0.85	0.50	0.85	0.20

5.4.4 Observations from microstructural analysis

Fracture surface (*x*-*z* plane) micrographs from two tension- and shear-dominated fracture events are presented in (Figure 5-29).

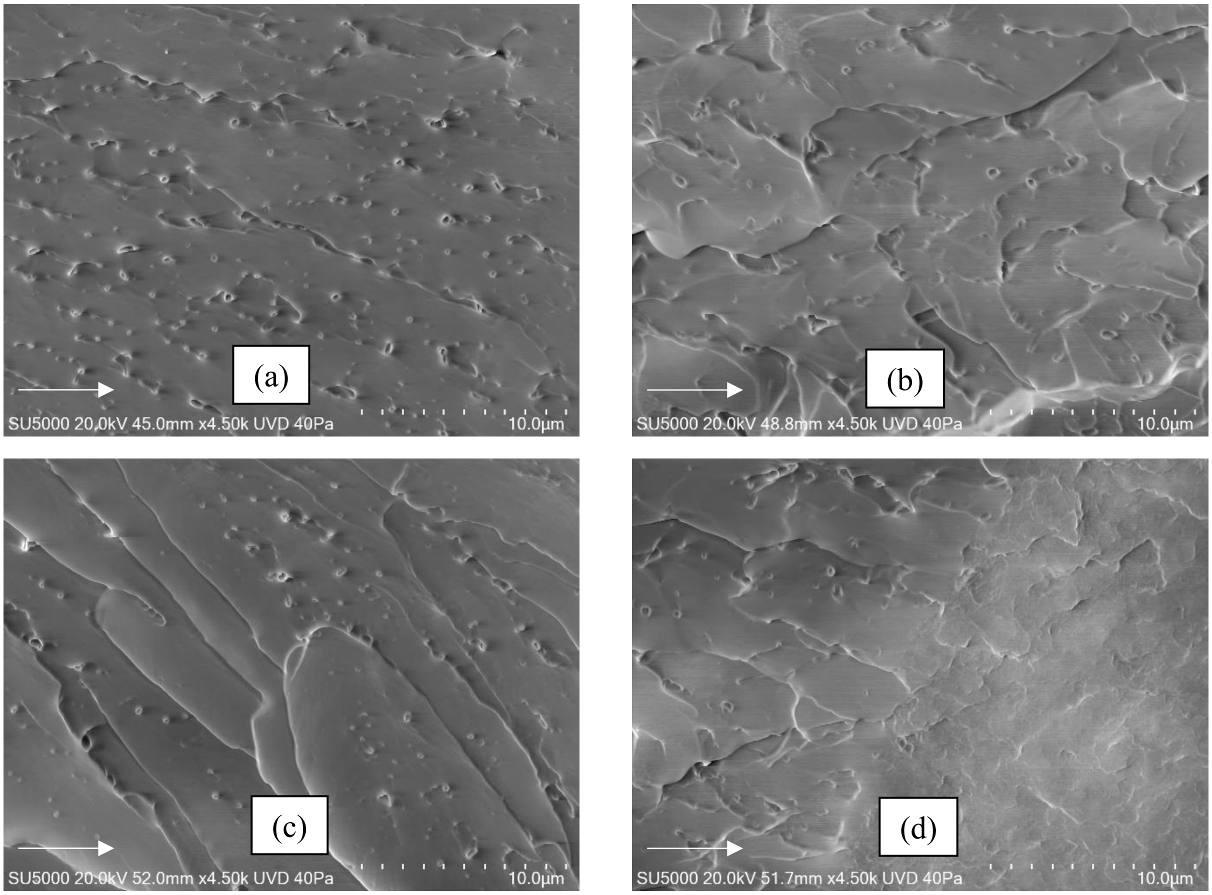

Figure 5-29: Micrographs of dynamically failed specimens (a) 90°, mode I, (b) 65°, mode II, (c) 50°, mode II with compression (arrow indicates propagation direction)

The images were taken at a magnification of 4500X. Evidently, the fractographs from quasi-static and dynamic mode I and mode II cases show visible differences. The dynamically loaded specimens appear to have fewer finer features relative to the quasi-static ones. In the mode I case, numerous locations where crack pinning has occurred are clearly visible whereas the same are less dominant and mostly interspersed amongst broad, randomly cleaved features in the dynamic counterpart. Particle cavitation is another potentially significant mechanism dominant under quasi-static conditions appearing as pronounced localized features in contrast to the dynamic surface features. In the mode-II case, the fracture surface features are again visibly dominant under quasi-static conditions relative to the dynamic counterparts. The crack has numerous pinned and cavitated locations besides cleaved structures. The same features are relatively muted under dynamic conditions. These textural differences are consistent with the lower critical stress intensity factor values at initiation for the dynamic case. Some sections on the fracture surface were also identified that had less particles present at the fracture surface as illustrated in Figure 5-30.

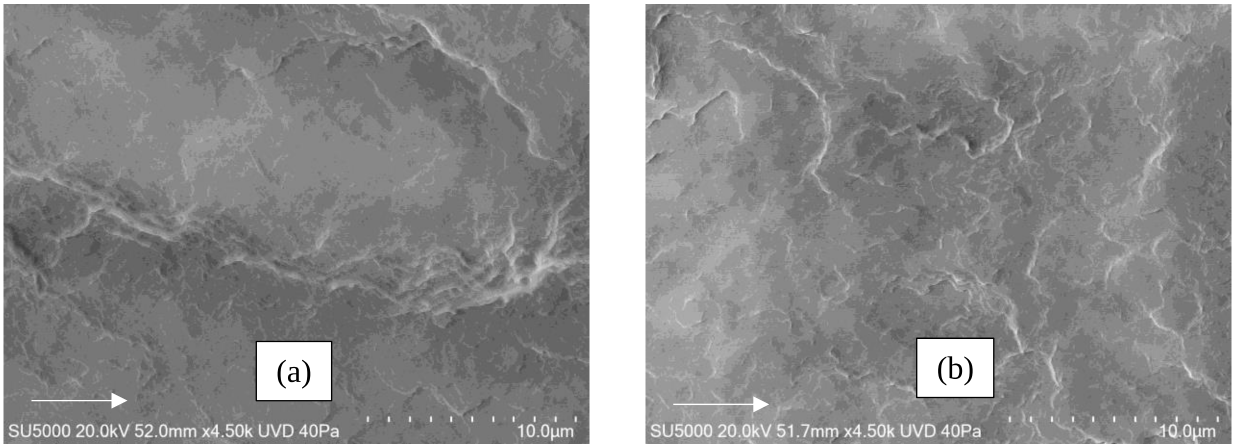

Figure 5-30: Micrographs of mode II (a) static vs. (b) dynamic failed specimens extracted from regions with limited particles present at the surface (arrow indicates propagation direction)

In the case of these surface locations, the texture differences between the static and dynamic samples were consistent with those of the prior images taken from sites that had higher concentrations of particle cavitation sites. Some visible surface feature differences were noted between samples that had cracks that initiated under pure mode II conditions vs specimens that had cracks that initiated under mode II conditions in the presence of compression. Two micrographs are compared in Figure 5-31.

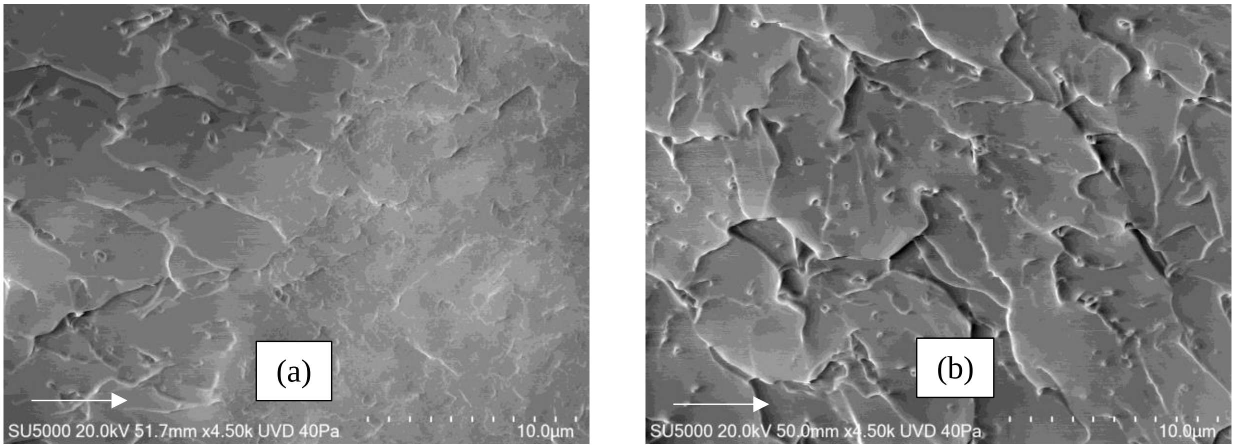

Figure 5-31: Micrographs of dynamic mode II specimens with initial crack inclination angles of (a) 65° – pure shear vs. (b) 50° – combined shear and compression (arrow indicates propagation direction)

Chapter 6

Towards an Improved Crack Tip Identification Procedure

A persistent challenge for experimental fracture mechanics investigations using vision-based methods is the accuracy with which the crack tip is located in the region of interest for extracting fracture parameters. Specifically, when using full-field displacement measurement methods such as DIC, positioning of the crack tip coordinate system has a direct influence on the accuracy of the stress intensity factors extracted. Although this generally does not pose major problems when the crack tip is stationary, in problems involving moving fracture fronts, such as the ones during dynamic crack growth, this becomes a major challenge. The detection of the instantaneous crack tip amidst random grayscale speckles as well as the sheer number of temporally distinct images to be analyzed in an experiment exacerbates the issue. Usage of domain integral approaches can mitigate this problem to some extent. However, with brittle materials that produce fractures at lower magnitudes of stresses and deformations, the apparent discontinuities in the displacement fields, commonly used in conjunction with visual evidence in DIC, are often not obvious to the operator. Also, for high crack propagation speeds, there can be significant averaging effects that occur at the crack tip in the optical measurement data, thereby introducing additional uncertainty. Lee, et al. [106] noted the challenges associated with crack tip location identification in the study of graphite epoxy composite materials. Their work estimated an error of approximately 0.5 mm in crack tip position due to the relatively small magnitudes of displacements in a stiff, brittle composite. Sundaram and Tippur [107] pointed out the same challenge in their experiments with glass where the choice of the contour increment in the visualization of the displacement field could lead to drastically varying interpretations of the crack tip location. An objective comparison of various optical techniques in [108] revealed the difficulty of crack tip location identification associated with DIC measurements as compared to other methods such as photoelasticity.

For these reasons, an improved method for identifying the location of a dynamically propagating crack tip was pursued. The current chapter documents this proposed automated procedure for more systematically and reliably locating the crack tip location in a dynamically propagating crack.

6.1 Prior methods for crack tip location identification

Several methods have been used in prior experimental work where there was a need to locate the crack tip position. Fracture quantity extraction from experimental data has been summarized by Redner in [109] and Etheridge, et al. in [110]. One noteworthy work by Sanford [63] developed linear and nonlinear least squares methods to determine parameters (photoelastic fringe constant) from a calibration experiment using a disk in diametrical compression. The approach was then used to determine the opening-mode stress intensity factor in a specimen with a crack. In the crack tip analysis, the location of the crack tip was treated as an unknown. In this approach, the fringe order is related to a combination of the theoretical solution and an unknown linear error term.

$$N(x,y) = \frac{t}{f_\sigma} \bar{G}(x,y) + E(x,y) \qquad [6\text{-}1]$$

where $\bar{G}(x,y)$ is the theoretical solution for the difference of the principal stresses in Cartesian coordinates, f_σ, is the stress-optic constant, and $E(x,y)$ is a linear error term, $E(x,y) = Ax_i +$

$By_i + C$. By expanding this equation out for multiple N_i (i being the fringe order), an overdetermined set of equations can be established and solved for the stress-optic constant, f_σ, and the coefficients of the linear error term. This works well for the linear relationship between the error term, the fringe order, and the theoretical solution for the disk in diametrical compression. However, for more complex relationships between fringe order and desired output quantities, the equations cannot be readily solved. For the fracture problem investigated in the work reported in [63], the relationship between fringe order, stress-optic constant, and stress intensity factor is:

$$\left(\frac{Nf_\sigma}{t}\right)^2 = \frac{K_I^2}{2\pi r}\sin^2\theta + \frac{2\sigma_{0X}K_I}{\sqrt{2}\pi r}\sin\theta\sin\frac{3\theta}{2} + \sigma_{0X}^2 \qquad [6\text{-}2]$$

where r and θ are the radial and tangential coordinates of the crack tip and are unknown due to the crack tip position being unknown in the Cartesian coordinate system. Both coordinates are functions dependent on the coordinates of the crack tip, x_0 and y_0. For this problem, Sanford introduced a nonlinear, least squares approach to identify the stress intensity factor, K_I. While the nonlinear, iterative procedure is fully documented in [63], the general approach involves guessing values of the K_I, σ_{0X}, x_0, and y_0 and then adjusting the initial guesses iteratively until the values themselves converge to a stable value. One of the challenges of working with the data from the DIC method is that the displacement fields do not give a clear indication of the crack tip location. It is further challenged by the fact that data is often not available directly at the crack tip, but at best, is available at half a subset radius away from the crack tip. The previously described method of extracting stress intensity factors from the displacement field (section 2.2) involves first choosing a crack tip location and computing the displacement values with the crack tip as the origin. For each point in the displacement field, the analytical equations are formed such that the stress intensity factors are unknown and the displacements are known. By choosing a set of points in the field, an over-determined set of equations is formed and can be solved for the unknowns. Yoneyama [67] proposed an alternative to this where not only the stress intensity factors were unknown but the crack tip coordinate is also unknown. An iterative procedure was used based on the Newton-Rhapson method where equations were derived to estimate the correction to the stress intensity factor estimation based on the results of the previous guess, such that the procedure eventually converges to a result. Pacey and colleagues [111] studied crack closure conditions using photoelasticity. In their work, the analytical stress field was calculated mathematically using Muskhelishvili's stress potential function and the analytical model was fit to the experimental data using a genetic algorithm and the downhill simplex algorithm. Roux and Hill [112] developed a method to estimate the crack tip location using a similar optimization approach by using the digital image correlation data to match the amplitude of a reference displacement field and minimize the error between the measured and reference fields. A method proposed by Hamam [113] utilized the concept of an elastic crack tip and its detection using the first super-singular term in the Williams' expansion. This approach was shown to be relatively robust with an estimated uncertainty of 20 micro-meters in the study of fatigue crack growth in steel. Zanganeh, et. al. [114] studied several methods based on this concept of minimizing the error between a measured displacement field and an analytical solution. They performed a comparison of multiple Newton-based optimization methods, a direct search method (Nelder-Mead Simplex), a genetic algorithm, and a pattern search method. Their investigation had the best success with the pattern search method which was reported to locate the crack tip within an average of 0.22 mm and 0.04 mm in the *x*- and *y*-directions, respectively. More recently, Rethore, et. al [115] introduced a method based on elastic regularization along with finite element kinematics on an adapted mesh and a truncated Williams' expansion to identify the crack path. This method was shown to be helpful in the analysis of experiments where the crack is propagating along a curved path.

6.2 Image processing-based edge detection

For the present work, however, an image processing technique used for edge detection was chosen as the basis for developing a method to improve the accuracy with which the crack tip can be identified. The concept of edge detection in the image processing community has been widely studied for a number of problems. In typical image processing problems, an edge can be caused by a number of situations such as drastic changes in depth or object orientation, a change in material (for instance land verses water in cartography applications), or changes in illumination in the image. The typical goal of edge detection in image processing is to locate a series of connected pixels that outline these discontinuities. For example, there may be a need to stitch together a series of images taken over a geographical space, and the edges of certain features that are present in adjacent images can be used to align images and stitch them together. A second example would be to track the position and calculate the velocity of an object in a series of images or in a video stream. In this example, the goal would be to locate the outline of the object and differentiate it from other outlines in each image frame. This second scenario finds many applications in machine vision and industrial automation problems. Another edge detection type of problem might be found in the medical field where certain features need to be identified and assessed in various diagnostic techniques. This might be used for assessing whether a certain feature in the image was within an acceptable size or volume range.

The general concepts of edge detection extend well to the cracked test specimen problem. Ahead of the crack tip, displacement fields are continuous while behind the crack tip, they are discontinuous. Thus, the problem to be solved is to identify the most likely location within the field where the field transitions from continuous to discontinuous. The discontinuity in the in-plane displacement field has very similar features to an edge in an image processing problem, namely, the derivatives of the field quantities are very high, the main difference being that the image processing problem deals with abrupt changes in pixel intensity values whereas the crack tip identification problem deals with changes in displacement magnitudes.

Several methods have been employed to detect crack paths using image-based techniques. Work by Abdel-Qader, et al. [116] explored edge-detection methods to identify cracks present in concrete structures. The work demonstrated the ability to use changes in intensity across an image to locate cracks and crack-like features from images. Lopez-Crespo, et al. [117] utilized Sobel edge detection to locate the crack tip to extract mixed-mode stress intensity factors from a tension-shear test geometry. They evaluated the stress intensity factor uncertainty due to position errors and showed relatively low error in the measurement using the Sobel-based technique for fatigue cracks. More recently, several authors have made advancements to the crack tip location identification problem. Finite element simulations of displacement fields around cracks were used to train convolutional neural networks [118] and track crack tip position. The method was utilized to study fatigue crack growth in planar 2024 aluminum alloy specimens with a crack central subjected to uniform tension. Miao, et al. [119] used Canny edge detection [120] and [121] with manual thresholding to approximate the crack path and use the results as a basis for an improved subset-splitting technique. The technique was demonstrated to enable improved reconstruction of the displacement fields near the discontinuity.

The first step in the algorithm involves filtering the image to remove noise in the image to aid in the subsequent processing steps. While the smoothing process introduces blur into the image, the reason it is introduced is to reduce the number of edges that will occur simply due to noise in the image. The typical implementation utilizes a Gaussian smoothing function,

$$G(x,y) = \frac{e^{\frac{-(x^2+y^2)}{2\sigma^2}}}{2\pi\sigma^2} \qquad [6\text{-}3]$$

where σ is the filtering parameter that determines how much smoothing is applied. In practice, it is much easier to numerically approximate a value for the smoothing function. The matrix defined in [6-4] provides an adequate level of smoothing for the present work for a 5 × 5 filtering kernel and can efficiently be applied through a convolution operation. This filtering kernel is an approximation of the Gaussian smoothing function with $\sigma \approx 1.4$. The least common denominator of the 5×5 matrix has been extracted to present the matrix in terms of integer values.

$$G(x,y) = \begin{bmatrix} 2 & 4 & 5 & 4 & 2 \\ 4 & 9 & 12 & 9 & 4 \\ 5 & 12 & 15 & 12 & 5 \\ 4 & 9 & 12 & 9 & 4 \\ 2 & 4 & 5 & 4 & 2 \end{bmatrix} \left(\frac{1}{159}\right) \qquad [6\text{-}4]$$

Once the smoothing has been applied to the pixel intensity values (or displacement field magnitudes in the present work), the gradients within the field can be computed. The underlying assumption with this step is that the edges occur due to sudden changes in intensity in the image and that areas away from the edges are more uniform. One way to measure the magnitude of the change is to calculate the partial derivatives or the gradient magnitudes at each pixel. For an image, with an intensity I, that varies spatially, the first order partial derivatives, $E_x = \frac{\partial I}{\partial x}$ and $E_y = \frac{\partial I}{\partial y}$, can be approximated for the *x*- and *y*-directions, respectively. For the typical implementation of the Canny algorithm, the Sobel operator, which is based on two 3 × 3 filtering kernels, is used to approximate the first order derivatives. This is readily implemented numerically by convolving the filtered intensity field with the filtering kernels:

$$K_x = \begin{bmatrix} -1 & 0 & 1 \\ -2 & 0 & 2 \\ -1 & 0 & 1 \end{bmatrix}, \tag{6-5}$$

$$K_y = \begin{bmatrix} 1 & 2 & 1 \\ 0 & 0 & 0 \\ -1 & -2 & -1 \end{bmatrix}. \tag{6-6}$$

This gradient computation was suggested by Sobel [122] as an isotropic gradient operator and is widely used in edge detection problems. In practice, this produces a rudimentary approximation of the partial derivatives, however, it is very efficient from a computational standpoint. The gradient magnitude is calculated from the individual directional gradient values using:

$$\|M(i,j)\| = \sqrt{E_x[i,j]^2 + E_y[i,j]^2} \tag{6-7}$$

Once the magnitude and individual components in each direction are known, the directions can be computed using:

$$\theta(i,j) = \tan^{-1}\frac{E_y[i,j]}{E_x[i,j]} \tag{6-8}$$

A simple example with an edge running in the horizontal or vertical direction can be used to illustrate this concept. A 5 × 5 excerpt from a random magnitude intensity field with an edge oriented in the vertical direction is shown in Figure 6-1 with resulting simple gradient computations.

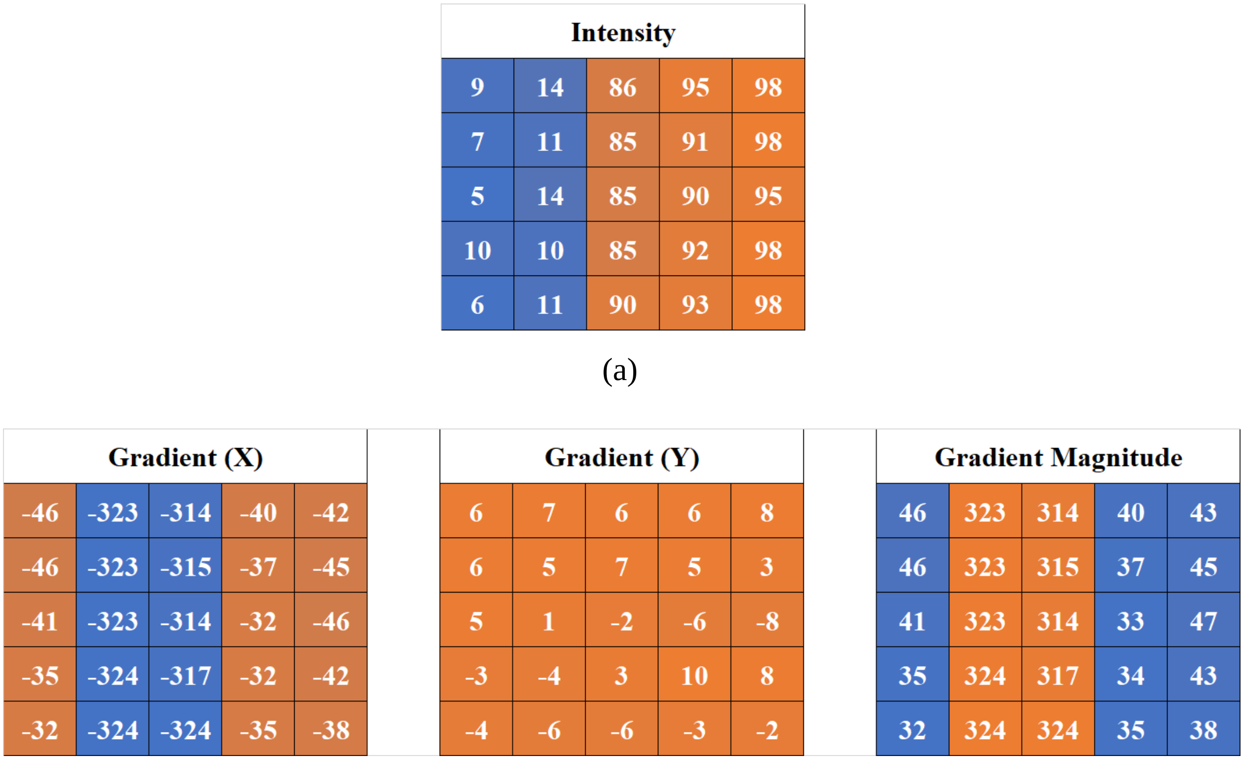

Intensity				
9	14	86	95	98
7	11	85	91	98
5	14	85	90	95
10	10	85	92	98
6	11	90	93	98

(a)

Gradient (X)				
-46	-323	-314	-40	-42
-46	-323	-315	-37	-45
-41	-323	-314	-32	-46
-35	-324	-317	-32	-42
-32	-324	-324	-35	-38

Gradient (Y)				
6	7	6	6	8
6	5	7	5	3
5	1	-2	-6	-8
-3	-4	3	10	8
-4	-6	-6	-3	-2

Gradient Magnitude				
46	323	314	40	43
46	323	315	37	45
41	323	314	33	47
35	324	317	34	43
32	324	324	35	38

(b)

Figure 6-1: Example intensity gradient (a) with edge running in vertical direction, and (b) example resulting gradient computation

With the magnitude and direction of the partial derivatives known, the edge points can next be separated from the non-edge points. This information is used to adjudicate points within the field of gradient values that may be an actual edge, with the objective being to arrive at an edge that is exactly 1 pixel or 1 data point wide. The first step here is to organize the gradient values according to direction, such that they are grouped into “bins”, [0, 45°, 90°, 135°].

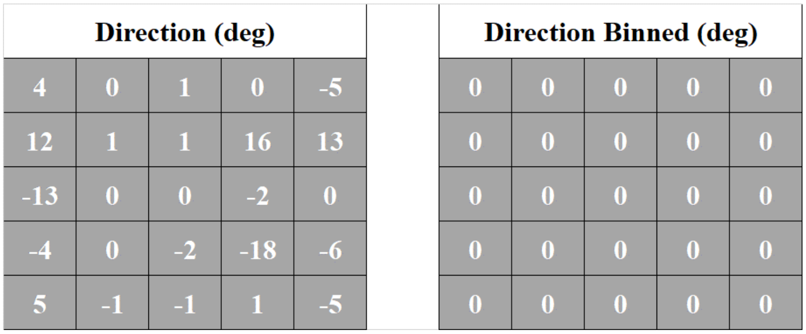

Direction (deg)

4	0	1	0	-5
12	1	1	16	13
-13	0	0	-2	0
-4	0	-2	-18	-6
5	-1	-1	1	-5

Direction Binned (deg)

0	0	0	0	0
0	0	0	0	0
0	0	0	0	0
0	0	0	0	0
0	0	0	0	0

Figure 6-2: Gradient direction calculations (left) and direction values binned to the nearest 45° increment (right)

With the directions known, each given gradient value can then be compared to the 8 data points that surround it. More specifically, each point is compared to its neighboring points only in the direction of the gradient. For instance, if the direction is determined to be closest to the 45° direction, the data point is compared to the point to its upper right and lower left. The value at the given data point is then taken as the maximum of the 3 points along that direction. In the current example, the direction values are all 0°, thus each gradient value is only compared to its left or right neighbor.

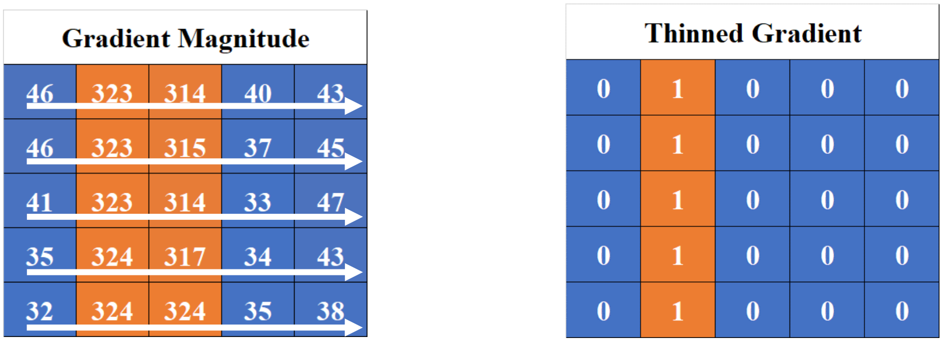

Gradient Magnitude

46	323	314	40	43
46	323	315	37	45
41	323	314	33	47
35	324	317	34	43
32	324	324	35	38

Thinned Gradient

0	1	0	0	0
0	1	0	0	0
0	1	0	0	0
0	1	0	0	0
0	1	0	0	0

Figure 6-3: Original gradient values (left) with arrows showing the general direction along which maximum values are determined, resulting thinned matrix (right)

The resulting intensity gradient field further isolates the true edge locations. By separating out these possible edge points, it will be guaranteed that each candidate edge is only one pixel wide, or in the case of the displacement field, the edge is only one output point wide. This procedure is known as non-maximum suppression (NMS).

The last step in the Canny edge detection algorithm is thresholding. The points above a certain threshold are identified as edge points and the points below a separate, lower threshold value are excluded from the edge point group. The points in between the threshold values are identified as candidate edge points and are tested to determine if they are connected to edge points that were above the higher threshold value. If they are connected to the points that have magnitudes above the threshold, they are included in the edge point group. These threshold values are determined through trial and error and tend to be problem specific. More recently, it has been suggested [123] that an adaptive thresholding method may be advantageous. In images where there may be a wide range of edge features, one set of upper and lower threshold values might be inadequate to properly categorize the gradient values across the entire image. With adaptive thresholding, not only are the gradient values considered but the overall distribution of gradient values is binned in a histogram. This can be done locally for each pixel or data point in the field of values to adjust the threshold values depending on the local characteristics of the gradient results.

6.3 Specific adaptations required for crack tip location identification

As previously stated in the introduction of the present chapter, the crack tip identification problem carries many similarities to the edge detection problems in image processing. The general concept is that regions within the displacement field with steep discontinuities must be identified as potential crack faces and within those potential crack faces, the most likely termination point must be identified. In the most basic implementation, the Canny edge detection method described in the previous section can be implemented by simply scaling the displacement field to the equivalent of a gray-scale image. Once the displacement field is in the gray-scale format, the algorithm can be implemented directly. However, several modifications to the algorithm are necessary to improve its performance to meet the goals of the present problem. For the crack tip identification problem in the present work, the following methodology is proposed and will be detailed in the following sections:

- Decompose image space into two domains on each side of crack path and perform DIC
- Perform Gaussian smoothing
- Calculate partial derivatives and their magnitudes and directions at each output point
- Perform non-maximum suppression
- Compute histogram and far-field component of gradient to remove spurious edges
- Perform regression to determine crack tip

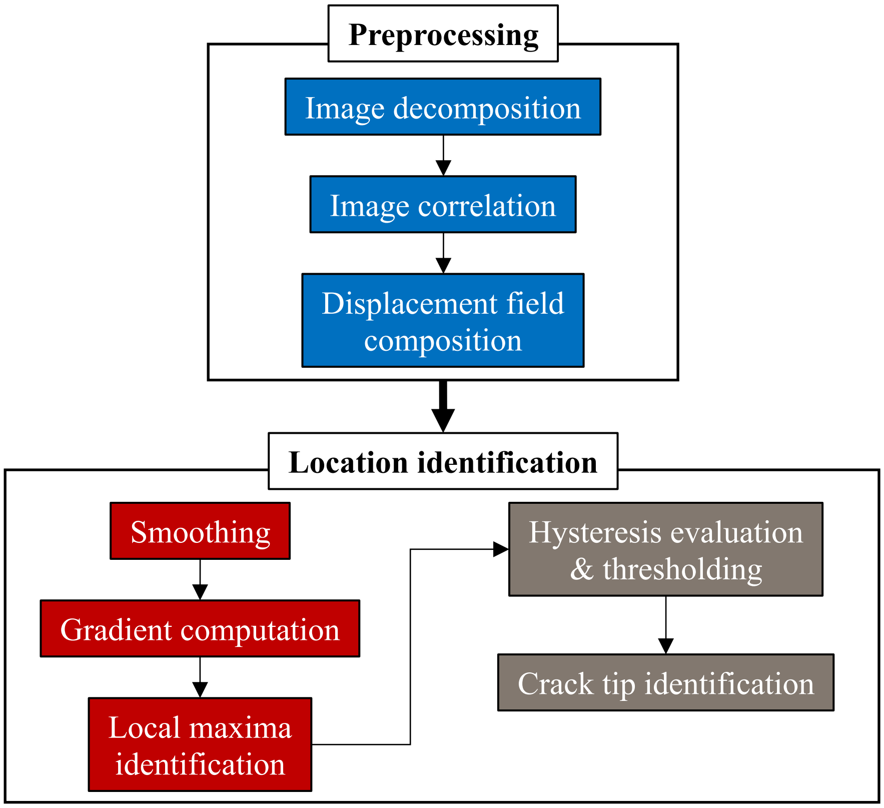

Figure 6-4: Workflow for the proposed crack tip detection/location procedure

6.3.1 Displacement field decomposition

The first step in the proposed procedure is to identify the edge of the fractured specimen (the crack path) and use it to split the image space into two separate domains. The path is identified by first selecting an image that contains the fully propagated crack. This image is taken preferably at a time instant well after the crack has fully propagated such that the displacement field primarily consists of rigid body motion of the failed specimen halves (Figure 6-5). The selected image is manually marked with a series of points along one of the crack faces and then imported into MATLAB®.

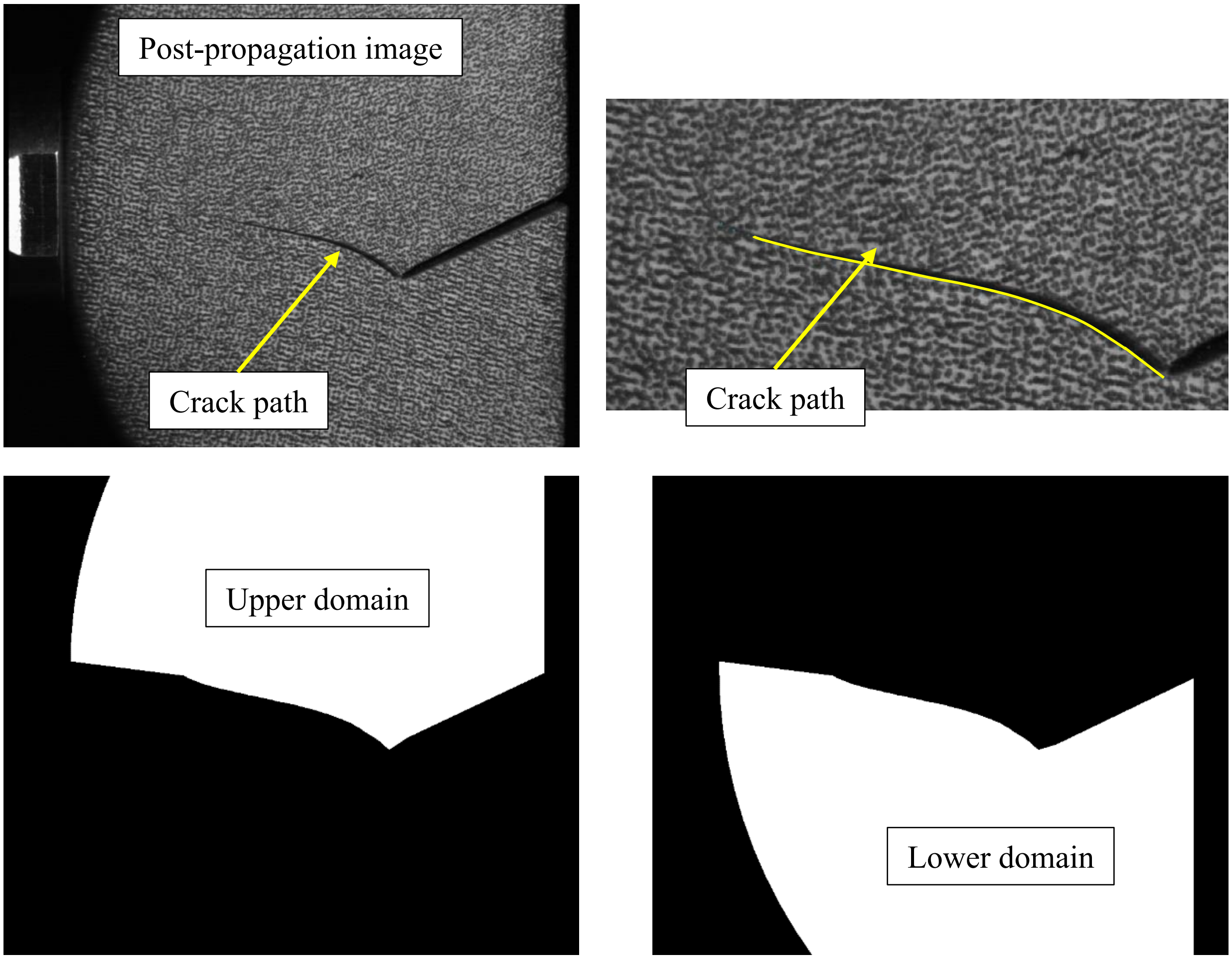

Figure 6-5: Illustration of crack path from failed specimen and decomposition of image space to create masks of the upper domain and lower domain

Once in MATLAB®, the points along the manually marked edge are extracted. Multiple points along the specimen edge or crack face are extracted from an image captured prior to loading and compared with the same edge points extracted from an image captured after full separation. The rigid body motion is calculated using the two images, one from prior to loading state and the second after separation/fracture. It is assumed that the specimen deformation is dominated by recoverable elastic deformation. The calculated rigid body motion (displacement and rotation) is used to transform the crack edge from the deformed coordinate system back into the undeformed coordinate system to remove the rigid body motion. The edge in the undeformed coordinate system is then used to create the boundary between say the upper domain and the lower domain for the image correlation procedure as illustrated in Figure 6-6. This results in an upper domain mask (all pixels outside of the upper domain are removed from the image correlation procedure) and a lower domain mask (all pixels outside the lower domain are removed from the image correlation procedure).

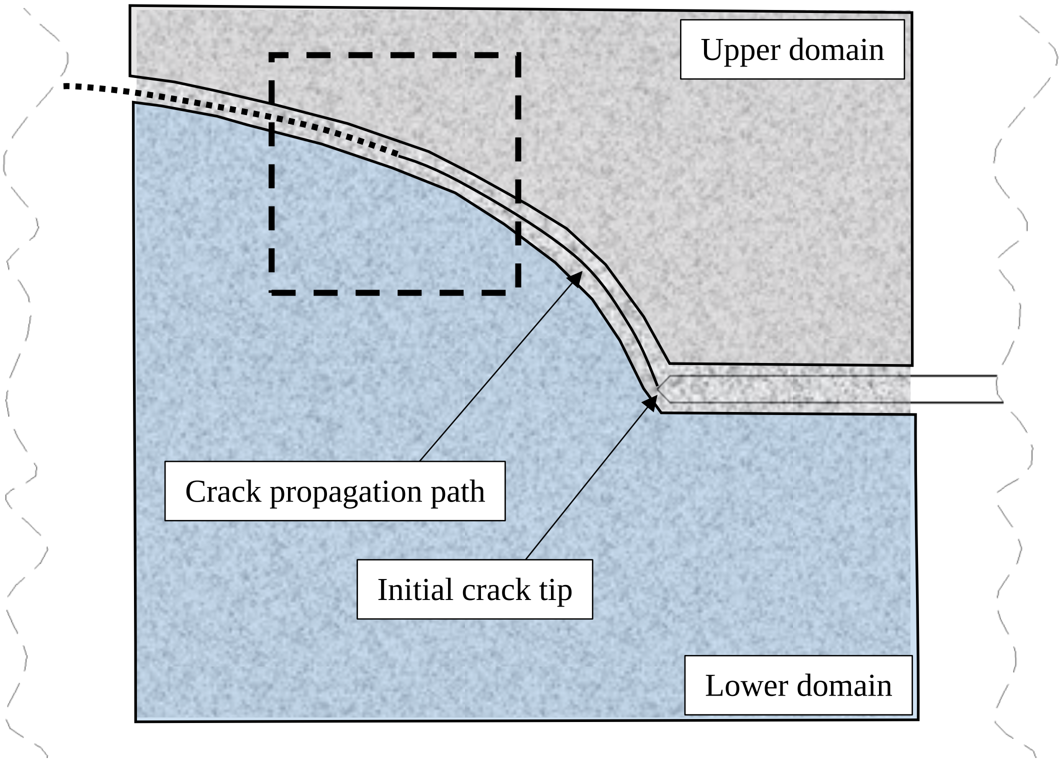

Figure 6-6: Upper and lower image correlation domains as they relate to the position of the crack tip and crack propagation path

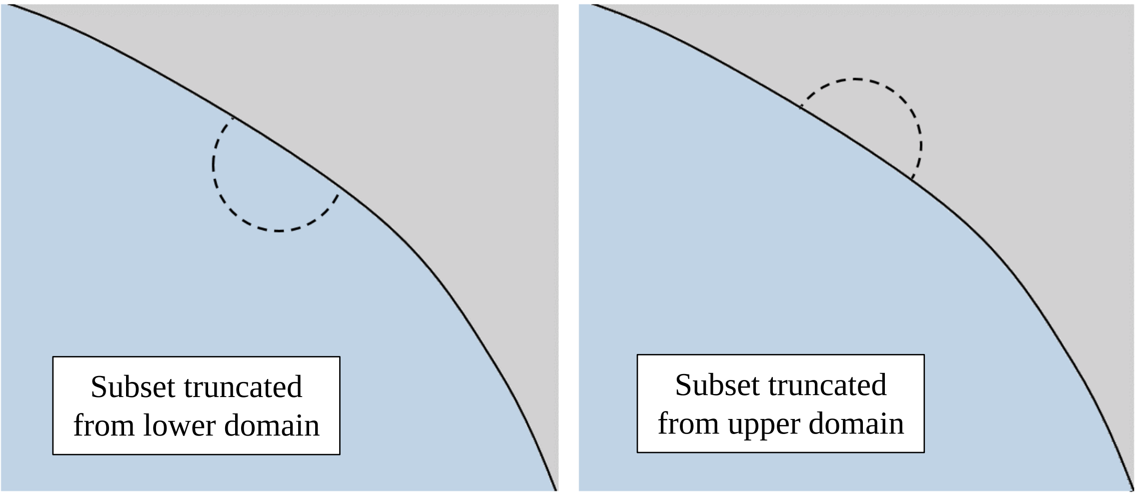

Figure 6-7: Subset truncation illustration showing lower domain subset truncated at boundary (left) and upper domain subset truncated at boundary (right)

By splitting the image into two separate domains (one domain on each side of the failure surface), the image correlation process can utilize subset truncation. Subset truncation is a procedure which allows correlation to be performed on partial subsets. For points within the image that are close to the edge, truncating subsets enables the ability to acquire displacement data to within a few pixels of the edge. As the crack propagates across the specimen, each individual domain remains continuous and subsets are not allowed to cross the boundary between the two domains. This prevents issues that occur when a subset is allowed to cross the boundary. In those situations, pixels from both domains are considered in the correlation and either correlation quality degrades or the displacement becomes smeared or averaged across the boundary/edge (or the crack in the present work). The truncation avoids these two forms of data degradation.

After the images have been processed, the two domains of displacement data are stitched back together. Since the masks for the decomposed domains were created in the same original image space and the same images were used for the correlation process, the resulting two displacement field sets also exist in the same image reference space. That is, each data array has numeric values for each subset within its own domain and is zero padded in areas outside of its domain. Thus, they can thus be stitched together via a simple matrix operation. The two displacement fields are imported as 2-dimensional arrays into MATLAB® and added together resulting in a single 2-dimensional array consisting of a continuous field of data ahead of the crack tip and a discontinuous field of data behind the crack tip for any given point in the crack tip propagation history. It should be noted that a minimal amount of noise is present ahead of the crack tip that will be addressed in later sections.

6.3.2 Displacement field gradient estimation

The resulting displacement field is then normalized to create a normalized displacement field, *I(x,y)*, associated with each component of displacement such that the maximum value is 1 and the minimum value is 0. This is calculated as follows:

$$I(x,y) = \frac{\delta(x,y) - \min\{\delta(x,y)\}}{\max\{\delta(x,y)\} - \min\{\delta(x,y)\}} \qquad [6\text{-}9]$$

where δ can be the taken as the global x-direction displacement (u), the global y-direction displacement (v), or the magnitude of the displacement ($\sqrt{u^2+v^2}$). The displacement components can be given equal weight in subsequent analysis steps or could potentially be weighted towards the more dominant displacement component such that the gradient computations are more pronounced. An example of a resulting intensity field is shown in Figure 6-8 for one of the sets of displacement data for a homogeneous specimen just after crack initiation.

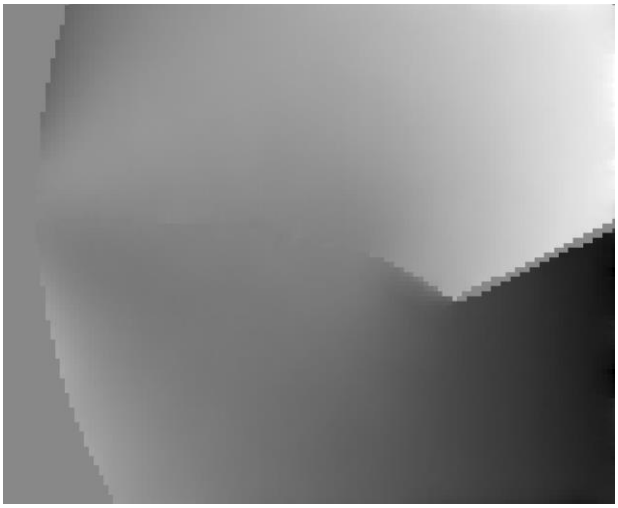

Figure 6-8: Intensity image of displacement field computed by normalizing displacement field data

The normalized intensity field is then convolved with the Gaussian filtering kernel defined in Equation [6-4], resulting in a smoothed version of the normalized displacement field. The intensity gradients are then computed from the filtered intensity field using 2-dimensional convolution of the filtered intensity values with the kernels from Equations [6-5] and [6-6]. A contour plot of the vertical direction gradients (computed by convolving I with K_y) is shown in Figure 6-9.

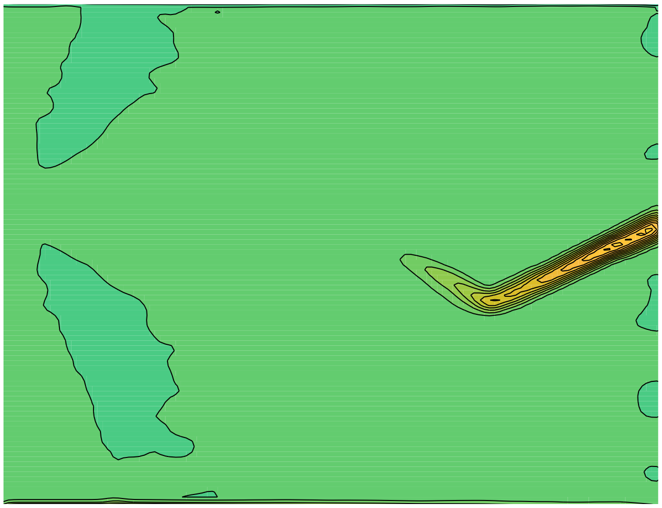

Figure 6-9: Vertical gradients of intensity field

As demonstrated in the figure, the contour lines become very tightly grouped in the vicinity of the crack. Away from the suspected crack tip, the specimen edges also show up as moderately high gradients. On the specimen surface in areas away from the crack tip, the gradients are relatively low. This computation serves as a basis for positively identifying the crack tip in the subsequent steps.

6.3.3 Crack edge estimation

The magnitude of the gradient results and the directions are computed using Equations [6-7] and [6-8] respectively. The non-maximum suppression technique described earlier can then be used to thin the edge down with the objective being to obtain an edge that is a single data point wide. Figure 6-10 illustrates the results of this step. For the present work, an additional step is taken at this point to filter out points that are known to not lie in close proximity to the edge. This helps remove potential edge candidates that are away from the propagating crack.

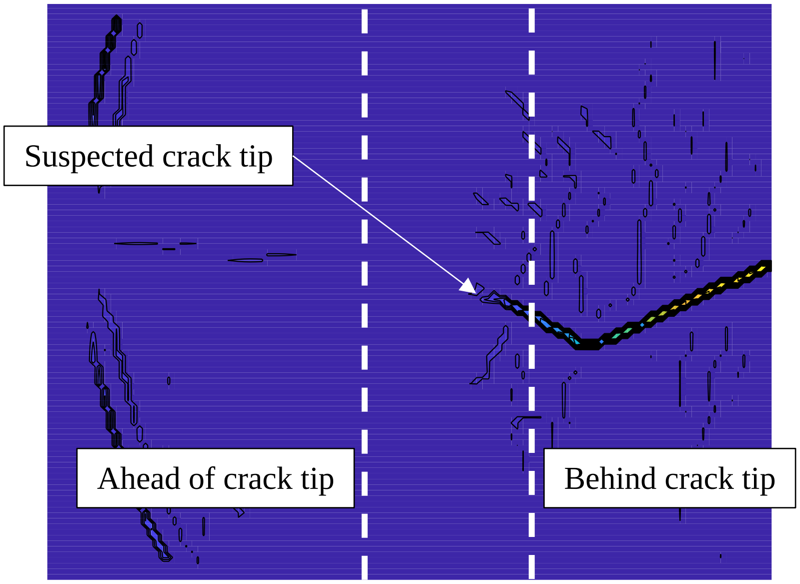

Figure 6-10: Intensity field gradients after non-maximum suppression

6.3.4 Thresholding

The final step is to identify the most likely position of the crack tip within this subset of candidate points of the edge. The typical method in image processing problems is to use an approach referred to as adaptive thresholding similar to what has been proposed by Rong in [123]. This approach takes a histogram of the field of partial derivative values and selects a threshold value that results in a certain percentage of output data points occurring above the threshold and a certain percentage of points falling below the threshold. This has been shown to work well on certain image processing problems, however, it is still subjective, and does not appear to be sufficiently robust for the crack tip identification problem at hand. Thus, a more robust approach was desired. For the present implementation, a histogram of the partial derivative is first taken, and used to compute the distribution of the partial derivative values. An example histogram is shown in Figure 6-11 from mixed-mode example problem.

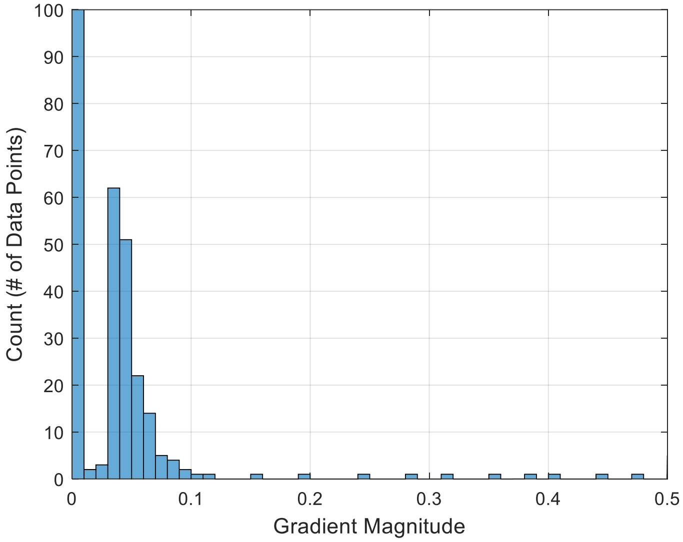

Figure 6-11: Example histogram of gradient data showing pronounced secondary peak due to noise in the gradient field ahead of the crack tip

One interesting feature of the histogram is that it has a distinctive peak at a magnitude of 0 and a secondary distinctive peak at another non-zero value. The first peak occurs near 0 and accounts for the majority of the data in the partial derivative field where the strain in the material is relatively low (as compared to the discontinuous crack faces). This has been truncated in the figure to more clearly see the secondary peak. This secondary peak is attributed to noise in the partial derivative field and ahead of the crack tip and also away from the gradients associated with the crack faces which are much higher in magnitude. The second peak, centered at a magnitude of 0.04 for the example plotted here, is relatively subtle, but can be used for filtering out additional unwanted edge candidates. For the present implementation, this secondary peak was used to separate spurious far-field data from the location of the crack tip. There is relatively high confidence that partial derivative values that are higher than this secondary peak occur on the crack faces behind the crack tip. A series of values were selected that were known to be slightly higher than this secondary peak and used for tracking the crack tip position. The thresholding procedure is adaptive in the sense that the value of the far field noise can fluctuate as the displacements evolve and can ensure that the points that are being tracked are above this noise threshold. The crack tip is then taken as an approximation of where these values that are slightly higher than the far-field noise regress towards a value slightly higher than this secondary value. Since there is still uncertainty as to whether or not the crack tip is precisely located at this location, the positional error can be estimated based on the initial data sets where the crack tip is stationary and the physical crack tip is known. Locations of the propagating crack tip can be corrected for this error since it is known with relatively good confidence.

6.4 Verification of position identification for mode I problem

A finite element model was utilized to study the performance of the edge detection algorithm for specific application to the crack tip problem and establish confidence in the algorithm's performance. The intent of the verification is to ensure that the methodology correctly meets the objectives of positively identifying the crack tip where the crack tip is known a priori since it is manually inserted into each of the finite element models. Verifying the performance of the methodology provides an opportunity to investigate the confidence with which the crack tip can be located. Additionally, it establishes the sensitivity to certain parameters and assumptions inherent to the procedure, namely the resolution of the experimental displacement data. The verification procedure also enables the investigation of the ability of the algorithm to perform on more challenging fracture problems such as those involving higher modulus materials and lower critical fracture toughness where experimentally measured displacements are much lower in magnitude.

The proposed verification process is to create a set of displacement fields to test the methodology. The algorithm implemented in the present work is primarily developed and scripted to work with data structures analogous to those found in image processing problems. More specifically, for the present problem, displacement data at uniformly spaced points in an orthogonal coordinate system.

6.4.1 Three-point bend finite element model

A simple three-point bending model with an edge crack, loaded in pure mode I was used for the first test model. This is a relatively straightforward model for testing purposes due to the known, self-similar crack path, and the fact that one of the displacement field components accounts for a majority of the crack face motion. The beam dimensions were 38 mm height, 203 mm length, and 152 mm support span. The length of the edge crack was varied from 12.7 mm to 25.4 mm in 2.5 mm increments. The boundary conditions and displacement field from the finite element model are illustrated in Figure 6-12. The first case used an elastic modulus of 2.2 GPa, similar to the modulus of the material in the present work and the applied load in the model was scaled to a target stress intensity factor of 1.1 MPa-√m.

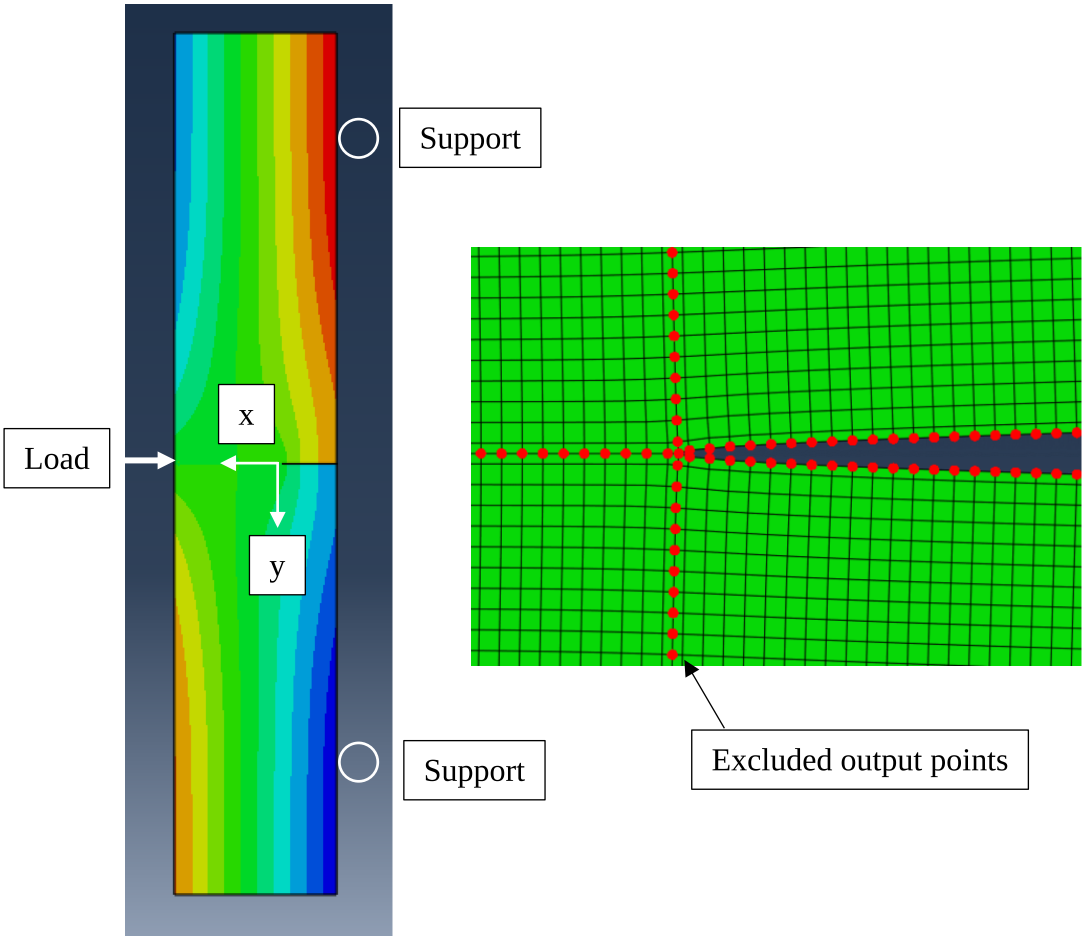

Figure 6-12: Edge detection verification finite element model and crack tip mesh

For this first test problem, the mesh around the crack tip was structured to artificially mimic the positioning of the output points from the experimentally measured digital image correlation data. As shown in the figure, the nodal output points along the crack faces and directly ahead of the crack tip (highlighted in red) are ignored in the edge detection algorithm since those points would not physically be reported in the digital image correlation output data.

6.4.2 Three-point bend crack tip location comparisons

For each analysis run, the crack edge was manually extended, thus manually repositioning the crack tip. The displacement field from the finite element model was then extracted using a python script and subsequently read into MATLAB® in the same data format as the digital image correlation results would typically be in. The gradients computed from the edge detection algorithm visually provide a very concise estimation of the crack location as shown in Figure 6-13.

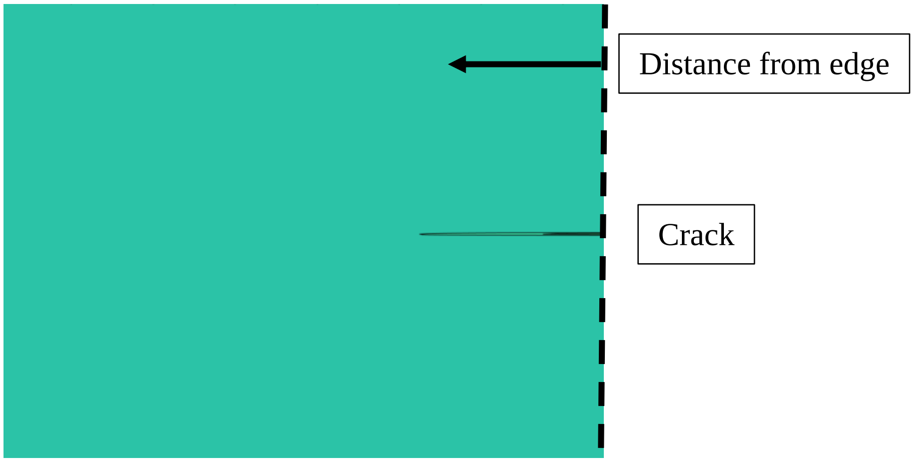

Figure 6-13: Vertical gradient of displacement field for 12.7 mm crack length

The maximum gradient value is extracted at each horizontal position in the displacement field. Behind the crack tip, the gradient is significant due to the discontinuity, whereas ahead of the crack tip, the gradient approaches some constant value. These values are plotted for each successive crack tip position in Figure 6-14.

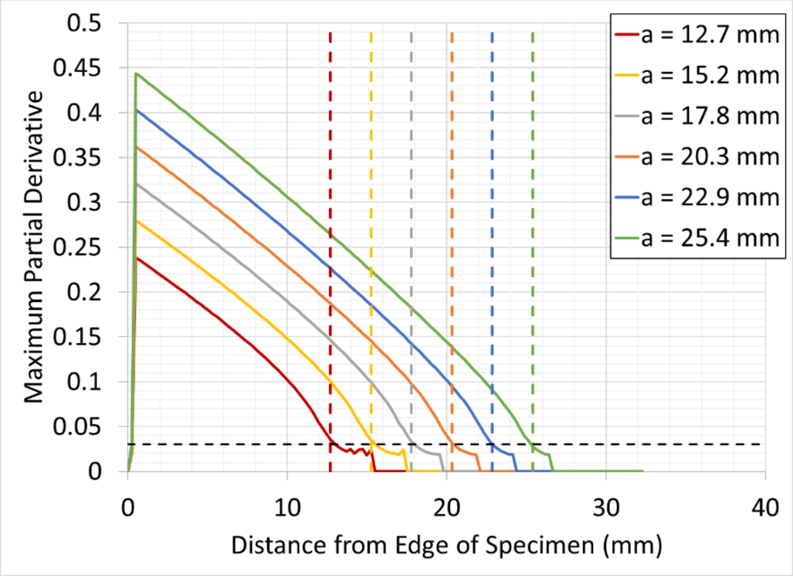

Figure 6-14: Maximum intensity gradient value

The vertical, dashed lines in Figure 6-14 are plotted for reference to show the position of the actual crack tip. The black, horizontal dashed line is approximately aligned to the point on the gradient plot where the actual crack tip resides. As shown in the figure, it is evident that the crack tip position occurs generally in the same location relative to the far field gradient ahead of the crack tip. For this simple test case, it was relatively straightforward to identify a threshold value and track the threshold value as the crack tip propagates in space thus using the simplest implementation of the Canny edge detector. For this test problem, the estimated crack lengths from the edge detector are tabulated in Table 6-1. The estimated values agree well with the actual crack tip positions with the amount of error decreasing with crack length, implying that the error is a constant value irrespective of crack length.

Table 6-1: Edge detection algorithm accuracy study on simple mode I crack problem

Position	Actual Crack Length (mm)	Estimated Crack Length (mm)	Difference
1	12.70	13.24	4.3%
2	15.20	15.73	3.5%
3	17.80	18.20	2.2%
4	20.30	20.64	1.7%
5	22.90	23.05	0.7%
6	25.40	25.45	0.2%

6.5 Verification of position identification for mixed-mode problem

The three-point bending geometry in the last section demonstrates the feasibility of the general procedure and workflow of the edge detection algorithm. However, the mode I behavior produces a relatively simple displacement field around the crack tip. Additionally, the algorithm performs well even by simply thresholding the gradient results (partial derivatives of displacement in each direction) manually. To demonstrate the full utility of the methodology, it is necessary to investigate its use on more complex geometries and more complex displacement fields. For this next level of verification, a semi-circular beam geometry was selected. First, this geometry can be configured for a full range of mode mixities [124], and second, the geometry creates a crack propagation path that is not self-similar. This part of the verification was divided into two key sections. First, a finite element model was setup to provide simulated displacement fields. From an experimentally failed test specimen, a representative crack path was extracted so that different crack tip locations along that crack path can be simulated using the model. Second, an inverse FEM mapping tool was developed and utilized to transform the simulated displacement fields into the same format as the typical DIC output displacement fields in the form of a two-dimensional array of vertical displacements and another two-dimensional array of horizontal displacements output on a uniformly spaced grid of output points. This mapper was necessary because the geometry of the propagating crack path does not lend itself to creating a structured mesh as in the mode I case.

6.5.1 SCB finite element model

The specimen section of the finite element model is shown in Figure 6-15. The main difference in this specific model and the model documented in 3.1.2 is the crack path. The coordinates of the crack path from a failed specimen were extracted manually using a script in MATLAB®. The coordinates of the crack path were imported into the finite element software to form a partition along the physical path.

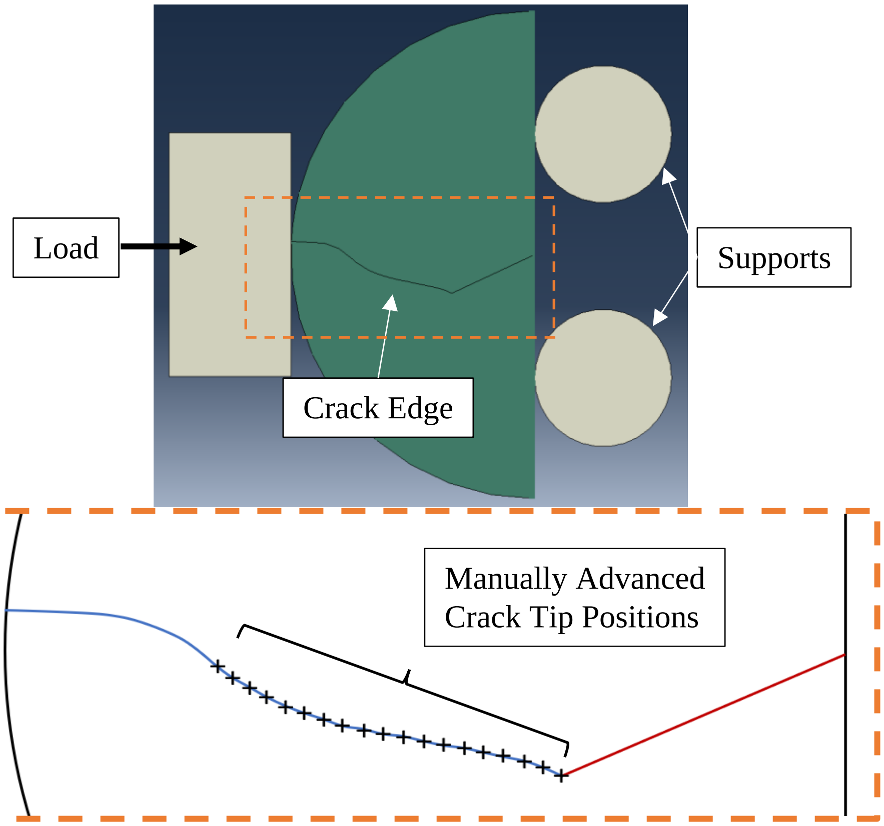

Figure 6-15: Specimen section of finite element model

A series of analyses were then performed by manually advancing the crack tip incrementally. This provided a series of displacement field results representing a range of mode mixities and a range of orientations to test out the edge detection algorithm.

6.5.2 Mapping from FE-space into gridded space

The finite element model does not create output on a uniformly spaced grid of points; however, the proposed crack tip location identification technique is formulated to operate on uniformly spaced output data. Because of specimen geometries, crack orientations, crack propagation paths, etc., the elements found within the FE mesh for each crack propagation step can have a variety of shapes and thus the nodal displacement data is not able to be output on a uniformly spaced grid. To that end, an inverse FE mapping technique was implemented in MATLAB® to map the output data from the finite element model (nodal displacements in the *x*- and *y*-directions). This concept has been shown to be a viable method for mapping between two coordinate spaces by several authors including Refs. [125] and [126]. An example of the dissimilarity between the two data point locations is shown in Figure 6-16. A set of *x*- and *y*-coordinates on a uniform grid was created at the desired "output" point locations, as shown in red. The source model elements and nodes are shown in black. For the mapper in the current effort, the input file for the source finite element model contains all of the node numbers, nodal coordinates, and element connectivity.

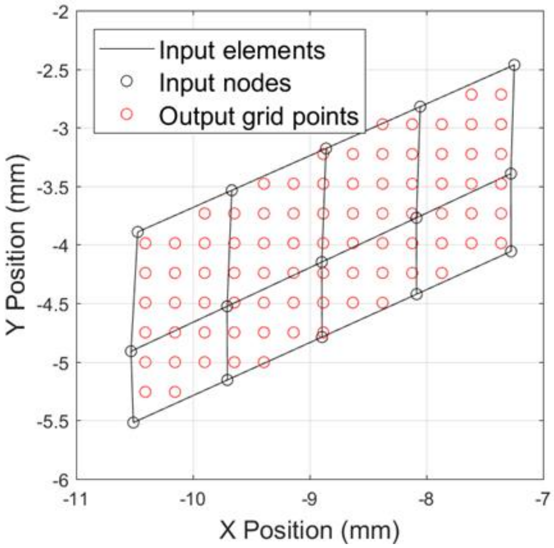

Figure 6-16: Example dissimilarity between simulated data and gridded data near crack faces with slightly distorted elements to illustrate nonuniform nature of FE mesh

For each of the 4-noded elements in the finite element model, the mapper locates the grid points that reside within its boundaries using the MATLAB® function, *inpolygon*. Since the element shape can be in the form of any four-sided polygon, potentially distorted, a numerical routine was then used to determine the parametric coordinates of each of the destination grid points within the space of their parent element in the original model. The relationship between the global space and the parametric space is illustrated in Figure 6-17 with an example map-to point shown by the dark-shaded point, x_p.

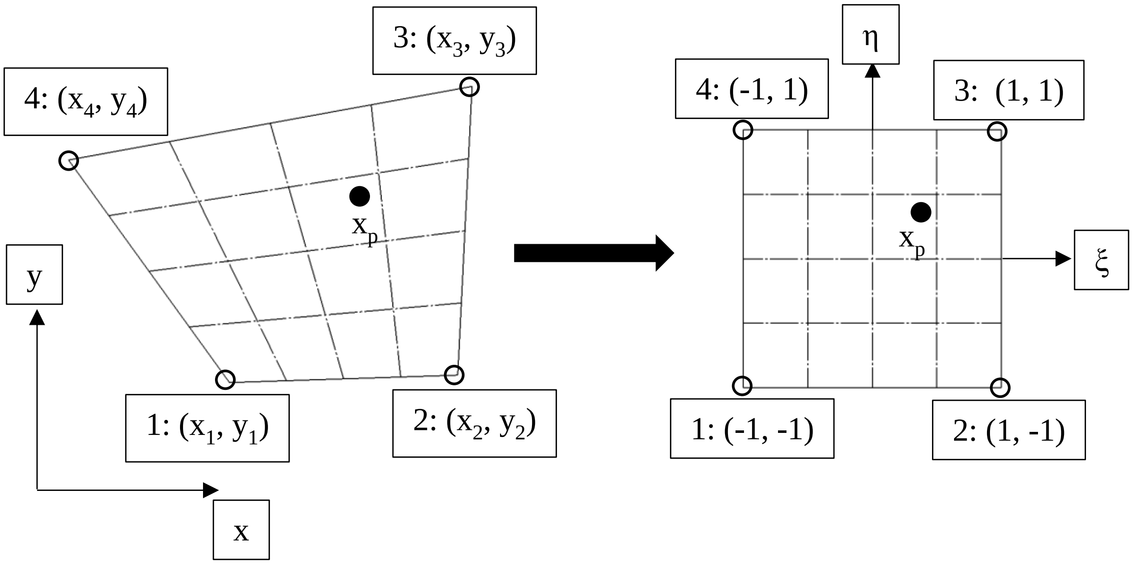

Figure 6-17: Illustration of mapping from global coordinate space (left) to parametric coordinate space (right)

The global coordinate of any point within the boundary of the element is a function of the parametric equation, *N*, and the global coordinates of the nodes that define the boundary of the polygon. For a 4-noded quadrilateral element, the global coordinate of a point, x_p and y_p,, is defined as:

$$(x_p; y_p) = \sum_{i=1}^{4} N_i(\xi, \eta)\,(x_i; y_i) \qquad [6\text{-}10]$$

where *i* is the node number, x_i and y_i are the global coordinates of the *i*-th node and ξ and η are the parametric coordinates.

The parametric equations, N, for a quadrilateral element were derived in [127] and are defined as:

$$
\begin{aligned}
N_1 &= \frac{1}{4}(1-\xi)(1-\eta) \\
N_2 &= \frac{1}{4}(1+\xi)(1-\eta) \\
N_3 &= \frac{1}{4}(1+\xi)(1+\eta) \\
N_4 &= \frac{1}{4}(1-\xi)(1+\eta)
\end{aligned}
\tag{6-11}
$$

The parametric coordinates, ξ and η, for the target "map-to" point can be located using an iterative procedure. For a given iteration, the parametric space is split up into a 5 × 5 grid of points. The values of ξ and η, are used to calculate the resulting global coordinates at each of these points on the 5 × 5 grid. The point within the grid that results in coordinates that have the shortest Euclidean distance to the actual point of interest is used as the initial guess of the next iteration. That initial guess becomes the center point of a smaller 5 × 5 grid that is part of a subdivision of the grid in the previous iteration. This iterative process continues to subdivide the parametric space into smaller and smaller 5 × 5 grids until a result is found that matches the coordinates of the desired point within an acceptable tolerance. For the present work, the algorithm was required to determine the values of ξ and η that resulted in an error between the calculated coordinates and the actual coordinates of less than 1e-6. While there are more efficient numerical techniques for this part of the process, this approach converges reasonably quickly, within 6-8 iterations and is relatively inexpensive computationally. The convergence rate is predictable as it is directly related to the original element edge length, L. The error, e, after iteration, n, is given by $e = \frac{L}{(s-1)^n}$ for a grid size, $s = 5$. The approach can suffer some difficulty when the elements are significantly distorted. However, for the present work, the mesh was controlled sufficiently, and significant element distortions were avoided.

For a given point of interest in the grid that is being mapped to, once the parametric coordinates are known with an acceptable accuracy, any desirable field quantities can then be calculated. For this work, the field quantities of interest, vertical and horizontal direction displacements, the following relationships are used to compute those values:

$$(u_p; v_p) = \sum_{i=1}^{4} N_i(\xi, \eta)\,(u_i; v_i) \tag{6-12}$$

This method is particularly advantageous because it avoids issues with averaging or smoothing around the crack tip or across the crack faces in the source data. This is largely because the target grid points are associated with elements from the output data. The nodal connectivity for the source elements is inherited from the source finite element model. Since the original mesh is created without elements spanning the crack tip or bridging across the crack faces, no averaging occurs due to target nodes on one side of the crack face being influenced by displacements of nodes on the opposing side of the crack. The method is similar to the bilinear method proposed in section 4.4.2, however, the bilinear method, as documented, only works for mapping from a set of points that are arranged in rectangular grid. However, it should be noted that in the case of a set of points that are arranged in a rectangular fashion, this general method simplifies to bilinear interpolation.

6.5.3 Mapping checks

The mapping scripts were tested to ensure that the simulated data (from the FEM) is being properly represented in the evenly spaced grid output data used for testing the robustness of the edge detection algorithm. A comparison is shown in Figure 6-18.

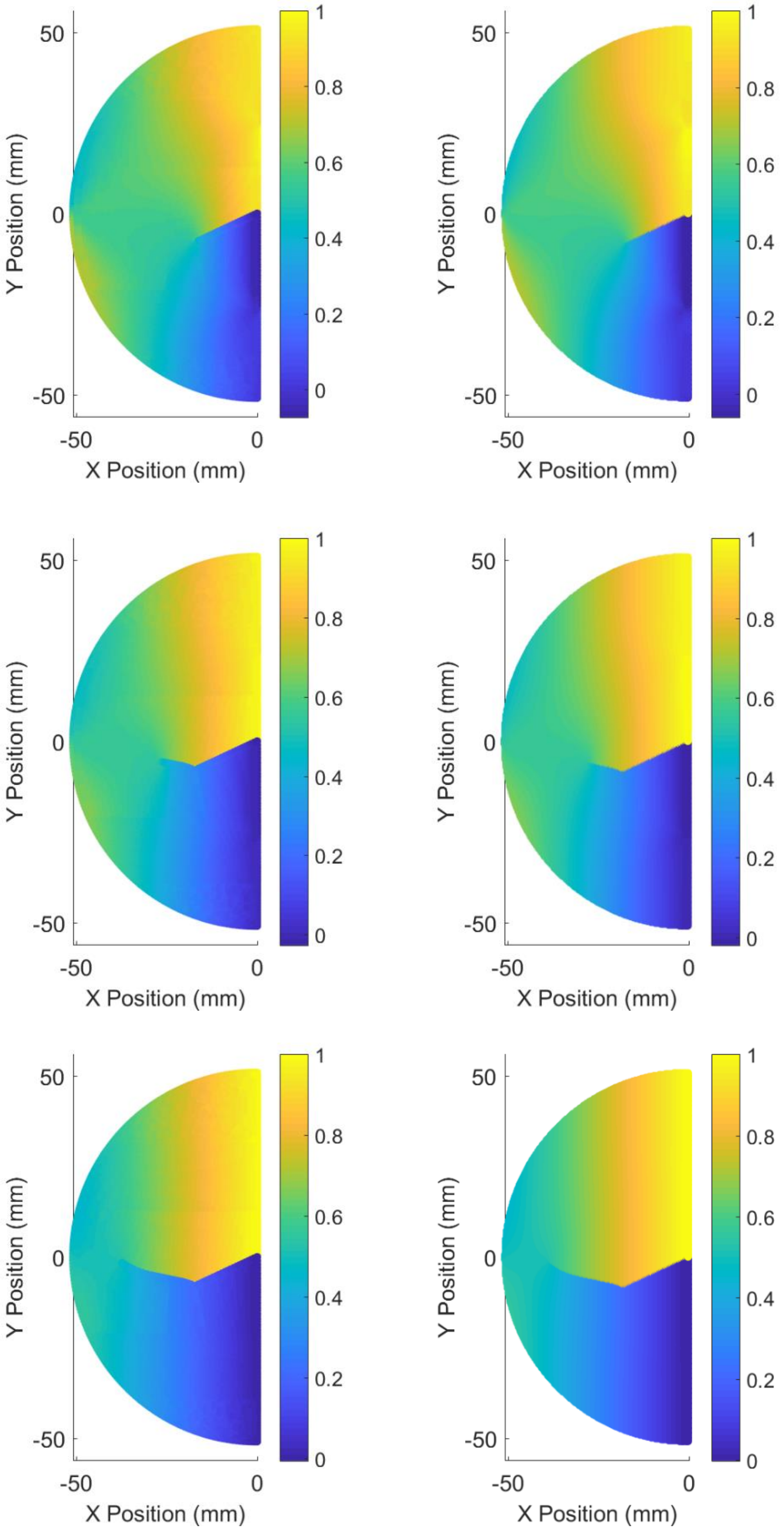

Figure 6-18: Source normalized displacements from simulation (left) compared with mapped normalized displacements (right) for three different crack tip positions

The two displacement fields match in terms of magnitude and distribution. The crack faces appear to be properly represented in the mapped displacement field.

6.5.4 Prediction comparisons

The simulated displacement fields from the SCB model were used to further test the edge detection algorithm performance for several specific scenarios to demonstrate its full utility. This test case was a mixed-mode fracture case where the crack initiates under shear-dominated conditions and transitions to tension-dominated growth. This is an excellent verification case because the crack face motion is initially dominated by in-plane sliding between the two crack flanks at the initial crack tip location, but as the crack propagates, it transitions to being dominated by opening between the two. The Sobel gradient operator is generalized to compute partial derivatives in both directions, so this case exercises the full range of possible partial derivatives and directions.

This part of the process is illustrated in Figure 6-19. The *x*- and *y*-positions are the planar coordinates in the displacement field space, and the *z*-position is the magnitude of the gradient with the origin of the coordinate system located at the original crack tip. A projection of the specimen boundaries is also plotted for reference. This figure shows how the partial derivatives are much higher at the furthest locations from the crack tip location and they progressively approach 0 at the crack tip. However, due to noise, the thresholding procedure is used to track a point at a small, but known, distance away from the crack tip. The gradient values are separately plotted in three-dimensional space for a series of crack tip locations to illustrate the evolution of the partial derivative computations as the crack propagates.

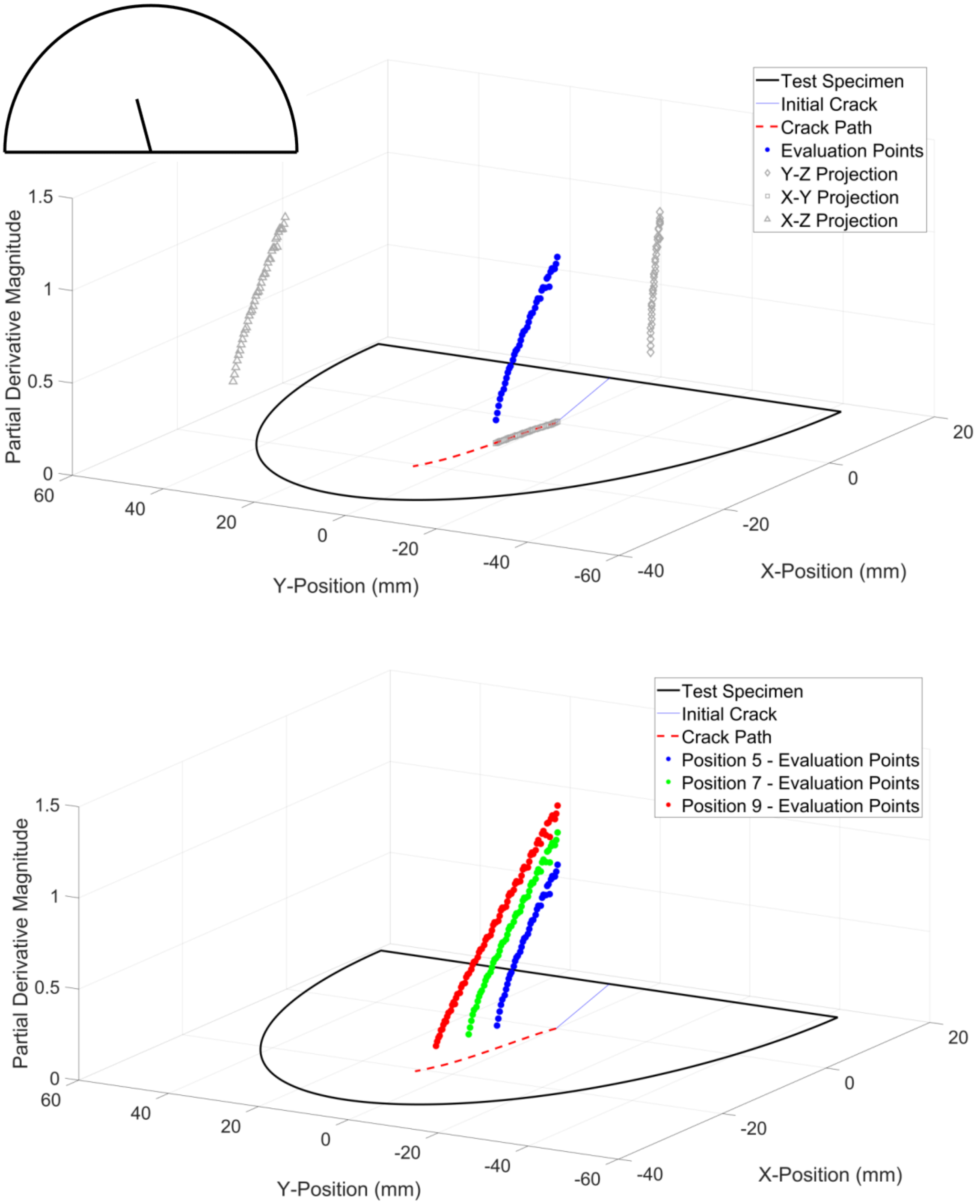

Figure 6-19: Field of gradient values illustrated in 3D space for single crack tip location

This figure shows how the gradients are much higher at the furthest locations from the crack tip location and they progressively approach 0 at the crack tip. However, due to noise, the thresholding procedure is used to track a point at a small, but known, distance away from the crack tip.

Using the results from this set of simulations, a series of test cases were run to examine the behavior of the algorithm and determine relationships between algorithm parameters and their ability to locate the crack tip. This work was split into four separate studies: first to study the thresholding value, second to determine the effect of subset/grid spacing, third to determine the effect of the Gaussian blur kernel size, and forth to study the effect of the Gaussian smoothing parameter. The operator has flexibility in choosing these parameters. The study parameters are summarized in Table 6-2.

Table 6-2: Edge detection algorithm parameters

Variable	Case Number	Gaussian Filter Kernel Size	Gaussian Filter Sigma Value	Threshold Value	Grid Spacing (mm)
Threshold	1	5 x 5	1.0	0.05	0.250
	2	5 x 5	1.0	0.10	0.250
	3	5 x 5	1.0	0.20	0.250
Grid Spacing	4	5 x 5	1.0	0.10	0.125
	2	5 x 5	1.0	0.10	0.250
	5	5 x 5	1.0	0.10	0.500
Kernel Size	2	5 x 5	1.0	0.10	0.250
	6	3 x 3	1.0	0.10	0.250
	7	7 x 7	1.0	0.10	0.250
Sigma Value	8	5 x 5	0.5	0.10	0.125
	2	5 x 5	1.0	0.10	0.250
	9	5 x 5	2.0	0.10	0.500

The range of threshold values was based on an investigation of the distribution of gradient magnitudes in the image (see Figure 6-11 for reference). The range of sub-image/facet spacing values were chosen based on the desired subset spacing for the DIC data extraction.

With respect to the Gaussian filter parameters, three plausible values were chosen based on several open source example problems. The comparison of crack coordinate position is shown in Figure 6-20. Figure 6-20(a) and (b) show the effects of threshold value and subset/grid spacing whereas Figure 6-20(c) and (d) show the effects of kernel size and sigma values.

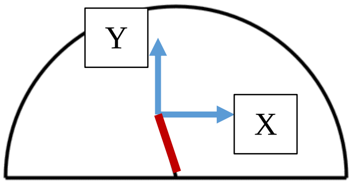

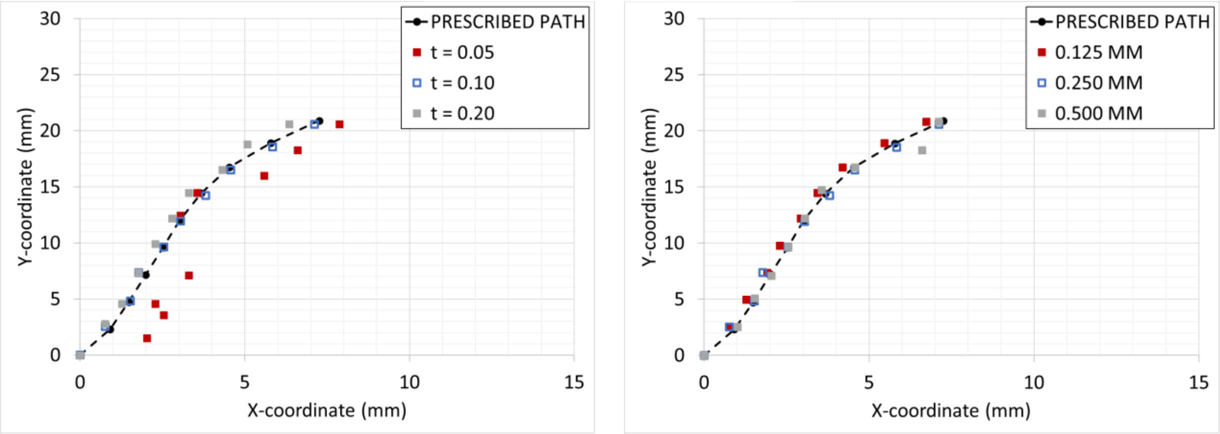

(a) Threshold Value (b) Grid Spacing

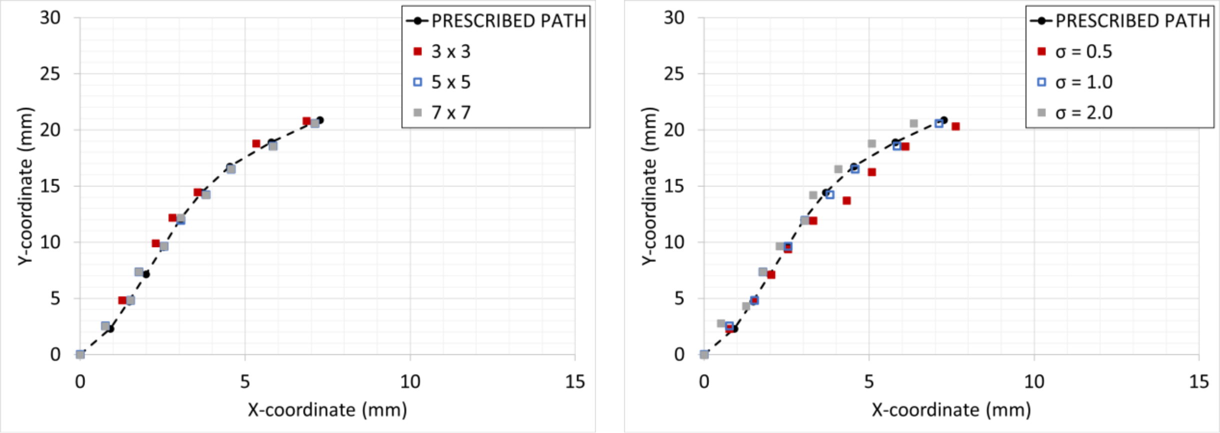

(c) Gaussian Kernel Size (d) Gaussian Blur Parameter

Figure 6-20: Effect of edge detection algorithm parameters on crack tip location. (Note that X and Y represent spatial coordinates, different from the crack tip coordinates, x and y.)

Note that the values are plotted in terms of the static X-Y coordinate system centered at the initial crack tip and as illustrated in the inset in Figure 6-20 which is different from the instantaneous crack tip coordinate system (x, y) reported elsewhere. These plots in the X-Y coordinate system illustrate that generally the prescribed crack path is the shortest distance and the fact that the estimated crack tip points oscillate between one side and the other of the actual path, the edge detection algorithm tends to overpredict total crack length. With regard to investigation of the threshold parameter, a value of 0.1 (accompanied by the subset spacing of 0.25 mm) worked particularly well for this test problem. The most significant effect with respect to thresholding occurred in case #1 where a low threshold value (0.05) was greatly influenced by noise in the gradient estimation near the crack tip and hence had a poor outcome on the crack tip position identification. With respect to the grid spacing, case #5 which had the largest grid spacing (0.5 mm), had a few results with noticeably large position errors approaching 1 mm; however, on average, it performed similar to the other cases analyzed across many of the test points. The effect of Gaussian kernel size was minimal. Almost no difference was found between the 5 x 5 kernel size and the 7 x 7 kernel size. With respect to the choice of σ, a value of 1.0 was found to produce acceptable results, with the higher and lower values potentially introducing too little or too much smoothing. In general, the automated procedure was able to locate the crack tip with a high degree of accuracy. For most of the test cases, the average location error across each of the 10 test locations ranged from 0.2 mm to 0.4 mm. Only select cases exceeded this range with case #1 having the highest average error (1.33 mm), followed by case #3 (0.46 mm) and case #9 (0.48 mm). Considering that the algorithm is operating on a grid of uniformly spaced data, the algorithm should be able to detect the crack tip position to within 1 increment of the spacing of the gridded data which seems to be reflected in this study. For the present work, it was determined that the thresholding procedure documented in earlier sections would maintain threshold values that were within a favorable range based on this study. A spacing value of 0.36 mm was chosen. It performed well in the correlation procedure while fitting within the range of values that worked well on the test problem.a Gaussian filter kernel size of 5 × 5 was chosen and implemented with $\sigma \approx 1$.

6.6 Results and discussion

6.6.1 Extraction of crack tip position in dynamic experiments – manual methods

For each of the dynamic experiments, the crack tip position was tracked as a function of time using traditional manual methods using a user interface created in MATLAB®. The user interface contains a display of the raw image, the *u*- and *v*-displacement contour plots, and the correlation coefficient from the image correlation process (Figure 6-21). The raw image frame is used to visually identify the crack tip position, but the contour plots are used to help confirm the crack tip position is chosen appropriately. When the crack tip is selected, the corresponding location is plotted in all four figures simultaneously to review the selection in all versions of the data set. This process is tedious and sometimes takes multiple attempts to estimate the crack tip. It is also highly subjective and lacks consistency.

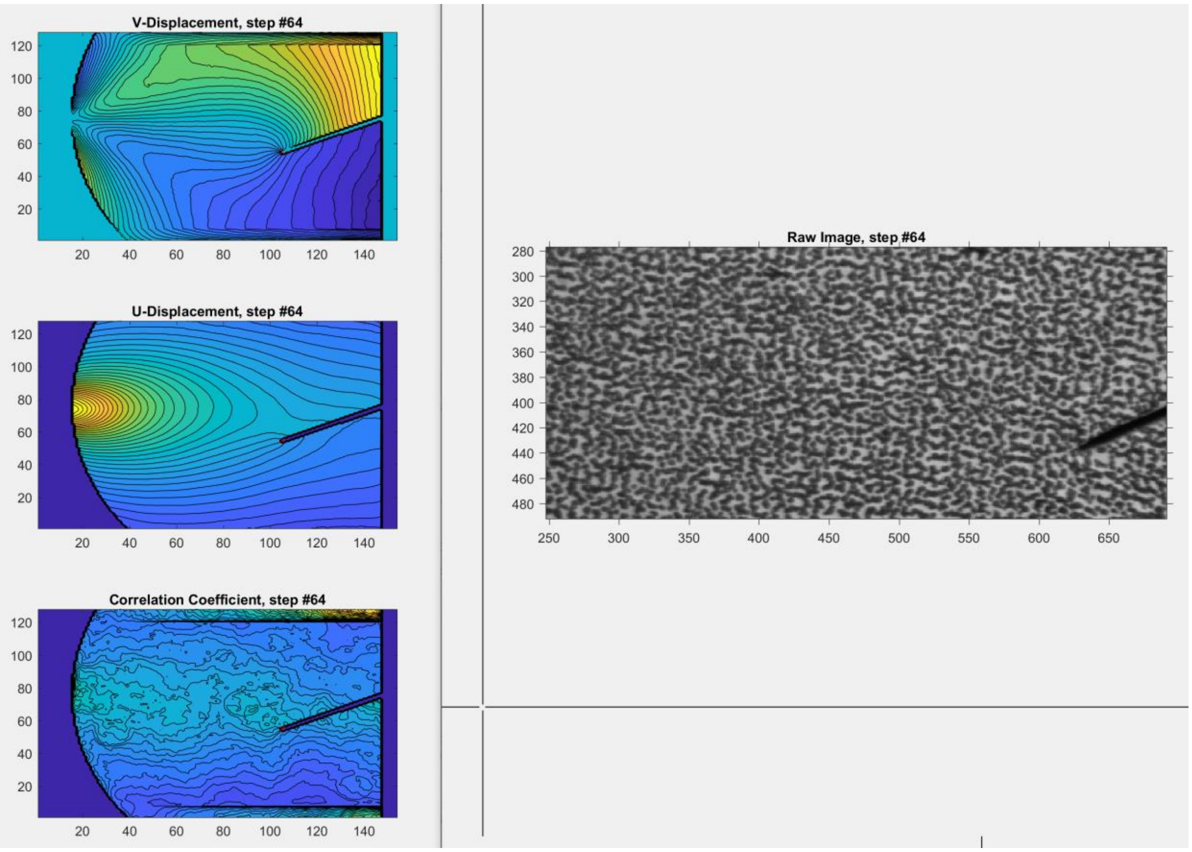

Figure 6-21: Screenshot of user interface for manual crack tip selection showing displacement contour plot (upper left and middle left), correlation coefficient plot (lower left), and raw image (right)

From the crack tip position data, a quadratic Bezier function was used to evaluate crack tip velocity from the crack tip position estimations similar to what was used in [106]. For a generic point, *i*, the smoothing function is evaluated as:

$$a_i(s) = (1-s)^2\hat{a}_i + 2s(1-s)\hat{a}_{i+1} + s^2\hat{a}_{i+2}, \quad 0 \le s \le 1 \qquad [6\text{-}13]$$

where s is the smoothing parameter, $\hat{a}$ is the crack length derived from the optical images, and $\hat{a}$ is the locally smoothed crack tip position. A value of $s = 0.5$ was chosen for the present work which results in the middle point of the interval carrying the most weight in the smoothing function. The velocity is then evaluated using backward numerical differentiation,

$$V_i = \frac{a_i - a_{i-1}}{t_i - t_{i-1}} \qquad [6\text{-}14]$$

The crack tip positions as a function of time are plotted in Figure 6-22 for the 90°, 80°, and 65° cases. The displacement histories follow very similar trends for all cases.

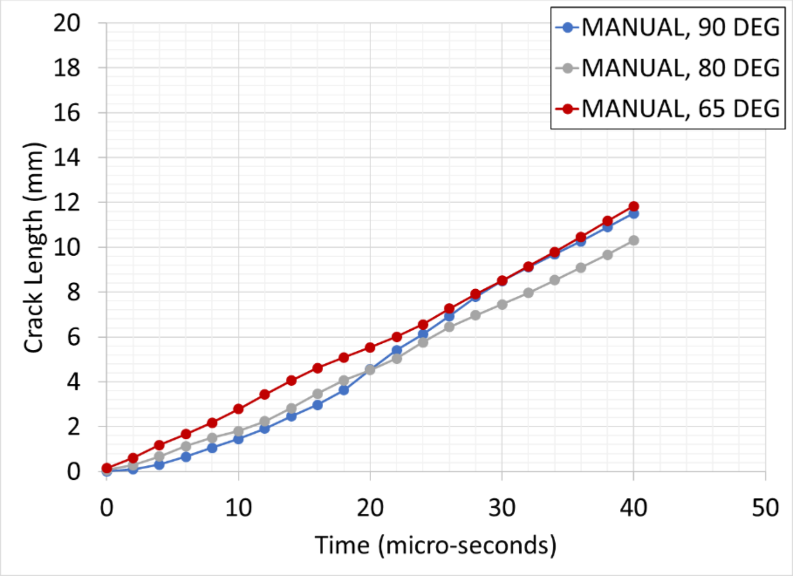

Figure 6-22: Crack tip position history

The velocity for each of the cases was estimated using numerical differentiation of the displacement histories and is plotted in Figure 6-23. The velocity is relatively consistent between the three different crack inclination angles.

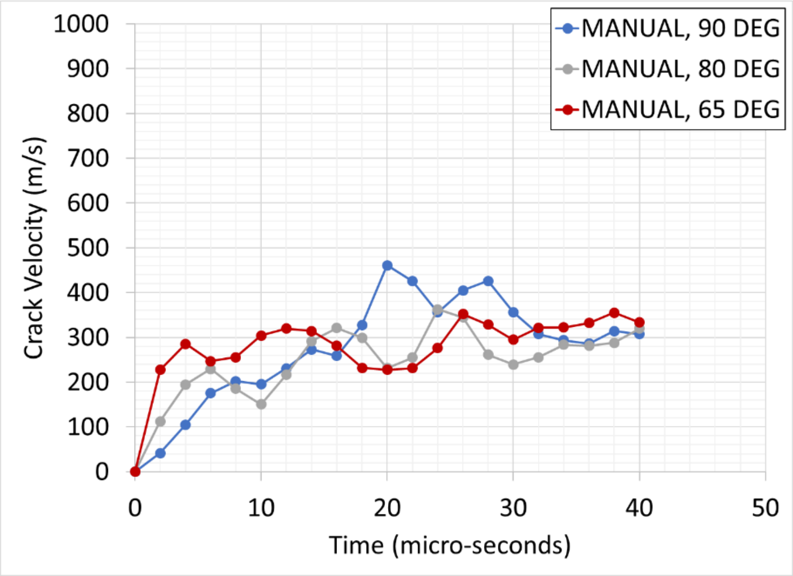

Figure 6-23: Crack tip velocity history

The velocity histories for the three experiments generally reach a steady state crack propagation velocity between 250-300 m/s after a brief ramp up period. The 90° and 80° experiments appear to have an initial period where the crack is accelerating whereas the 60° experiment appears to almost instantaneously reach the stable velocity. The velocities were all very consistent within the range of 15 µs to 35 µs.

6.6.2 Extraction of crack tip position in dynamic experiments – Canny-based automated edge detection method

The crack tip positions were separately extracted using the image processing-based edge detection method and the resulting positions estimates were once again differentiated using the quadratic Bezier smoothing technique. The positions and velocities are plotted in Figure 6-24 and Figure 6-25 respectively. The position and velocity histories are generally similar to those produced by the manual crack tip estimation method.

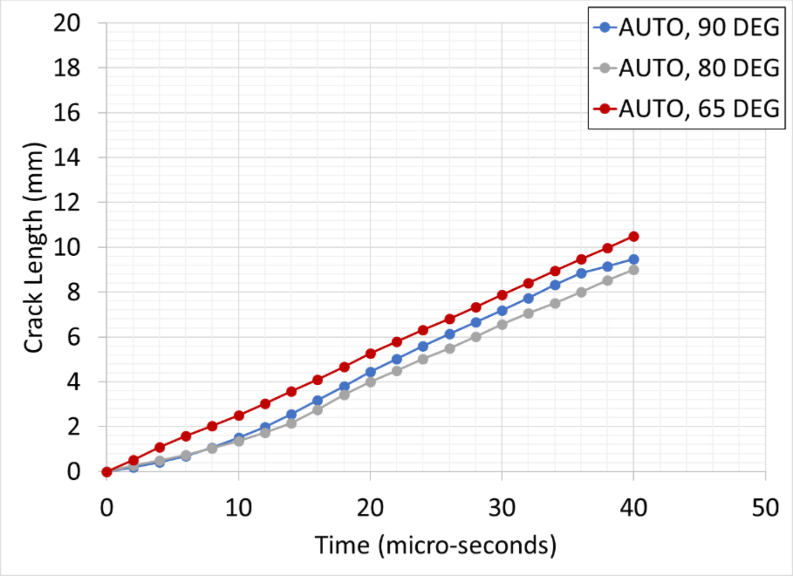

Figure 6-24: Crack tip position history as extracted using edge automated method derived from Canny edge detection

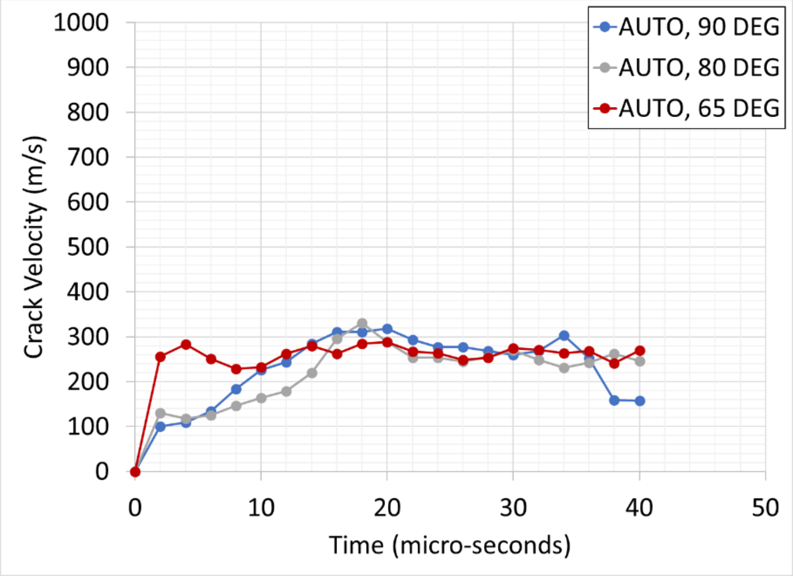

Figure 6-25: Crack tip velocity history calculated from position history extracted using automated Canny edge detection method

The edge detection method and the manual detection method resulted in similar estimates of velocity. For instance, considering a segment between 15 and 40 μs the manual method estimated 312 m/s with a standard deviation of 34 m/s whereas the edge detection algorithm estimated a propagation velocity of 265 m/s with a standard deviation of 34 m/s. These two measurements are within 10% of each other across the majority of the propagation history. A second set of results were evaluated to determine the sensitivity of the method to variations in the thresholding criteria. The thresholding criteria is used to ensure that the point that is being tracked is above any noise level that may exist in locations within the field far away from the expected crack tip location. Recall that the current thresholding method first uses a histogram to estimate the noise in the field of partial derivative data far away from the crack faces. Using the noise estimate, a threshold value is calculated that is slightly above this noise estimate (e.g. 1.05X, 1.10X, etc). Several threshold values were chosen to test the consistency of the output relative to the calculated threshold values. The crack tip position was very consistent regardless of threshold value as presented in Table 6-3. Across the 5 runs and the multiple crack tip position estimates obtained, the standard deviation was approximately 0.15 mm which illustrates that the edge detection algorithm is relatively insensitive to selection of this thresholding value, provided that the value is properly chosen based on the range of gradients present in the image and the amount of noise in the gradient field values away from the crack tip.

Table 6-3: Results of threshold ratio study

	Crack Length (mm)						
	Ratio						
Time (μs)	**0.20**	**0.25**	**0.30**	**0.35**	**0.40**	**Average**	**Standard Deviation**
0	0.00	0.00	0.00	0.00	0.00	0.00	0.00
2	0.54	1.13	0.76	0.38	0.54	0.67	0.29
4	0.91	0.91	0.91	0.91	0.91	0.91	0.00
6	1.67	1.29	1.29	1.29	1.45	1.40	0.17
8	2.20	2.20	2.04	2.20	2.20	2.17	0.07
10	2.95	2.73	2.73	2.58	2.58	2.71	0.15
12	3.48	3.48	3.71	3.33	3.33	3.47	0.16
14	4.33	4.24	4.02	4.02	4.02	4.13	0.15
16	4.86	4.86	4.86	4.70	4.70	4.80	0.09
18	5.39	5.39	5.24	5.70	5.24	5.39	0.19
20	6.23	6.23	6.23	6.14	6.23	6.21	0.04
22	6.61	6.99	6.77	6.77	6.99	6.83	0.16
24	7.36	6.99	7.36	7.14	6.99	7.17	0.19
26	7.90	8.12	7.90	8.12	8.55	8.12	0.27
28	8.65	8.27	8.27	8.43	8.27	8.38	0.17
30	9.02	9.02	9.02	9.02	9.02	9.02	0.00
32	9.40	9.87	9.40	9.40	9.78	9.57	0.23
34	9.93	9.78	9.78	9.78	9.78	9.81	0.07
36	10.69	10.31	10.47	10.31	10.31	10.42	0.17
38	11.06	11.06	11.06	10.69	10.69	10.91	0.20
40	11.82	11.60	11.44	11.60	11.44	11.58	0.16

6.6.3 Post-initiation stress intensity factors extracted using Canny-based edge detection technique

One of the key objectives of the edge detection technique is to show its fitness for fully automating the stress intensity factor extraction process. More specifically, the hybrid DIC-FE method has already been shown to be robust with respect to errors in crack tip position. The stress intensity factors were extracted using the 4 separate approaches tabulated in Table 6-4.

Table 6-4: Stress intensity factor extraction methods

Group	**Tracking Method**	**Extraction Method**
1	Manual	Over deterministic least squares
2	Automated	Over deterministic least squares
3	Manual	DIC-FE
4	Automated	DIC-FE

The processes for the second and fourth approaches are almost entirely automated with a minimal amount of intervention from the operator. The only noteworthy user intervention required is to initially trace out the crack path after the completion of the experiment. The various phases of the post-processing occur in a series of MATLAB® scripts. Aside from the manual crack edge tracing, minimal intervention is required to define parameters as necessary (e.g. subset spacing, image scale factors, etc.) and start the execution of the various segments of the code. The first and fourth approaches require a significant amount of user intervention that requires, in many cases, a certain level of subjective interpretation of images for locating the crack tip.

Results from the hybrid DIC-FE method without the automated position location method and the over-deterministic least squares method with and without the automated position location method are plotted in Figure 6-26.

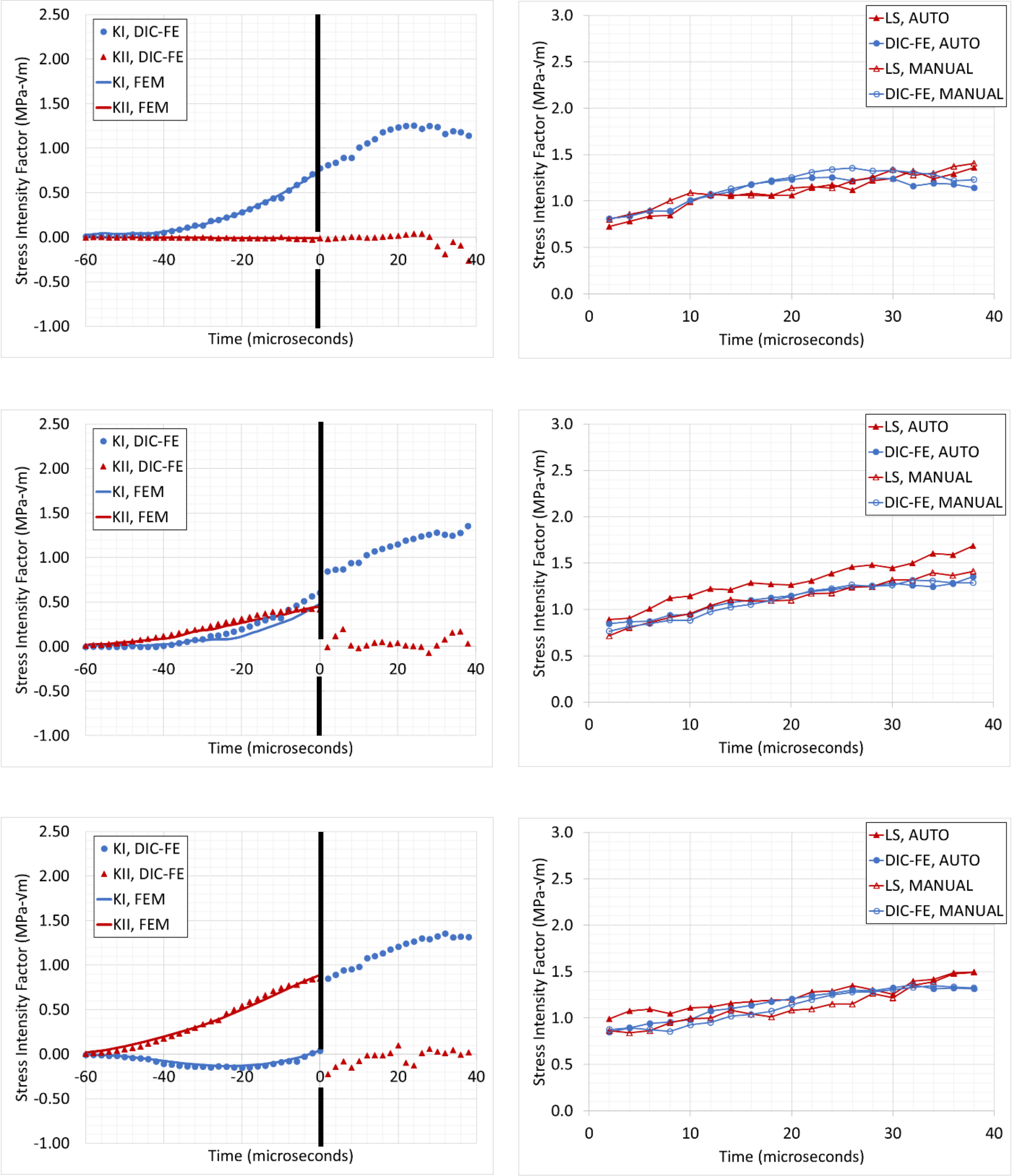

Figure 6-26: Stress intensity factor histories for 90° (top), 80° (center), and 65° (bottom) dynamic experiments using different crack tip location methods. (t = 0 corresponds to crack initiation, right column is K_I only)

The left-hand column of images shows the entire pre- and post-initiation mode I and mode II stress intensity factor histories for the three different experiments, with the data being extracted using the automated crack tip identification method coupled with the hybrid DIC-FE results. Pre-initiation, the results of an elasto-dynamic finite element simulation are included for reference. The mode II stress intensity factors drop to near zero once the crack initiates. The right-hand column of plots shows the post-initiation, mode I stress intensity factor histories for each of the four methods listed in Table 6-4.

In the post-initiation phase, the data from dynamic finite element model is not available since no attempt to simulate crack growth was made in the present work. For the two experiments that have a dominant mode I component (the 90° and 80° cases), the slope of the mode I SIF component undergoes very little change between the pre- and post-initiation states. This implies that the initial crack is likely very sharp geometrically. For all three of the experiments, the mode I stress intensity factor plateaus at approximately 1.4 MPa-√m. In general, for the latter two cases, the mode II stress intensity factor rapidly decreases to near zero soon after initiation and approaches zero as the crack approaches a mode I dominant state during propagation. Post-initiation, the mode I component of the least squares results appear to have more noise. This is likely due to uncertainties with respect to crack tip location, as that influences the displacement values used to form the over-determined equations in the asymptotic expansion. Conversely, the mode II component of the results extracted using the DIC-FE method appear to have more noise. While this method has been shown [124] to be relatively insensitive to the selection of the crack tip location, it is believed that uncertainties in the crack tip orientation may still contribute to deviations in this measurement.

It should be noted that the measurements were quite consistent across the four methods. The DIC-FE method (domain integral based) was particularly consistent between the manual and automated approaches. This is to be expected since it has been shown in prior works from the present authors [124] to be fairly independent of selection of crack tip position. Conversely, the over deterministic least squares method had more variability as it is sensitive to several factors including crack tip position, crack orientation as well as the number of terms considered in the asymptotic expansion during analysis. To assess the variability across the four methods, the stress intensity values from each of the four methods was averaged and the standard deviation was evaluated. The calculations are summarized in Table 6-5. The summary shows that the typical standard deviation values were rather low relative to the average. This further illustrates the consistency as well as the utility of the automated method.

The results presented in the present work are highly encouraging, and suggest that the method is relatively robust for identifying the crack tip for the current problem. Possibly the most important thing to note regarding the procedure is that it is repeatable and is able to estimate the crack tip positions in a matter of seconds due to its computational efficiency. For this analysis, a study of 10 images required approximately 9 seconds to pre-process and then approximately 0.51 seconds per image to locate the crack tip.

Table 6-5: Average and standard deviation of post-initiation mode I stress intensity factors

	K_I (MPa-√m)					
	Average			**Standard Deviation**		
Time (μs)	**90°**	**80°**	**65°**	**90°**	**80°**	**65°**
2	0.79	0.79	0.89	0.04	0.07	0.07
4	0.83	0.85	0.93	0.03	0.05	0.10
6	0.88	0.91	0.94	0.03	0.09	0.11
8	0.91	0.97	0.95	0.07	0.13	0.08
10	1.02	1.02	1.00	0.04	0.12	0.08
12	1.07	1.10	1.04	0.01	0.12	0.08
14	1.09	1.13	1.09	0.04	0.08	0.06
16	1.13	1.18	1.10	0.06	0.11	0.07
18	1.14	1.20	1.11	0.09	0.08	0.09
20	1.17	1.22	1.16	0.09	0.07	0.06
22	1.22	1.27	1.21	0.08	0.07	0.08
24	1.23	1.31	1.24	0.09	0.10	0.06
26	1.23	1.35	1.27	0.10	0.11	0.09
28	1.26	1.36	1.29	0.04	0.11	0.02
30	1.29	1.36	1.28	0.05	0.07	0.05
32	1.27	1.35	1.36	0.07	0.13	0.03
34	1.25	1.37	1.37	0.05	0.20	0.04
36	1.27	1.40	1.41	0.08	0.26	0.09
38	1.28	1.46	1.41	0.12	0.32	0.10

Chapter 7

Conclusions and Future Work

The present work implemented a hybrid method of quantifying fracture quantities of interest by measuring in-plane surface displacements using digital image correlation and mapping those displacements into a finite element model to utilize widely accepted algorithms in the finite element code to perform contour integration and extract the quantities of interest. A semi-circular beam geometry was critically examined using this technique and utilized to measure critical stress intensity factors for a homogeneous epoxy adhesive material under quasi-static loading conditions. The quasi-static experimental setup was then utilized to investigate crack initiation in the presence of a compressive stress field, namely a combined state of shear-compression at the crack tip. The effect of the compression on the shear-initiated crack was quantified for the homogenous material and shown to have a considerable effect on the apparent critical stress intensity factors. A linear relationship was found to reasonably describe the relationship between negative in-plane mode I stress intensity factor and mode II stress intensity factor.

A bimaterial specimen was then introduced and an accompanying load fixture was developed to examine this effect on a crack lying along an interface between two elastically dissimilar materials. Finite element simulations were utilized to develop the fixture and define the desired experimental conditions. The specimen geometry was then critically examined using the hybrid DIC-FE method and experiments were performed to evaluate the crack initiation behavior under the combined shear-compression load state. The fixture enabled the effect of the compressive load state to be quantified. Comparisons were made to the response observed under shear-tension stress states measured using a more traditional asymmetric four-point bending fixture.   Microstructural evaluations were performed to gain additional insight into the material failure behavior and the role that the local in-plane compression plays in shear-initiated fracture.

The homogeneous specimen geometry was then adapted to study rate-dependent fracture characteristics. A long bar apparatus was configured for loading the specimen dynamically. In the long bar setup, a gas gun was used to accelerate an aluminum striker bar to the desired velocity. Upon impact a stress wave with controlled amplitude and duration propagates into the test specimen. The geometry of the test specimen, specifically the crack inclination angle, was utilized to control the mode mixity at the crack tip at the point of crack initiation. Fracture parameters for mixed-mode loading were quantified to include behavior under the desired shear-compression stress states.

Lastly, a new automated edge detection method was introduced for locating the crack tip using experimentally measured displacement data. The primary motivation for developing the method was to reduce uncertainty with respect to fracture quantity calculations that are sensitive to the crack tip position. This is especially important for the dynamic experiments, where measurements are being made on a propagating crack and the crack tip location isn’t known a priori. The extraction method was evaluated using simulated data sets where the crack tip position was inserted manually and shown to have excellent ability to properly locate the crack tip. The method was then utilized to evaluate the dynamic experiments from the present work and compare crack tip position estimates from the edge detection algorithm with those from manually selecting the crack tip from the raw experimental images.

7.1 Future work

In the course of the present work, several items were identified for potential follow-on investigation. As this work focused on experimentally quantifying the role of local in-plane compressive stress on crack initiation, future research should investigate these effects on a broader range of material configurations. This work was isolated to a model system of core shell rubber-toughened epoxy. Follow-on work should extend this work to investigate other process parameters and how those process parameters interrelate with this local compressive stress effect. Other research has shown how parameters such as cure temperature affect the microstructural mechanisms by which core shell particles toughen an epoxy matrix. The cure temperature of the epoxy effects the residual stress in the rubber particles and this residual stress state can contribute to the way the crack interacts with the particles. It is of interest to see if these mechanisms are the same in the scenario where the crack initiates under a state of compression.

With respect to modeling, the present research has provided beneficial insight into the relationship between compression and shear at crack initiation. This will enable computational fracture models that account for these observed effects. The current state-of-the-art in fracture modeling usually relies on cohesive elements that are essentially zero thickness elements created along a fracture path that is known. These element formulations are generally for responses that consider shear traction and separation. The element response involves a monotonic loading response followed by a monotonic degradation response. A myriad of crack initiation criteria has been introduced and explored in the literature to define the transition point at which the response begins to degrade or soften. However, these initiation criteria are only formulated to consider opening displacements. The model descriptions do not have considerations for a state of crack closure. An interesting approach for future work would be to implement a cohesive element-based failure technique that considers not only the state of opening/closing and sliding displacements of each individual element along the interface on an element-by-element basis, but also considers the state of loading in a larger domain around the crack tip to include whether the domain around the crack tip is generally in tension or compression. This could extend the functionality of such cohesive zone models to account for the shear-compression response as well as alleviate some of the mesh sensitivities associated with cohesive element modeling.

Lastly, with respect to the crack tip location algorithm that was introduced in Chapter 6 of the present work, a number of future opportunities were identified. The method was demonstrated to work well on the epoxy fracture problem studied herein, and it was shown to produce a relatively reliable estimate of the crack tip position in a dynamically propagating crack. Through the finite element investigations, it was shown that the predicted location agreed quite well with the actual location. Additionally, studies were performed that showed it was sufficiently robust to potentially identify crack tip positions in problems where the displacements at failure were relatively low due to high material stiffness, low fracture toughness, or a combination of both. One uncertainty that remains is its potential for use in applications where the propagation speed is relatively high and the incremental progression of the crack tip between sampling points is low relative to the uncertainty in the location estimation. This can potentially be resolved by increased resolution in the DIC output data. It would be beneficial to investigate these limitations more thoroughly. For instance, extending the technique to address these limitations through experimental investigations on stiffer, lower toughness materials and on materials with relatively high crack propagation speeds would be interesting. Also, due to the complex nature of the gradient pattern, the uncertainty in the technique could potentially leverage advanced pattern recognition techniques built on machine learning methodologies. One other area of interest for future work would be to extend the method to be used in other full field experimental measurement techniques used in fracture studies such as interferometry-based techniques.

References

[1] R. J. H. Wanhill, "Milestone case histories in aircraft structural design," 2002.

[2] T. Swift, *Damage tolerance in pressurised fuselages,* Warley, UK, 1987.

[3] C. E. Inglis, "Stresses in a plate due to the presence of cracks and sharp corners," in *Proceedings of the Institute of Naval Architects*, 1913.

[4] A. A. Griffith, "The phenomena of rupture and flow in solids, series A," *Philosophical Transactions of the Royal Society of London,* vol. 221, pp. 163-198, 1920.

[5] G. W. Irwin, "Fracture dynamics," in *Fracturing of Metals, American Society for Metals,* Cleveland, OH, 1948.

[6] S. E. Orowan, "Fracture and strength of solids," *Report of Progress in Physics,* vol. 12, p. 185, 1949.

[7] H. M. Westergaard, "Bearing pressures and cracks," *Journal of Applied Mechanics,* vol. 6, pp. A49-A53, 1939.

[8] O. Volkersen, "Die niektraftverteilung in zugbeanspruchten mit konstanten laschenquerschritten," *Luftfahrtforschung,* vol. 15, pp. 41-47, 1938.

[9] M. Goland and E. Reissner, "The stresses in cemented joints," *Journal of Applied Mechanics,* vol. 11, pp. A17-A27, 1944.

[10] E. G. Coker, "An optical determination of the variation of stress in a thin rectangular plate subjected to shear," *Proceedings of the Royal Society of London. Series A, Containing Papers of a Mathematical and Physical Character,* vol. 86, no. 587, pp. 291-319, 1912.

[11] A. S. McLaren and I. McInnes, "The influence on the stress distribution in an adhesive lap joint of bending of the adhering sheets," *British Journal of Applied Physics,* vol. 9, pp. 72-77, 1958.

[12] D. Kutscha, "Photoelastic analysis of shear stress distribution in adhesive-bonded lap joints," 1962.

[13] P. A. Cooper and J. W. Sawyer, "A critical examination of stresses in an elastic single lap joint," NASA Technical Paper 1507, 1979.

[14] J. K. Sen and R. M. Jones, "Stresses in double-lap joints bonded with a viscoelastic adhesive: Part I. Theory and experimental corroboration," *AIAA Journal,* vol. 18, no. 10, pp. 1237-1244, 1980.

[15] C. P. Burger and A. S. Voloshin, "A new instrument for whole field stress analysis," *ISA Transactions,* vol. 22, no. 2, pp. 85-95, 1983.

[16] A. S. Voloshin and C. P. Burger, "Half fringe photoelasticity: a new approach to whole field stress analysis," *Experimental Mechanics,* vol. 23, no. 3, pp. 304-313, 1983.

[17] D. Mallik, C. P. Burger, A. S. Voloshin and E. Matsumoto, "Stress analysis of adhesive joints in composite structures through half-fringe photoelasticity," *Composite Structures,* vol. 4, pp. 97-109, 1985.

[18] Z. Lei, H. Yun, Y. Zhao, Y. Xing and X. Pan, "Study of shear transfer in Al/epoxy joint by digital photoelasticity," *Optics and Lasers in Engineering,* vol. 47, pp. 701-707, 2009.

[19] D. Post, "Moire interferometry at VPI & SU," *Experimental Mechanics,* vol. 23, no. 2, pp. 203-211, 1983.

[20] D. Post, R. Czarnek, J. Wood, D. Joh and S. Lubowinski, "Deformation and strains in adhesive joints by moiré interferometry," 1984.

[21] A. Asundi, "Deformation in adhesive joints using moiré interferometry," *International Journal of Adhesion and Adhesives,* vol. 7, no. 1, pp. 39-42, 1987.

[22] M. Y. Tsai, J. Morton, R. B. Krieger and D. W. Oplinger, "Experimental investigation of thick adherend lap shear test," *Journal of Advanced Materials,* vol. 27, no. 3, pp. 28-36, 1996.

[23] D. H. Mollenhauer and G. A. Schoeppner, "Strain measurement and prediction in a composite double-lap shear bonded joint," *Applied Mechanics: Progress and Applications,* pp. 461-466, 2002.

[24] M. Y. Tsai and J. Morton, "An investigation into the stresses in double-lap adhesive joints with laminated composite adherends," *International Journal of Solids and Structures,* vol. 47, pp. 3317-3325, 2010.

[25] P. Ruiz, F. Jumbo, J. Huntley, I. Ashcroft and G. Swallowe, "Experimental and numerical investigation of strain distributions within the adhesive layer in bonded joints," *Strain,* vol. 47, pp. 88-104, 2011.

[26] M. L. Williams, "The stresses around a fault or crack in dissimilar media," *Bulletin of the Seismological Society of America,* vol. 49, no. 2, pp. 199-204, 1959.

[27] J. R. Rice and G. C. Sih, "Plane problems of cracks in dissimilar media," *Journal of Applied Mechanics,* vol. 32, no. 2, pp. 418-423, 1965.

[28] J. R. Rice, "Elastic fracture mechanics concepts for interfacial," *Journal of Applied Mechanics,* vol. 55, no. 1, pp. 98-103, 1988.

[29] G. P. Cherepanov, "The stress state in a heterogeneous plate with slits," *Izvestia AN SSSR, OTN Mekhan,* vol. 1, pp. 131-137, 1962.

[30] A. H. England, "A crack between dissimilar media," *Journal of Applied Mechanics,* vol. 32, pp. 400-402, 1965.

[31] F. Erdogan, "Stress distribution in bonded dissimilar materials with cracks," *Journal of Applied Mechanics,* vol. 32, pp. 403-410, 1965.

[32] J. W. Hutchinson, M. Mear and J. R. Rice, "Crack paralleling an interface between dissimilar materials," *Applied Mechanics,* vol. 54, no. 4, pp. 828-832, 1987.

[33] J. F. Yao and S. S. Wang, "An analysis of interface cracks between dissimilar isotropic materials using conservation integrals in elasticity," *Engineering Fracture Mechanics,* vol. 20, no. 3, pp. 423-432, 1984.

[34] C. F. Shih and R. Asaro, "Elastic-plastic analysis of cracks on bimaterial interfaces: Part I: Small scale yielding," *Journal of Applied Mechanics,* vol. 55, no. 2, pp. 299-316, 1988.

[35] A. N. Gent and A. J. Kinloch, "Adhesion of viscoelastic materials to rigid substrates. III. Energy criterion for failure," *Journal of Polymer Science: Part A2,* vol. 9, pp. 659-668, 1971.

[36] K. M. Liechti and W. G. Knauss, "Crack propagation at material interfaces: I. Experiments on mode interaction," *Experimental Mechanics,* vol. 22, pp. 383-391, 1982.

[37] K. M. Liechti and W. G. Knauss, "Crack propagation at material interfaces: II. Experiments on mode interaction," *Experimental Mechanics,* vol. 22, pp. 383-391, 1982.

[38] P. G. Charalambides, J. Lund, A. G. Evans and R. M. McMeeking, "A test specimen for determining the fracture resistance of bimaterial interfaces," *Journal of Applied Mechanics,* vol. 56, pp. 77-82, 1989.

[39] H. C. Cao and A. G. Evans, "An experimental study of the fracture resistance of bimaterial interfaces," *Mechanics of Materials,* vol. 7, pp. 295-304, 1989.

[40] A. G. Evans, M. Ruhle, B. J. Dalgleish and P. G. Charalambides, "The fracture energy of bimaterial interfaces," *Metallurgical Transactions A,* vol. 21A, pp. 2419-2429, 1990.

[41] K. M. Liechti and Y. S. Chai, "Biaxial loading experiments for determining interfacial fracture toughness," *Journal of Applied Mechanics,* vol. 58, pp. 680-687, 1991.

[42] E. D. Reedy and T. R. Guess, "Comparison of butt tensile strength data with interface corner stress intensity factor prediction," *International Journal of Solids and Structures,* vol. 30, no. 21, pp. 2929-2936, 1993.

[43] W. K. Loh, A. D. Crocombe, M. M. A. Wahab, J. F. Watts and I. A. Ashcroft, "The effect of moisture on the failure locus and fracture energy of an epoxy-steel interface," *Journal of Adhesion Science and Technology,* vol. 16, no. 11, pp. 1407-1429, 2002.

[44] P. H. Melville, "Fracture mechanics of brittle materials in compression," *International Journal of Fracture,* vol. 13, pp. 532-534, 1977.

[45] M. Comninou and D. Schmueser, "The interface crack in a combined tension–compression and shear field," *Journal of Applied Mechanics,* vol. 46, pp. 345-348, 1979.

[46] M. Comninou and J. Dundurs, "Effect of friction on the interface crack loaded in shear," *Journal of Elasticity,* vol. 10, pp. 203-212, 1980.

[47] W. Qian and C. T. Sun, "A frictional interfacial crack under combined shear and compression," *Composites Science and Technology,* vol. 36, pp. 1753-1761, 1998.

[48] I. Carol, P. Prat and C. M. and Lopez, "Normal/shear cracking model: Application to discrete crack analysis," *Journal of Engineering Mechanics,* vol. 123, no. 8, pp. 765-773, 1997.

[49] P. Isaacson, *On crack growth under compressive stresses,* 2001.

[50] K. Ravi-chandar and W. G. Knauss, "An experimental investigation into dynamic fracture: I. Crack initiation and arrest," *International Journal of Fracture,* vol. 25, pp. 247-262, 1984.

[51] J. J. Mason, J. Lambros and A. J. Rosakis, "The use of a coherent gradient sensor in dynamic mixed-mode fracture mechanics experiments," *Journal of the Mechanics and Physics of Solids,* vol. 40, no. 3, pp. 641-661, 1992.

[52] M. S. Kirugulige and H. V. Tippur, "Measurement of fracture parameters for a mixed-mode crack driven by stress waves using image correlation technique and high-speed digital photography," *Strain,* vol. 45, pp. 108-122, 2009.

[53] M. Nakano, K. Kishida, Y. Ymauchi and Y. Sogabe, "Dynamic fracture initiation in brittle materials under combined mode I/II loading," *Journal de Physique IV Colloque,* vol. 04, no. C8, pp. 695-700, 1994.

[54] G. Gao, S. Huang, K. Xia and Z. Li, "Application of digital image correlation (DIC) in dynamic notched semi-circular bend (NCSB) tests," *Experimental Mechanics,* vol. 55, pp. 95-104, 2015.

[55] A. J. Kinloch, S. J. Shaw, D. A. Tod and D. L. Hunston, "Deformation and fracture behaviour of a rubber-toughened epoxy: 1. Microstructure and fracture studies," *Polymer,* vol. 24, pp. 1341-1354, 1983.

[56] A. J. Kinloch, S. J. Shaw and D. L. Hunston, "Deformation and fracture behaviour of a rubber-toughened epoxy: 2. Failure criteria," *Polymer,* vol. 24, pp. 1355-1363, 1983.

[57] R. A. Pearson and A. F. Yee, "Influence of particle size and particle size distribution on toughening mechanisms in rubber-modified epoxies," *Journal of Materials Science,* vol. 26, pp. 3828-3844, 1991.

[58] R. Bagheri, B. T. Marouf and R. A. Pearson, "Rubber-toughened epoxies: A critical review," *Journal of Macromolecular Science, Part C: Polymer Reviews,* vol. 49, no. 3, pp. 201-225, 2009.

[59] W. Peters and W. Ranson, "Digital Imaging Techniques in Experimental Stress Analysis," *Optical Engineering,* vol. 21, no. 3, pp. 427-432, 1982.

[60] M. A. Sutton, W. J. Wolters, W. J. Peters, W. H. Peters, W. F. Ranson and S. R. McNeill, "Determination of displacements using an improved digital correlation method," *Image and Vision Computing,* vol. 1, no. 3, pp. 133-139, 1983.

[61] W. H. Peters, W. F. Ranson, M. A. Sutton, T. Chu and J. Anderson, "Applications of Digital Correlation Methods to Rigid Body Mechanics," *Optics Engineering,* vol. 22, no. 6, pp. 738-742, 1983.

[62] T. C. Chu, M. A. Ranson and M. A. Sutton, "Applications of digital-image-correlation techniques to experimental mechanics," *Experimental Mechanics,* vol. 25, no. 3, pp. 232-244, 1985.

[63] R. J. Sanford, "Application of the least-squares method to photoelastic analysis," *Experimental Mechanics,* vol. 20, pp. 192-197, 1980.

[64] R. J. Sanford, "Determining fracture parameters with full-field optical methods," *Experimental Mechanics,* vol. 29, pp. 241-247, 1989.

[65] S. R. McNeill, W. H. Peters and M. A. Sutton, "Estimation of stress intensity factor by digital image correlation," *Engineering Fracture Mechanics,* vol. 28, pp. 101-112, 1987.

[66] J. Andanto-Buento and J. Lambros, "Investigation of crack growth in functionally graded materials using digital image correlation," *Engineering Fracture Mechanics,* vol. 69, pp. 1695-1711, 2002.

[67] S. Yoneyama and M. Takashi, "Automatic determination of stress intensity factor utilizing digitial image correlation," *Journal of the Japanese Society of Experimental Mechanics,* vol. 1, pp. 202-206, 2001.

[68] M. S. Kirugulige and H. V. Tippur, "Measurement of surface deformations and fracture parameters for a mixed-mode crack driven by stress waves using image correlation technique and high-speed photography," *Strain,* vol. 45, pp. 108-122, 2009.

[69] M. S. Kirugulige, H. V. Tippur and T. S. Denney, "Measurement of transient deformations using digital image correlation method and high-speed photography: Application to dynamic fracture," *Applied Optics,* vol. 46, pp. 5083-5096, 2007.

[70] S. Yoneyama, S. Arikawa, S. Kusayanagi and K. Hazumi, "Evaluating J-integral from displacement fields measured by digital image correlation," *Strain,* vol. 50, pp. 147-160, 2014.

[71] J. R. Yates, M. Zanganeh and Y. H. Tai, "Quantifying crack tip displacement fields with DIC," *Engineering Fracture Mechanics,* vol. 77, pp. 2063-2076, 2010.

[72] T. V. Hareesh and F. P. Chiang, "Integrated experimental-finite element approach to study elasto-plastic crack tip field," *Engineering Fracture Mechanics,* vol. 31, pp. 451-461, 1988.

[73] F. Dubois, M. Meite, O. Pop and J. Absi, "Characterization of timber fracture using the digital image correlation technique and finite element method," *Engineering fracture mechanics,* vol. 96, pp. 107-121, 2012.

[74] J. P. Isaac, S. Dondeti and H. V. Tippur, "Crack initiation and growth in additively printed ABS: Effect of print architecture studied using DIC," *Additive Manufacturing,* 2020.

[75] J. Blaber, B. Adair and A. Antoniou, "Ncorr: Open-source 2D digital image correlation Matlab software," *Experimental Mechanics,* vol. 55, no. 6, pp. 1105-1122, 2015.

[76] K. He, J. Sun and X. Tang, "Guided image filtering," *IEEE Transactions on Pattern Analysis and Machine Intelligence,* vol. 35, no. 6, pp. 1397-1408, 2013.

[77] C. F. Shih, B. Moran and T. Nakamura, "Energy release rate along a three-dimensional crack front in a thermally stressed body," *International Journal of Fracture,* vol. 30, pp. 79-102, 1986.

[78] H. M. Westergaard, "Bearing pressure and cracks.," *Journal of Applied Mechanics,* vol. 6, pp. 49-53, 1939.

[79] K. P. Chong and M. D. Kuruppu, "New specimen for fracture toughness determination for rock and other materials," *International Journal of Fracture,* vol. 26, pp. R49-R62, 1984.

[80] K. P. Chong, M. D. Kuruppu and J. S. Kuszmaul, "Fracture toughness determination of rocks with core-based specimens," in *SEM/RILEM International Conference on Fracture of Concrete and Rocks*, Texas, 1987.

[81] I. L. Lim, I. W. Johnston and S. K. Choi, "Stress intensity factors for semi-circular specimens under three-point bending," *Engineering Fracture Mechanics,* vol. 44, no. 3, pp. 363-382, 1993.

[82] B. Pan, Z. Lu and H. Xie, "Mean intensity gradient: An effective global parameter for quality assessment of the speckle patterns used in digital image correlation," *Optics and Lasers in Engineering,* vol. 48, pp. 469-477, 2010.

[83] "ASTM D638-14 - Standard Test Method for Tensile Properties of Plastics," ASTM International, West Conshohocken, PA, 2014.

[84] "ASTM D695-15 - Standard Test Method for Compressive Properties of Rigid Plastics," ASTM International, West Conshohocken, PA, 2015.

[85] I. Campione, T. M. Brugo, G. Minak, J. J. Tomic, N. Bogojevic and S. N. Kostic, "Investigation by digital image correlation of mixed mode I and II fracture behavior of metallic IASCB specimens with additive manufactured crack-like notch," *Metals,* vol. 10, no. 3, p. 400, 2020.

[86] M. L. Williams, "On the stress distribution at the base of a stationary crack," *Journal of Applied Mechanics,* vol. 24, pp. 109-114, 1957.

[87] D. J. Smith, M. R. Ayatollahi and M. J. Pavier, "The role of T-stress in brittle fracture for linear elastic materials under mixed-mode loading," *Fatigue and Fracture of Engineering Materials and Structures,* vol. 24, pp. 137-150, 2001.

[88] Simulia, *Abaqus Reference Manual*, 2020.

[89] K. Hayashi and S. Nemat-Nasser, "Energy-release rate and crack kinking under combined loading," *Journal of Applied Mechanics,* vol. 48, pp. 520-524, 1981.

[90] M. Y. He and J. W. Hutchinson*, Kinking of a crack out of an interface: Tabulated solution coefficients,* Cambridge, MA: Harvard University Division of Applied Mechanics, 1989.

[91] B. N. Whittaker, R. Singh and G. Sun, Rock Fracture Mechanics: Principles, Design, and Applications, Netherlands, 1992.

[92] Z. Eliezer, C. J. Schulz and J. W. Barlow, "Friction and wear properties of an epoxy-steel system," *Wear,* vol. 46, pp. 397-403, 1978.

[93] L. Xu and H. V. Tippur, "Fracture parameters for interfacial cracks: An experimental-finite element study of crack tip fields and crack initiation toughness," *International Journal of Fracture,* vol. 71, pp. 345-363, 1995.

[94] N. P. O'Dowd, C. F. Shih and M. G. Stout, "Test geometries for measuring interfacial fracture toughness," *International Journal of Solids and Structures,* vol. 29, no. 5, pp. 571-589, 1992.

[95] R. G. Keys, "Cubic convolution interpolation for digital image processing," *IEEE Transactions on Acoustics, Speech, and Signal Processing,* Vols. ASSP-29, no. 6, pp. 1153-1160, 1981.

[96] B. M. Sundaram and H. V. Tippur, "Dynamic mixed-mode fracture behavior of PMMA and polycarbonate using Digital Gradient Sensing," *Engineering Fracture Mechanics,* vol. 176, pp. 186-212, 2017.

[97] A. D. Mulliken and M. C. Boyce, "Mechanics of the rate-dependent elastic-plastic deformation of glassy polymers from low to high strain rates," *International Journal of Solids and Structures,* vol. 43, pp. 1331-1356, 2006.

[98] J. L. Jordan, J. R. Foley and C. R. Siviour, "Mechanical Properties of Epon 826/DEA Epoxy (AFRL-RW-EG-TP-2008-7418)," Air Force Research Laboratory, 2008.

[99] I. L. Lim, I. W. Johnston, S. K. Choi and J. N. Boland, "Fracture testing of a soft rock with semi-circular specimens under three-point bending. Part 2 - Mixed-mode," *International Journal of Rock Mechanics and Mining Sciences,* vol. 31, no. 3, pp. 199-212, 1994.

[100] T. C. Miller, "Analysis of mixed-mode cracks in a rubbery particulate composite," Air Force Research Lab, 1998.

[101] J. Jamali, Y. Fan and J. T. Wood, "The mixed-mode fracture behavior of epoxy by the compact tension shear test," *International Journal of Adhesion and Adhesives,* vol. 63, pp. 79-86, 2015.

[102] J. F. Kalthoff, J. Beinert and S. Winkler, "Measurements of dynamic stress intensity factors for fast running and arresting cracks in double cantilever beam specimens," in *Fast Fracture and Crack Arrest, ASTM STP 627*, G. T. G. T. Hahn and M. F. Kanninen, Eds., American Society for Testing and Materials, 1977, pp. 161-176.

[103] P. R. Marur, R. C. Batra, G. Garcia and A. C. Loos, "Static and dynamic fracture toughness of epoxy/alumina composite with submicron inclusions," *Journal of Materials Science,* vol. 39, pp. 1437-1440, 2004.

[104] V. Joudon, G. Portemond, F. Lauro and B. Bennani, "Experimental procedure to characterize the mode I dynamic fracture toughness of advanced epoxy resins," in *4th International Conference of Impact Loading on Lightweight Structures (ICILLS 2014)*, Cape Town, South Africa, 2014.

[105] E. Pittman, S. Koumlis, H. N. Aung, A. Bellafatto and L. Lamberson, "Rate-dependent fracture behavior of aerospace epoxies: PR-520 and 3502," *Journal of Aerospace Engineering,* vol. 35, no. 1, 2022.

[106] D. Lee, H. V. Tippur and P. Bogert, "Experimental study of dynamic crack growth in unidirectional graphite/epoxy composites using digital image correlation method and high-speed photography," *Journal of Composite Materials,* vol. 43, no. 19, pp. 2081-2108, 2009.

[107] B. M. Sundaram and H. V. Tippur, "Full-field measurement of contact-point and crack-tip," *International Journal of Applied Glass Science,* vol. 9, pp. 123-136, 2018.

[108] S. Dondetti and H. V. Tippur, "A comparative study of dynamic fracture of soda-lime glass using photoelasticity, digital image correlation and digital gradient sensing techniques," *Experimental Mechanics*, 2019.

[109] A. S. Redner, "Experimental determination of stress intensity factors: A review of photoelastic approaches," in *International Conference on Fracture Mechanics and Technology*, Hong Kong, 1977.

[110] J. M. Etheridge and J. W. Dally, "A critical review of methods for determining stress-intensity factors from isochromatic patterns," *Experimental Mechanics*, vol. 17, no. 7, pp. 248-254, 1977.

[111] M. N. Pacey, M. N. James and E. A. Patterson, "A new photoelastic model for studying fatigue crack closure," *Experimental Mechanics,* vol. 45, no. 1, pp. 42-52, 2005.

[112] S. Roux and F. Hild, "Stress intensity factor measurements from digital image correlation: post-processing and integrated approaches," *International Journal of Fracture,* vol. 140, pp. 141-157, 2006.

[113] R. Hamam, F. Hild and S. Roux, "Stress intensity factor gauging by digital image correlation: Application in cyclic fatigue," *Strain,* vol. 43, pp. 181-192, 2007.

[114] M. Zanganeh, P. Lopez-Crespo, Y. H. Tai and J. R. Yates, "Locating the crack tip using displacement field data: A comparative study," *Strain,* vol. 49, pp. 102-115, 2013.

[115] J. Rethore, "Automatic crack tip detection and stress intensity factor estimation of curved cracks from digital images," *International Journal for Numerical Methods in Engineering,* vol. 103, pp. 516-534, 2015.

[116] I. Abdel-Qader, O. Abdudayyeh and M. E. Kelly, "Analysis of edge-detection techniques for crack identification in bridges," *Journal of Computing in Civil Engineering,* vol. 17, no. 4, pp. 255-263, 2003.

[117] P. Lopez-Crespo, A. Shterenlikht, E. A. Patterson, J. R. Yates and P. J. Withers, "The stress intensity of mixed mode cracks determined by digital image correlation," *Journal of Strain Analysis,* vol. 43, pp. 769-780, 2008.

[118] T. Strohmann, D. Starostin-Penner, E. Breitbarth and G. Requena, "Automatic detection of fatigue crack paths using digital image correlation and convolutional neural networks,"

Fatigue and Fracture of Engineering Materials and Structures, vol. 44, pp. 1336-1348, 2021.

[119] S. Miao, P. Pan, S. Li, J. Chen and P. Konicek, "Quantitative fracture analysis of hard rock containing double infilling flaws with a novel DIC-based method," *Engineering Fracture Mechanics,* p. 252, 2021.

[120] J. Canny, "A computational approach to edge detection," *IEEE Transactions on Pattern Analysis and Machine Intelligence,* vol. 8, no. 6, pp. 679-698, 1986.

[121] W. McIlhagga, "The Canny edge detector revisited," *International Journal of Computer Vision,* vol. 91, pp. 251-261, 2011.

[122] I. Sobel and G. Feldman, "A 3X3 isotropic gradient operator for image processing," in *Stanford Artificial Intelligence Project*, 1968.

[123] W. Rong, Z. Li, W. Zhang and L. Sun, "An improved Canny edge detection algorithm," 2014.

[124] A. T. Owens and H. V. Tippur, "Measurement of mixed-mode fracture characteristics of an epoxy-based adhesive using a hybrid Digital Image Correlation (DIC) and Finite Elements (FE) approach," *Optics & Lasers in Engineering,* vol. 140, p. 106544, 2021.

[125] J. Samareh, "Discrete data transfer technique for fluid-structure interaction," in *18th AIAA Computational Fluid Dynamics Conference*, 2007.

[126] G. H. C. Silva, R. Le Riche, J. Molimard and A. Vautrin, "Exact and efficient interpolation using finite elements shape functions," *European Journal Of Computational Mechanics,* vol. 18, no. 3-4, pp. 307-331, 2009.

[127] C. Hua, "An inverse transformation for quadrilateral isoparametric elements: Analysis and application," *Finite Element in Analysis and Design,* pp. 159-166, 1990.

[128] A. T. Owens, D. Hayduke, E. Clark, J. Hansen and J. Grupp, "Development of a method for characterizing adhesive joints under mixed mode states of stress," Department of Defense Technical Report RDMR-WD-16-44, 2016.

[129] Rachmawan, "Matlab Central File Exchange," Mathworks, 2021. [Online]. Available: Canny Edge Detection (https://www.mathworks.com/matlabcentral/fileexchange/46859-canny-edge-detection).

[130] Rachael, "Matlab Central File Exchange," Mathworks, 2021. [Online]. Available: Guided Image Filter (https://www.mathworks.com/matlabcentral/fileexchange/33143-guided-filter).

Appendix A

Alternate Interface Crack Test Methods

A key objective of the present effort was to investigate the effects of compression stress on fracture to include the effect of in-plane compression stresses on fracture initiation and propagation in homogeneous samples. Additionally, and most relevant to the stated objectives, was the study of cracks positioned along an interface between elastically dissimilar materials in this combined state of stress. The work was carried out using the specimen design and fixture design documented in section 4.1.1. However, in the development of that experimental setup, several other fixture designs were explored for the interface crack problem and are documented in this appendix.

A.1. Alternate 1 – Biaxial clamp geometry

The first concept was based on a fixture design used in a prior test series [128] to explore a lap shear joint performance under compressive loading conditions. A schematic of the test setup is shown in Figure A-1. The fixture utilizes a typical double notch lap shear geometry that is sandwiched between two platens. The two platens are positioned in a larger caliper that surrounds the entire stack up. One of the platens is fixed and the other platen is floating with a small hydraulic actuator positioned at its center. In this fixture, the actuator provides the compressive clamping load on the specimen and the end load is accomplished using a traditional single axis load frame. The main disadvantage of this approach is that the load mixity is not readily repeatable without synchronizing the control system of the hydraulic actuator to the control system of the single axis load frame. Without this ability, the lateral load, and thus the compressive stress in the test specimen, is constant throughout the test. Thus, as the end load increases linearly during the test, the load mixity is also increasing linearly. This was undesirable for the present work.

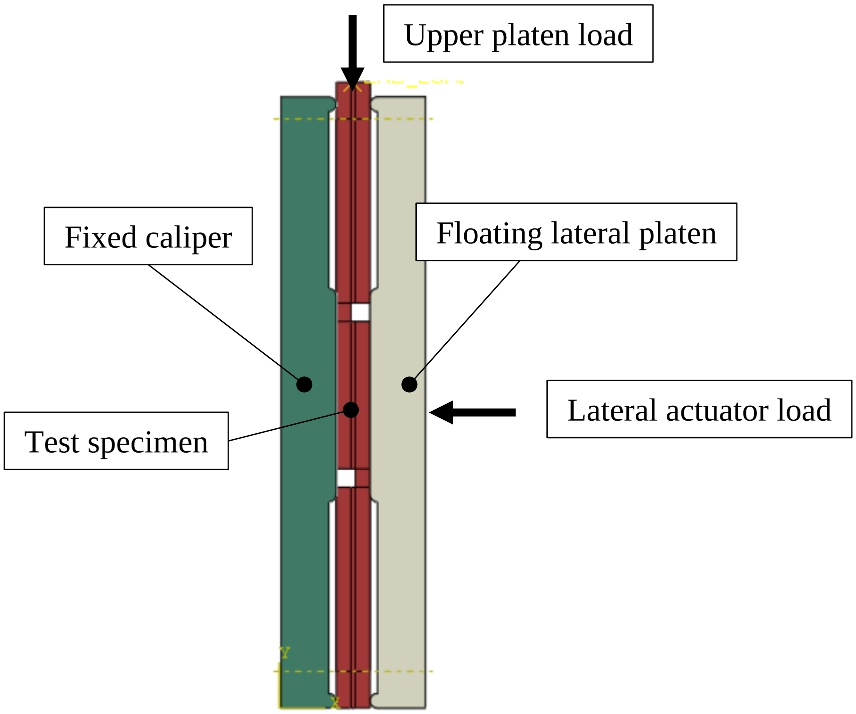

Figure A-1: Alternate loading fixture – biaxial clamp

A.2. Alternate 2 – Wedge fixture

The second concept was based on a modification to the first concept and is shown schematically in Figure A-2. In this, the load is transferred into the test sample using a pair of wedges. The wedges and the test sample are sandwiched between a fixed frame. As the end load is applied to one piece of the wedge pair, the load is transferred to the test sample. The load mixity is thus controlled by the wedge angle. Based on the analytical studies, this approach was able to produce very uniform distributions of shear and normal stress in the test specimen. The main disadvantage of this test fixturing approach, however, is that a different set of wedges (cut at a different angles) would be required for each desired load mixity. Also, from an implementation standpoint, the contact surfaces between the wedges and at the specimen interface would require a high degree of precision at each of the three interfaces (between the outer wedge and the caliper, between the inner wedge and the specimen, and between the two wedge pieces. Deformation in the fixture could also contribute to nonuniformity in the load.

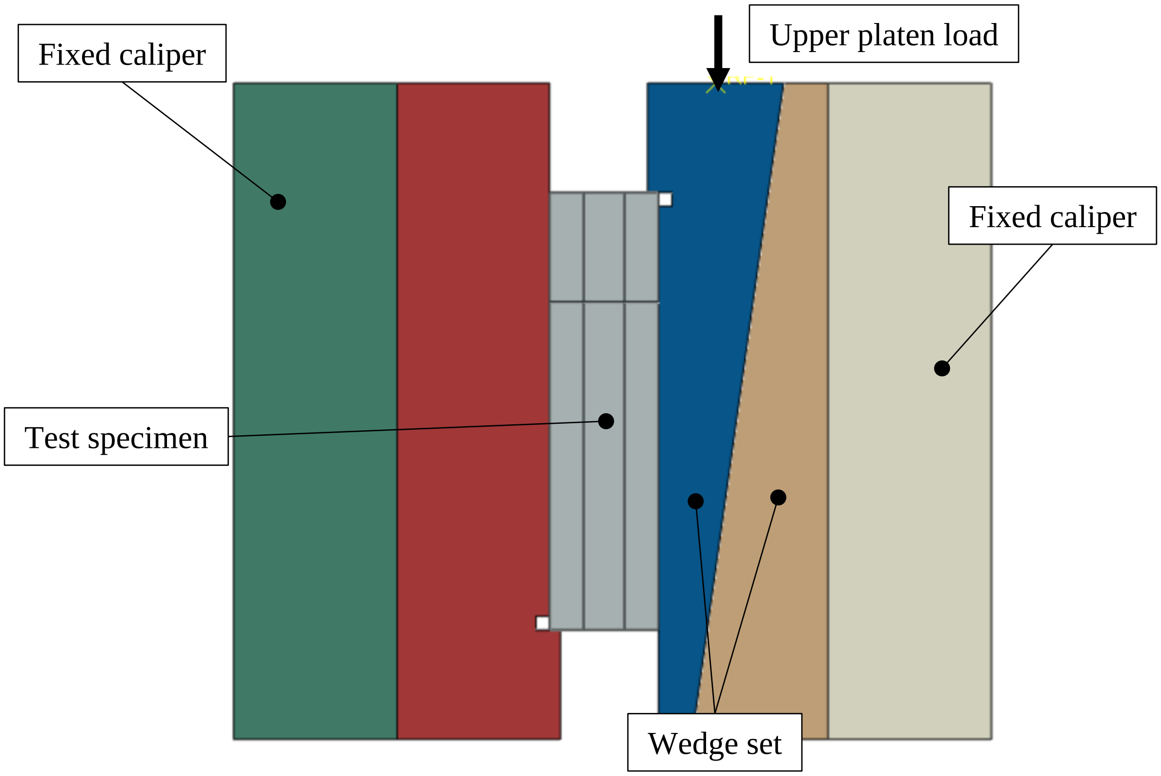

Figure A-2: Alternate loading fixture – wedge fixture

A.3. Alternate 3 – Hybrid semi-circular beam

The third concept was based on a hybrid version of the semi-circular beam geometry and is shown in Figure A-3. The specimen is the same size and shape as that of the homogeneous semi-circular beam geometry, however, the specimen is split into two pieces with an interface.

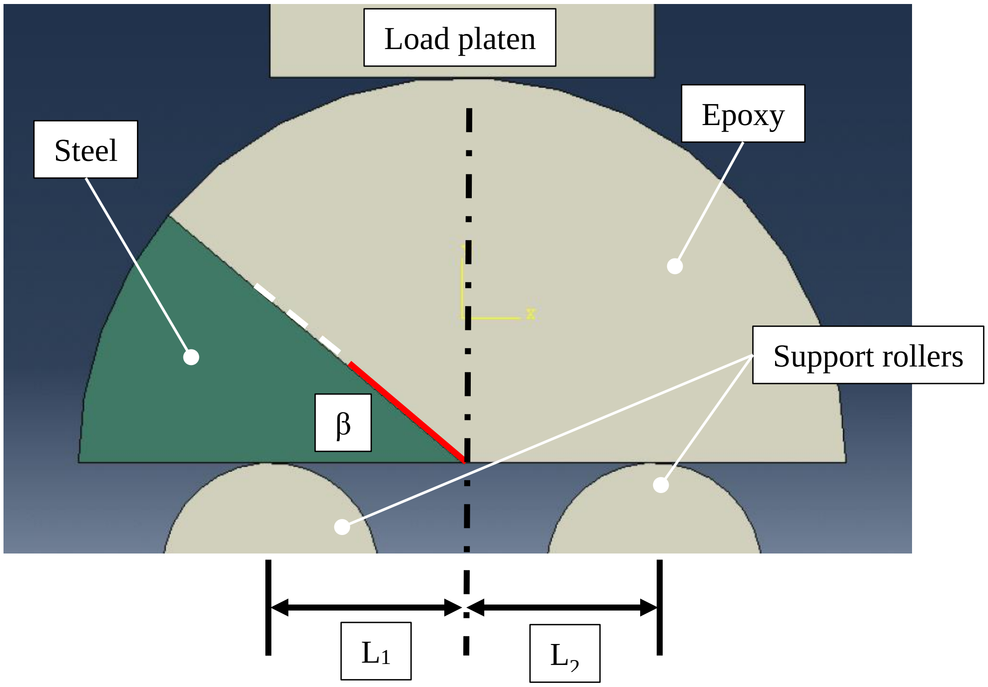

Figure A-3: Hybrid semi-circular beam geometry

This specimen geometry has several interesting characteristics. The mode mixity can be controlled in the same manner as that of the homogeneous sample using changes in the inclination angle, β, of the interface. Additionally, by introducing asymmetry in the support points of the two rollers, the mode mixity can be altered. By changing the distances, L_1 and L_2, from the centerline to each of the two support rollers, a full range of mode mixities can be achieved, meaning that a single crack inclination angle could be used for all specimens. Further, by choosing two crack inclination angles, one of them being a low angle where the majority of the specimen is steel, and the other of them being a high angle where the majority of the specimen is epoxy, the desired in-plane compression can be introduced and controlled at the crack tip. Figure A-4 shows the relationship between crack tip mode mixity and support point asymmetry for two such inclination angles.

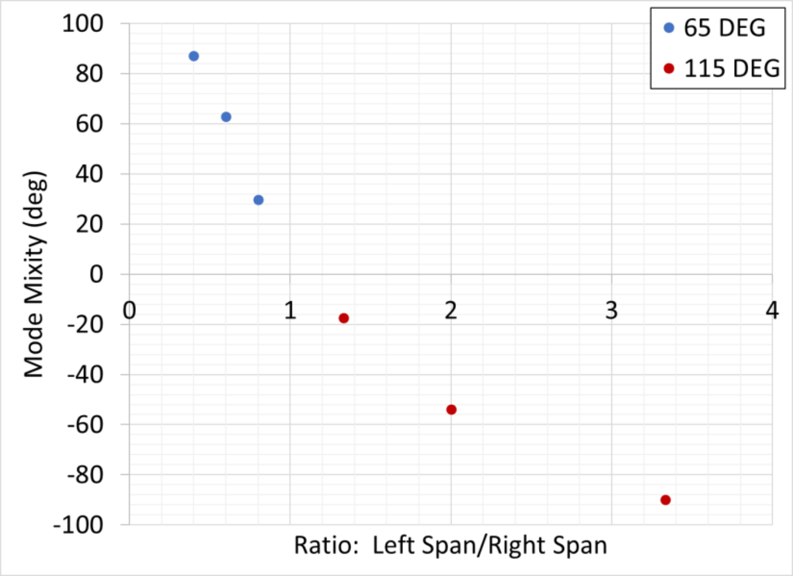

Figure A-4: Mode mixity for different crack inclination angles and span ratios

As shown, a full range of mixed-mode behavior is achieved with only two crack inclination angles. While this geometry is capable of producing the desired mixed-mode behavior, the shear and compression stresses ahead of the crack tip along the interface are not as uniform as those that are produced by the interfacial specimen geometry that was ultimately chosen for the present work. Since the length of the interface is equal to the radius of the test specimen, the interface is relatively short. At the uncracked edge of the interface, there remains a singularity (however not as strong as the singularity at the cracked edge of the interface). The potential interaction of these two singularities is not particularly desirable, and thus the reason that the other test specimen was chosen. The other test specimen, having a longer overall interface length, sufficiently separates these two stress singularities such that interaction is minimized. Even still, experimental investigations using this hybrid geometry could still provide beneficial contributions understanding the problem of interest.

Appendix B

Select Excerpts from Crack Tip Location Script

The work presented in this dissertation was accomplished using a variety of pre- and post-processing scripts primarily built in MATLAB®. This appendix seeks to highlight select excerpts from the crack tip location script. In the development of several sections of this code, specifically in the calculation of convolutions to determine the gradients, gradient magnitudes, and directions, open-source code published by Rachmawan [129] was adapted to be used for this work.

B.1. Initial input data and pre-processing

Several files are required to be defined for input into the edge detection script. Specifically, two separate files are required that contain the output displacement data from the image correlation process from each of the domains (upper and lower domain or left and right domain depending on the orientation of the data). These data files are formatted such that a cell array contains the displacement data at each frame in the image sequence as illustrated in Figure B-1.

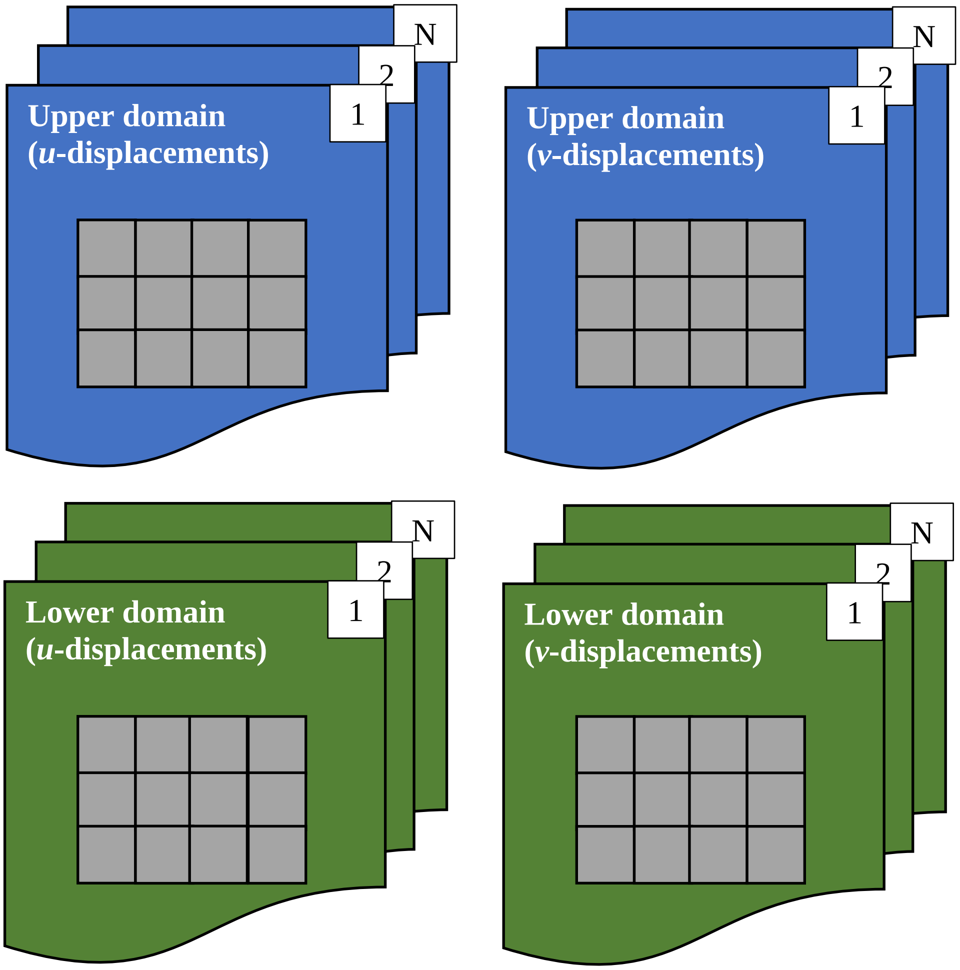

Figure B-1: Data format for edge detection script

For each image index, b $(1 \leq b \leq N)$, the relevant data files are read into the script and the upper domain is stitched to the lower domain and the magnitude is calculated. The code to extract the data array from the cell array and stitch it together is:

```
data_l_u = data_lower.disp(b).plot_u_ref_formatted;

data_l_v = data_lower.disp(b).plot_v_ref_formatted;

data_u_u = data_upper.disp(b).plot_u_ref_formatted;

data_u_v = data_upper.disp(b).plot_v_ref_formatted;

data_u_full = data_l_u + data_u_u;

data_v_full = data_l_v + data_u_v;

img = sqrt(plot_data_u_full.^2 + plot_data_v_full.^2);
```

A separate text file is read into the script to define the crack path. This text file contains the *x*- and *y*-positions of the crack path as calculated from an image of one of the failed test specimens which establishes a locus of possible crack tip points.

B.2. Computation of gradient information

For the current image, *b*, the resulting variable, *img*, contains the current image stitched displacement magnitudes. Once the upper and lower domain data is stitched together, a grid of coordinates is established based on the subset spacing:

```
sz = size(data_l_u);

for i = 1:sz(1)

     for j = 1:sz(2)

          x_coord_grid(i,j) = (j-1).*subset_spacing;

          y_coord_grid(i,j) = (i-1).*subset_spacing;

     end

end
```

The next step is to normalize the displacement magnitudes.

```
val_max = max(img(:));

val_min = min(img(:));

range = val_max - val_min;

image_normalized = (img - val_min) ./ range;

min_norm = 0;

max_norm = 1;

range2 = max_norm - min_norm;

image_normalized = (image_normalized*range2) + min_norm;

img_final(:,:,1) = image_normalized;

img = double (img_final);
```

The next step in the process is to apply the Gaussian filter and compute the gradients in the *x*- and *y*- directions. The Gaussian filter kernel, *B*, is used to filter the array, *img*, via convolution.

```
B = [2, 4, 5, 4, 2;

4, 9, 12, 9, 4;

5, 12, 15, 12, 5;

4, 9, 12, 9, 4;

2, 4, 5, 4, 2];

B = 1/159.* B;

A=conv2(img, B, 'same');
```

The *x*- and *y*- filtering kernels for gradient calculation are then defined and applied:

```
Grad_x = [-1, 0, 1; -2, 0, 2; -1, 0, 1];

Grad_y = [1, 2, 1; 0, 0, 0; -1, -2, -1];

X_Filter = conv2(A, Grad_x, 'same');

Y_Filter = conv2(A, Grad_y, 'same');
```

Gradient directions (variable = *Grad_Ang*) and magnitudes (variable = *magnitude2*) are then calculated:

```
Grad_Ang = atan2 (X_Filter, Y_Filter);

Grad_Ang = Grad_Ang*180/pi;

magnitude = (X_Filter.^2) + (Y_Filter.^2);

magnitude2 = sqrt(magnitude);
```

The directions calculation is then grouped according to the nearest 45° increment and stored in the variable *Grad_Ang2*. Once the direction calculations are grouped, the non-maximum suppression procedure can be accomplished based on the gradient angles in the variable *Grad_Ang2*. This portion is accomplished as follows and results in the variable, *BW*:

```
for i=2:len-1
    for j=2:wid-1
        if (Grad_Ang2(i,j)==0)
            BW(i,j) = (magnitude2(i,j) == ...
            max([magnitude2(i,j), magnitude2(i,j+1), ...
            magnitude2(i,j-1)]));
        elseif (Grad_Ang2(i,j)==45)
            BW(i,j) = (magnitude2(i,j) == ...
            max([magnitude2(i,j), magnitude2(i+1,j-1), ...
            magnitude2(i-1,j+1)]));
        elseif (Grad_Ang2(i,j)==90)
            BW(i,j) = (magnitude2(i,j) == ...
            max([magnitude2(i,j), magnitude2(i+1,j), ...
            magnitude2(i-1,j)]));
        elseif (Grad_Ang2(i,j)==135)
            BW(i,j) = (magnitude2(i,j) == ...
            max([magnitude2(i,j), magnitude2(i+1,j+1), ...
            magnitude2(i-1,j-1)]));
        end;
    end;
end;
```

B.3. Processing of gradient data to locate crack tip

Once the gradient magnitudes are known, the points in the image space are filtered out based on their proximity to the *x*- and *y*-positions (variables *x_near* and *y_near*) imported in from the text file containing the crack edge information:

```
BW = magnitude2;
for i = 1:len
    for j = 1:wid
        dist = ((i-y_near).^2 + (j-x_near).^2).^(0.5);
        min_dist = min(dist);
        if min_dist<10
            BW_new(i,j) = BW(i,j)*1;
        else
            BW_new(i,j) = BW(i,j)*0;
        end
    end
end
```

The resulting variable, *BW_new*, contains an array of gradient magnitude points that are above the desired threshold values and meet a couple of other criteria. Specifically, the values have been filtered out to only contain points that are close to the expected crack path. Second, the values are sufficiently high to avoid any noise. The next step is to locate a point just trailing the crack tip. Theoretically, the crack tip is located where the trail of gradient values regress down to zero as illustrated in earlier chapters (see Figure 6-14 and Figure 6-19). However, due to noise near the crack tip, it is more convenient to track a point that is at a small, but known, distance behind the physical crack tip. The variable, *spl_pt*, is used to define the value corresponding to the gradient magnitude at that desired point. The value of this variable is determined using the hysteresis analysis described in earlier sections. The code to locate this point in each image is as follows:

```
BW_min = abs(BW_new - spl_pts);

test_loc = min(min(BW_min));

[row,col] = find(BW_min==test_loc);
```

The resulting variables, *row* and *col*, are the *x*- and *y*-indices of the current crack tip position. This step is performed several times to track multiple points behind the crack tip to improve the technique and minimize the effects of any incorrectly identified points.

Appendix C

Select Excerpts from Hybrid DIC-FE Script

At the core of the present work is a technique to take displacement data measured from digital image correlation and automatically build a finite element model to conveniently extract fracture parameter quantities using robust domain-based algorithms built into commercial finite element codes. A script was developed in MATLAB® to perform this function. In the present work, several different versions of this script were created to handle specific nuances associated with the individual experimental approaches. However, this appendix documents select excerpts from the basic script that operates at the core of each of the derived scripts.

C.1. Initial input

The primary input to the script is a data file containing the *u*- and *v*-displacement data from a given frame in each experiment saved as a data structure containing all of the digital image correlation parameters. The data is loaded and then the relevant information is extracted into the data arrays *plot_data_u* and *plot_data_v*.

```
ncorr_filename = ‘DISP_DATA.mat’;

data = load(ncorr_filename);

subset_spacing =

     (data.dispinfo.spacing+1)*data.dispinfo.pixtounits;

plot_data_u = data.disp(b).plot_u_ref_formatted;

plot_data_v = data.disp(b).plot_v_ref_formatted;
```

C.2. Data processing and formatting

The size of the data array is then used to build a grid of *x*-coordinates and *y*-coordinates. An array of 1’s and 0’s is created based on which grid points have displacement values reported and which ones do not. The data arrays are then filtered based on the smoothing value (*smoothValue*) and neighborhood size (*nhoodSize*). The guided filter is a separate function based partially on the code presented in [130].

```
sz = size(plot_data_u);

for i = 1:sz(1)

     for j = 1:sz(2)

          x_grid(i,j) = (j-1).*subset_spacing;

          y_grid(i,j) = (i-1).*subset_spacing;

     end

end

submask = double(((plot_data_u~=0)));

filtered_u =

GUIDED_FILTER(u_data_gray,submask,smoothValue,nhoodSize);
```

Nested for loops are used to create a grid of node identification numbers and *x*- and *y*-coordinates. An if statement is used to limit the nodal coordinates to only points containing calculated displacements.

```
for i = 1:sz(1)
     for j = 1:sz(2)
          u_cur = plot_data_u(i,j);
          v_cur = plot_data_v(i,j);
          if flags(i,j)~=0
               node_id_grid(i,j) = w;
               x_coord_plot(i,j) = node1(i,j);
               y_coord_plot(i,j) = node2(i,j);
               w = w+1;
          else
          end
     end
end
```

For each point containing calculated displacement data, the surrounding points are evaluated to determine if a quadrilateral element can successfully be formed. If a quadrilateral can be formed, the element number and its associated nodes are stored in the ABAQUS® input deck node ordering format.

```
for i = 1:sz(1)-1

    for j = 1:sz(2)-1

        x_ind_el_nodes = [j:j+1];

        y_ind_el_nodes = [i:i+1];

        el_nodes = [y_ind_el_nodes' x_ind_el_nodes'];

        flag_test = flags([i:i+1],[j:j+1]);

        x_pts1 = [];y_pts1 = [];

        if all(all(flag_test)) == 1

            el_conn(el_id,:) =

            [el_id,node_id_grid(i,j),node_id_grid(i,j+1),..
            .
            node_id_grid(i+1,j+1),node_id_grid(i+1,j)];

            el_id = el_id+1;

        else

        end

    end

end
```

The displacement data in each direction is then ordered to associate it with its corresponding node number (variable name *full_node_list*) and write it to the ABAQUS® input deck.

```
for i = 1:sz(1)
    for j = 1:sz(2)
        u_cur = plot_data_u(i,j);
        v_cur = plot_data_v(i,j);
        w = node_id_grid(i,j);
        LI = (j-1)*sz(1)+i;
        if flags(i,j) && sum(sum(ismember(w,C)))==0
            if b==1
                full_node_list = [full_node_list;...
                [w x_coord_plot(i,j) y_coord_plot(i,j)]];
            end
            bc_array1 = [bc_array1;[w u_cur]];
            bc_array2 = [bc_array2;[w v_cur]];
        else
        end
    end
end
```

A range of desired contour domain radii is determined and a loop is used to identify the node sets associated with each circular contour domain.

```
rad_inc = [s_contour:s_contour:s_contour*n_contours];

for i = 1:length(rad_inc)

     n_ids_contour = find(node_list_radial(:,2)<rad_inc(i));

     contour_nodes = node_list_radial(n_ids_contour,1);

end
```

The nodes are formatted into node sets and written into the ABAQUS® input deck. A history output is created for each node set to force the software to perform the domain integral calculations on the desired circular contours of increasing radius.